

## **INFORMATION TO USERS**

**This manuscript has been reproduced from the microfilm master. UMI films the text directly from the original or copy submitted. Thus, some thesis and dissertation copies are in typewriter face, while others may be from any type of computer printer.**

**The quality of this reproduction is dependent upon the quality of the copy submitted. Broken or indistinct print, colored or poor quality illustrations and photographs, print bleedthrough, substandard margins, and improper alignment can adversely affect reproduction.**

**In the unlikely event that the author did not send UMI a complete manuscript and there are missing pages, these will be noted. Also, if unauthorized copyright material had to be removed, a note will indicate the deletion.**

**Oversize materials (e.g., maps, drawings, charts) are reproduced by sectioning the original, beginning at the upper left-hand corner and continuing from left to right in equal sections with small overlaps.**

**ProQuest Information and Learning  
300 North Zeeb Road, Ann Arbor, MI 48106-1346 USA  
800-521-0600**

**UMI<sup>®</sup>**



## **NOTE TO USERS**

**Page(s) not included in the original manuscript are unavailable from the author or university. The manuscript was microfilmed as received.**

**216-217**

**This reproduction is the best copy available.**

**UMI<sup>®</sup>**



**University of Alberta**

*Support Stiffness Effect on Tall Load Bearing Masonry Walls*

by

*Erum Mohsin*



**A thesis submitted to the Faculty of Graduate Studies and Research in partial fulfillment of  
the**

**Requirements for the degree of Doctor of Philosophy**

in

*Structural Engineering*

**Department of Civil and Environmental Engineering**

**Edmonton, Alberta**

*Spring 2005*



Library and  
Archives Canada

Bibliothèque et  
Archives Canada

0-494-08277-1

Published Heritage  
Branch

Direction du  
Patrimoine de l'édition

395 Wellington Street  
Ottawa ON K1A 0N4  
Canada

395, rue Wellington  
Ottawa ON K1A 0N4  
Canada

*Your file* *Votre référence*

*ISBN:*

*Our file* *Notre référence*

*ISBN:*

**NOTICE:**

The author has granted a non-exclusive license allowing Library and Archives Canada to reproduce, publish, archive, preserve, conserve, communicate to the public by telecommunication or on the Internet, loan, distribute and sell theses worldwide, for commercial or non-commercial purposes, in microform, paper, electronic and/or any other formats.

The author retains copyright ownership and moral rights in this thesis. Neither the thesis nor substantial extracts from it may be printed or otherwise reproduced without the author's permission.

**AVIS:**

L'auteur a accordé une licence non exclusive permettant à la Bibliothèque et Archives Canada de reproduire, publier, archiver, sauvegarder, conserver, transmettre au public par télécommunication ou par l'Internet, prêter, distribuer et vendre des thèses partout dans le monde, à des fins commerciales ou autres, sur support microforme, papier, électronique et/ou autres formats.

L'auteur conserve la propriété du droit d'auteur et des droits moraux qui protègent cette thèse. Ni la thèse ni des extraits substantiels de celle-ci ne doivent être imprimés ou autrement reproduits sans son autorisation.

---

In compliance with the Canadian Privacy Act some supporting forms may have been removed from this thesis.

Conformément à la loi canadienne sur la protection de la vie privée, quelques formulaires secondaires ont été enlevés de cette thèse.

While these forms may be included in the document page count, their removal does not represent any loss of content from the thesis.

Bien que ces formulaires aient inclus dans la pagination, il n'y aura aucun contenu manquant.

  
**Canada**

## **ABSTRACT**

This research investigates the behavior of tall masonry walls under the influence of reactive support stiffness. Current design practice does not recognize the effect of actual support stiffness in estimating masonry block wall load capacity and ignoring this effect leads to underestimated wall capacity. This indicates the need to evaluate the actual boundary conditions and to investigate the behavior of masonry tall walls in the context of actual boundary conditions.

The research has three main phases. The first phase encompasses the evaluation of support stiffness as a function of footing dimensions and supporting soil properties and then to simulate this support stiffness in a full scale testing setup. The support stiffness of commonly used strip footing foundations was evaluated for a variety of footing dimensions and soil properties. A full scale testing setup was designed by simulating the different levels of support stiffness. Eight wall specimens were tested into two groups with slenderness ratios of 28.6 and 33.9. All walls were loaded with a common load eccentricity ratio of 0.33. The test results were analyzed to study the effect of support condition on load capacity as well as on Flexural rigidity of the tested walls. The test results were found consistent.

In the second phase all wall specimens were modeled using a nonlinear finite element macro modeling approach. ABAQUS Explicit V 6.3 was used for analysis. The non-linear finite element model was verified against the test results

and found satisfactory. The model was then employed to perform a comprehensive parametric study. The support stiffness was considered a primary parameter and was combined with other geometric and material parameters. The axial capacity and the flexural rigidity of the walls were investigated under the coupled effect of these parameters.

In the third and final phase of the research, the results obtained from parametric study were utilized and non-linear regression analysis was performed. Two sets of equations to estimate the axial load capacity and the effective flexural rigidity under the effect of reactive support condition were obtained. Validity of proposed mathematical expressions was assessed using available experimental results and found satisfactory.

## **ACKNOWLEDGEMENTS**

I would like to express my sincere gratitude to my supervisor Dr A.E Elwi for not only providing me technical guidance throughout the research work but also to encourage me in all difficult phases of the thesis.

This research was funded by the Natural Sciences and Engineering Research Council of Canada (NSERC) and the University of Alberta. I would also like to acknowledge the valuable and kind assistance received to conduct this project from Alberta Masonry Contractors Association (North).

I would like to thank the University of Alberta I.F Morrison Laboratory Technicians Mr. Richard Helfrich and Larry Burden for their knowledgeable technical assistance during the experimental phase of the project. I greatly appreciate the help from all previous students in particular from Dr. Mohammad Behbahanifard for guiding me about ABAQUS Explicit.

# TABLE OF CONTENTS

Abstract

Acknowledgments

Table of Contents

List of Tables

List of Figures

List of Symbols and Abbreviations

<b>1.0 INTRODUCTION.....</b>	<b>1</b>
<b>1.1 Introduction.....</b>	<b>1</b>
<b>1.2 Scope and Objectives of the Thesis.....</b>	<b>2</b>
<b>1.3 Organization of the Thesis.....</b>	<b>4</b>
<b>2.0 LITERATURE REVIEW.....</b>	<b>6</b>
<b>2.1 Introduction.....</b>	<b>6</b>
<b>2.2 The Experimental Investigations.....</b>	<b>7</b>
<b>2.3 Analysis and Behavior of Masonry Block Walls.....</b>	<b>9</b>
<b>2.4 Finite Element Modeling and Material Constitutive Relationship.....</b>	<b>16</b>
<b>2.5 Flexural Rigidity.....</b>	<b>22</b>
<b>3.0 EXPERIMENTAL PROGRAM.....</b>	<b>31</b>
<b>3.1 Introduction .....</b>	<b>31</b>
<b>3.2 Numerical Estimation of Support Stiffness.....</b>	<b>32</b>
<b>3.3 Material Testing.....</b>	<b>34</b>

## TABLE OF CONTENTS (Cont.)

3.3.1	Masonry Assemblages.....	34
3.3.2	Mortar and Grout.....	34
3.3.3	Steel Reinforcement.....	35
3.4	Test Specimens and Test Setup.....	35
3.4.1	System for Vertical Load Application.....	36
3.4.2	Lateral Bracing System.....	37
3.4.3	Simulation of Support Stiffness.....	37
3.5	Instrumentation.....	38
3.6	Testing Procedure.....	38
3.7	Test Observations.....	39
3.7.1	Group-I (5-meter Tall Walls – $h/t = 28.6$ ).....	39
3.7.2	Group-II: (6-meter Tall Walls – $h/t = 33.9$ ).....	41
3.8	Test Results and Discussions.....	42

## 4.0 FLEXURAL RIGIDITY OF LOAD BEARING MASONRY

<b>BLOCK WALLS</b> .....	69
4.1 Introduction .....	69
4.2 Effective Flexural Rigidity ( $EI_{eff}$ ) of Masonry Block Walls .....	69
4.3 Evaluation of Flexural Rigidity of Masonry Block Walls .....	71
4.4 Evaluation of Flexural Rigidity from Experimental Data.....	73
4.4.1 Comparison of Flexural rigidity of Group-I and Group-II.....	75

## TABLE OF CONTENTS (Cont.)

4.5	Comparison of Experimentally Obtained $EI_{eff}$ to CSA S304.1 values .....	76
<b>5.0</b>	<b>NUMERICAL ANALYSIS.....</b>	<b>82</b>
5.1	Introduction .....	82
5.2	Numerical Model.....	82
5.2.1	Element Type.....	83
5.2.2	Approach of Finite Element Mesh.....	83
5.2.3	Material Properties.....	85
5.2.4	Solution Control.....	88
5.3	Simulation of Test Results.....	90
5.3.1	Load Deflection Characteristics.....	91
5.3.2	Load-rotation Characteristics.....	94
5.3.3	Load Moment Characteristics.....	96
5.3.4	Deflected Shapes.....	97
5.3.4	Effective Flexural Rigidity ( $EI_{eff}$ ).....	101
<b>6.0</b>	<b>PARAMETRIC STUDY.....</b>	<b>135</b>
6.1	Introduction .....	135
6.2	Numerical Model.....	135
6.3	Selection of Parameters for the Numerical Study.....	136
6.3.1	Constant Parameters.....	136
6.3.2	Primary Parameter.....	137

## TABLE OF CONTENTS (Cont.)

6.3.3	Secondary Parameters.....	138
6.4.	Combination of Parameters.....	140
6.5	Output Parameters.....	140
6.6	Failure Modes.....	141
6.7	Results and Discussions.....	142
6.7.1	Effect of Support Stiffness.....	142
6.7.2	Effect of Support Stiffness on Flexural Rigidity(EI).....	152
6.8	Behavior of Masonry Walls with no Support Stiffness.....	155

## 7.0 REGRESSION MODEL FOR AXIAL LOAD CAPACITY AND

## FLEXURAL RIGIDITY .....196

7.1	Introduction .....	196
7.2	Axial Load Capacity.....	197
7.2.1	Parameters affecting the Axial Load Capacity.....	197
7.2.2	Development of Equation for the estimation of the normalized Axial Load Capacity.....	199
7.2.3	Assessment of Regression Model for Axial Load Capacity.....	202
7.3	Flexural Rigidity.....	205
7.3.1	Parameters affecting the Flexural Rigidity.....	205
7.3.2	Development of Equation for the Estimation of Effective Flexural Rigidity.....	207

## **TABLE OF CONTENTS (Cont.)**

<b>7.3.3 Assessment of Regression Model for Rigidity Ratio.....</b>	<b>209</b>
<b>7.4 Comparison of Regression Model with Current Canadian Masonry Design</b>	
Code-S304.1-94.....	211
<b>8.0 SUMMARY, CONCLUSIONS AND RECOMMENDATIONS.....</b>	<b>254</b>
<b>8.1 Summary .....</b>	<b>254</b>
<b>8.2 Conclusions.....</b>	<b>256</b>
<b>8.3 Recommendations for Future Research.....</b>	<b>258</b>
<b>REFERENCES.....</b>	<b>259</b>

## LIST OF TABLES

### **Chapter 3**

Table 3.1	Modulus of sub-grade reaction of different soils.....	46
Table 3.2	Relationship between numerical and simulated support stiffness...	46
Table 3.3(a)	Compressive strength of hollow concrete block prisms.....	47
Table 3.3(b)	Compressive strength of grouted concrete block prisms.....	47
Table 3.3(c)	Modulus of elasticity of concrete block prisms.....	47
Table 3.4(a)	Compressive strength of mortar.....	48
Table 3.4(b)	Compressive strength of grout.....	48
Table 3.5	Properties of steel rebars.....	48
Table 3.6	Specifications of test specimens.....	49
Table 3.7	Summary of test results.....	50
Table 3.8	Relative increase in axial load capacity.....	50

### **Chapter 4**

Table 4.1	Effective flexural rigidity obtained from experimental data.....	78
Table 4.2	Numerical comparison of experimental $EI_{eff}$ with CSA S304.1....	78

### **Chapter 5**

Table 5.1	Material parameters of masonry.....	104
Table 5.2	Summary of analysis results.....	105

### **Chapter 6**

Table 6.1 (a)	Combination of different parameters at support stiffness = 0kN-m/rad.....	158
Table 6.1 (b)	Combination of different parameters at support stiffness =500 and 1000 kN-m/rad.....	159
Table 6.1 (c)	Combination of different parameters at support stiffness =5000kN-m/rad.....	160
Table 6.1 (d)	Combination of different parameters at support stiffness =10,000kN-m/rad.....	161

### **Chapter 7**

Table 7.1	Finite element data for regression analysis.....	216
Table 7.2	Comparison of load capacity and rigidity ratio with S304.1-94.....	217

## LIST OF FIGURES

### **Chapter 2**

Figure 2.1	Boundary conditions (after Yokel 1971).....	29
Figure 2.2	Equivalent column (after Colville 1979).....	29
Figure 2.3	Concept of representative volume element (RVE) in material homogenization (after Ma et al. 2001).....	29
Figure 2.4	Moment curvature relationship limits of flexural rigidity (after Aboud et al. 1995).....	30
Figure 2.5	$\frac{EI_{eff}}{EI_0}$ versus load eccentricity ratio (after Liu and Dawe 2003)....	30

### **Chapter 3**

Figure 3.1	Numerical model of strip footing.....	51
Figure 3.2 (a)	Typical failure of grouted prism.....	52
Figure 3.2 (b)	Typical failure of un-grouted prism.....	52
Figure 3.3	Standard grout tests.....	53
Figure 3.4	Typical cross-section of wall specimen.....	53
Figure 3.5	Alignment of vertical rebar.....	54
Figure 3.6	Test set-up details.....	55
Figure 3.7	Test set-up photo.....	56
Figure 3.8	Details of boundary conditions-top assembly details.....	57
Figure 3.9	Bottom boundary conditions .....	57
Figure 3.10	Photo of simulated support stiffness.....	58
Figure 3.11	Instrumentation details.....	59
Figure 3.12	Local failure of W1.....	60
Figure 3.13	Cracking of W3 at failure.....	60
Figure 3.14	Typical deflected shape of Group-I walls at failure.....	61
Figure 3.15	Typical deflected shape of Group-II walls at failure.....	62

## LIST OF FIGURES(Cont.)

### **Chapter 3(Cont.)**

Figure 3.16	Simulated support stiffness versus eccentric axial load at failure.....	63
Figure 3.17	Load deflection response of Group-I.....	64
Figure 3.18	Load deflection response of Group-II.....	64
Figure 3.19	Deflection at failure along the height of walls f Group-I.....	65
Figure 3.20	Deflection at failure along the height of walls f Group-II.....	65
Figure 3.21	Total bending moment at failure along the height of Group-I....	66
Figure 3.22	Total bending moment at failure along the height of Group-II....	66
Figure 3.23	Blown-up plot of deflection at failure of bottom part of Group-II.....	67
Figure 3.24	Blown-up plot of deflection at failure of bottom part of Group-I.....	67
Figure 3.25	Trend of mid-span deflection at failure of Group-II.....	68
Figure 3.26	Trend of maximum bending moment at failure of Group-II.....	68

### **Chapter 4**

Figure 4.1	Boundary conditions of masonry wall with support stiffness.....	79
Figure 4.2	Boundary conditions of masonry wall without support stiffness.	79
Figure 4.3	Flexural rigidity versus eccentric axial load (Group-I).....	80
Figure 4.4	Flexural rigidity versus eccentric axial load (Group-II).....	80
Figure 4.5	Effective stiffness versus support stiffness.....	81

### **Chapter 5**

Figure 5.1	Finite element mesh.....	106
Figure 5.2(a)	Uni-axial response of concrete in tension (after Hibbitt et al. 2002).....	107
Figure 5.2(b)	Uni-axial response of concrete in compression (after Hibbitt et al. 2002).....	107
Figure 5.3(a)	Typical stress-displacement curve.....	108
Figure 5.3(b)	Typical stress-strain curve for compression.....	108

## LIST OF FIGURES (Cont.)

### *Chapter 5(Cont.)*

Figure 5.4	Smooth load step curve.....	109
Figure 5.5	Typical energy history curves.....	109
Figure 5.6	Cross-sectional details of beam element.....	110
Figure 5.7	Load deflection response of specimen W1.....	111
Figure 5.8	Load deflection response of specimen W2.....	111
Figure 5.9	Load deflection response of specimen W3.....	112
Figure 5.10	Load deflection response of specimen W4.....	112
Figure 5.11	Load deflection response of specimen W5.....	113
Figure 5.12	Load deflection response of specimen W6.....	113
Figure 5.13	Load deflection response of specimen W7.....	114
Figure 5.14	Load deflection response of specimen W8.....	114
Figure 5.15	Load versus Bottom rotation of specimen W1.....	115
Figure 5.16	Load versus bottom rotation of specimen W2.....	115
Figure 5.17	Load versus bottom rotation of specimen W3.....	116
Figure 5.18	Load versus bottom rotation of specimen W4.....	116
Figure 5.19	Load versus bottom rotation of specimen W5.....	117
Figure 5.20	Load versus bottom rotation of Specimen W6.....	117
Figure 5.21	Load versus bottom rotation of specimen W7.....	118
Figure 5.22	Load versus bottom rotation of specimen W8.....	118
Figure 5.23	Load versus mid-span bending moment of specimen W1.....	119
Figure 5.24	Load versus mid-span bending moment of specimen W2.....	119
Figure 5.25	Load versus mid-span bending moment of specimen W3.....	120
Figure 5.26	Load versus mid-span bending moment of specimen W4.....	120
Figure 5.27	Load versus mid-span bending moment of specimen W5.....	121
Figure 5.28	Load versus mid-span bending moment of specimen W6.....	121
Figure 5.29	Load versus mid-span bending moment of specimen W7.....	122
Figure 5.30	Load versus mid-span bending moment of specimen W8.....	122

## LIST OF FIGURES (Cont.)

### *Chapter 5(Cont.)*

Figure 5.31	Bending moment along wall height at local failure of Specimen W1.....	123
Figure 5.32	Deflection along wall height at local failure of specimen W1....	123
Figure 5.33	Bending moment along wall height at local failure of Specimen W2.....	124
Figure 5.34	Deflection along wall height at local failure of specimen W2....	124
Figure 5.35	Bending moment along wall height at failure of specimen W3.....	125
Figure 5.36	Deflection along wall height at failure of specimen W3.....	125
Figure 5.37	Bending moment along wall height at failure of specimen W4..	126
Figure 5.38	Deflection along wall height at failure of specimen W4.....	126
Figure 5.39	Bending moment along wall height at failure of specimen W5..	127
Figure 5.40	Deflection along wall height at failure of specimen W5.....	127
Figure 5.41	Bending moment along wall height at failure of specimen W6..	128
Figure 5.42	Deflection along wall height at failure of specimen W6.....	128
Figure 5.43	Bending moment along wall height at failure of specimen W7..	129
Figure 5.44	Deflection along wall height at failure of specimen W7.....	129
Figure 5.45	Bending moment along wall height at failure of specimen W8..	130
Figure 5.46	Deflection along wall height at failure of specimen W8.....	130
Figure 5.47	Load versus Flexural rigidity of specimen W1.....	131
Figure 5.48	Load versus Flexural rigidity of specimen W2.....	131
Figure 5.49	Load versus Flexural rigidity of specimen W3.....	132
Figure 5.50	Load versus Flexural rigidity of specimen W4.....	132
Figure 5.51	Load versus Flexural rigidity of specimen W5.....	133
Figure 5.52	Load versus Flexural rigidity of specimen W6.....	133
Figure 5.53	Load versus Flexural rigidity of specimen W7.....	134
Figure 5.54	Load versus Flexural rigidity of specimen W8.....	134

## LIST OF FIGURES (Cont.)

### Chapter 6

Figure 6.1	Finite element modeling of masonry wall.....	162
Figure 6.2	Compressive strength of masonry for 15 MPa unit strength.....	163
Figure 6.3	Typical material curve.....	164
Figure 6.4	Location of equivalent plastic strains in the wall cross-section....	165
Figure 6.5	Normalized axial load capacity versus support stiffness for variable slenderness ratio( $NC = 3$ ).....	166
Figure 6.6	Normalized load deflection response showing effect of support stiffness at various slenderness ratios ( $e/t = 0.1, NC = 3$ ).....	167
Figure 6.7	Normalized mid-span deflection versus support stiffness at various slenderness ratios ( $e/t = 0.1, NC = 3$ ).....	168
Figure 6.8	Wall deflection at failure under influence of support stiffness at various slenderness ratios ( $e/t = 0.1, NC = 3$ ).....	169
Figure 6.9	Bending moment along the wall height at failure under influence of support stiffness at various slenderness ratios ( $e/t = 0.1, NC = 3$ ).....	170
Figure 6.10	Equivalent plastic strains versus support stiffness at $e/t = 0.1$ .....	171
Figure 6.11	Normalized load deflection response showing effect of support stiffness at various slenderness ratios ( $e/t = 0.33, NC = 3$ ).....	172
Figure 6.12	Wall deflection at failure under influence of support stiffness at various slenderness ratios ( $e/t = 0.33, NC = 3$ ).....	173
Figure 6.13	Bending moment along the wall height at failure under influence of support stiffness at various slenderness ratios ( $e/t = 0.33, NC = 3$ ).....	174
Figure 6.14	Normalized mid-span deflection versus support stiffness at various slenderness ratios ( $e/t = 0.33, NC = 3$ ).....	175
Figure 6.15	Equivalent plastic strains versus support stiffness at $e/t = 0.33$ ...	176
Figure 6.16	Load versus mid-span bending moment ( $h/t=30, e/t=0.1, NC=3$ ).....	177

## LIST OF FIGURES (Cont.)

### *Chapter 6(Cont.)*

Figure 6.17	Mid-span bending moment versus support stiffness for constant slenderness ratios ( $NC = 3$ ).....	178
Figure 6.18	Load deflection response for variable amount of grouting at constant support stiffness ( $h/t = 30, e/t = 0.1$ ).....	179
Figure 6.19	Plots of equivalent plastic strain showing effect of grouting under the influence of support stiffness ( $h/t = 30, e/t = 0.1$ ).....	180
Figure 6.20	Load deflection response showing effect of grouting at various support stiffness ( $h/r = 36, e/t = 0.1$ ).....	181
Figure 6.21	Equivalent plastic strain showing effect of grouting under the influence of support stiffness.....	182
Figure 6.22	Load deflection response showing effect of grouting ( $h/t = 30, e/t = 0.33$ ).....	183
Figure 6.23	Equivalent plastic strain showing effect of grouting under influence of support stiffness ( $h/t = 30, e/t = 0.33$ ).....	184
Figure 6.24	Load deflection response showing effect of grouting under influence of support stiffness ( $h/t = 36, e/t = 0.33$ ).....	185
Figure 6.25	Equivalent plastic strain showing effect of grouting under influence of support stiffness ( $h/t = 36, e/t = 0.33$ ).....	186
Figure 6.26	Effect of load eccentricity at various levels of support stiffness ( $h/t = 30, NC = 3$ ).....	187
Figure 6.27	Effect of load eccentricity at various levels of support stiffness ( $h/t = 36, NC = 3$ ).....	188
Figure 6.28	Normalized axial load capacity versus support stiffness at various $e/t$ ratios ( $NC = 3$ ).....	189
Figure 6.29	Flexural rigidity versus eccentric axial load (N-mm <sup>2</sup> ) ( $NC = 3, e/t = 0.1$ ).....	190
Figure 6.30	Flexural rigidity versus eccentric axial load (N-mm <sup>2</sup> ) ( $NC = 3, e/t = 0.33$ ).....	191

## LIST OF FIGURES(Cont.)

### *Chapter6(Cont.)*

Figure 6.31	Flexural rigidity versus eccentric axial load (NC = 3, e/t = 0.42).....	192
Figure 6.32	Effective Flexural rigidity versus support stiffness (NC=3).....	193
Figure 6.33	Load deflection response of stocky walls without support stiffness at variable amount of grouting (h/t = 18).....	194
Figure 6.34	Normalized load deflection response without support stiffness for various slenderness ratios.....	195

### *Chapter7*

Figure 7.1	Normalized axial load capacity versus slenderness ratio at NC = 3 for constant support stiffness ratio.....	218
Figure 7.2	Normalized axial load capacity versus load eccentricity ratio at NC = 3 for constant support stiffness ratio.....	219
Figure 7.3	Normalized axial load capacity versus slenderness ratio at NC = 3 for constant support stiffness ratio.....	220
Figure 7.4	Normalized axial load capacity versus load eccentricity ratio at NC = 3 for constant support stiffness ratio.....	221
Figure 7.5	Variation of normalized axial load predictions against support stiffness ratio at h/t = 30.....	222
Figure 7.6	Variation of normalized axial load predictions against support stiffness ratio at h/t = 36.....	223
Figure 7.7	Variation of normalized axial load predictions against support stiffness ratio at h/t = 42.....	224
Figure 7.8	Variation of normalized axial load predictions against support stiffness ratio at e/t = 0.42.....	225
Figure 7.9	Variation of normalized axial load predictions against load eccentricity ratio at r = 0.....	226
Figure.7.10	Variation of normalized axial load predictions against load eccentricity ratio at r = 0.03.....	227

## LIST OF FIGURES(Cont.)

### *Chapter7(Cont.)*

Figure 7.11	Variation of normalized axial load predictions against load eccentricity ratio at $r = 0.05$ .....	228
Figure 7.12	Variation of normalized axial load predictions against load eccentricity ratio at $r = 0.26$ .....	229
Figure 7.13	Variation of normalized axial load predictions against slenderness ratio at $r = 0$ .....	230
Figure 7.14	Variation of normalized axial load predictions against slenderness ratio at $r = 0.03$ .....	231
Figure 7.15	Variation of normalized axial load predictions against slenderness ratio at $r = 0.05$ .....	232
Figure 7.16	Variation of normalized axial load predictions against slenderness ratio at $r = 0.26$ .....	233
Figure 7.17	Scatter of the normalized axial load data.....	234
Figure 7.18	Correlation between flexural rigidity ratio and slenderness ratio at constant support stiffness ratio.....	235
Figure 7.19	Correlation between flexural rigidity ratio and load eccentricity ratio at constant support stiffness ratio.....	236
Figure 7.20	Correlation between flexural rigidity ratio and slenderness ratio at constant load eccentricity ratio.....	237
Figure 7.21	Correlation between flexural rigidity ratio and load eccentricity ratio at constant slenderness ratio.....	238
Figure 7.22	Variation of flexural rigidity ratio predictions against support stiffness ratio at $e/t = 0.1$ .....	239
Figure 7.23	Variation of flexural rigidity ratio predictions against support stiffness ratio at $e/t = 0.33$ .....	240
Figure 7.24	Variation of flexural rigidity ratio predictions against support stiffness ratio at $e/t = 0.42$ .....	241

## LIST OF FIGURES(Cont.)

### *Chapter7(Cont.)*

Figure 7.25	Variation of flexural rigidity ratio predictions against support stiffness ratio at $h/t = 30$ .....	242
Figure 7.26	Variation of flexural rigidity ratio predictions against support stiffness ratio at $h/t = 36$ .....	243
Figure 7.27	Variation of flexural rigidity ratio predictions against support stiffness ratio at $h/t = 42$ .....	244
Figure 7.28	Variation of flexural rigidity ratio predictions against load eccentricity ratio at support stiffness ratio = 0.....	245
Figure 7.29	Variation of flexural rigidity ratio predictions against load eccentricity ratio at support stiffness ratio = 0.03.....	246
Figure 7.30	Variation of flexural rigidity ratio predictions against load eccentricity ratio at support stiffness ratio = 0.05.....	247
Figure 7.31	Variation of flexural rigidity ratio predictions against load eccentricity ratio at support stiffness ratio = 0.26.....	248
Figure 7.32	Variation of flexural rigidity ratio predictions against slenderness ratio at support stiffness ratio = 0.....	249
Figure 7.33	Variation of flexural rigidity ratio predictions against slenderness ratio at support stiffness ratio = 0.03.....	250
Figure 7.34	Variation of flexural rigidity ratio predictions against slenderness ratio at support stiffness ratio = 0.05.....	251
Figure 7.35	Variation of flexural rigidity ratio predictions against slenderness ratio at support stiffness ratio = 0.26.....	252
Figure 7.36	Scatter of flexural rigidity ratio data.....	253

## LIST OF SYMBOLS AND ABBREVIATIONS

<b>A<sub>s</sub></b>	Total area of vertical rebars
<b>A<sub>e</sub></b>	Effective cross-sectional area of masonry wall
<b>b</b>	Thickness of the foundation wall
<b>B</b>	Width of the strip footing base
<b>c<sub>1</sub>,c<sub>2</sub>,c<sub>3</sub>,c<sub>4</sub></b>	Constants
<b>C<sub>L</sub></b>	Centerline
<b>C<sub>m</sub></b>	Factor to incorporate unequal moment conditions
<b>D1</b>	Height of foundation wall
<b>D2</b>	Thickness of strip footing base
<b>d<sub>c</sub></b>	Damage parameter
<b>e</b>	Load eccentricity
<b>e<sub>a</sub></b>	Actual load eccentricity
<b>e<sub>1</sub></b>	Wall top eccentricity
<b>e<sub>2</sub></b>	Wall bottom eccentricity
<b>e<sub>k</sub></b>	$= \frac{S}{A_e}$
<b>e/t</b>	Load eccentricity ratio
<b>E</b>	Modulus of elasticity
<b>E<sub>0</sub></b>	Initial modulus of elasticity
<b>E'</b>	Instantaneous tangent elastic modulus
<b>E<sub>i</sub></b>	Initial tangent modulus of elasticity
<b>E<sub>m</sub></b>	Modulus of elasticity of masonry assemblage
<b>EI</b>	Flexural rigidity
<b>EI<sub>eff</sub></b>	Effective flexural stiffness
<b>(EI)<sub>cr</sub></b>	Cracked section flexural stiffness
<b>E<sub>m</sub> I<sub>0</sub></b>	Flexural stiffness of un-cracked masonry wall cross-section
<b>EI<sub>0</sub></b>	Flexural stiffness of un-cracked masonry wall cross-section
<b>E<sub>m</sub> I<sub>cr</sub></b>	Flexural stiffness of cracked masonry wall cross-section
<b>(EI)<sub>g</sub><sup>f</sup></b>	Modified gross-section flexural rigidity

## LIST OF SYMBOLS AND ABBREVIATIONS (Contd.)

<b><math>f_1, f_2</math> and <math>f_3</math></b>	Individual functions to represent the behavior of different parameters
<b>{F}</b>	Force vector
<b>FEM</b>	Finite element method
<b><math>F_n</math></b>	Normal force per unit length of joint element
<b><math>F_s</math></b>	Shear force per unit length of joint element
<b><math>f_m</math></b>	Compressive strength of masonry assemblage
<b><math>f_y</math></b>	Yield strength of steel reinforcement
<b>G'</b>	Shear modulus related to a particular state of shear stress
<b>h</b>	Clear height of wall above the base
<b>h/t</b>	Slenderness ratio of wall
<b>I</b>	Moment of inertia of masonry wall cross-section
<b><math>I_g</math></b>	Gross moment of inertia
<b><math>I_n</math></b>	Moment of inertia of un-cracked section
<b><math>I_0</math></b>	Moment of inertia of un-cracked section
<b><math>I_g^f</math></b>	Modified moment of inertia of gross-section
<b>k</b>	$= \sqrt{\frac{P}{EI}}$
<b>kh</b>	Effective height of wall
<b>[k]</b>	Material property matrix
<b><math>k_n</math></b>	Joint stiffness per unit length normal to join
<b><math>k_s</math></b>	Joint stiffness per unit length parallel to join
<b>K</b>	Effective length factor
<b>L</b>	Wall height
<b><math>L_h</math></b>	Wall span
<b>LVDT</b>	Linear variable displacement transducer
<b>M</b>	Bending moment
<b><math>M_1</math></b>	Moment at bottom of wall
<b><math>M_2</math></b>	Moment at top of wall
<b><math>M_{cr}</math></b>	Cracking bending moment

## LIST OF SYMBOLS AND ABBREVIATIONS (Contd.)

$M_{max}$	Maximum bending moment
$M_u$	Ultimate bending moment
NC	Number of grouted cores
P	Axial compressive load
$P_c$	Critical buckling load
$P_0$	Cross-sectional axial load capacity
$P_{cr}$	Critical buckling load
$P_{ec}$	Equivalent critical load
$P_E$	Euler buckling load
$P_f$	Factored axial load
$P_u$	Ultimate axial load
$(P/P_0)_{predicted}$	Predicted load capacity ratio
$(P/P_0)_{actual}$	Actual capacity ratio
r	Support stiffness ratio
$r_g$	Radius of gyration
R	Support stiffness
$R^2$	Coefficient of multiple determinations
$R_m$	Moment ratio
RVE	Representative volume element
S	Section modulus
SS	Support stiffness
SSS	Simulated support stiffness
SSSM	Simulates support stiffness moment
t	Wall thickness
T	Wall thickness
$t_m$	Mortar joint thickness
URM	Un-reinforced masonry walls
$u_1$	Load eccentricity
$u_c$	Cracking displacement

## LIST OF SYMBOLS AND ABBREVIATIONS (Contd.)

$\{W\}$	Relative displacement vector for joint element
$w_n$	Displacement normal to joint
$w_s$	Displacement parallel to joint
$w$	wall width
$x$	Distance from top of wall to any point of interest along the wall height
$y$	Wall deflection
$Y$	Wall deflection at specified location along the wall height
$\beta$	Factor to incorporate different load conditions
$\Delta$	Deflection
$\Delta_{cr}$	Cracking displacement
$\varepsilon_c$	Compressive strain
$\varepsilon_t$	Strain at tension face
$\varepsilon_c$	Strain at compression face
$\bar{\varepsilon}$	Variation of eccentricity along wall height
$\varepsilon_c$	Compressive strain
$\varepsilon_t$	Tensile strain
$\varepsilon_c^{el}$	Elastic compressive strain
$\varepsilon_t^{el}$	Elastic tensile strain
$\varepsilon_t^{\sim pl}$	Equivalent tensile plastic strain
$\varepsilon_c^{\sim pl}$	Equivalent compressive plastic strain
$\varepsilon_t^{\sim pl}$	Equivalent tensile plastic strain
$\varepsilon_c^{\sim in}$	Inelastic compressive strain
$\tilde{\varepsilon}_t^{pl}$	Tensile plastic strain of concrete
$\tilde{\varepsilon}_c^{pl}$	Compressive plastic strain of concrete
$\lambda$	Constant to incorporate different load conditions
$\phi$	Curvature of masonry wall
$\Phi_m$	Resistance factor of the ultimate limit states
$\sigma_m$	Masonry compressive stress
$\sigma_c$	Compressive stress of concrete

## **LIST OF SYMBOLS AND ABBREVIATIONS (Contd.)**

$\sigma_t$	Tensile stress of concrete
$\sigma_{t0}$	Failure tensile stress
$\sigma_{c0}$	Initial uni-axial compressive stress
$\sigma_{cu}$	Ultimate uni-axial compressive stress
$\theta$	Bottom rotation of wall
$\nu_c$	Poisson's ratio

# **CHAPTER 1**

## **INTRODUCTION**

### **1.1 Introduction**

The advantages of masonry construction such as durability, sound protection, fire protection and above all simple construction procedure have promoted its use in commercial buildings. Among different types of masonry construction masonry load bearing block walls are the most frequently used structural components in the construction of industrial buildings (Drysdale and Hamid 2001). The desired characteristics of a masonry load bearing wall in structural application are the capability to resist eccentric axial load and out of plane bending by offering adequate axial capacity and bending stiffness. To acquire effective structural application a rationalized design procedure is vital.

The development of a rational design procedure of slender masonry wall has been a challenging task. Continuous research efforts to improve design rules have redirected the design process from working stress design method to limit state design method. Better understanding of masonry as a material and better understanding of behavior of load bearing walls has promoted the use of tall masonry walls in building construction with increasingly higher slenderness ratios.

Researchers (Colville 1979, Hatzinikolas et al. 1980, Hamid and Drysdale 1980, Suwalski and Drysdale 1986) have recognized that without considering material and geometric non-linearity it is not possible to adequately design masonry load bearing walls. Many researchers have tested tall masonry walls (Hatzinikolas et al. 1978, Amrhein et al. 1982). Up to some extent the current Canadian code (S304.1) has incorporated the findings of research in calculating the axial load capacity of masonry load bearing block walls. However, there are some aspects related to behavior of masonry load bearing walls such as rational estimate of

flexural rigidity and realistic consideration of boundary conditions that require further consideration.

For instance while calculating the axial load capacity of slender masonry load bearing block walls the current Canadian code does not allow an effective length factor less than 1, which reflects lack of information regarding the influence of boundary conditions on axial load carrying capacity of the walls. According to research work (Liu et al. 1998) on behavior of slender masonry load bearing walls, the current Canadian masonry code conservatively estimates the effective flexural rigidity of such walls, which in turn results in gross underestimation of the wall capacity. In order to improve the current design rules related to estimation of axial load capacity it is necessary to investigate aspects of masonry load bearing wall behavior that have not been addressed yet or need further investigation. This thesis examines two aspects, flexural rigidity and boundary conditions. To achieve this goal it is required to perform full scale testing of masonry load bearing walls by simulating actual support conditions in the testing so that more data can be generated to predict the behavior of the slender load bearing masonry block walls and recommendations can be made towards more rationalized design rules.

## **1.2 Scope and Objectives of the Thesis**

Evaluation of the critical buckling load of tall load bearing masonry block walls is one of the basic design criteria in the magnified moment method. The critical load is based on effective height and effective stiffness ( $EI_{eff}$ ) of the wall. Traditionally, masonry construction methods provide dowel reinforcement between the support and the wall at locations of grouted and reinforced cores. The support for masonry walls may be reinforced concrete strip footings or grade beams. The flexural strength of the base connection is not smaller than the strength of any cracked block wall joint. However, there is no clear guideline in the current standards to incorporate the effect of the restraint at the base on the

stiffness and load bearing capacity of masonry block walls. This thesis is focused on the effect of reactive restraints implied by support conditions on the behavior of load bearing masonry block walls carrying eccentric loads. There may be several possibilities of support conditions that can influence the bottom rotation of the wall. Because of the frequent use of strip type foundation in construction of slender masonry load bearing walls, the current study focuses on this type for the purpose of exploring the wall-support interaction.

To achieve the goal of the thesis it is necessary to estimate the rotational stiffness of the strip foundation as a function of soil properties and strip-footing dimensions. This allows a starting point for full scale testing of masonry load bearing walls with different support restraints at the wall bottom. Traditional testing of masonry walls has relied on constant top and bottom eccentricities. To the best of the author's knowledge, the type of testing proposed in this thesis, using reactive boundary conditions rather than constant eccentricities has not been used before.

Following the full scale testing the next objective is to develop a numerical model capable to deal with geometric as well as material non-linearity and then verify the numerical model by predicting the experimental results. Due to limited time and laboratory resources it is not possible to conduct experimental investigation with a full range of parameters on the wall behavior. The range of rotational stiffness generated by different types of support conditions, which are encountered in practice, can be further explored in an extensive numerical parametric study. Conventional design practice of masonry load bearing walls mainly deals with the axial load carrying capacity by estimating effective flexural rigidity, including P- $\Delta$  effects but ignoring effects of actual boundary conditions. In order to investigate the effect of support stiffness on the wall behavior, the current study aims directly to estimate the effect of support restraint on load carrying capacity and flexural rigidity of the wall so that design rules of current Canadian code can be reviewed.

The axial load carrying capacity is investigated under the coupled effect of several geometric, material and support condition parameters. Alternately, effective flexural rigidity is a strongly representative estimate of wall behavior, comprising the geometric and material properties as well as support conditions of the wall. Therefore, the current study also attempts to correlate the support stiffness and other parameters with the flexural rigidity of the wall. The study stops short of correlating the effective stiffness obtained in the context of this thesis with the axial load carrying capacity. This could be the base of future work.

### **1.3 Organization of the Thesis**

The thesis consists of eight chapters. Chapter one describes the scope and objective of the current study. In chapter two, literature review related to testing, numerical modeling, block masonry material models and flexural rigidity of tall masonry block wall is presented.

Chapter three describes the numerical evaluation of support stiffness, the experimental program, testing procedure, observations, experimental results and discussions. The procedure to evaluate the flexural rigidity is derived in chapter four and applied to test results.

Chapter five presents the development of a simple finite element model of masonry load bearing block walls and presents the selection of the finite element mesh, material model and solution strategy. For the purpose of verification of the model chapter five also includes a comparison of the experimental results with the numerical results obtained from finite element model.

In chapter six, considering support stiffness as a primary parameter, other major parameters related to masonry block wall behavior are identified. A thorough parametric study is presented in this chapter comprising load deflection response,

load moment response, response at failure of the walls and trends to illustrate the interaction of support stiffness with several geometric and material parameters. To completely describe the wall behavior, flexural rigidity plots are also presented in chapter six.

Chapter seven further extends the results obtained from the parametric study and presents the regression analysis and development of mathematical model for the estimation of axial load carrying capacity of masonry load bearing block walls.

Finally, chapter eight summarizes the results and final conclusions of the study as well as recommendations for future extension of the research work.

## **CHAPTER 2**

### **LITRATURE RIVIEW**

#### **2.1 Introduction**

The behavior of masonry load bearing walls has been investigated by several researchers in the past. Valuable contributions in this area of research had helped to implement limit state design approach in the current masonry design practice. Previous researchers have tested the walls having smaller and intermediate slenderness ratios. Very few researchers performed full scale testing to investigate the behavior of walls with high slenderness ratios (i.e.  $h/t > 30$ ). Because of unavailability of enough research data, the current Canadian Code S304.1-94 treats such walls over-conservatively.

The current Canadian code underestimates the load capacity of masonry load bearing walls, in two ways. It underestimates the flexural rigidity and neglects the support conditions in case of walls with  $h/t > 30$ . For the walls with  $h/t < 30$ , the code allows the incorporation boundary conditions in terms of effective length factors in estimation of the load capacity of the load bearing walls, The method, however, is not able to encompass the actual support conditions.

In all previous experimental work the walls have been tested with pinned condition at top and but with constant eccentricity at either or both ends. To the best knowledge of the author no experimental research is available about the incorporation of actual support conditions in investigation of masonry load bearing block wall behavior.

The effective flexural rigidity has been investigated by many researchers to further understand the masonry load bearing wall behavior. Several attempts have been made to experimentally investigate this parameter and to find out the

relevancy of effective flexural rigidity with the load carrying capacity of the walls.

In several research investigations the computer simulation of masonry load bearing walls has also been the topic of interest. Several finite element approaches have been suggested by the researchers. The material modeling has also been treated with special attention and has transformed the modeling approach from micro to macro model and recently towards homogenization of the masonry material.

This chapter presents a review of the available literature covering the topics related to experimental, numerical and analytical investigations of masonry load bearing walls. Specifically the chapter aims to cover the literature related to finite element modeling, testing, material modeling, flexural rigidity and the failure modes of the masonry load bearing block walls.

## **2.2 Experimental investigations**

Yokel and Dikkers (1971) performed comprehensive experimental and analytical work on brick and block masonry. The experimental program consisted of one hundred and ninety two specimens out of which, 13 were solid concrete masonry walls, 48 were hollow concrete masonry and 28 were reinforced concrete masonry walls. The wall specimens were up to 6 m (20 ft) high and ranged from 0.6 m (2 ft) to 1.2 m (4 ft) in width. The test program also included prism tests and based on prism test results it was concluded that increasing strain gradient caused the increase in flexural compressive strength of the masonry. Therefore, cross-sectional capacity of masonry walls using interaction curves developed by employing flexural compressive strength equal to axial compressive strength of prism was stated as a conservative way of determining the wall cross-sectional strength. The boundary conditions were described as a factor which might eliminate the moment magnification if the wall Flexural rigidity is adequate. The

boundary conditions for eccentrically loaded masonry walls, which may be practically encountered in masonry construction were described as shown in Figure 2.1. Load moment interaction curves were presented with strength reduction factor caused by wall slenderness. It was suggested that for more accurate prediction the load-moment interaction curves could be modified by considering strain gradient effects. As an extension of the work, Yokel (1971) also derived the differential equation for the deflection curve of a wall with prismatic cross-section and an elastic material with no tensile strength. The exact solution of the differential equation was used to obtain an expression for an equivalent critical load ( $P_{ec} = \frac{9 \pi^2 E b u_1^3}{4 h^2}$ ) and it was concluded that elastic instability will occur at the critical load ( $P_{cr}$ ) given in equation 2.1.

$$P_{cr} = 0.64 \frac{\pi^2 E b u_1^3}{h^2} \quad [2.1]$$

in which, E is the modulus of elasticity,  $u_1$  is the eccentricity and h is the member height.

Cranston and Roberts (1976) tested eccentrically loaded plain concrete block wallets. From the wallett test results the stress-eccentricity-rotation curves were plotted and reported to be efficient in establishing the response of concrete block masonry under eccentric load. Based on test results it was concluded that limit state procedure gave good indication of wall behavior as compared to working stress procedure which was found uneconomical.

Hatzinikolas et al. (1978) conducted a comprehensive full scale testing program consisting of 78 plain and reinforced concrete masonry walls. The main parameters of test specimens were slenderness ratio and top and bottom eccentricities. All walls were tested with pinned end conditions, but with load eccentricities designed to create single as well as double curvature conditions. The experimental program also covered the effect of joint reinforcement and main

vertical reinforcement. For walls with double curvature an analytical procedure of estimating the buckling loads of the masonry walls was also presented. To obtain the critical load an energy based approach was used and a fifth order interpolating function was applied to a stepped column assuming cracking because of axial load and double curvature in the upper part of prismatic section. The effective flexural rigidity was suggested to be a function of the amount of cracking of the cross-section. The moment magnification method for the design of slender masonry walls was introduced using suggested critical loads and effective flexural rigidities.

Amrhein et al. (1982) tested slender hollow block concrete walls subjected to combined vertical and horizontal loadings. The reinforced solid grouted masonry wall specimens were 7.52 m high and 1.22 m wide with wall thickness of 152 mm, 203 mm and 254 mm resulting in slenderness ratio of 48, 36 and 30 respectively. Pin end conditions were provided during testing. Ductile failure because of yielding of vertical reinforcement was reported, cracking was observed at the bed joints. The P delta effect was found to be 10% of the total deflection and lateral moment on the wall. It was suggested to limit lateral deflection of slender walls under service loads and to limit the wall strength under seismic loads.

### **2.3 Analysis and Behavior of Masonry Block Walls**

Chen and Atsuta (1973) used the beam-column concepts to investigate load bearing walls. They generated curves for the axial strength valid for different material types. It was concluded in the paper that even the small tensile strength of plain concrete or masonry walls has a significant effect on the strength of walls and should not be neglected.

Hatzinikolas et al. (1978) suggested the moment magnifier method for analysis and design of masonry walls loaded under eccentric axial load. Using the basic

differential equation the equation to estimate the magnified bending moment for equal end moment condition was derived and suggested to be applicable for other end moment conditions:

$$M = Pe \left( \frac{C_m}{1 - \frac{P}{P_{cr}}} \right) \quad [2.2]$$

in which  $P$  is the axial load,  $e$  is load eccentricity,  $C_m$  is a factor to incorporate unequal end moment condition,  $P_{cr}$  is the critical load which is based on amount of cross-sectional cracking along the wall height. An iterative procedure was suggested to evaluate the ultimate load capacity by using equation 2.2 until the load converges. The load moment interaction diagrams for plain and reinforced masonry at different load eccentricities were plotted using a computer program developed by the author. The introduction of  $C_m$ , intended to account for shape of primary bending moment diagram, is quite conservative for masonry walls but its use remains to date as part of all design code procedures.

Colville (1979) presented a design procedure based on stress reduction design factors for solid prismatic walls made up of un-reinforced concrete, brick or concrete masonry. The proposed procedure was based on the concept of the equivalent column, which was defined as the column subjected to an axial load with equal end eccentricities and whose deflection curve between floors is representative of an actual wall as shown in Figure 2.2. The tensile strength of the wall was assumed to be zero. Considering the variation of bending displacement along the height of the wall the effect of slenderness and load eccentricities was included. Based on the above described considerations the equation to evaluate stress reduction factors were derived to account for effects of slenderness and load eccentricity on the load bearing capacity of the walls. The design procedure consisted of three steps, identifying the type of wall bending, determining the end eccentricities and finally estimating the stress reduction factor. The stress failure

was described as the condition when the wall end rotation was less than the rotation at failure of the wall.

Hamid and Drysdale (1979) proposed failure criteria for grouted masonry by using the strength of the constituent materials of masonry assemblage. Failure criteria were suggested for two failure conditions: first case is when unconfined compressive strength of grout is reached because of its lower strength as compared to face shell, second case is when at the level of maximum stress the strain in grout exceeds the strain in the face shell resulting in face shell failure.

Hatzinikolas et al. (1980) studied the behavior of plain concrete walls loaded with eccentric axial load. Short wall specimens were tested with pinned ends and variable top and bottom eccentricity of 0,  $t/6$  and  $t/3$ . The failure of an eccentrically loaded wall was reported to occur when the compressive strength of the wall reached the compressive strength of the unit. Block thickness and the type of construction were described as factors affecting the net-cross-sectional area which might cause variation in the actual failure stress.

Drysdale and Hamid (1984) discussed the possible mode of tension failure of unreinforced concrete masonry. The macro modeling approach of defining concrete masonry as a globally homogeneous material was stated as the suitable approach for analytical treatment of concrete masonry. Tensile strength normal to bed joints and the tensile strength parallel to bed joints were discussed separately. In case of tensile failure normal to the bed joint the tensile bond strength between mortar and the block, grout tensile strength were reported to control the tensile strength of masonry assemblage, while mechanical properties of the block did not have any direct influence. For the tensile failure parallel to bed joint two types of failure modes were illustrated. The first mode was splitting failure along the plane parallel to face shell and the head joint, while the second type of failure mode was called as stepped failure which was stated as the failure along the plane established the plane of head joints and the bed joints. In case of first type of

failure, the tensile strength of the block reported as the influencing parameter on tensile strength of masonry assemblage as compared to mortar tensile bond strength while grout strength was observed to have no effect. Mode two was reported to be affected by shear bond and tensile bond strengths of the mortar and the grout tensile strength. Increase in net area of the block reduced the tensile strength of the masonry assemblage in resisting the tensile failure parallel to the bed joint. It was concluded that ignoring block strength and its geometry and considering only the mortar bond strength in estimating the capacity of masonry assemblage would underestimate the capacity, specially in case of tensile failure parallel to bed joints.

Suwalski and Drysdale (1986) proposed the reduction factor approach to incorporate the effect of slenderness ratio in estimating the capacity of eccentrically loaded concrete masonry walls. The technique developed for the case of symmetric single curvature was applicable to a limited range of material and geometric properties. The parametric study using the FEM model was performed and walls with slenderness ratios of 4, 12, 16, 20 and 24 were analyzed by choosing material properties from a previous material testing program at McMaster University and the load eccentricity ratio was varied. The parametric study concluded that the effect of wall slenderness was not significant at lower load eccentricity. Incorporating the relationship between load eccentricity ratio and slenderness ratio of the walls, two separate equations were proposed for the estimation of the axial load capacities of reinforced and plain concrete masonry walls; one for low slenderness and one for high slenderness.

Yao and Nathan (1989) studied the slenderness of concrete masonry load bearing walls. The study consisted of experimental work on small wall specimens of 1 m high and one block wide with constant block thickness of 100 mm, reinforced with vertical as well as lateral steel. The walls were analyzed using a parabolic stress distribution and an equivalent rectangular stress block distribution compared with experimental results. It was concluded that for slender walls

subjected to eccentric loads the vertical reinforcement improves the axial strength and ductility of the walls. It was reported that confinement reinforcement could possibly increase the axial capacity of the walls from 8% to 10%. For the cross-section analysis a rectangular stress block was recommended using the compressive strength of masonry assemblage rather than the compressive strength of block unit.

Yao (1989) proposed the unit strength as the basis of predicting strength of eccentrically loaded masonry walls. Load moment interaction curves based on unit strength were compared with test results. Material failure was reported to govern in case of lower load eccentricity cases and buckling failure was found before the yield strain was attained for higher load eccentricity cases.

El-Metwally et al. (1991) presented a method to analyze concrete masonry load bearing walls by treating eccentrically loaded masonry walls as beam-columns. A modified Newmark integration method, which included geometric and material non-linearities, was incorporated in the method. The parameters affecting the load carrying capacity of the masonry walls were identified as the slenderness ratio, end conditions, load eccentricity and the mechanical properties of the material. Large slenderness ratios were linked to stability failure and smaller slenderness ratios were reported in material failure cases. The effect of end moments was reported to be significant in case of smaller slenderness ratios where material governs the wall behavior. It was concluded that the wall subjected to unsymmetrical end moments showed more strength as compared to walls with symmetrical end moments.

Colville (1992) conducted a study of the stability of hollow masonry walls and suggested that hollow or partially grouted walls should be differentiated from solid masonry walls in estimating the axial load capacity. It was concluded that the maximum allowable eccentrically applied working load on an un-reinforced masonry wall or column should be limited to one fourth of the buckling load.

Maksoud and Drysdale. (1993b) discussed the use of moment magnification factor in the design of masonry walls. It was emphasized that without taking into account the material and geometric non-linearity the behavior of masonry walls could not be predicted correctly. The ultimate capacity was described as a function of not only geometric non-linearity but also the material non-linearity. The effect of stiffness degradation because of high level of stresses in the cross-section was found to significantly influence the ultimate response of the walls. The wall capacity based on an elastic modulus or even on a secant modulus was reported to be overestimated. It was suggested to use a tangent modulus instead. A parametric study to demonstrate the wall behavior was also performed by using  $h/t$  ratios ranging from 6 to 42, the load eccentricity ratio ranging from 0.05 to 0.3 and considering the ratio of top to bottom eccentricity as 1, 0 and -1. It was observed that because of the coupling effect of geometric and material non-linearity, walls with higher slenderness ratios showed rapid stiffness degradation at failure as compared to stocky walls, which did not show any stiffness degradation until failure. At constant slenderness ratio, higher eccentricities created the larger displacements at the same load level. This correlation was reported to be eliminated for the cases having eccentricity ratios larger than or equal to 0.5; potentially because of buckling dominating the mode of failure.

The moment gradient was also reported as an influencing parameter on the capacity of the masonry walls, and was reported to change the mode of failure from tensile to compression failure. It was emphasized that the moment gradient helped to reduce the displacements by holding the load within kern limit and as a result the load capacity was significantly increased. This phenomenon supports consideration of the effect of support stiffness, which is possibly, able to influence the moment gradient along the height of the wall. Buckling failure was also reported for slender walls, which could not experience material non-linearity. To incorporate the material and geometric non-linearities in estimating the moment magnification factor a reduction factor of the elastic modulus of rigidity was computed for all the cases considered in the parametric study then using stepwise

regression the equation for evaluating a reduction factor was obtained for single and double curvature separately.

Schultz et al. (2001) reported the effect of out-of-plane bending on buckling capacity of un-reinforced masonry walls. The interaction between peak bending moment and the critical axial load was defined as :

$$M_{\max} = 1.732 \left( \frac{P_c r}{\lambda} \right) \left[ 1 - 0.577 \left( \frac{e_a}{r} \right) - \sqrt[3]{\frac{P_c}{P_E}} \right] \quad [2.3]$$

in which  $P_c$  is the critical buckling load,  $\lambda$  is the constant to incorporate different load conditions,  $e_a$  is the actual load eccentricity at the end of member,  $r$  is the radius of gyration,  $P_E$  is the Euler buckling load.  $M_{\max}$  was defined as the critical bending moment buckling state and beyond which there was no real solution. The experimental investigation was also conducted to determine the behavior of URM walls loaded with constant axial load and variable uniformly distributed lateral load. From the test results the stability interaction between out-of-plane bending moment and axial load was evident and it was suggested that axial load instability in the presence of transverse loading is the failure mode most likely to control the design of URM walls.

Jäger and Pflücke(2001) addressed the non-linear stress-strain relationship on buckling safety of slender masonry walls. It was suggested that buckling safety of slender masonry walls is significantly affected by the non-linear stress distribution, which is a function of the stress-strain relationship. It was concluded that the assumption of linear elastic material could not predict the real behavior of the walls.

## 2.4 Finite Element Modeling and Material Constitutive Relationship

Review of research work regarding finite element modeling showed two approaches, micro and macro modeling. The microscopic approach was found computationally expensive and mostly recommended to capture local behavior of masonry walls, while the macroscopic approach was found efficient in investigating the global behavior of the walls. Much of the work reported below reflects efforts to model in-plane behavior.

Page (1978) presented an FEM model for brick masonry subjected to in-plane loading. An eight node plane stress continuum element having isotropic elastic properties was used to define brick masonry units. The mortar joints were defined as linkage elements. The element displacement matrix was defined in terms of the relative displacement vector in the normal and shear directions for the top and bottom movement of the joint element. Equation 2.4 shows the equilibrium relation for the joint element

$$\{F\} = [k] \{w\} \quad [2.4]$$

$$\text{in which } [k] = \begin{bmatrix} k_s & 0 \\ 0 & k_n \end{bmatrix}, \{w\} = \begin{Bmatrix} w_s(\text{top}) - w_s(\text{bottom}) \\ w_n(\text{top}) - w_n(\text{bottom}) \end{Bmatrix}, \{F\} = \begin{Bmatrix} F_s \\ F_n \end{Bmatrix}$$

are the stiffness matrices., displacement vector and the force vector respectively. The values of  $k_n$  and  $k_s$  were dependent on joint thickness “ $t_m$ ” and suggested to be computed as  $k_n = \frac{E'T}{t_m}$  and  $k_s = \frac{G'T}{t_m}$ , in which  $E'$  is the instantaneous tangent elastic modulus,  $T$  is the wall thickness and  $G'$  is the shear modulus related to a particular state of shear stress. The iterative procedure was employed in a FEM program to incorporate the material non-linearity for joint elements and the process continued until convergence. Since the failure criteria for the masonry

was not included in the model, the model was not able to predict the ultimate load and was thought to be suitable for working stress design method only.

Ali et al. (1986) incorporated progressive local failure of both joint and brick masonry elements in a plane stress two dimensional non-linear FEM model. Solid concrete brick masonry subjected to concentrated load was considered. The stress-strain relationship for brick and joint elements was obtained through experimental investigations for both materials separately. The failure criteria covered three types of situations, firstly the bond failure at the interface of joint and brick elements, secondly the fracture of mortar or brick element under biaxial tension-compression or tension-tension state of stresses and finally crushing failure because of biaxial compression. The FEM model was adopted with incremental loading procedure for concentrated in-plane loading of masonry walls. The finite element mesh of the wall consisted of four noded quadrilateral elements. To obtain computational efficiency and to avoid the use of complex type of elements a dense mesh was used at the point of loading as compared to other parts of the mesh. The model was also compared with test results of masonry wallets for concentrated and eccentric loadings.

Sayed-Ahmed and Shrive (1993) suggested the use of shell element with sub-structuring technique for the computationally efficient finite element model. Use of 3-D continuum element in modeling masonry walls was reported to require a finer finite element mesh for capturing the true web splitting stresses in hollow concrete walls and resulted in high computational effort. Shell elements were found computationally efficient and able to capture web splitting and behavior of masonry unit and mortar behavior at failure.

Maksoud and Drysdale (1993a) developed the combined macro-micro finite element model. The number of degree of freedoms was reduced by considering the inelastic response of anisotropic masonry assemblages at macro level. The non-linear geometric effects were incorporated in the model by using total

Lagrangian formulation assuming large displacement, large rotation and small strain conditions. The model was verified against available experimental results.

Lotfi and Shing (1994) proposed a FEM model using interface elements to define the mortar joints and a smeared crack approach was used for the masonry units. The finite element model was able to handle the shear behavior of mortar joints. The constitutive model employed in the FEM model, was capable of dealing with crack initiation and propagation under the influence of tension and shear stresses in the region of tension-shear and compression-shear. The use of interface element in modeling masonry structures was reported efficient in predicting the load carrying capacity and also to provide information about other details regarding the wall behavior at failure.

Sayed-Ahmed and Shrive (1996) stated that simulation of behavior of masonry walls related to both block and mortar interaction in capturing progressive failure of the wall was not possible without using a 3-D finite element model. A geometric and material non-linear finite element model using 8-noded shell element was developed and ABAQUS was employed to obtain numerical results. The FEM model treated the block and joint elements separately and was able to include elasto-plastic behavior of both mortar and masonry. Interface elements were used to implement discrete cracking and the associated flow rule along with Drucker-Prager failure criteria was adopted to define the material plasticity under compressive stresses. The solution strategy used in finite element procedure included the incremental method and an iterative procedure based on arc-length method of fixing the length of load increment in load-deflection space. Previous experimental results were used for the verification of proposed finite element model. The model was reported to have the ability of capturing the failure of the wall from appearance of first crack to final buckling of the wall.

Wang et al. (1997a and b) developed a finite element model using macro-modeling approach to study the behavior of slender masonry cavity walls. The

masonry walls were modeled using beam element by assigning the material properties of the masonry assemblage as a whole using prism test results. The weakness of the mortar layer in tension was modeled by using bond strength between mortar joints and the masonry unit. The commercial software ABAQUS was used to perform numerical analysis and the built-in cracking model for concrete was utilized. The cracking failure criterion was defined by using crack-detection surface similar to a yield criterion and a tension-stiffening model was adopted in post-cracking zone. The solution strategy included two steps. In the first step the load control strategy with standard Newton-Raphson iterative procedure was applied before the ultimate load point and in the second step the Modified Riks algorithm was employed to obtain the ultimate load and post buckling behavior of the walls. The model was reported to have good agreement with experimental results.

Lopez et al. (1999) proposed the “homogenization” technique to model anisotropic elasto-plastic material behavior of masonry. The model is able to generate cracking in all directions and required less computational effort because of the capability of defining larger elements (as compared to a micro modeling approach) without losing accuracy of the analysis.

Giambanco et al. (2001) developed a finite element model based on the micro-modeling approach by considering fully elastic masonry units and interface modeling for the joints. The non-linear behavior accounted for joints behavior by applying the interface constitutive model. The model was formulated to simulate the loss of cohesion process in the joints because of tensile and shear stresses. The finite element procedure incorporated an algorithm based on a time step integration method.

Ma et al. (2001) presented a numerical simulation for large masonry structures using a homogenization technique. The concept of representative volume element (RVE) was introduced to simulate the masonry unit and joint material as a whole

in numerical analysis, as shown in Figure 2.3. Constitutive relationships of masonry unit and mortar behavior were used to drive an equivalent stress-strain relationship for RVE. Various stress-strain curves for compression-tension and compression-compression states of stress were presented to implement in the numerical simulation. It was recommended to use a significantly smaller RVE as compared to the whole masonry structure to avoid edge effects. The technique was reported to be applicable only for in-plane behavior and not recommended to obtain out-of-plan behavior. In case of intensively variable stress-strain field the homogenization of material was found undesirable.

Yi and Shrive (2001) developed a 3-D finite element model by treating masonry units, joints and grout separately. Masonry walls with bond beams were also modeled. For and mortar masonry units, iso-parametric shell elements were used, while solid elements were assigned to grouted cores. The model was capable to deal with eccentric and concentric types of loadings on masonry walls. The cracking was modeled by using smeared crack approach. Multi point constraints were used to model link between shell elements of units and the solid elements of grouted cores. Modified Riks method was implemented in the finite element procedure and set of prescribed displacements were assigned to loading plat for the application of incremental loading. An iterative process was adopted to trace non-linear response and to obtain progressive cracking in the walls. The model was verified against experiments and reported in good agreement with test results. The model was reported to have the ability to capture failure mechanism related to progressive cracking and web-splitting followed by spalling of face shell or crushing of mortar. It was suggested to avoid local crushing in the units situated under loading plate.

Giordano et al. (2002) compared the contemporary techniques of modeling masonry structures. A full-scale specimen representing the part of structure of an actual historic building was tested and modeled using different modeling techniques and the results were compared. The FEM model based on smeared

cracking and homogenized material constitutive laws, the FEM model with discontinuous elements considering both horizontal and vertical mortar joints of masonry assemblage and the discrete element modeling were used by employing commercially available software and the numerical results were compared with actual test results. All the techniques were reported working well with monotonic type of loading and to obtain global behavior. ABAQUS cracking model of concrete was reported to be efficient in handling monotonic loading but for cyclic loading some modifications related to material damage were suggested to be included. The modeling of masonry structures with discontinuous elements and also with discrete elements was stated to be difficult in terms of modeling the exact distribution of bricks/blocks and the mortar joints because of application of finishing material. The smeared crack approach was stated to have no such limitations. However, the input parameters related to material behavior are crucial and need to be calibrated with special attention.

Creazza et al. (2002) adopted a macro model combined with 3-dimensional plasticity damage approach. Using two independent damage variables related to equivalent effective tensile and compressive stresses an isotropic damage model was formulated. The model was calibrated for brick masonry and used to analyze masonry vault and compared with actual test results. The proposed method of analyzing masonry structures was reported efficient in predicting the peak load and failure modes. However, the maximum deflection obtained from the model was smaller than the actual maximum displacement obtained from experiment.

Cecchi and Marco (2002) discussed constitutive aspects of the homogenization of masonry material. The macro modeling methodology with homogenized approach was reported efficient to model heterogeneous masonry assemblages. Homogenized constitutive functions were presented in the study and found helpful in incorporating the behavior of individual constituents of masonry in a global stiffness matrix.

Liu and Dawe (2003,b) developed a finite element model by idealizing the masonry load bearing walls as beam-columns. The technique was implemented into a computer program for the analysis of a masonry member subjected to various loading combinations. The model was based on a stiffness matrix having geometric and material non-linearity effects. The stress-strain relationship was adopted from a previous research work on un-confined grouted masonry walls:

$$\sigma_m = 1.067 f'_m \left[ \frac{2\varepsilon_c}{0.002} - \left( \frac{\varepsilon_c}{0.002} \right)^2 \right], \quad \varepsilon_c < 0.0015 \quad [2.5]$$

An iterative procedure was adopted to apply incremental loading and a “reduced” stiffness matrix was employed. The convergence criterion included both force and the deflection with a tolerance of 0.1%.. The moment curvature relationship was also traced at every load increment after convergence was established. The buckling load was obtained using an Eigenvalue problem approach. At every iteration step, the material failure was checked by assessing if the total bending moment of the cross-section was less than the bending moment capacity. After achieving convergence, the stability failure criterion was also checked by comparing applied axial load level with the buckling load of the wall. The model results were compared to experimental results and were reported satisfactory.

## 2.5 Flexural Rigidity

The research work related to flexural rigidity is limited to very few experimental and analytical investigations. The review of available literature about flexural rigidity of masonry load bearing walls is presented below:

Yokel (1971a and b) described Flexural rigidity as a function of level of stress and the cracking of the wall cross-section under influence of vertical and transverse loading. For walls with eccentric loading, approximate equations were suggested

to estimate the Flexural rigidity of the wall, as shown in equation 2.6 (a) and 2.6 (b) for reinforced and un-reinforced masonry walls respectively.

$$EI = \frac{E_i I_n}{2.5} \quad [2.6(a)]$$

$$EI = \frac{E_i I_n}{3.5} \quad [2.6(b)]$$

in which  $E_i$  is the initial tangent modulus of elasticity, while  $I_n$  is the moment of inertia of the un-cracked net section. For walls subjected to excessive cracking another approximate equation was suggested to calculate Flexural rigidity of masonry walls, as given in equation 2.7.

$$EI = E_i I_n \left( 0.2 + \frac{P}{P_0} \right) \leq 0.7 E_i I_n \quad [2.7]$$

in which  $E_i$  is the initial tangent modulus of elasticity, while  $I_n$  is the moment of inertia of the un-cracked net section,  $P_0$  = cross-sectional axial load capacity and  $P$  is the applied vertical compressive load. The effect of stresses in the cross-section of the wall and cracking effect were included crudely by using a factor of  $\left( 0.2 + \frac{P}{P_0} \right)$ . The other factors such as load eccentricity ratio and slenderness effect were not included directly in equation 2.7.

Hatzinikolas et al. (1978) reported that the moment of inertia is influenced by parameters related to construction such as mortar penetration and mortar overhang and type of masonry units. Therefore, it was recommended to perform experimental testing for the determination of actual flexural rigidity of the walls. Factors similar to those recommended for concrete design were suggested to be used to incorporate the effect of load eccentricity and time dependent effects on flexural rigidity of concrete masonry. The estimation of flexural rigidity with a

conservative approach valid for both reinforced and plain concrete masonry walls and without time dependent effects was suggested :

$$EI = EI_0 \left[ 0.5 - \frac{e}{t} \right] \geq 0.1EI_0 \quad [2.8]$$

in which E is the modulus of elasticity of masonry,  $I_0$  is the un-cracked moment of inertia, e is the load eccentricity and t is the wall thickness. Equation 2.8 is similar to the equation recommended for slender reinforced concrete columns.

Aridru and Dawe (1995) performed extensive experimental work to investigate flexural rigidity of masonry walls. The effects of reinforcement ratio, load eccentricity ratio and the slenderness ratio on flexural rigidity of masonry walls were the main parameters included in the research. Both reinforced and plain concrete partially grouted walls with slenderness ratio of 8.5 were tested. It was reported that the measurement of strain at the surface of the short wall could be an effective tool for the estimation of flexural rigidity. The bending moment and the flexural rigidity were found to be exponentially related to each other.

About et al. (1995) used the moment curvature relationship to define upper and lower bound of flexural rigidity as shown in Figure 2.4. A mathematical model was proposed based on a wall panel loaded with monotonic two equal line loads at the middle third height of the wall. In the proposed model the out-of-plane deflection was defined as a function of Flexural rigidity of the wall and the term effective flexural rigidity was introduced by taking into account the variation in modulus of elasticity and in the cross-sectional moment of inertia, as illustrated by equation 2.9:

$$(EI)_{\text{eff}} = (EI)_g^f R + (EI)_{cr}(1 - R) \quad [2.9]$$

in which  $R$  is a function of moment ratio.,  $(EI)_{cr}$  is the cracked sectional stiffness and  $(EI)_g^f = \frac{\beta M_{cr} L^2}{\Delta_{cr} I_g^f}$  is the modified gross-sectional stiffness, where  $\beta$  is the factor to incorporate the combined effect of load, span and support conditions,  $M_{cr}$  is the cracking moment,  $L$  is the wall span,  $\Delta_{cr}$  is the cracking displacement.  $I_g^f$  is a modified moment of inertia of gross-section calculated by considering that tensile resistance for un-cracked section mainly provided by the grout and therefore the wall cross-section with only one face shell was used in the calculation. Although Equation 2.9 appears to be complicated with dependency of many factors and more suitable for laterally loaded walls, but still it indicates that out-of-plane deflection can also be used to evaluate the Flexural rigidity if details related to cracking and cross-sectional stress are known.

Liu et al. (1998) conducted a comprehensive testing of seventy-two full-scale concrete masonry wall specimens subjected to eccentric axial load. For the determination of flexural rigidity of the masonry walls the goal was to measure the strain at tension and compression face of the wall cross-section so that the curvature could be determined. Based on moment curvature relationship  $EI$  could be evaluated. Wall specimens were 800 mm long and 1200 mm high with nominal thickness of 150 mm and 190 mm. The load eccentricity ratio was ranged from 0.0 to 0.36. The reduction in flexural rigidity was observed with increasing axial load. No reduction in modulus of elasticity was observed while the stress-strain relationship of masonry remained linear. However, when the stress-strain relationship became non-linear, at higher loads a reduction in Flexural rigidity was observed because of cracking. Based on experimental data, two equations were proposed for the estimation of flexural rigidity:

$$EI_{eff} = 0.7E_m I_0, \quad 0 \leq e/t \leq 0.18 \quad [2.10]$$

$$EI_{eff} = 2.70 E_m I_0 \exp\left[-7.5 \frac{e}{t}\right] \geq E_m I_{cr}, \quad e/t > 0.18 \quad [2.11]$$

in which  $E_m$  is the modulus of elasticity of masonry,  $I_0$  is the un-cracked moment of inertia,  $I_{cr}$  is the cracked moment of inertia and  $e/t$  is the load eccentricity ratio.

Although equation 2.10 and equation 2.11 were described to have P-delta effects no direct inclusion of slenderness ratio was suggested. The values of flexural rigidity suggested by current Canadian Code S304.1-M94 were found conservative when compared with the test results.

Liu and Dawe (2001) tested another set of reinforced concrete masonry walls. 36 wall specimens of size 1200 mm high, 800 mm long and 150 mm thick were tested with axial and lateral loads. Single and double layers of vertical reinforcement were used with two cores grouted wall cross-section. It was observed for both single and double layers of reinforcement that the lateral load capacity was increased with increasing axial load up to the level of 60% of pure axial load capacity and after that the increase in axial load caused the decrease in lateral load capacity. Three types of failure modes were observed during testing. The gradual and ductile tensile failure because of cracking along the horizontal joint near the mid-height occurred in the specimens which were failed at the axial load level less than 30% of the pure axial load, while a combined tension-compression type failure was reported for the wall specimens which were failed under pre-compressive load level of about 30 to 60% of pure axial load. An explosive and sudden failure categorized as pure compression failure in which masonry crushing and spalling was observed at both compression and tension faces for the specimens which failed at the pre-compressive load level between 60% to 80% of pure axial load. In case of tensile failure the effect of single layered reinforcement was reported more beneficial in increasing the lateral load capacity and ductility of the wall. Using the strain values recorded during experiment at tension and compression face of the wall cross-section the moment curvature relationship as shown in equation 2.12, was employed to estimate the effective Flexural rigidity of the wall specimens.

$$EI = \frac{M}{\phi} \quad [2.12]$$

in which  $\phi = \text{curvature} = \frac{\varepsilon_1 - \varepsilon_2}{t}$  and  $\varepsilon_1, \varepsilon_2$  are the strains at tension and compression faces of masonry wall. The experimentally obtained Flexural rigidity of the wall was compared with the values estimated according to recommendations of CSA-S304.1-M-94. The experimental values of  $EI_{eff}$  were reported larger than the code values. Therefore it was concluded that the current Canadian code is conservative in predicting the effective flexural rigidity of the walls failed under higher compressive loads and having lower slenderness ratios. The study included a very small slenderness ratio of 8.6, which could only cover the stocky walls and rendered the research to be extended for intermediate to tall masonry walls.

Liu and Dawe (2003) performed a computer based study on effective Flexural rigidity of the masonry load-bearing walls. The numerical model developed by the author as discussed in section 2.3 was employed to obtain effective flexural rigidity of the walls considering effect of various parameters such as reinforcement ratio, load eccentricity ratio, end eccentricities and the slenderness effect. The Flexural rigidity for eccentrically loaded walls obtained from numerical model was compared with limits recommended by CSA-S304.1-M-94 and the relationship between key parameters with regard to flexural rigidity described as shown in Figure 2.6. It was reported that increasing load eccentricity ratio caused decrease in the ratio  $\frac{EI_{eff}}{EI_0}$ , while at constant load eccentricity and increasing slenderness ratio an increase was recorded in  $\frac{EI_{eff}}{EI_0}$ , where  $EI_0$  is the

Flexural rigidity of un-cracked section. The current Canadian Code was reported to provide significantly conservative estimate of effective flexural rigidity for all types of failure modes. This underestimation was found more prominent in case of walls with higher slenderness ratios loaded with higher load eccentricity. Based

on numerical results regression analysis was performed and following equation was suggested for the reinforced concrete walls as the lower-bound approximation to define the relationship between load eccentricity ratios, slenderness ratios and  $\frac{EI_{eff}}{EI_0}$  for the range of slenderness ratio from 6 to 36 and load eccentricity ratio less than 0.4, as given in equation 2.13 and 2.14.

$$\frac{EI_{eff}}{EI_0} = 0.8 - 1.95 \left( 1 - 0.01 \frac{h}{t} \right) \left( \frac{e}{t} \right), \quad 0.0 \leq \frac{e}{t} \leq 0.4 \quad [2.13]$$

$$\frac{EI_{eff}}{EI_0} = 0.022 \left( 1.00 + 0.35 \frac{h}{t} \right), \quad \frac{e}{t} > 0.4 \quad [2.14]$$

Equation 2.11 and 2.12 were reported to have the capability to provide lower-bound of effective flexural rigidity valid for both stability and material failure in reinforced concrete walls. For plain walls the value of  $EI_{eff}$  suggested by the current Canadian Code i.e.  $EI_{eff} = 0.4EI_0$  was found satisfactory.

It is evident from the available literature, reviewed in the current chapter that to date there is no research work performed about the incorporation of actual boundary conditions effects on either the axial capacity or the flexural rigidity. This underscores the need to investigate the effect of actual boundary conditions on the behavior of masonry wall. Thus, it is required to conduct the intended research both experimentally and numerically for validation purposes and also for the future extension of the work.

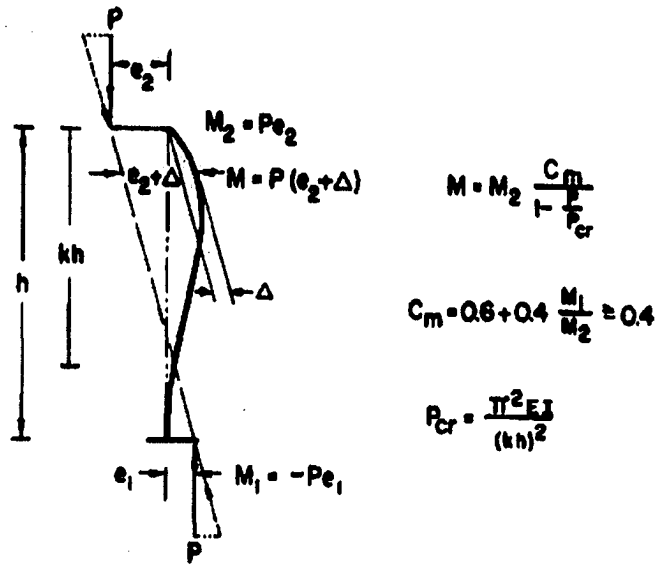


Figure 2.1 Boundary conditions (after Yokel 1971)

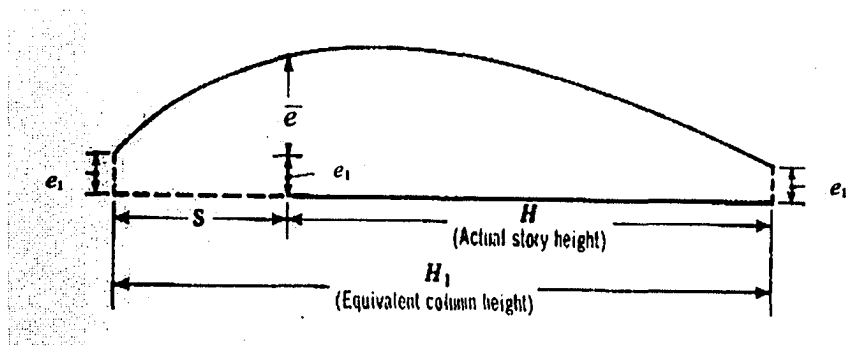


Figure 2.2 Equivalent column (after Colville 1979)

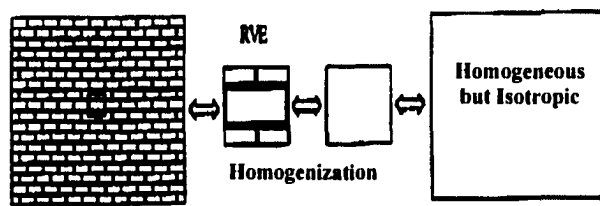


Figure 2.3 Concept of representative volume element (RVE) in material homogenization (after Ma et al. 2001)

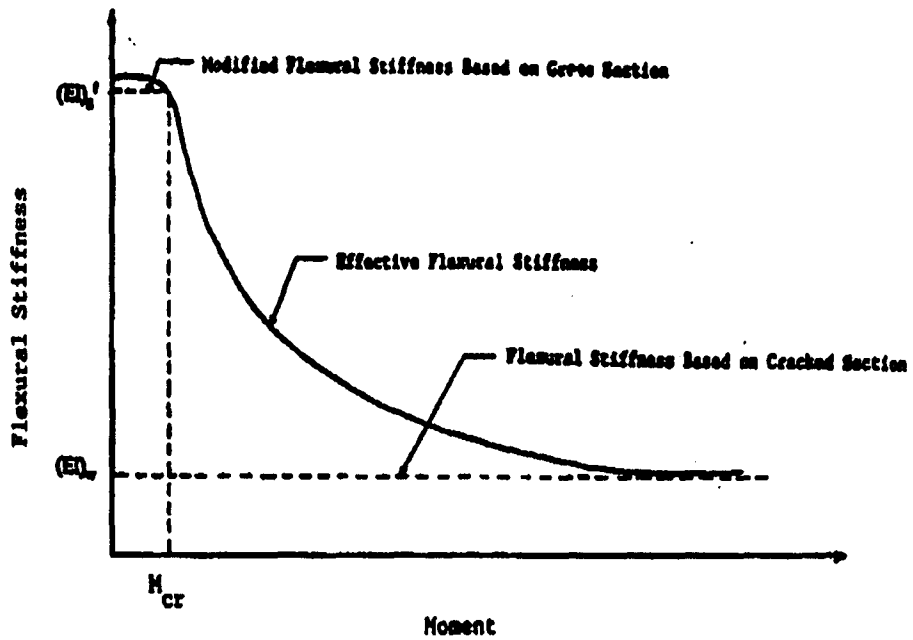


Figure 2.4 Moment curvature relationship limits of flexural rigidity (after Aboud et al. 1995)

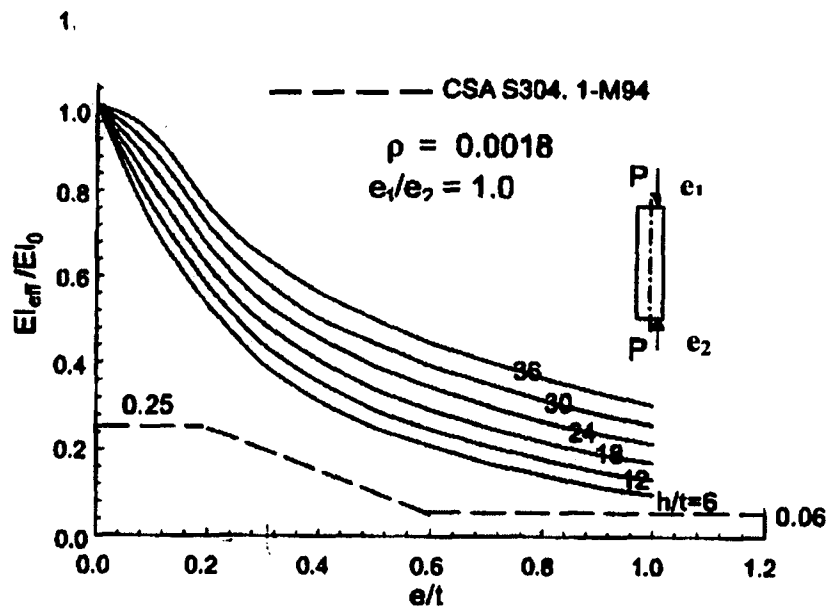


Figure 2.5  $\frac{EI_{eff}}{EI_0}$  versus load eccentricity ratio (after Liu and Dawe 2003)

## **CHAPTER 3**

### **EXPERIMENTAL PROGRAM**

#### **3.1 Introduction**

Masonry load bearing walls have been a topic of interest for many researchers. It is evident from available literature that, to date, no experimental work has been performed to investigate the stability of masonry slender walls with consideration of effect of reactive restraints implied by support conditions. To explore the effect of reactive support conditions on stability of masonry load bearing block walls a full scale testing program was carried out.

The experimental program was designed to test full scale masonry walls and to determine their material properties by testing steel rebars and masonry prism assemblages as well as grout and mortar. Eight wall specimens were tested in two groups. The first group consisted of four walls with common slenderness ratio ( $h/t$ ) of 28.6 while in the second group four walls with slenderness ratio of 33.9 were built. To study the extent of rotational restraint of wall support interface on axial load carrying capacity of the walls, a steel arm with a controlled flexural stiffness was rigidly connected at the base of the wall specimens to simulate support stiffness. The flexural stiffness of this arm was a primary parameter of the test specimens. Detailed descriptions of the test set-up and wall specimens, followed by instrumentation and testing procedure will be presented in this chapter. Results obtained from the test program will also be discussed in this chapter.

Discussion of the experimental results of each group deals with the histories of load-deflection, load-support moment and load-mid-span bending moment responses.

### **3.2 Numerical Estimation of Support Stiffness**

Before starting the experimental program, an extensive numerical study was performed to estimate the rotational stiffness provided by different support conditions. Masonry walls are generally supported by concrete grade beam or strip type foundations. These foundations provide restraint against out-of-plane rotation of the walls, and thus affect both stiffness and effective height of the wall. Single story load bearing masonry walls are generally constructed on strip footing or grade beams and are rotationally restrained at the bottom. In case of multi-story buildings load bearing walls derive rotational restraints from floor slab-wall connections. For the current study, strip type foundations were selected for numerical investigation of the magnitude and range of rotational stiffness. Support stiffness of strip foundation is affected by its dimensions (size) and soil type. Contribution of soil in overall support stiffness comes from modulus of sub-grade reaction of the soil. Stiff soils possess higher values of modulus of sub-grade reaction as opposed to soft soils. Thus, stiff soils contribute more to support stiffness as compared to soft soils. Table 3.1 shows the values of the modulus of sub-grade reaction of different types of soils. Because the support stiffness offered by strip footing is a function of strip footing dimension and soil stiffness, a variety of cases with combination of these two parameters were numerically investigated. The numerical model used in evaluating support stiffness is shown in Figure 3.1. A total of 400 cases were numerically examined, corresponding to different combinations of stiff to soft soils with smaller to larger strip footing dimensions. It is important to mention here that these cases correspond to commonly used field values of strip footing dimensions and soil types. The numerical model shown in Figure 3.1 is based on the following assumptions:

- i) Footing subjected to eccentric axial load, causing stability failure of masonry block walls. The main focus of the current study is single storey masonry load bearing block walls standing on strip footings.

Those walls are subjected to eccentric axial loads and in turn the foundation has to resist the corresponding moment.

- ii) Support stiffness is a function of strip footing dimensions and modulus of sub-grade reaction of underlying soil. Thus, the effect of side soil is neglected. However, it is also assumed that the top of the footing is not allowed to move horizontally.
- iii) Minimum frost cover is 1500 mm and foundation is shallow, which is a common practice for masonry load bearing block walls.
- iv) Soil is elastic and the wall response is not limited by any nonlinear behaviour of the geotechnical mass.

Numerical analysis was performed for different cases as mentioned earlier and a database of different support stiffness values corresponding to different soil conditions and strip footing dimensions was prepared. The stiffness ranges from 1000kN-m/rad for narrow strip footings on clayey sand to 10,000kN-m/rad for wide foundation strips on dense sand.

The next step was the simulation of the support rotational stiffness in the laboratory. The main consideration was that the system should be simple and practical for laboratory implementation. A simple system of steel beams was selected and its flexural stiffness was controlled to simulate support rotational stiffness. The support stiffness offered by strip foundations under different soil conditions were translated into HSS structural beams simply supported at one end and rigidly connected at other end to the masonry wall base, Table 3.2 shows different support conditions and their relevant laboratory simulated supports. Variable cross-section and span of the HSS structural steel beams were used to apply different amounts of support stiffness. Details of laboratory simulation of support stiffness will be discussed in Section 3.4.3 of this chapter.

### **3.3 Material Testing**

#### **3.3.1 Masonry Assemblages**

Standard 200 mm concrete blocks (15MPa compressive strength) were used to construct five hollow and five fully grouted prisms. Each prism was five courses high and one and half blocks wide with type-S mortar placed horizontally between face shells and vertically along the two end webs. Prism specimens were aligned in the MTS-6000 material testing machine and to ensure uniform application of compressive load. 10 mm thick fiberboard pieces were placed at top and underneath the specimens, standard prism test procedures were used as per requirement of CAN/CSA-A369.1. The test data recorded included load as well as traveling head displacement.

Grouted prisms typically failed because of diagonal cracking followed by crushing of face shells, while in all un-grouted prisms splitting of face shells was observed at failure. Grouted prisms showed more axial load but lower compressive strength as compared to ungrouted prisms, because of increased effective area of cross-section because of grouting. Figure 3.2(a) and Figure 3.2(b) show the typical failure of grouted and un-grouted prisms. In accordance with Clause 9.2.2 of CSA S304.1 average compressive strength was determined for both grouted and un-grouted prisms and found to be 10.18 MPa and 14.5 MPa respectively. Modulus of elasticity was also calculated and mean of the values of grouted prism was 7379 MPa, while for un-grouted it was 14355 MPa. Table 3.3 shows the prism test results in detail.

#### **3.3.2 Mortar and Grout**

The specified strength of mortar and grout was verified by performing mortar and grout test as per Clause 9.2.2. CSA S304.1-94. Six cubes (50x50x50 mm) of Type-S mortar were tested and mean mortar strength was observed as 38.82 MPa.

For grout three 5 x 75 x 150 mm prisms were tested. The mean grout strength was 32.43 MPa. Figure 3.3 shows the grout test procedure, Tables 3.4(a) and 3.4(b) summarize mortar and grout test results respectively.

### **3.3.3 Steel Reinforcement**

The same batch of 15M rebars was used in the construction of all wall specimens. Therefore, one standard rebar test consisting of the two rebar specimens was performed. 15M weldable rebars were used to serve as dowels at bottom of masonry wall specimens, the rebar test for weld able rebars was also performed in which two specimens were tested with standard rebar testing procedure. Average results of the rebar test are shown in Table 3.5. Both sets satisfy grade 400 requirements.

### **3.4 Test Specimens and Test Setup**

Eight wall specimens were constructed using 200 mm hollow concrete masonry units with a specified compressive strength of 15 MPa with typical cross-section as described in Figure 3.4. Four wall specimens were constructed to a height of 5m (25 courses) and four were constructed to a 6 m (30 courses) height. Each specimen was approximately 1.2 meter wide. Units were laid in running bond with type-S mortar by professional masons. Each wall was constructed on a reinforced concrete beam section to simulate a wall foundation during testing and to facilitate handling of the walls before and after testing. Table 3.6 provides the specifications of each test specimen.

All wall specimens were typically designed according to common masonry block wall design practice. No.9 gauge ladder type horizontal joint reinforcement was placed at every second course conforming to the design code requirements. 15M steel reinforcing dowels, already fixed in the concrete bases were placed vertically in the second core from each end of the wall at a spacing of 600 mm on center.

These two cores were then fully grouted. Vertical 15M reinforcing bars were also placed by providing 600 mm lap with the dowels and at mid height of the walls, typical cross-section of wall specimen is shown in Figure 3.4. These vertical reinforcing bars were centrally located within the cores using the same No.9 gauge wire installed every fifth course, as shown in Figure 3.5.

The test-set-up used in this experimental program consisted of three major parts: a system for vertical load application, a simulation of support stiffness and a lateral bracing system. Figure 3.6 explains the test-setup details. Figure 3.7 shows a photo of the test set-up. A thorough description of the test-setup follows.

### **3.4.1 System for Vertical Load Application**

The system for vertical load application was designed with pin-type connections at both top and bottom supports of the walls. A testing machine with 6000 kN compression capacity and 600 mm diameter compression head was used to apply axial load to the top of the walls through a true pin-type arrangement. On top of each wall before testing, a C-shaped steel cradle was placed. The experience gained in previous testing programs under eccentric compression had shown premature failures at the top of the wall because of anchorage slippage. To maintain the proper anchorage force on the top part of the reinforcement bars, a 12.5 mm thick steel plate was welded to these bars. A leveling compound was placed between the top plate of the wall and steel cradle to obtain a smooth and leveled surface suitable for a uniform load distribution. The bottom support of the wall specimen was provided through a pin assembly that consisted of a 150 mm diameter steel shaft supported by spherical bearing at each end. The spherical bearings were pressed into large steel housings, which had provisions to bolt into the T-slots in the base of the testing machine. A 38 mm thick steel plate was bolted along a machined flat surface on the shaft. Top assembly details are shown in Figure 3.8.

### **3.4.2 Lateral Bracing System**

Lateral support was provided at the top loading point to control the lateral movement of the wall specimen and the top loading assembly. To accomplish this task a stiff column (W360 x 72) was fixed at the base to the strong floor at approximately 1.5 m from the wall center and at the level of the load point, two lateral braces (L64 x 64 about 1 meter long) were attached to the column. These braces were then connected with an eye-bolt to each end of the top pin assembly.

### **3.4.3 Simulation of Support Stiffness**

Simulation of support stiffness was provided in the lab using the flexural stiffness of a steel arm with HSS cross section (Hollow steel rectangular cross-section) rigidly connected to the wall base at one end and simply supported on the floor at its other end. Figure 3.9 demonstrates the boundary conditions at both ends of simulated support stiffness. To achieve different levels of support stiffness, the flexural stiffness of the HSS steel arm was varied by varying its span and cross-section. Two different cross-sections were used to provide three types of support stiffness, one was HSS 152 x 152 x13 and the other was, HSS 102 x 102 x 6.4, in each case an end plate, 1200 x 200 x 50mm thick was concentrically attached to the HSS-beam. Two rows of 41-mm diameter holes (four in each row) were made in the steel plate to attach this assembly to the base of the wall specimen.

A 1190 mm long and 200 mm wide concrete prism confined with two (C 75 x 7) steel channels was used as a base for the construction of each wall specimen. The concrete prism had a series of holes to facilitate the attachment of HSS arm by means of 38 mm diameter, high strength bolts. For dowel action between wall and concrete base, two 15M bars were welded to a 19 mm thick steel plate that was in turn welded to the top of the confining channels of concrete base. The weld thickness used for welding of steel bar to the plate was designed to provide sufficient strength required to develop yield force in the bars. The concrete base

was capable of providing a solid platform having enough torsional stiffness to avoid distortion. The assembly for simulated stiffness of support (HSS and plate assembly) was rigidly connected to the concrete wall base with eight 38 mm diameter high strength bolts. Figure 3.10 shows a photo of the simulated support stiffness.

### **3.5 Instrumentation**

For each test, data was recorded electronically from 35 channels. The vertical load and vertical arm travel of the testing machine were provided through an integral pressure transducer and integral displacement transducer. Horizontal displacement of the wall specimen was recorded with seven to eight LVDTs (Linear Variable Displacement Transducers) ranging from  $\pm 75$  mm, placed along the wall height. Three rows of strain gauges were mounted on the bottom dowels of the wall. Each dowel was fitted with six strain gauges, three on each face, placed at about the level of the bottom, middle and top height of the bottom course of the wall.

The objective was to verify the bending moment measured at the bottom of the wall. Six rotation meters monitored the rotational displacement during testing. Of these, two were mounted on the top and two were at the bottom of the wall specimen, one was placed 100mm from the junction of the HSS steel arm and the wall base and the last was mounted on the far end of the HSS steel arm Figure 3.11 explains the details of instrumentation. The behavior of the HSS arm assembly (i.e. Simulated Support Stiffness (SSS)) was monitored by mounting two strain gauges at the bottom of the arm.

### **3.6 Testing Procedure**

Each specimen was loaded in displacement control. Two stroke rates were used to trace the response. A stroke rate of 0.19 mm/min was used up to the maximum load and a comparatively higher stroke rate i.e. 0.5mm/min was used in the post

failure region of the response. In all the tests, eccentricity of the axial load at the top of the wall was set at 1/3 of the total thickness of the wall, while at the bottom of the wall nominal zero eccentricity was set for all tests, in so far as wall alignment is considered. Naturally the reactive load arm would modify the eccentricity as the test progresses.

### **3.7 Test Observations:**

A summary of each test specimen is given in Table 3.6. Observations noted during the testing of each group of walls are discussed in detail in the following.

#### **3.7.1 Group-I (5-meter Tall Walls – $h/t = 28.6$ )**

Four masonry block wall specimens (W1,W2,W3,W4) built with an  $h/t$  ratio 28.6 were tested with variable bottom support conditions at a common eccentricity to thickness ratio ( $e/t$ - ratio) of 0.33 at top of the wall.

Specimen W1 was tested with a simulated support stiffness of 5000kN-m/rad. Up to a load of about 950 kN, there was no sign of failure but at a load level of 964 kN, a sudden failure occurred and the top course was crushed along with an opening of the bed joint between the second and third course from the top as shown in Figure 3.12. This was a localized failure of the face shell and the wall could not reach its projected maximum load (983kN). The wall, however, showed a considerable increase in axial load carrying capacity (964kN) over that of a simply supported wall which attained 514.2kN. This verified the effectiveness of the simulated support system.

The reasons for the local failure were bond slippage and anchorage failure of the reinforcement at the top of the wall. To avoid local failure in the next test, the reinforcing bars, which were left to project freely almost 600 mm above the top course of the wall specimen during construction, were cut and welded to a 12.5 mm thick steel plate as described above.

Specimen W2 was tested with increased simulated support stiffness of 10,000 kNm/rad. The same type of local failure occurred during this test as well. The probable reason was improper leveling of the top steel plate of the wall. Because of local failure, W2 could not achieve its expected load level and failed locally at a load level of 812.6kN, which is even smaller than the local failure load of W1. After testing, when W2 was laid down, some extra grouting of the cores was observed. The cores, which were supposed to remain empty, were filled up to 7 courses from the bottom. Apparently this happened during construction of the wall when masons lost control of the pumping hose and filled the empty courses from bottom to top. Although, extra grouting affected the behavior of the wall it behaved well up to the load level where local failure occurred prematurely.

Wall specimen W3 was tested with zero rotational stiffness at the bottom. It did not have reinforcing bars projecting above the top of the wall. The C-cradle was leveled but set loose on top. W3 achieved its full axial load capacity and did not show any local failure. The first horizontal crack appeared at mid height of the wall (bottom of course No.13). At the end of the test the face shell cracked at course No.14 exactly at the place where the reinforcing bars were lap spliced. W3 carried a much lower load than W1 and W2 because of the zero rotational stiffness at the bottom. Figure 3.13 shows the cracking of W3 at failure.

Specimen W4 was tested with 1000 kNm/rad rotational stiffness at the base. In this case, the top steel plate was grinded and leveled with a leveling compound for smooth distribution of the load from top loading assembly to the wall. W4 also achieved the full load carrying capacity without having any local failure, so the failure of W4 was defined as the condition limiting the axial load capacity of the wall specimen. After failure, the wall was unloaded for safety reasons, and to avoid yielding of the HSS-steel beam. It was observed that horizontal cracks appeared at top and bottom bed-joint of course No. 5, and no cracking at the face shell was observed.

Figure 3.14 illustrates the typical deflected shape at failure of Group-I, support stiffness caused prominent deflection of the top portion of the wall. Testing of Group-I shows that the effect of support stiffness on load carrying capacity of the wall is rational and quantifiable.

### **3.7.2 Group-II: (6-meter Tall Walls – $h/t = 33.9$ )**

Group-II consisted of four full-scale 6 m high walls. To avoid localized failure, a 12.5 mm thick plate was used at the top of every specimen welded to the vertical reinforcing bars. The plate was placed on a self-leveling compound, similarly to the procedure used for walls W3 and W4.

The first specimen of Group-II, W5, was tested with a simulated support stiffness of 10,000kNm/rad and under the influence of support stiffness the specimen was able to sustain a high load carrying capacity at failure. The first horizontal crack appeared above the mid height of the wall at course No.20 from the bottom. It is noted that cracking started just after the peak load was achieved.

W6 was tested with simulated support stiffness of 5000 kNm/rad. Like W5, specimen W6 also failed at high eccentric axial load. The first horizontal crack appeared at course No.17. After the peak load was achieved further cracks appeared on higher courses from 17 to 27

Specimen W7 was tested with support stiffness of 1000 kNm/rad and showed excessive cracking and deflection at failure. W7 carried a lower axial load capacity of 601 kN as compared to specimens W5 and W6.

The specimen W8 was tested with zero support stiffness and failed at much lower axial load capacity as compared to other specimens of Group-II. W8 experienced the cracking at middle of the height on top of course No. 15. Test results of

Group-II established the fact that because of effect of simulated support stiffness, double curvature exists at the failure of tall masonry block walls, also confirmed by typical deflected shape at failure of Group-II shown in Figure 3.15. The walls of this group behaved rationally with the peak span moment (the location of the horizontal cracks) moving down as fixity at the bottom decreased.

The test results for each group are presented in Table 3.7

### **3.8 Test Results and Discussions:**

Observation of the failure pattern of walls shows that, as expected, the slenderness ratio affected the over all axial load capacity of the walls in such a manner that the walls with lower slenderness ratio( $h/t=28.6$ ), showed higher load carrying capacities as compared to walls with higher slenderness ratio ( $h/t=33.9$ ). This phenomenon became more significant in terms of effectiveness of support stiffness (more effective for low  $h/t$  ratios and less effective for higher  $h/t$  ratios). Higher slenderness ratio of Group-II caused the walls to fail under non-linear geometric effects, although support stiffness influenced the degree of the non-linearity of these walls by controlling the out-of-plane deflection but still Group-II could not sustain as high axial load capacity as was obtained by Group-I. The higher axial load capacity of Group-I walls showed that support stiffness was more effective in improving the behavior of these walls at failure. The effect of support stiffness on Group I ( $h/t =28.6$  as compared to  $h/t = 33.9$  of Group-II) was not severely counteracted by non-linear geometric effects. As a result the failure of the walls was delayed (to the point where local failure was achieved in case of specimen W1 and W2) and the walls were able to sustain higher load capacity.

Test observations show that for a particular  $h/t$  ratio, the relative increase in axial load capacity decreases with increase in support stiffness as the wall approaches a full fixity condition. Table 3.7 shows consistent increase in the axial load carrying capacity of walls with increasing support stiffness. The detailed comparison in

varying axial load capacities with respect to Simulated Support Stiffness is presented in Table 3.8. Even though walls with  $h/t=28.6$  and simulated support stiffness of 10,000 kNm/rad and 5000 kNm/rad were failed by premature local failures they showed increased load carrying capacity as compared to the wall with no rotational stiffness. Figure 3.16 summarizes the increase in load capacity of walls with respect to increase in simulated support stiffness

The load deflection responses of Group-I and Group-II indicate the increase in stiffness of the wall. Initial slopes of load-deflection responses increase with increase in support stiffness and finally results in higher load capacity for the walls tested with higher simulated support stiffness with exception of W2, which failed locally. The load-deflection responses of Group-I and Group-II demonstrate a consistent increase in load carrying capacity and stiffness of the wall with the increasing level of support stiffness. The responses are shown in Figure 3.17 and Figure 3.18 for Group-I and Group-II respectively.

With increase in support stiffness, the point of maximum deflection moves upward relative to the wall with zero simulated support stiffness. This is true for walls with both low and high slenderness ratios. Figure 3.19 and Figure 3.20 show the plot of deflection along the height of walls at failure for Group-I and Group-II, respectively. It is observed that with an increase in simulated support stiffness, the bottom rotation of the walls decreases at failure. This was obviously because of the increase in resisting moment at the bottom of the walls that provided a counter rotation. It is noticed in Figure 3.20 that although W7 was tested with support stiffness of 1000kN-m/rad, at failure, this specimen experienced larger deflection as compared to the reference wall W8. The reason was that support stiffness delayed the failure of W7 and the specimen was able to sustain more cracking as compared to W8, which failed at 26.6% lower axial load capacity and because of absence of support stiffness it was not able to undergo further cracking and deflection

Figure 3.21 and Figure 3.22 show plots of the total bending moment of the walls (including the load eccentricity at the top as well as the P- $\Delta$  effects). It can be observed from these two plots that the point of maximum deflection as well as the point of maximum bending moment moved upward as the support stiffness is increased. All are indications of a change to the deflected shape of a wall from single curvature to double curvature. To highlight the effect of support stiffness, the bottom part of deflection at failure is blown up in Figure 3.23 and Figure 3.24 for Group-I & Group-II respectively, showing the reduction in curvature in the bottom part of the wall with increase in magnitude of support stiffness. Formation of double curvature and reduction in curvature near simulated support illustrated that because of effect of support stiffness, the effective length of the walls was reduced which caused the increase in axial load capacity of the walls.

Figure 3.25 shows the trend of mid-span deflection at failure of Group-II walls. The mid span deflection of specimens W8 and W7 are almost same at failure but the deflection significantly dropped in case of W6 and W5 which were tested with support stiffness of 5000kN-m/rad and 10,000kN-m/rad. The drop in mid-span deflection of W5 and W6 shows that support stiffness controlled the detrimental effects of high slenderness ratio ( $h/t = 33$ ) of Group-II walls and as a result the point of maximum deflection moved from mid-span portion to upper half portion of the walls.

Figure 3.26 shows the trend of maximum bending moment carried by Group-II walls. A progressive increase in maximum bending moment is clearly shown. All wall specimens tested with non-zero support stiffness (W5, W6 and W7) were able to maintain higher stress levels at failure and showed increasing bending moment capacity with increase in support stiffness. Figure 3.22, which shows the bending moment diagrams at failure of Group-II, indicates that support stiffness caused the point of maximum bending moment to move to upper half portion of the walls.

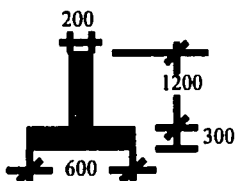
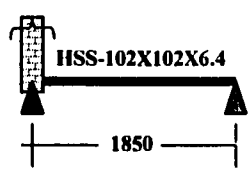
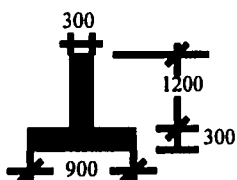
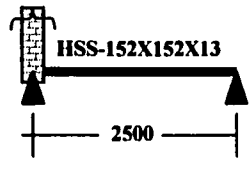
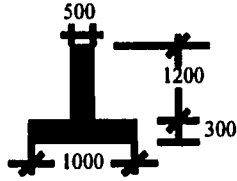
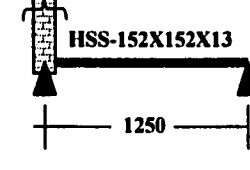
The consistent increase in load carrying capacity of the tested wall specimens under the influence of support stiffness shows that support stiffness might also influence Flexural rigidity of the walls. Therefore, the response of both Group-I and Group-II needs to be investigated in terms of their Flexural rigidity (EI) for further implication of support stiffness on the behavior of masonry block walls. The next chapter deals with estimation of flexural rigidity of the tested specimens.

**Table 3.1 Modulus of sub-grade reaction of different soils**

Soil type	Modulus of sub-grade reaction (kN/m <sup>3</sup> )
Loose Sand	4,800 – 16,000
Medium Dense Sand	9,600 – 80,000
Dense Sand	64,000 – 128,000
Clayey Medium Dense Sand	32,000 – 80,000
Silty Medium Dense Sand	24,000 – 48,000
Clay Soil	12,000 – 48,000

*Reference: Foundation Analysis and Design by Joseph E. Bowles*

**Table 3.2 Relationship between numerical and simulated support stiffness**

Support Stiffness (kN-m/rad)	Strip footing dimensions (mm)	Modulus of sub-grade reaction (kN/m <sup>3</sup> )	Laboratory simulated support stiffness dimensions (mm)
1,000		56,000 (Clayey medium dense sand)	
5,000		76,000 (Medium and dense sand)	
10,000		108,000 (Dense sand)	

**Table 3.3(a) Compressive strength of hollow concrete block prisms**

Specimen	Ultimate load (kN)	*Ultimate strength (MPa)
1	624.91	13.98
2	669.16	14.97
3	683.02	15.26
4	590.04	13.20
5	642.34	15.37
<b>Average</b>	<b>650.83</b>	<b>14.56</b>

\* Based on Bedded Cross-sectional Area = 44700 mm<sup>2</sup>

**Table 3.3(b) Compressive strength of grouted concrete block prisms**

Specimen	Ultimate load (kN)	*Ultimate strength (MPa)
1	1562.27	12.89
2	1201.09	9.91
3	1106.56	9.13
4	974.45	8.04
5	1324.72	10.93
<b>Average</b>	<b>1233.82</b>	<b>10.18</b>

\* Based on Gross Cross-sectional Area = 121200 mm<sup>2</sup>

**Table 3.3 (c) Modulus of elasticity of concrete block prisms**

Specimen	*Modulus of elasticity of grouted prisms (MPa)	**Modulus of elasticity of hollow prism (MPa)
1	8055	13215
2	7129	12412
3	8054	18647
4	5557	13819
5	8099	13585
<b>Average</b>	<b>7378.99</b>	<b>14335</b>

**Table 3.4 (a) Compressive strength of mortar**

<b>Specimen</b>	<b>Ultimate load (kN)</b>	<b>Ultimate strength (MPa)</b>
<b>1</b>	<b>87.90</b>	<b>35.20</b>
<b>2</b>	<b>102.90</b>	<b>41.20</b>
<b>3</b>	<b>100.50</b>	<b>40.20</b>
<b>4</b>	<b>95.80</b>	<b>38.32</b>
<b>5</b>	<b>102.50</b>	<b>41.00</b>
<b>6</b>	<b>92.50</b>	<b>37.00</b>
<b>Average</b>	<b>97.01</b>	<b>38.82</b>

**Table 3.4 (b) Compressive strength of grout**

<b>Specimen</b>	<b>Ultimate load (kN)</b>	<b>Ultimate strength (MPa)</b>
<b>1</b>	<b>210</b>	<b>38.0</b>
<b>2</b>	<b>212</b>	<b>26.4</b>
<b>3</b>	<b>185</b>	<b>32.9</b>
<b>Average</b>	<b>203.3</b>	<b>32.4</b>

**Table 3.5 Properties of steel rebars**

<b>Specimen</b>	<b>Nominal diameter (mm)</b>	<b>Nominal area (mm<sup>2</sup>)</b>	<b>Yield strength (MPa)</b>	<b>Ultimate strength (MPa)</b>	<b>Modulus of elasticity (MPa)</b>
<b>Rebar</b>	<b>15</b>	<b>200</b>	<b>423</b>	<b>568</b>	<b>215000</b>
<b>Weldable rebar</b>	<b>15</b>	<b>200</b>	<b>403</b>	<b>567</b>	<b>201000</b>

**Table 3.6 Specifications of test specimens**

<b>Specimen</b>	<b>Height</b>	<b>Slenderness ratio (h/t)</b>	<b>Support stiffness kN-m/rad</b>
<b><u>Group - I</u></b>			
W1	5437	28.6	5000
W2	5437	28.6	10000
W3	5437	28.6	0
W4	5437	28.6	1000
<b><u>Group - II</u></b>			
W5	6437	33.9	10000
W6	6437	33.9	5000
W7	6437	33.9	1000
W8	6437	33.9	0

**Table 3.7 Summary of test results**

Specimen	h/t	Support stiffness (kNm/rad)	Maximum load (kN)	Maximum moment (kN-m)	Support moment (kN-m)	Mid-span deflection at failure (mm)
W1*	28.6	5000	964.0	63.50	30.50	22.43
W2*	28.6	10000	812.6	54.50	33.53	16.60
W3	28.6	0	514.2	37.10	-	30.73
W4	28.6	1000	756.0	54.30	15.80	28.78
W5	33.9	10000	798.3	54.70	40.10	20.51
W6	33.9	5000	740.4	50.80	31.00	22.86
W7	33.9	1000	601.0	43.13	14.75	26.88
W8	33.9	0	476.0	33.20	-	27.05

\*Walls failed locally

**Table 3.8 Relative increase in axial load capacity**

Wall Designation	Increase in support stiffness (kNm/rad)	Increase in axial load capacity
W1*	0 to 5000	87.50%
W2*	0 to 10000	58.01%
W4	0 to 1000	47.02%
W5	0 to 10000	67.70 %
W6	0 to 5000	55.55 %
W7	0 to 1000	26.2 %

\*Walls failed locally

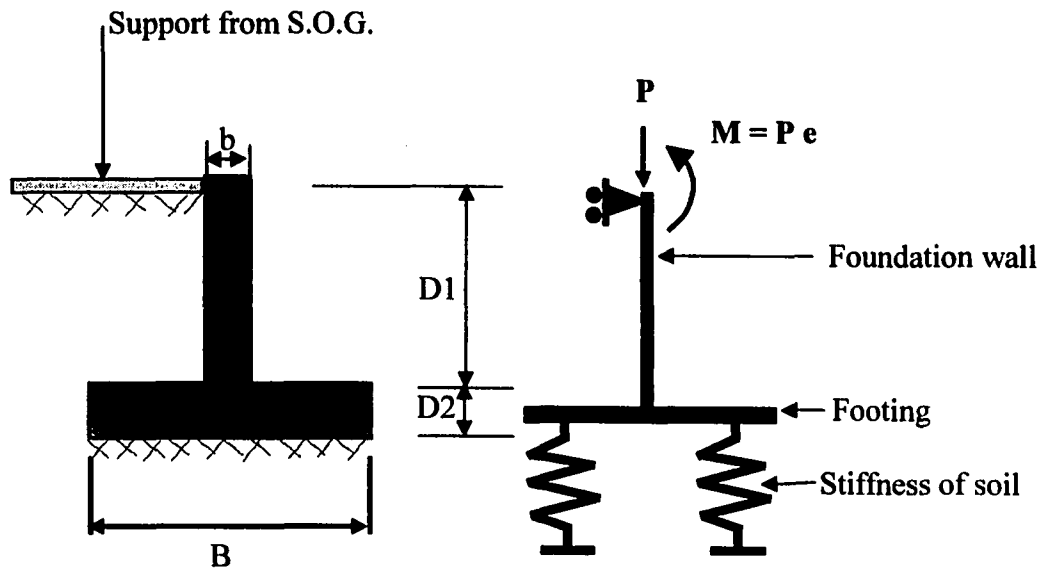


**Figure 3.1 Numerical model of strip footing**

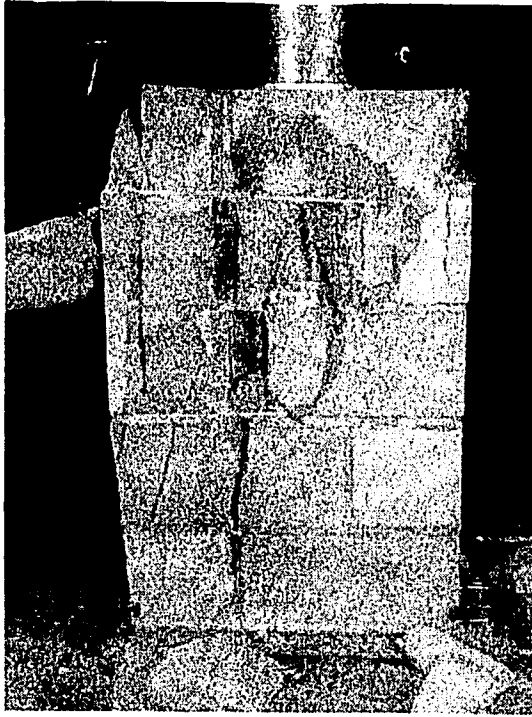


**Figure 3.2 (a) Typical failure of grouted prisms**

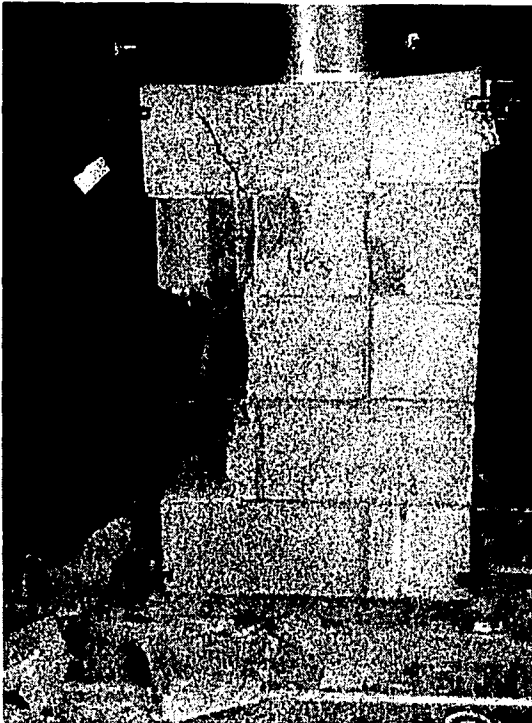


**Figure 3.2 (b) Typical failure of un-grouted prisms**

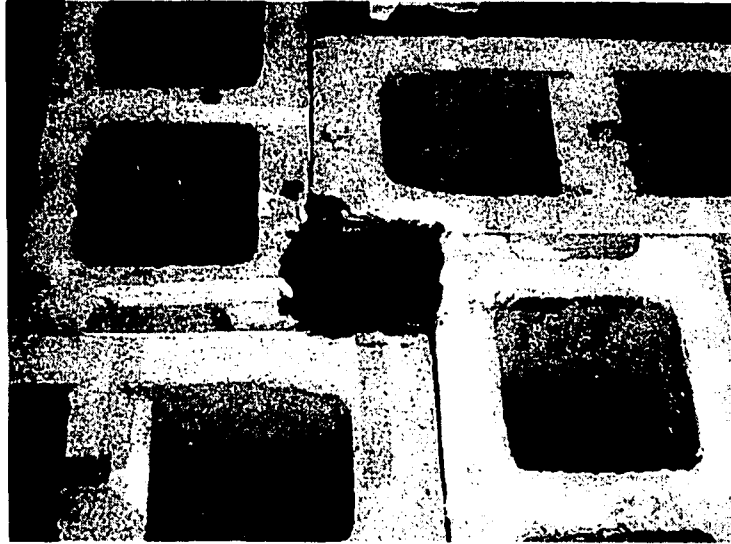


**Figure 3.3 Standard grout test**

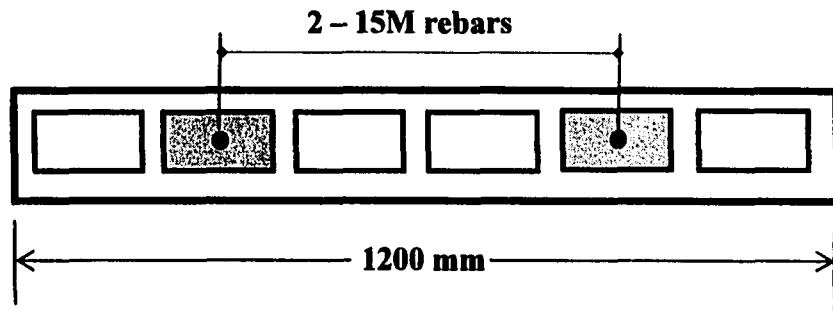


**Figure 3.4 Typical cross-section of wall specimen**

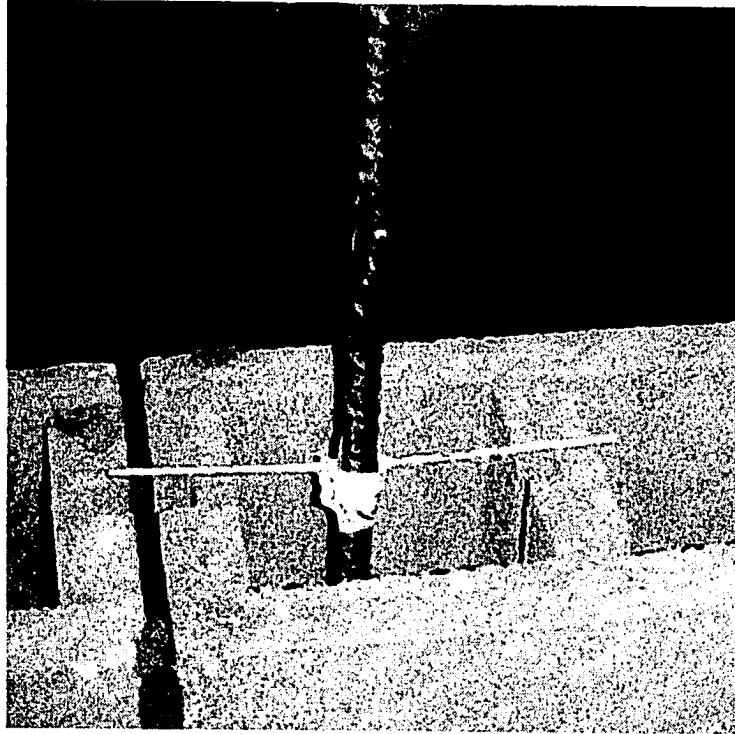


**Figure 3.5 Alignment of vertical rebar**

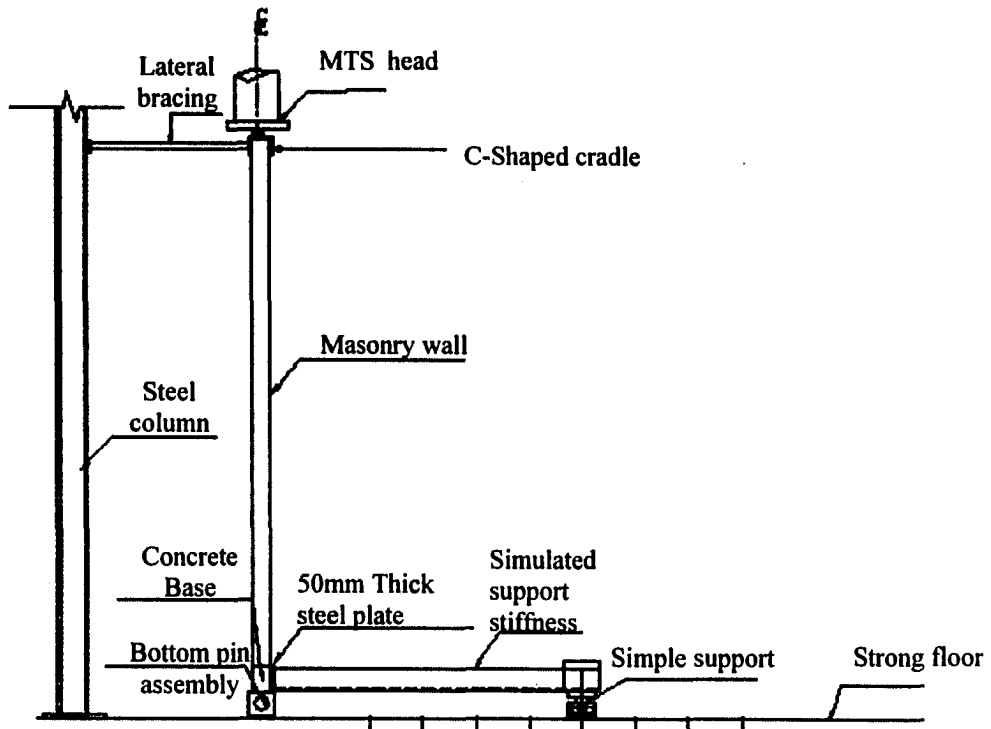


**Figure 3.6 Test-setup details**

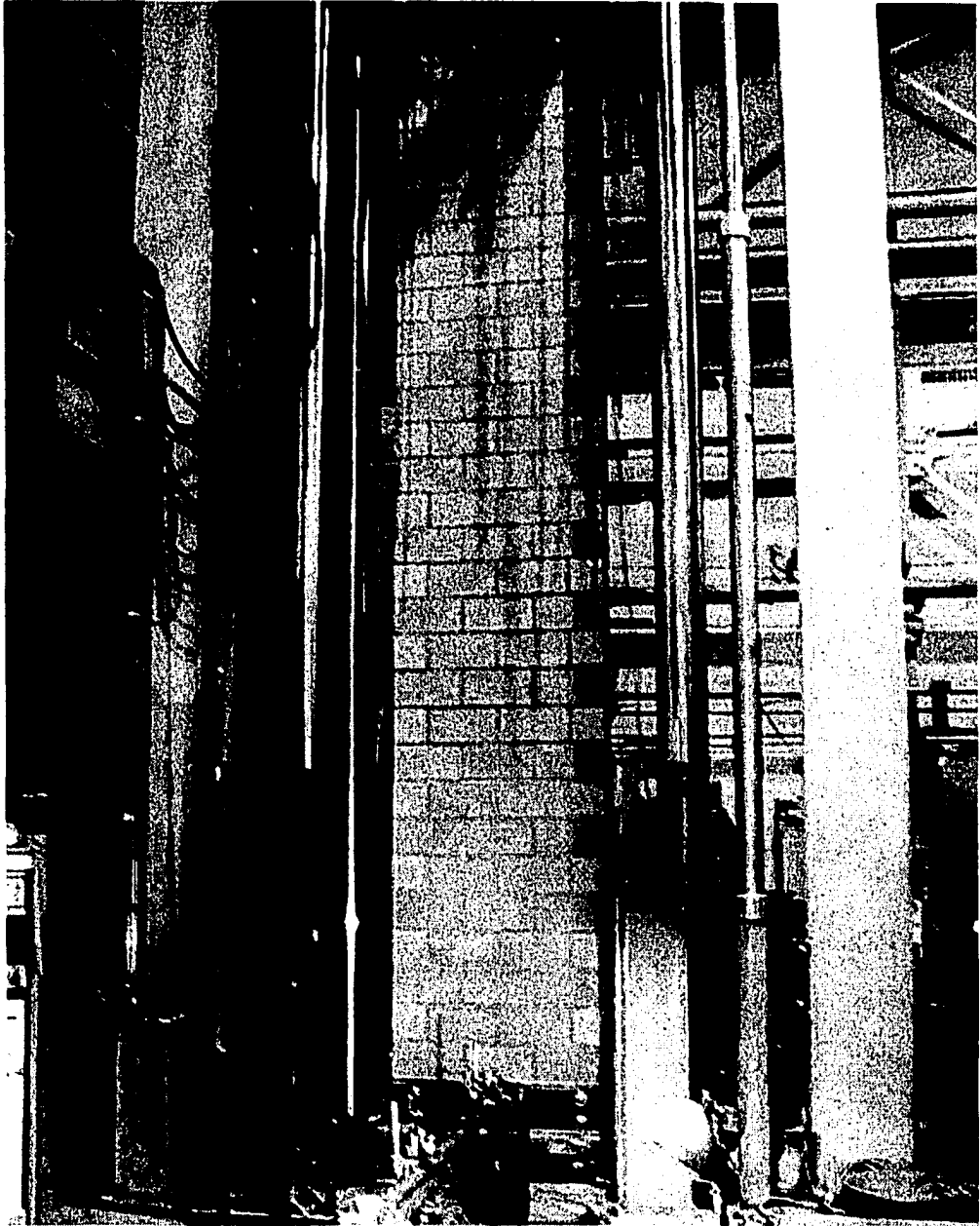


**Figure 3.7 Test setup photo**

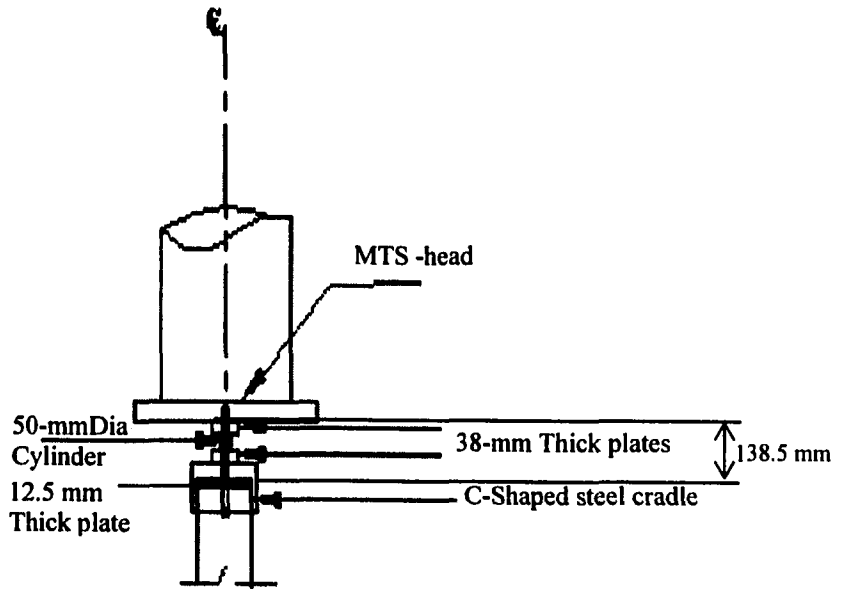


**Figure 3.8 Top assembly details**

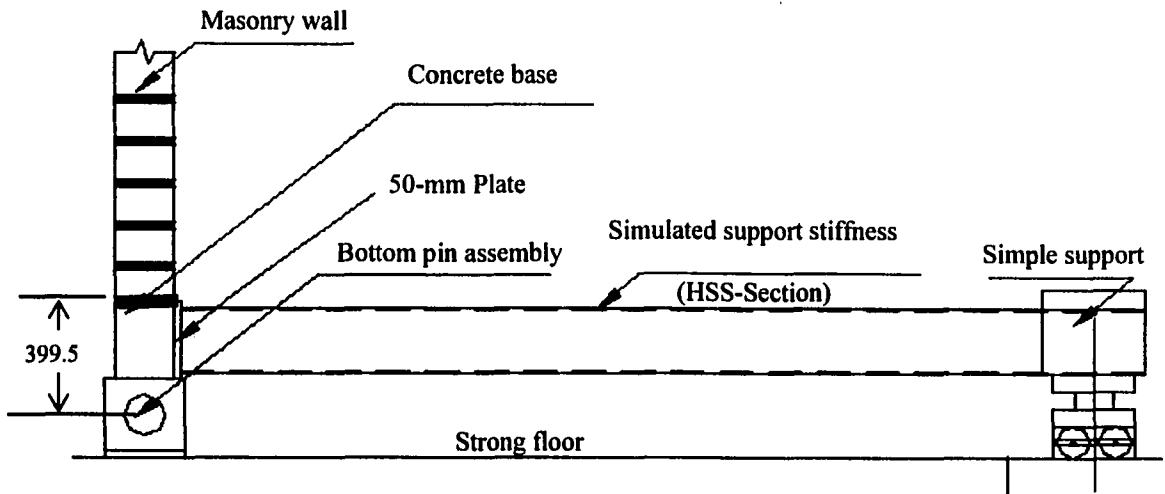


**Figure 3.9 Bottom boundary conditions**

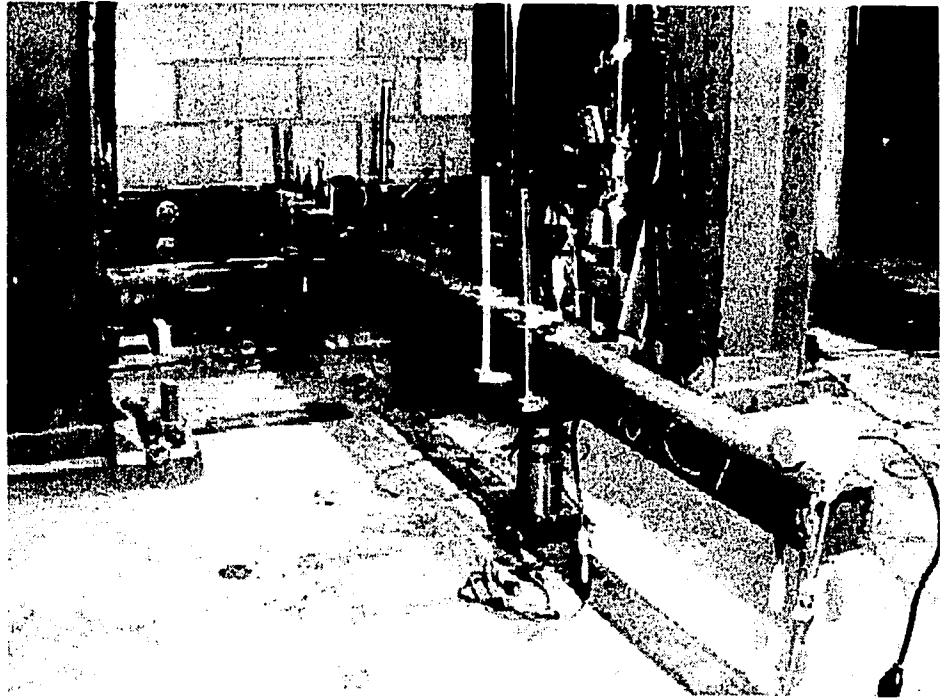


**Figure 3.10 Photo of simulated support stiffness**

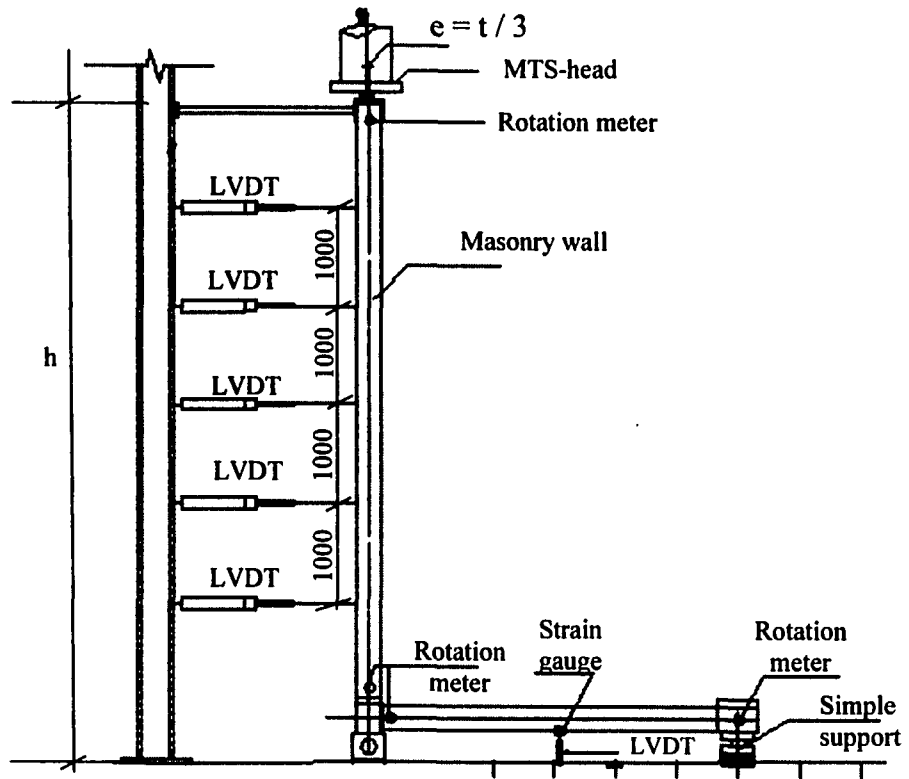


**Figure 3.11 Instrumentation details**

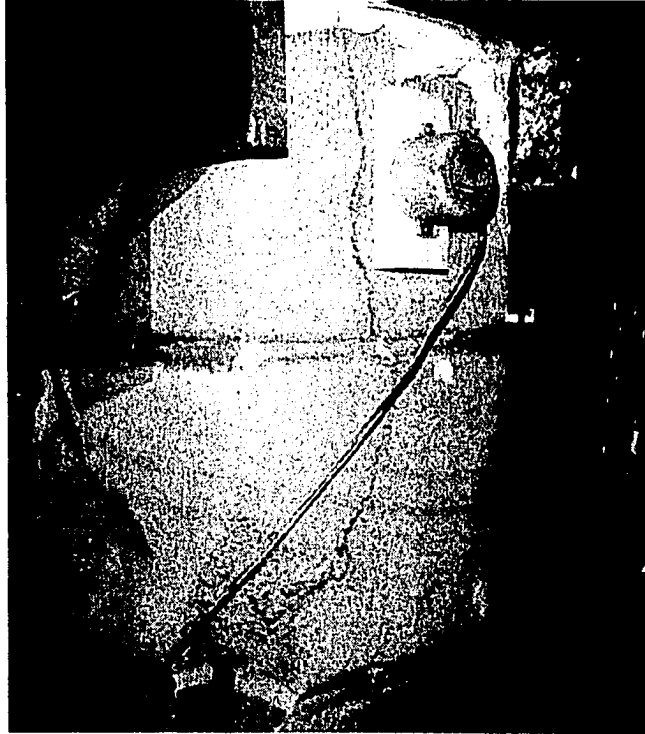


**Figure 3.12 Local failure of W1**

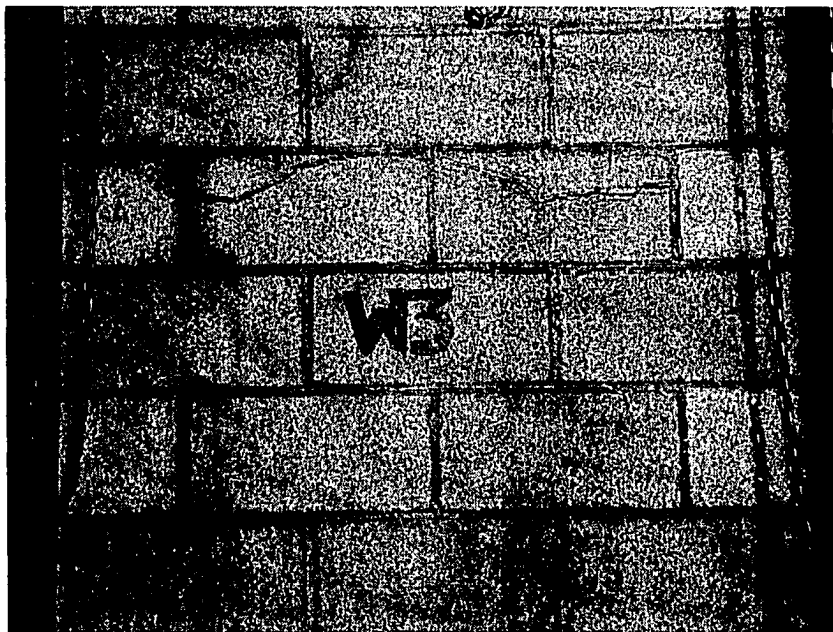


**Figure 3.13 Cracking of W3 at failure**

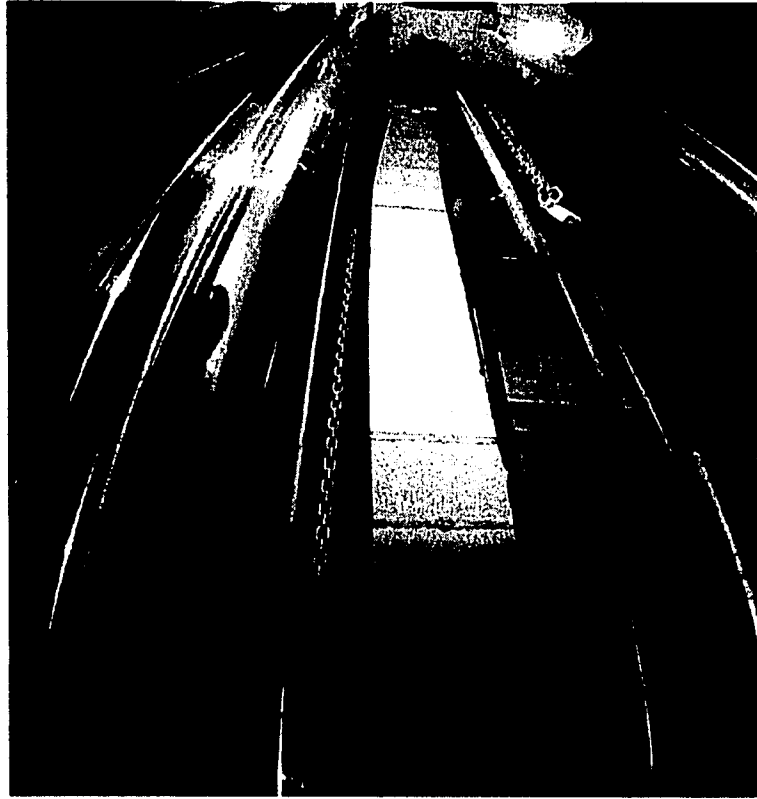


**Figure 3.14 Typical deflected shape of Group-I walls at failure**

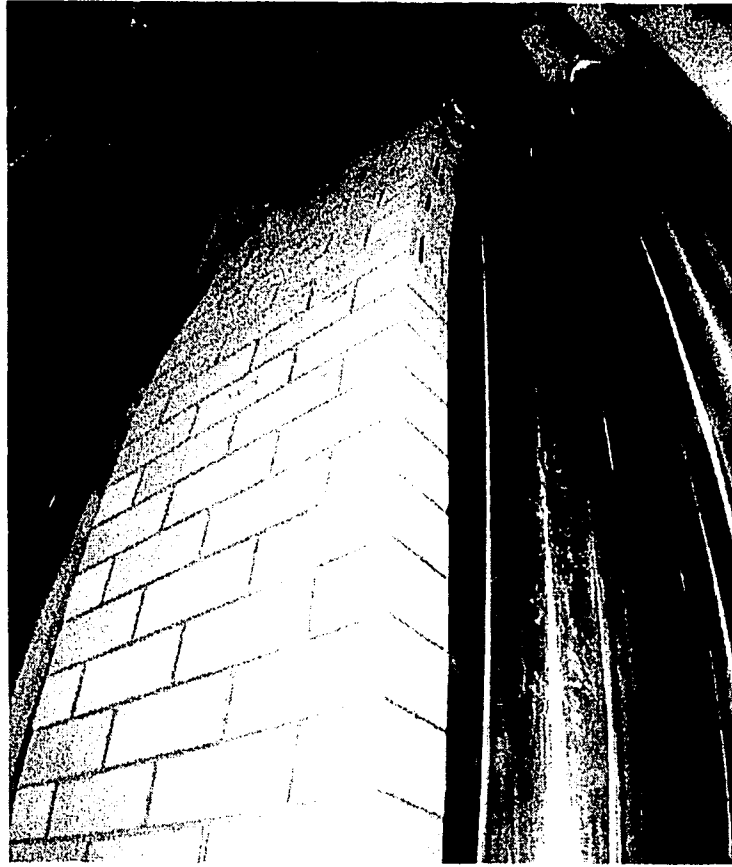


**Figure 3.15 Typical deflected shape of Group-II walls at failure**

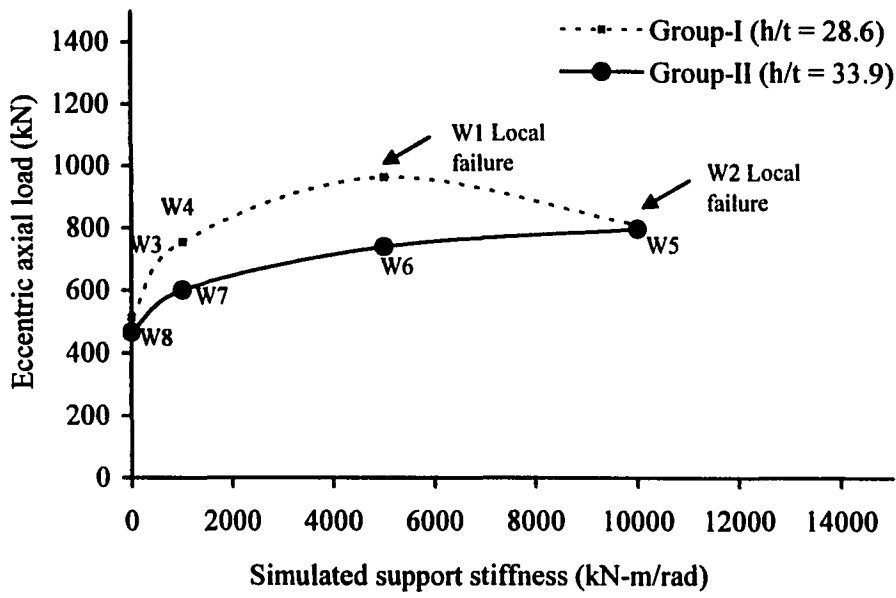


**Figure 3.16 Simulated support stiffness versus eccentric axial load at failure**

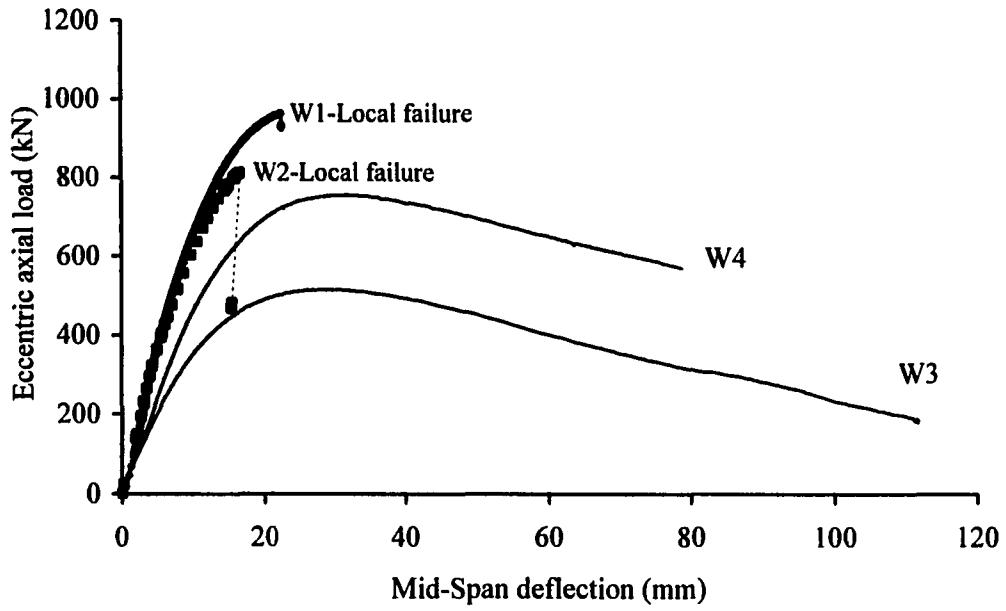


**Figure 3.17 Load deflection response of Group -I**

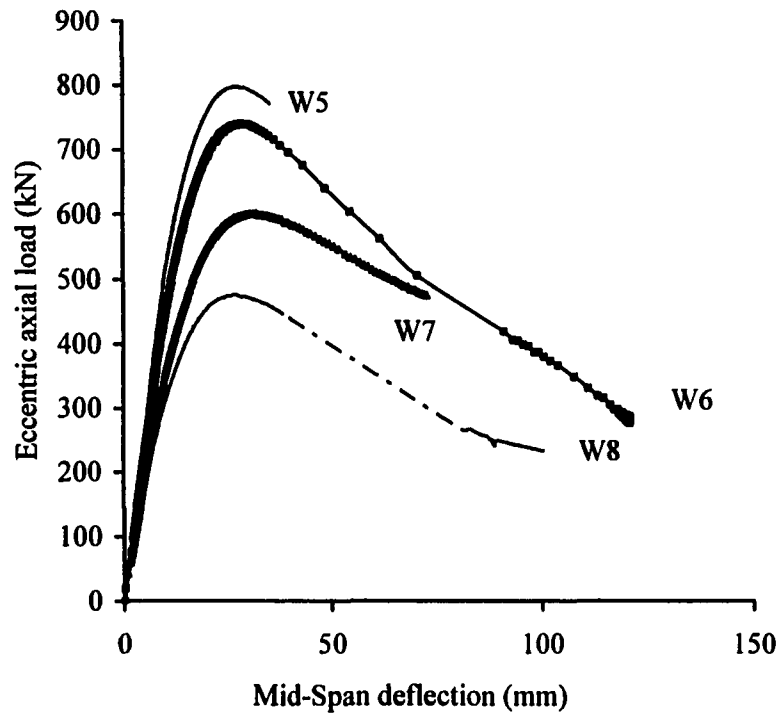


**Figure 3.18 Load deflection response of Group -II**

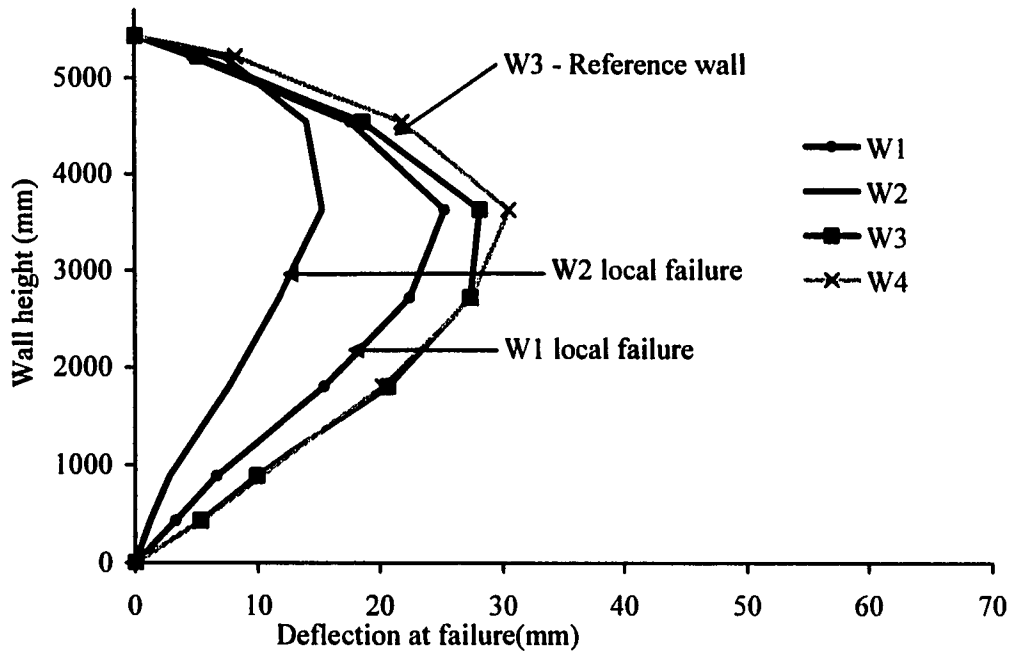


**Figure 3.19 Deflection at failure along the height of walls of Group-I**

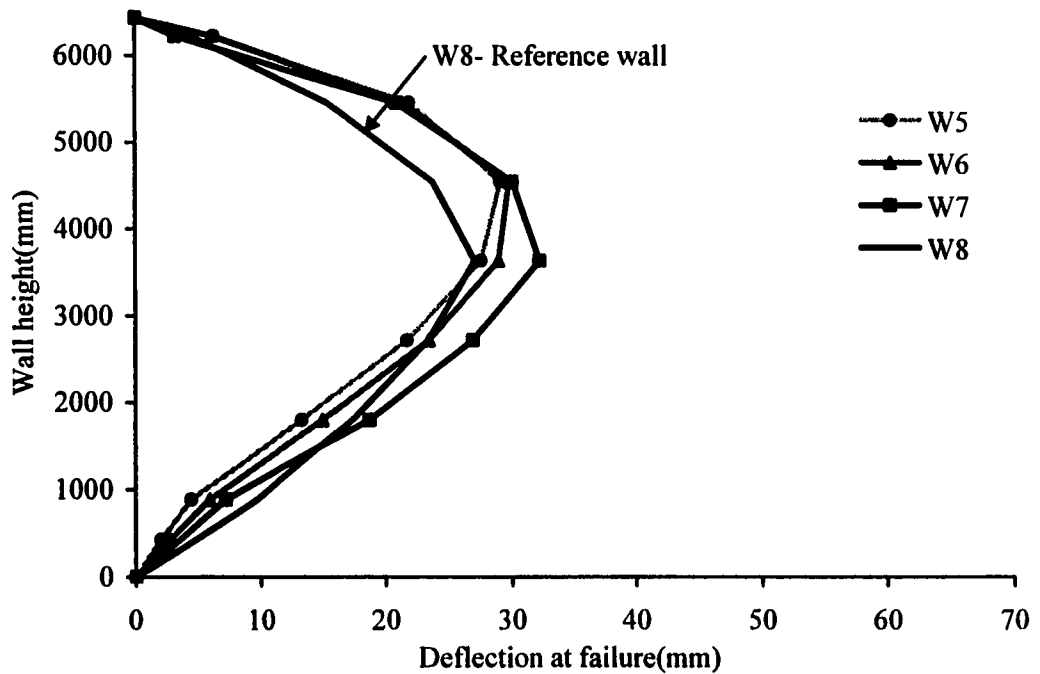


**Figure 3.20 Deflection at failure along the height of walls of Group-II**

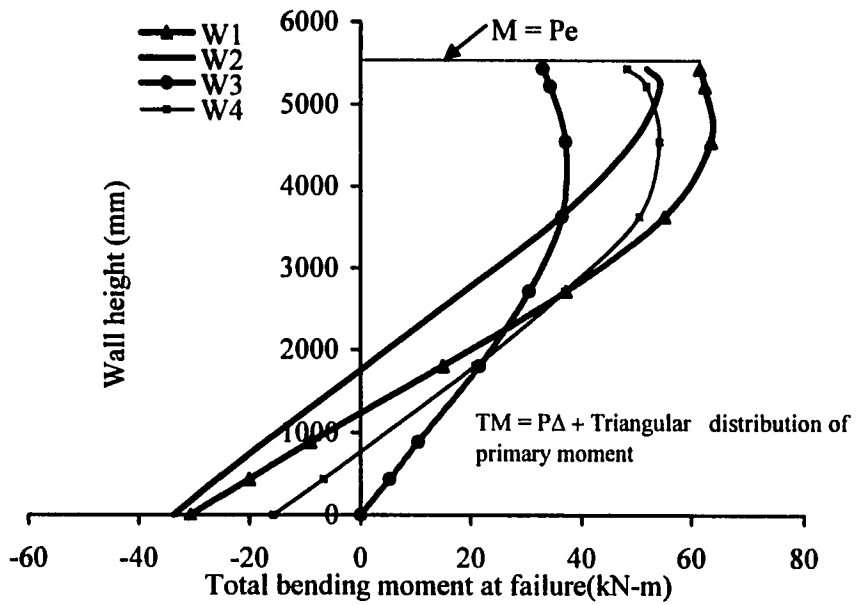


**Figure 3.21 Total Bending moment at failure along the height of Group-I**

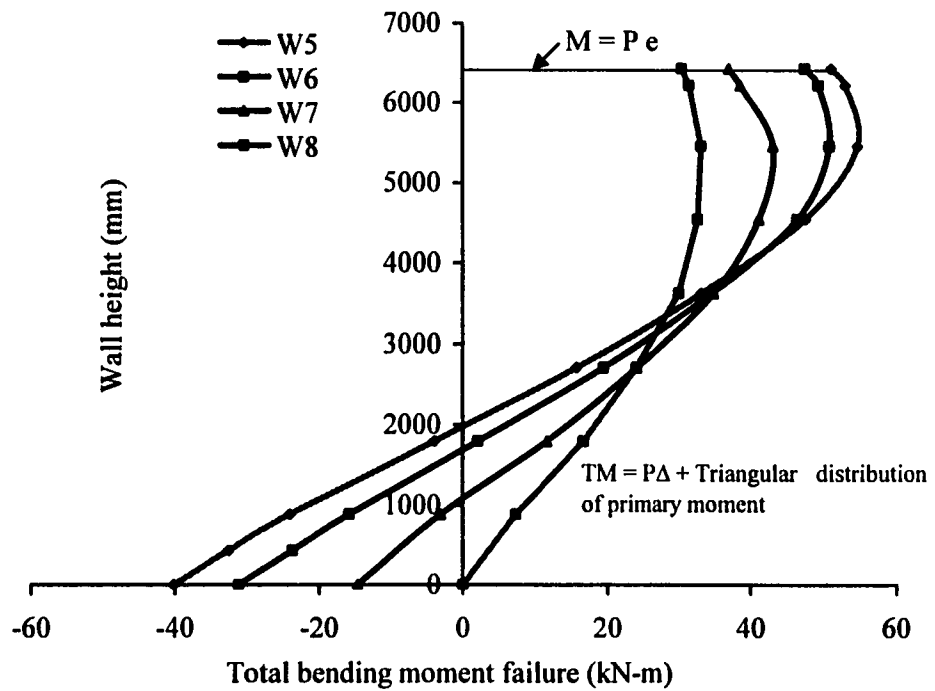


**Figure 3.22 Total bending moment at failure along the height of Group-II**

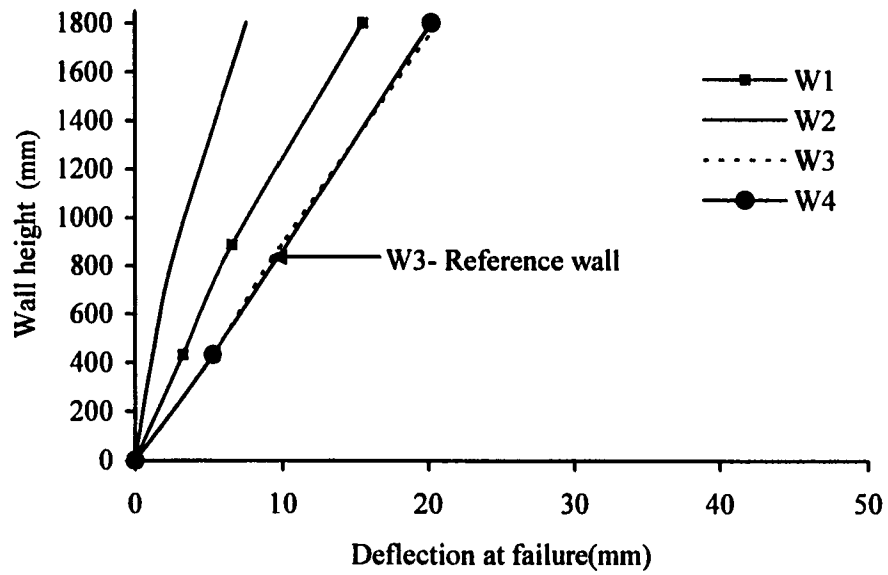


**Figure 3.23 Blown-up plot of deflection at failure of bottom part of Group-I**

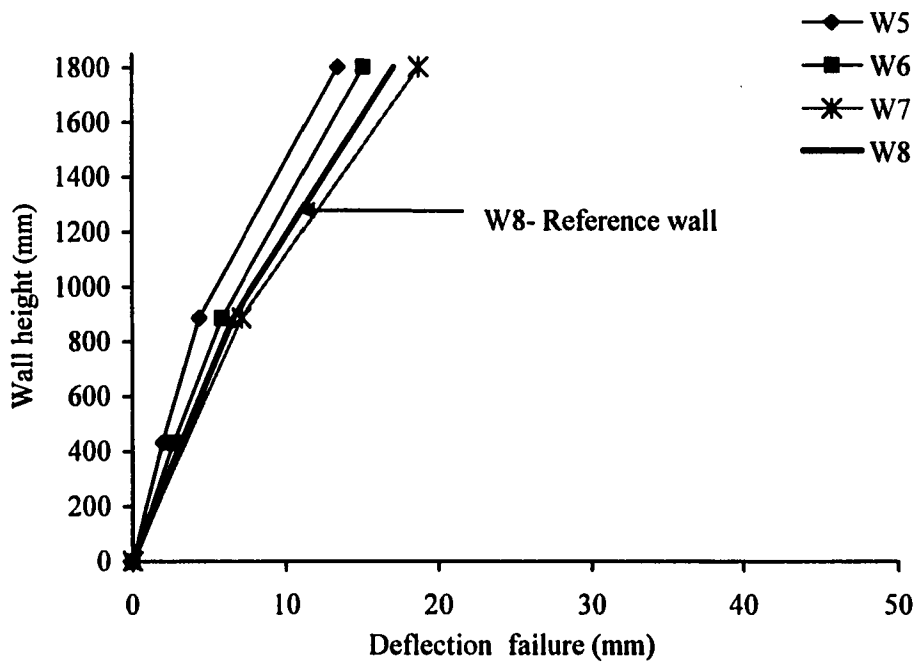


**Figure 3.24 Blown-up plot of deflection at failure of bottom part of Group-II**

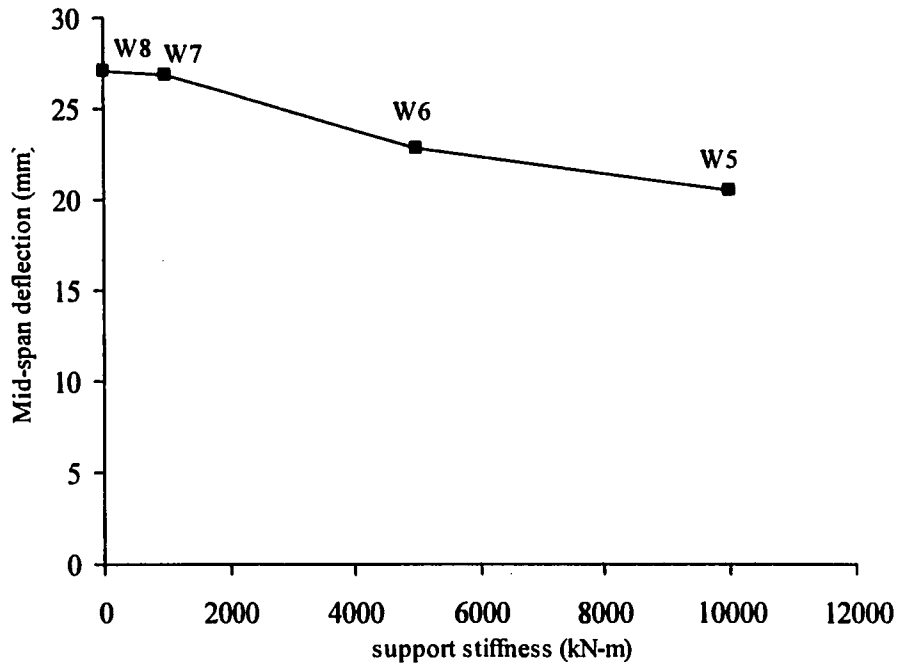


**Figure 3.25 Trend of mid-span deflection at failure of Group-II**

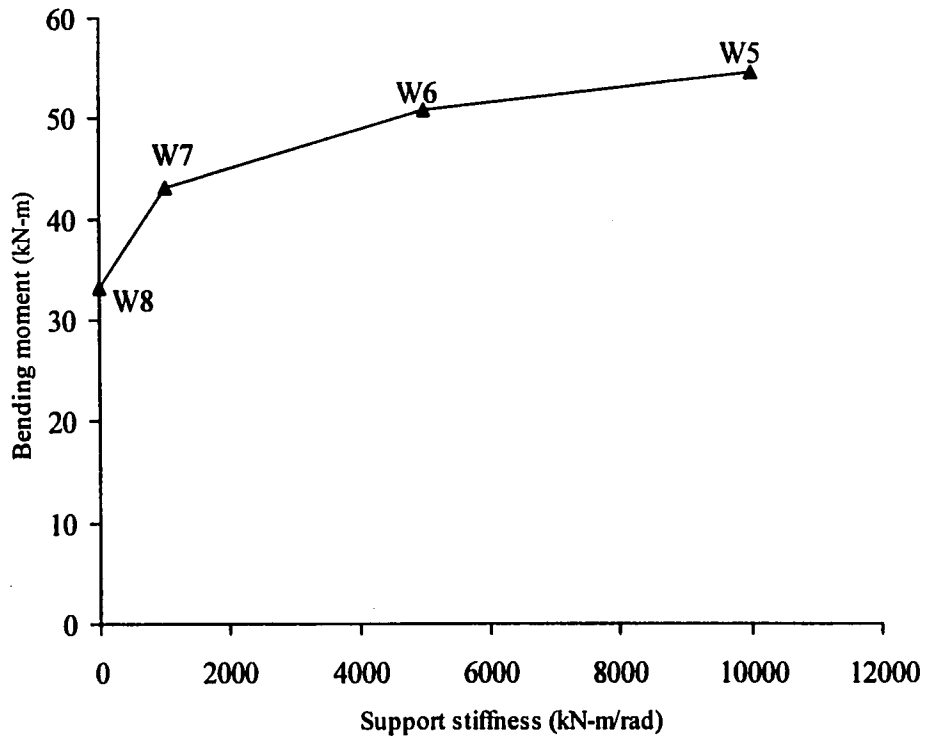


**Figure 3.26 Trend of maximum bending moment at failure of Group-II**

## CHAPTER 4

### FLEXURAL RIGIDITY OF LOAD BEARING MASONRY BLOCK WALLS

#### 4.1 Introduction

As illustrated in the literature review the wall flexural rigidity is a vital parameter, which directly influences the load carrying capacity of a load bearing tall masonry block walls. Experimental results demonstrated a consistent increase in axial load capacity of tested specimens caused by support stiffness. In addition the bending moment and deflection profile all change with changes in the support stiffness. This suggests strongly that changing the curvature value and distribution will influence the inelastic changes in the wall, which directly involves the wall stiffness. In other words, changing the support stiffness would influence the flexural rigidity of wall specimens as well as the axial load carrying capacity. The objective of Chapter 4 then, is to evaluate this particular aspect of behavior.

A straightforward analytical solution of the differential equation of a beam-column was obtained and used to establish mathematical expressions of flexural rigidity of the wall specimens with and without support stiffness. Experimental results were inserted in the derived mathematical expressions and flexural rigidity of all wall specimens was estimated. Different plots showing the variation of flexural rigidity with increasing loads are also presented along with other graphical and tabular discussions of the flexural rigidity of load bearing masonry block walls.

#### 4.2 Effective Flexural Rigidity ( $EI_{eff}$ ) of Masonry Block Walls

Flexural rigidity (stiffness) of masonry load bearing walls combines the effect of Young's modulus and moment of inertia of wall cross-section. These two factors

can be, phenomenologically, combined in a flexural rigidity term,  $EI$ . Simple prism tests show that Young's modulus changes as a function of the axial stress in the wall; mainly because of the non-linear stress-strain constitutive behavior of masonry. Likewise, the moment of inertia also changes both along the height of the wall as well as throughout the history of loading for the same reason. The term "effective flexural rigidity" refers to a single value of flexural rigidity representative of full height and obtained at the ultimate limit strength of a masonry block wall.

Masonry block walls are exposed to both material and geometric non-linearities. Depending on the geometric configuration it is possible that one type of non-linearity dominates the behavior. For example, walls subjected to geometric non-linearity (slender walls) experience variation in flexural rigidity caused by changes in the moment of inertia of the cross-section. These changes are caused by either or a combination inelastic compressive strains and tensile cracking. Changes in the moment of inertia in turn affect the geometrically nonlinear response of the wall, which feeds back into the inelastic behaviour particularly close to peak compressive load. Stocky walls on the other hand, are more prone to material non-linearity and much less to geometric nonlinearity.

According to the literature, (Liu et al. 1998, Liu and Dawe 2001, Liu and Dawe 2003), parameters such as slenderness ratio of walls, load eccentricity, amount of reinforcement and compressive strength of masonry are the factors influencing the flexural rigidity of masonry load bearing walls. In the current study support stiffness is introduced as an additional influencing factor on flexural rigidity of masonry load bearing block walls. Chapter 7 will discuss in detail the influence of each parameter on the flexural rigidity with regard to behavior of masonry block walls.

Evaluation of the effective flexural rigidity ( $EI_{eff}$ ) of masonry walls has been a challenging task for masonry researchers and different equations (Yokel 1971,

Hatzinikolas et al. 1978, Aboud et al. 1995, Liu and Dawe 2003) have been introduced for the appropriate estimation of  $EI_{eff}$ . However, to date no mention has been made of the effect of support stiffness in evaluating  $EI_{eff}$ . The following section will discuss the analytical relationship between flexural rigidity and support stiffness of masonry block walls.

### 4.3 Evaluation of Flexural rigidity of Masonry Block Walls

It is understood that the behavior is non-linear and history dependent. Moreover, it is understood that the level of material nonlinearity and, therefore, the cross-sectional properties vary along the wall height. This chapter obtains an equivalent elastic solution based on uniform properties along the wall height. The solution is applied at any point along the history yielding a fictitious, instantaneous, but generally representative EI value.

The solution of the fourth order differential equation of a beam-column was employed to establish the analytical relationship between support stiffness and flexural rigidity of masonry load bearing block walls, subjected to eccentric axial load at the top and with support stiffness at the bottom (Figure 4.1). Figure 4.2 presents the case in which no rotational support stiffness is applied at the bottom of the wall. The mathematical derivation is presented below:

The 4<sup>th</sup> order differential equation of an elastic beam-column with uniform properties is written as :

$$EIy'''' + P y'' = 0 \quad [4.1]$$

The general solution of Equation 4.1 assuming the axial load, P, is compressive is:

$$y = C_1 \sin(kx) + C_2 \cos(kx) + C_3 x + C_4 \quad [4.2]$$

in which, “x” is the distance from top of the wall to the point of interest located anywhere along the height of the wall and “k” is defined as:

$$k = \sqrt{\frac{P}{EI}} \quad [4.3]$$

Differentiating equation 4.2 yields expressions for the curvature

$$y'' = -c_1 k^2 \sin(kx) - c_2 k^2 \cos(kx) \quad [4.4]$$

Figure 4.1 shows that the following boundary conditions can be applied to Equation 4.2

$$y = 0 \quad \text{at } x = 0 \quad [4.5a]$$

$$y = 0 \quad \text{at } x = L \quad [4.5b]$$

$$y'' = \frac{Pe}{EI} \quad \text{at } x = 0 \quad [4.5c]$$

$$y'' = \frac{R\theta}{EI} \quad \text{At } x = L \quad [4.5d]$$

in which e is the eccentricity at the top, R is the support stiffness at bottom of wall and L is the wall height.

Equation 4.5a through 4.5d is a set of four equations in four unknowns,  $c_1$ ,  $c_2$ ,  $c_3$  and  $c_4$ . Solving this set yields an expression for deflection as:

$$y = \frac{1}{EIk^2} \left[ R\theta \left\{ -\frac{\sin(kx)}{\sin(kL)} + \frac{x}{L} \right\} + Pe \left\{ 1 + \frac{\sin(kx)\cos(kL)}{\sin(kL)} - \cos(kx) - \frac{x}{L} \right\} \right] \quad [4.6]$$

Eliminating support stiffness [R] term from Equation 4.6 yields the simplified expression:

$$y = \frac{Pe}{EI k^2} \left[ \frac{\cos(kL)\sin(kx)}{\sin kL} - \cos(kx) - \frac{x}{L} + 1 \right] \quad [4.7]$$

which is valid for wall deflection with no support stiffness offered by the support. Equations 4.6 and 4.7 are transcendental equations. In this study it is assumed that at any specified point along the history, the axial load, P, the deflection, y, at a specified point along the height, say  $x = L/2$  and the rotation,  $\theta$ , at the bottom, are all known. The only unknown is EI. To obtain the roots of these transcendental equations the popular Microsoft Excel Solver was employed and an iterative procedure was applied by targeting the mathematical expression of the derived differential Equation. The required variable EI was varied by constraining the results of Equations 4.6 or 4.7 to the mid height out-of-plane deflection and bottom rotation of the wall values corresponding to a particular loading event. This iterative procedure was continued until the equation was satisfied for the constraint condition. The procedure was repeated for the entire loading history by iterating at every event of the load history.

These equations have more than one root at the same set of input variables. Thus, it is important to select the initial value of the unknown variable, which should be capable of representing the true behavior of the function. The critical part of this method, therefore, was selection of the initial value of EI for very first event of loading. To obtain the correct root of the equation  $EI_0$  was selected as a reasonable initial value that is within neighborhood of the correct root and also to assure the proper behavior of the functions 4.6 and 4.7.

#### **4.4 Evaluation of Flexural rigidity from Experimental Data**

Employing equation 4.6 for the wall specimens tested with support stiffness and equation 4.7 for wall specimens tested without support stiffness, the flexural rigidity was estimated using test results along the load history for each load increment.

The plot of flexural rigidity versus load history of Group-I walls and Group-II walls is shown in Figures 4.3 and 4.4, respectively. It is observed, for both groups, that the slope drops initially rapidly, probably because of crack initiation at mortar face shell beds. Subsequently the plot shows a gradual and continuous change in flexural rigidity throughout the pre-peak load history. Upon approaching the axial load capacity a rapid decrease in the value of flexural rigidity is observed. After reaching the ultimate load the rate of decrease in flexural rigidity slows down as the load drops. The rapid decrease in stiffness is obviously caused by excessive deflection and cross section degradation. The plot of Group-I walls shows that even though wall specimens W1 and W2 could not reach their full capacity, they followed the trend which is common in all other walls. From Figure 4.3 and Figure 4.4 it is evident that support stiffness influences the flexural rigidity of wall specimens, this can be verified if the effective flexural rigidity is compared for all the specimens.

Flexural rigidity corresponding to the peak load is thought of as the “effective flexural rigidity”. Table 4.1 illustrates the effective flexural rigidity of all wall specimens for a 1-m width of wall. It is evident from Table 4.1 that for both groups an increase in  $EI_{eff}$  is observed for support stiffness values ranging from 0 kN-m/rad to 1000 kN-m/rad, while for support stiffness 5000 kN-m./rad and 10000 kN-m/rad a decrease in effective flexural rigidity is observed. For example specimens W3 and W4 respectively had  $EI_{eff}$  values of  $3.74E+12$  N/mm<sup>2</sup> and  $4.56E+12$  N/mm<sup>2</sup>.

As discussed in Chapter 3, at failure a change in curvature was observed because of the effect of support stiffness and this effect became more significant in case of wall specimens tested with support stiffness values of 5000 kN-m/rad and 10,000 kN-m/rad, resulting in greater load capacity. Because of higher axial loads experienced by these walls, the cross-section is subjected to higher compressive stresses along with cracking. These inelastic effects add up to cross section

degradation and as a result the decrease in effective rigidity was observed for the walls tested with higher support stiffness.

Walls tested with 1000kN-m/rad support stiffness showed an increase in axial load capacity but the cross-sectional stresses were not as high as they were in case of walls with greater support stiffness. The increase in  $EI_{eff}$  in case of support stiffness ranging from 0kN-m/rad to 1000kN-m/rad occurred mainly because in this range under the influence of support stiffness the geometric non-linear effects were controlled and the double curvature was formed. The bottom rotation of the wall also reduced as compared to the wall without any resistive moment at the bottom, this controlled the geometric non-linear effects and the wall was able to show comparatively higher  $EI_{eff}$ .

#### **4.4.1 Comparison of Flexural rigidity of Group-I and Group-II**

Figure 4.5 demonstrates the effective flexural rigidity of Group-I and Group-II plotted against the support stiffness. The plot shows that at all levels of support stiffness Group-II walls showed higher effective flexural rigidity as compared to Group-I. The probable reason is that the smaller slenderness ratio and higher peak load of Group-I walls resulted in higher material non-linearity and higher compressive stresses as compared to walls of Group-II, which exhibited stability failure and were exposed to primarily, geometric non-linearity and minor material non-linearity.

It is noticed in Figure 4.5 that the rate of decrease in  $EI_{eff}$  values between walls tested with support stiffness 5000kN-m/rad and 10,000kN-m/rad is higher in Group-I specimens than Group-II. This was because in Group-I walls the increase in support stiffness from 5000 kN-m/rad to 10,000 kN-m/rad caused the wall cross-section to undergo higher compressive stresses as compared to Group-II walls and as a result the reduction in EI because of material non-linearity was comparatively higher in Group-I walls and lower  $EI_{eff}$  was obtained.

In Group-I specimens the increase in support stiffness from 0kN-m/rad (specimen W3) to 1000kN-m/rad (specimen W4) provides 20% increase in effective flexural rigidity, while the same increase in support stiffness causes 10% increase in effective flexural rigidity between W8 and W7 of Group-II specimens.

#### **4.5 Comparison of Experimentally Obtained Effective Flexural Rigidity to CSA S304.1 Values**

The flexural rigidity of a masonry block wall changes throughout the load history and drops sharply after the load carrying capacity of the walls is reached. The slenderness, stress increase, tensile cracking and loading type are some of the factors, which cause the change in EI of the masonry block walls. In the current design practice, using an EI incorporates a constant E value and a reduced I value. The  $EI_{eff}$  depends on end eccentricity ratios, cracking of cross-section and long-term creep effects.

To assess the values of EI obtained from the experimental data a numerical comparison between CSA S304.1 recommendation and the experimental results was carried out. Details are shown in Table 4.2 for a one-meter width of wall. Clearly the code suggests conservative values of effective flexural rigidity of masonry block walls and it ignores support stiffness. Values obtained from the test results show that effective flexural rigidity is influenced by support stiffness of masonry block walls. Table 4.3 shows that even in case of specimens W3 and W8, where there is no support stiffness, a fairly high value of flexural rigidity was observed in the test as compared to the  $EI_{eff}$  obtained from CSA S304.1. Clause 11.2.5.4 further restricts the value of  $EI_{eff}$  by limiting the maximum allowed value to  $0.25E_m I_0$  (i.e.  $1.25E12 \text{ N-mm}^2$ ) for all test specimens. In Table 4.2 it is observed that even the maximum  $EI_{eff}$  allowed by the code is smaller than the experimental values of all specimens this confirms that the current code conservatively provides the values of  $EI_{eff}$  for the walls..

#### **4.5 Comparison of Experimentally Obtained Effective Flexural Rigidity to CSA S304.1 values**

The flexural rigidity of a masonry block wall changes throughout the load history and drops sharply after the load carrying capacity of the walls is reached. The slenderness, stress increase, tensile cracking and loading type are some of the factors, which cause the change in EI of the masonry block walls. In the current design practice, using an EI incorporates a constant E value and a reduced I value. The  $EI_{eff}$  depends on end eccentricity ratios, cracking of cross-section and long-term creep effects.

To assess the values of EI obtained from the experimental data a numerical comparison between CSA S304.1 recommendation and the experimental results was carried out. Details are shown in Table 4.2 for a one-meter width of wall. Clearly the code suggests conservative values of effective flexural rigidity of masonry block walls and it ignores support stiffness. Values obtained from the test results show that effective flexural rigidity is influenced by support stiffness of masonry block walls. Table 4.3 shows that even in case of specimens W3 and W8, where there is no support stiffness, a fairly high value of flexural stiffness was observed in the test as compared to the  $EI_{eff}$  obtained from CSA S304.1. Clause 11.2.5.4 further restricts the value of  $EI_{eff}$  by limiting the maximum allowed value to  $0.25E_m I_0$  (i.e.  $1.25E12 \text{ N-mm}^2$ ) for all test specimens. In Table 4.2 it is observed that even the maximum  $EI_{eff}$  allowed by the code is smaller than the experimental values of all specimens this confirms that the current code conservatively provides the values of  $EI_{eff}$  for the walls.

The above observations suggest there is a need to develop more realistic methods for the evaluation of effective flexural stiffness of the masonry block walls. Since in the experimental program many other parameters such as variation of  $e/t$  or amount of reinforcement could not be studied because of limited resources, the

The above observations suggest there is a need to develop more realistic methods for the evaluation of effective flexural rigidity of the masonry block walls. Since in the experimental program many other parameters such as variation of  $e/t$  or amount of reinforcement could not be studied because of limited resources, the extension of the work must be carried through a comprehensive numerical model so that the full range of different parameters can be studied in detail.

The current study aims to develop a numerical model which can be used as a tool to perform extensive parametric study and comprehensive data can be generated. The numerical model for the current study will be discussed in detail in the following chapter.

**Table 4.1 Effective Flexural rigidity obtained from experimental data**

Wall designation	Support stiffness (kNm/rad)	**Effective flexural stiffness (k-Nm/rad)
*W1	5000	3.51E+12
*W2	10000	2.98E+12
W3	0	3.11E+12
W4	1000	3.71E+12
W5	10000	3.56E+12
W6	5000	3.71E+12
W7	1000	4.25E+12
W8	0	4.15E+12

\*Specimens with local failure

\*\*Effective Flexural rigidity calculated for 1m width of wall specimens

**Table 4.2 Numerical comparison of experimental  $EI_{eff}$  with CSA S304.1**

Wall designation	Support stiffness kNm/rad	**Effective Flexural rigidity N-mm <sup>2</sup>	Effective Flexural rigidity from CSA S304.1 N-mm <sup>2</sup>	0.25EI <sub>0</sub> From CSA S304.1 N-mm <sup>2</sup>
W3	0	3.11E+12	0.828E12	1.25E12
W4	1000	3.71E+12	0.828E12	1.25E12
W5	10000	3.56E+12	0.828E12	1.25E12
W6	5000	3.71E+12	0.828E12	1.25E12
W7	1000	4.25E+12	0.828E12	1.25E12
W8	0	4.15E+12	0.828E12	1.25E12

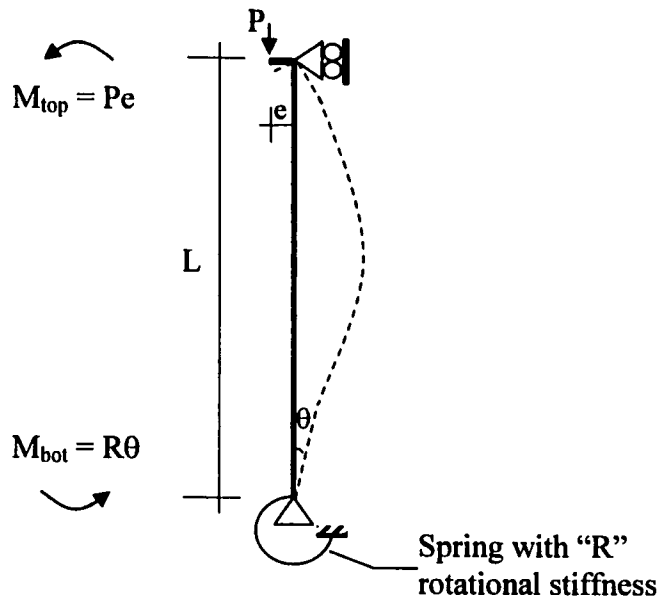


**Figure 4.1 Boundary conditions of masonry wall with support stiffness**

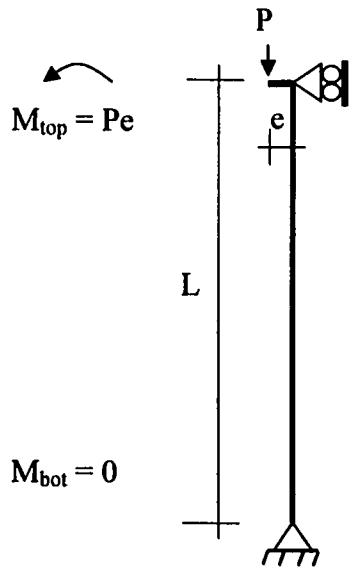


**Figure 4.2 Boundary conditions of masonry wall without support stiffness**

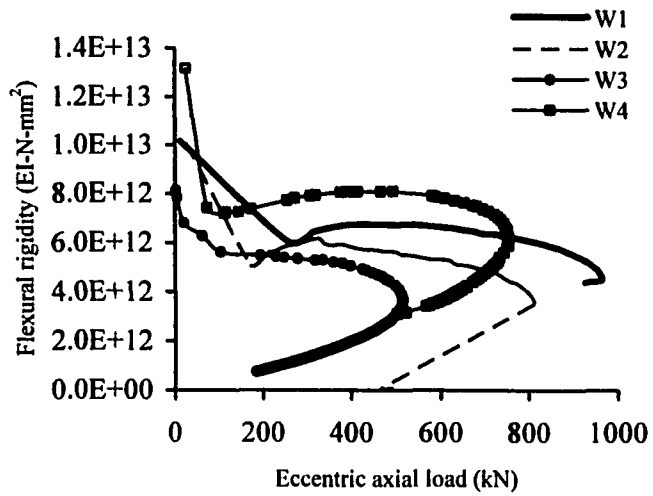


**Figure 4.3 Flexural rigidity versus eccentric axial load (Group-I)**

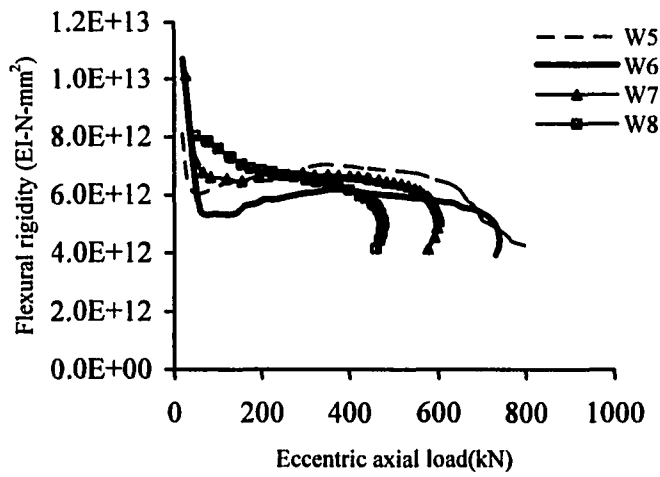


**Figure 4.4 Flexural rigidity versus eccentric axial load (Group-II)**

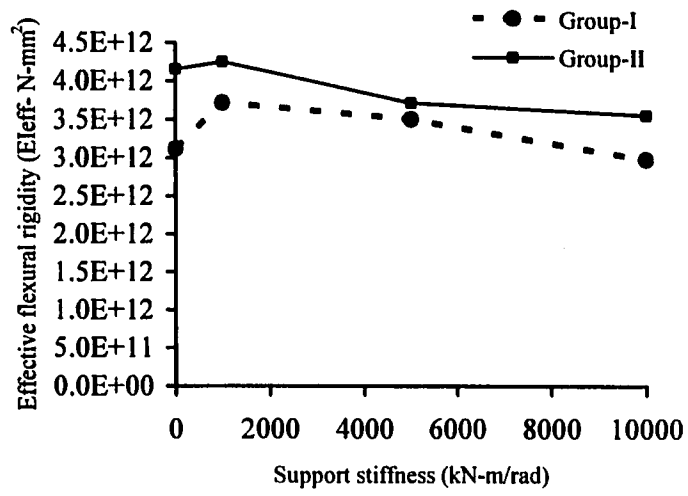


**Figure 4.5 Effective flexural rigidity versus support stiffness**

## **CHAPTER 5**

### **NUMERICAL ANALYSIS**

#### **5.1 Introduction**

This chapter describes finite element modeling of masonry block walls subjected to eccentric axial compressive forces. A number of these walls have already been tested in the experimental phase of the thesis. A simple and efficient non-linear finite element model was developed, incorporating material and geometric non-linear aspects of the test specimens. The non-linear finite element program ABAQUS (Hibbitt et al. 2002) was used to implement the proposed numerical model. The analysis is based on macroscopic analysis approach, which is best suited to capture overall behavior of masonry walls in this context. The details are presented later in the chapter.

The adequacy of numerical model was demonstrated against the test results by comparing the responses of axial load versus out-of-plane deflections, axial load versus out-of-plane rotations, bending moments and also axial load versus flexural rigidity response. Good agreement is found between experimental and numerical results.

#### **5.2 Numerical Model**

The description of the numerical model includes selection of element types, approach to the finite element mesh, material model and solution controls. These are discussed in detail in the coming paragraphs.

### **5.2.1 Element Type**

Eccentrically loaded masonry walls behave in the manner of beam-columns and are usually designed as members subjected to out-of-plan bending moment along the height of the wall. The design criterion is based in large part on the stability of these walls. Therefore, the behavior of such walls is treated as a structural stability problem in which reduction in the flexural rigidity occurs because of the axial loading and is further enhanced by cracking that arises from flexural effects.

To capture the strength and the stability failure mode of masonry load bearing walls with a finite element model a simple type of 2-D beam element is selected to best provide sufficient degrees of freedom to describe bending and axial load effects.

The primary purpose of developing the finite element model in this research is to investigate behavior at failure based on overall stiffness and strength of the walls. The effect of local distributions of stresses in the various shells and webs of the walls is irrelevant. Among several types of beam elements available in ABAQUS Element Library, type- B21 was selected. This is a line segment two-dimensional element having two translational and one rotational degree of freedoms at each node Element B21 sufficiently deals with in-plane large deformations caused by out-of-plane rotations. These elements also incorporate transverse shear deformation and can be used for thick as well as slender beams. Material non-linear effects are incorporated by integrating the stress distribution over a sufficient number of integration points on the centerline of the cross-section.

### **5.2.2 Approach of Finite Element Mesh**

The intention was to develop a mesh, which can reasonably predict the behavior of masonry walls until failure without causing unnecessary computational difficulties. A masonry wall is an assemblage of units arranged in horizontal

courses interspaced with mortar layers. In addition, some cores are grouted and vertical reinforcement is added.

There are three basic approaches of modeling to represent the mutual interaction of individual components of masonry in finite element mesh. In the first approach, the mortar layer is represented by continuum elements. Thus, the finite element mesh requires different material properties of block and mortar. In the second approach, the mortar layer is modeled as potential lines of failure because of cracking. It is introduced as a contact element with cohesion and friction and its elastic properties and associated local effects at the block-mortar interface are neglected. The third approach treats the masonry assemblage as a homogenous solid medium and the cracks are smeared out. From the behavior point of view, the first approach provides a highly detailed model, while the third approach gives a global view that is best suited for modeling the over-all response. The second approach is a middle-scale approach but still subject to more computational complexity as compared to the third one. The first approach is also known as a microscopic model. Previously this approach has been attempted at the University of Alberta to model masonry cavity walls (Wang et al. 1997) and reported unsatisfactory results because of difficulty of simulation of crack propagation between elements of mortar and unit after de-bonding. The second approach (also known as block-interface approach) is complicated by introducing the contact element and leads to a complex finite element model consisting of large numbers of elements.

By keeping in view, all above discussion and to concentrate on the objective of obtaining global behavior of masonry block walls the third approach was finally selected to model the masonry walls by using a simple finite element mesh in ABAQUS (Version 6.3-2002).

To define tensile failure of the mortar layers, the bond strength was used as the limiting tensile strength in the material model and cracks were allowed to

propagate in the cross-section of the element as the strain grows. The details of the material model will be discussed later in this chapter.

Every course of the masonry wall is defined by an individual element to accomplish the mesh configuration, as shown in Figure 5.1. To introduce load eccentricity at the top of the wall, a relatively stiffer element was attached out-of-plane of the wall having a length equal to the eccentricity in the test. Since in the experiment, the test specimen was laterally supported at the top and was also supported horizontally and vertically at the bottom a roller support at the top and hinge support at the bottom were applied to the model. Simulated support stiffness was incorporated by rigidly attaching one end of the steel beam to the bottom element of masonry assemblage and the other end was simply supported in a manner similar to that used in the test.

### **5.2.3 Material Properties**

#### ***Masonry assemblage***

Material properties of the masonry assemblage were assigned in both the elastic and inelastic ranges. Using average prism test results, the elastic modulus was defined by treating the masonry assemblage as an isotropic elastic material within the elastic range. The inelastic material behavior of masonry assemblage was modeled using the damage plasticity model of concrete as provided in ABAQUS - 6.3. This model primarily combines the concepts of isotropic damaged elasticity with tensile and compressive plasticity theory of concrete. The damage plasticity model is designed to handle reinforced concrete structures loaded under low confining pressure. This material model also has the capability to describe irreversible constitutive changes during fracturing or cracking processes.

Mechanical behavior of concrete in the damage plasticity model is defined by non-associated multi-hardening plasticity and isotropic damage elasticity rules.

The stress-strain relationship in the uni-axial tensile regime is considered linear until the stress level reaches the failure tensile stress ( $\sigma_{t0}$ ). Cracking in the concrete material occurs beyond the failure state. Macroscopic crack formation is introduced by softening of the stress-strain response. The uni-axial compressive behavior is considered linear up to the level of initial yield stress ( $\sigma_{co}$ ) followed by strain hardening, then strain softening beyond the peak stress ( $\sigma_{cu}$ ).

Figure 5.2 (a) and Figure 5.2 (b) (ABAQUS V. 6.3, Volume –II, Explicit User’s Manual -10.4.2-3) show the uni-axial response of concrete in tension and compression respectively. Tensile cracking and compressive crushing are assumed to be the two main failure mechanisms. The failure surfaces in tension and compression are controlled by equivalent tensile plastic strains ( $\epsilon_t^{pl}$ ) and equivalent compressive plastic strains ( $\epsilon_c^{pl}$ ) respectively.

This model allows introducing concrete softening in the post failure stress-strain relationship by using a fracture energy cracking criteria. Concrete behavior in the damage plasticity model is considered independent of rebar effects and, therefore, does not consider the effects associated with rebar-concrete interaction, such as dowel action and bond slip. However, reinforcement effects can be indirectly incorporated by modifying the response of plain concrete, through a concrete tension stiffening capability. To avoid any possible effect of mesh dependency and to eliminate unstable behavior in the current numerical model, concrete tension stiffening effect was introduced in terms of cracking displacement. This option implements the concept of characteristic length (crack spacing), and uses the integration point spacing or element geometry for the estimation of characteristic crack length. In the ABAQUS damage plasticity model for beam-element, the characteristic length is taken as the length of the element. Hence, to avoid mesh dependency an element was taken equal to a course height. In this manner, the cracks, which occur primarily in the mortar layer would have accurate spacing equal to the element length. A typical stress-displacement curve is shown in Figure 5.3(a). The peak tensile stress ( $\sigma_{t0}$ ) was taken equal to the bond

stress for mortar-masonry unit interface ( $\sigma_{i0} = 0.5 \text{ MPa to } 1\text{MPa}$ ), which is considerably less than the unit tensile strength.

To define the compressive behavior in the inelastic range of masonry assemblage behavior, strain hardening is assumed in the model. The strain softening regime in compression is defined by tabulating the stress beyond initial yield against the corresponding inelastic strain. The model automatically converts inelastic strains ( $\epsilon_t^{\sim in}$ ) into plastic strains ( $\epsilon_t^{\sim pl}$ ) as:

$$\epsilon_c^{\sim pl} = \epsilon_c^{\sim in} - d_c / (1 - d_c) \{ \sigma_c / E_c \} \quad [5.1]$$

Here  $d_c$  is the damage parameter which is zero because in the current study the masonry walls were not subjected to cyclic loading and no stiffness recovery reduction was required. Therefore:

$$\epsilon_c^{\sim pl} = \epsilon_c^{\sim in} \quad [5.2]$$

A typical stress-strain curve in the compression zone is shown in Figure 5.3 (b). The model assumes a non-associated plastic flow. The plastic flow is defined by a flow potential given by Drucker-Prager hyperbolic function. The dilation angle defines the asymptote to the hyperbolic function. In the current numerical model the dilation angle was assumed to be  $15^0$  as recommended by Lubliner et. al. (1989) for low confined concrete material modeling. The yield surface in the damage plasticity model is controlled by plastic strain in compression and in tension,  $\epsilon_c^{\sim pl}$  and  $\epsilon_t^{\sim pl}$ . These strains serve as hardening variables to trace the yield surface evolution. During analysis  $\epsilon_c^{\sim pl} > 0$  indicates the start of compressive yielding and when  $\epsilon_t^{\sim pl}$  becomes greater than zero and the principal plastic strain is positive, cracking is initiated. The material parameters used in the analysis are listed in Table 5.1 for each specimen.

### ***Rebar definition and material properties***

The rebars were defined as superimposed elements sharing the same nodes as the masonry assemblage. Thus strain compatibility is assumed at the nodes only. Material properties of the rebar elements were assigned with the same values as obtained by standard rebar test results. Plastic properties were introduced by using a  $J_2$  plasticity model in the context of a von Mises yield surface and an isotropic hardening rule.

### ***Simulated support stiffness***

In the current finite element model, simulated support stiffness was defined as simply supported steel beam rigidly connected to the masonry assemblage. A typical structural steel elastic material is used.

### **5.2.4 Solution Control**

Initially, ABAQUS-Standard was attempted to analyze the finite element model and both Newton-Raphson iteration and Modified Riks strategy were tried. Because of some numerical difficulties, an unstable response was obtained and the program was unable to trace the right solution path. The ABAQUS-Explicit module was then used to analyze the finite element model.

The solution concept is based on stress propagation. Acceleration is induced at the point of load application resulting in changes in velocity and displacements as the solution progresses. The total strain is calculated by adding the strain increments. Element stress changes are calculated by applying the material constitutive model. Dynamic equilibrium is evaluated at every node. The next increment is applied after satisfying the dynamic equilibrium. This process continues until the specified total time is accomplished. This process dealt satisfactorily with the post

behavior at failure of all wall specimens assuming the small increments of loading.

Although ABAQUS-Explicit is a true dynamic solution module, it is able to successfully deal with quasi-static problems by minimizing the inertial effects and keeping the level of kinetic energy very low compared to internal and external work done. This is done through the adoption of a number of measures.

The first measure applies the velocity changes smoothly to avoid large transient effects at the beginning and end of a step. ABAQUS automatically allows smooth loading amplitudes by applying displacement-time histories with zero, first and second derivatives at the beginning and end of each step as shown in Figure 5.4. Thus, the solution process is implemented in the manner of displacement control applied by giving the initial and final data points required.

This was all carried out in the context of a central difference scheme. The stable time step length is smaller than the time required for a sound wave to travel through the smallest element. If true material densities are used the analysis can take hundreds of thousands of time steps. Since we are not interested in a true dynamic response the mass was magnified three orders of magnitude. This has the effect of reducing the velocity and increasing the stable time step value. The first reduces the kinetic energy to a negligible level, while the second reduces the number of time steps.

To confirm the validity of quasi-static response, the energy history was plotted for the numerical analysis of all wall specimens. Figure 5.5 illustrates a typical energy history curve obtained. It is clearly indicated by the energy plots that the kinetic energy is negligible as compared to the external work done and internal energy of the system. The external work done and internal energy established the energy balance throughout the analysis.

### 5.3 Simulation of Test Results

Using the finite element model discussed in the previous section, the tests of Group-I and Group-II specimens were simulated. To assign the cross-sectional properties of the partially grouted masonry assemblage, the masonry wall cross-section was treated as I-section having flange width equal to width of the wall specimen (1200 mm). The flange thickness was defined as the average thickness of the face shell (32mm), while the web height of the I-section was taken as the actual thickness of the wall and the thickness of web was considered as the width of grouted core plus thickness of interior web of the concrete blocks (390 mm). The cross-sectional detail for beam element used for masonry assemblage is shown in Figure 5.6. The in-plane I-section in ABAQUS is sufficient to capture the desired behavior. The cross-section contains five integration points along the depth of the cross-section and is capable to provide the cross-sectional stresses on extreme tension and compression faces (integration point 1 and 5 in Figure 5.6) as well as at intermediate locations.

As mentioned in chapter 3 all tested specimens were identical except that Group-I consisted of walls W1, W2, W3 and W4, with a slenderness ratio of 28.6, with implied rotational stiffness of 5000, 10000, 1000 and 0 kN-m/rad respectively. While Group-II consisting of walls W5, W6, W7 and W8 was built with a slenderness ratio of 33.9 and had bottom rotational stiffness 10000, 5000, 1000 and 0 kN-m/rad respectively.

Table 5.2 summarizes the analysis results. A comparison between test results and numerical output is presented in the next section within four contexts: load-deflection response, moment rotation, failure mode and flexural rigidity.

### **5.3.1 Load Deflection Characteristics**

Load-deflection responses for Group-I are plotted with the deflection measured at mid height, i.e. 2719mm from bottom of the walls, in Figure 5.7 through 5.10. The responses for Group-II are also plotted at mid-height in Figure 5.11 through 5.14.

Specimen W1 was tested with a support rotational stiffness of 5000 kN-m/rad. In the experiment a local (premature) failure occurred. Therefore, it was intended to capture the initial slope of the load-deflection curve. Beyond the load level of premature failure, the probable response can be traced by the analysis results only. A comparison of the experimental load deflection response with the numerical model results is shown in Figure 5.7. Since the numerical model was not subjected to local failure it shows more stiffness after a load level of 600 kN and fails at higher peak load of 984.4 kN as compared to 964 kN which was carried by locally failed W1 specimen. In Figure 5.7 numerical model shows more stiffness as compared to the experimental curve because the experiment response tends to local failure and fails before attaining its peak load as opposed to numerical response which attains its full capacity without facing any local failure.

Specimen W2 was tested with support rotational stiffness of 10000 kN-m/rad. The load deflection response of W2 is shown in Figure 5.8. W2 also locally failed in the test but not in the numerical analysis. Figure 5.8 shows that since the numerical model does not include local failure effects, it demonstrates more stiffness as compared to the experimental curve, attains its full load carrying capacity (990.14 kN) and continues to carry the load for an additional 8mm of mid-span deflection.

W3 is the reference wall of Group-I and was tested without any simulated support stiffness. The load-deflection from the ABAQUS analysis data showed satisfactory response parallel with the experimental results. The peak load

obtained from the experiment is only 0.281% less than the load obtained from analysis. The corresponding deflection acquired from the analysis is also adequate and only 0.281 % more than the experimental value. The response plotted in Figure 5.9 shows that the initial slope of the numerical results matches the slope obtained from the experiment and demonstrates a reasonable response in the peak and post-peak range. The modulus of elasticity used in the analysis was  $E = 10500$  MPa, which lies within a standard deviation (1510 MPa) of the value of the mean modulus of elasticity obtained from the standard prism test results.

W4 was analyzed with support rotational stiffness of 1000kN-m/rad. The load-deflection plot is shown in Figure 5.10. The difference in peak load between the experimental and numerical results is 0.28% and the corresponding deflection differs by 0.30%, which also validates the numerical model. A reasonable agreement in the post-peak response exists as shown in Figure 5.10. The numerical model traces the same response up to a 22% drop from the peak load (400kN). The modulus of elasticity used in the numerical model, was  $E = 12400$  MPa, which again remains within a standard deviation of the experimental modulus of elasticity. The ultimate ductility achieved W4 in the real test could not be captured. However, the objective of the study is focused on behavior at failure of the masonry block walls and, therefore, it is not important to match the numerical results up to the ultimate ductility level.

Figure 5.11 presents the plots of Load-deflection curves of W5, which belongs to Group II. It is observed from the plot that the numerical analysis is in good agreement with experimental data. Both curves show exactly the same slope in initial response, as well as when approaching the peak load. After that the load carrying capacity from experimental data becomes slightly higher than the numerical load deflection curve and finally there is a minor difference of 0.13% in the peak load carrying capacities. The numerical value of deflection at peak load is 4.6 % higher than the experimental value.

The load deflection response of W6 is shown in Figure 5.12. Experimental and numerical plots are concurrent and exhibit similar stiffness up to peak load level, with a minor reduction of 0.55% in peak load relative to that obtained from the experiment. The displacement corresponding to the numerical peak load is 11% more than the value obtained from experimental results and shows that the numerical model provides a conservative comparison.

The load deflection response of W7 is quite satisfactory as shown in Figure 5.12. Both experimental and numerical responses exhibit the same elastic response and differ slightly in the nonlinear range. The peak load from the numerical analysis is only 0.16% higher than the experimental peak load. The corresponding displacement at numerical peak load is also in good agreement with experimental value and only a 5.6% difference is observed

The load deflection response of W8 in Figure 5.14 shows good agreement between numerical and experimental response. Numerical analysis gives 1.5% lesser load carrying capacity as compared to the experimental value. It is observed from the plot that the numerical curve lags behind the experimental response and achieves failure at lesser displacement level as compared to the experimental response, (10.7% less displacement) Although the post-peak behavior given by numerical model seems reasonable, the model was unable to follow the complete response up to the maximum displacement; possibly because the tension stiffening curve in the numerical model might not be able to trace the actual response of the test specimen in the post-peak behavior regime. However, the overall response provided by the numerical model was found to be satisfactory in terms of elastic response as well as achieving the peak load capacity.

### **5.3.2 Load-rotation Characteristics**

It is worth while noting that the bending moment at the bottom of the wall is independent from that at the top of the wall. Therefore, the only meaningful comparison regarding the bottom rotation would be between the load and rotation.

Axial load versus bottom rotation response of W1 is plotted in Figure 5.15. It is observed from the plots that the response of the numerical model and the experimental response remain similar up to a load level of approximately 450 kN. Beyond that test specimen W1 was approaching local failure. As a result it shows more rotation and less stiffness compared to the numerical model. At local failure of test specimen W1 the bottom rotation is 0.0077 radians as compared to a numerical value of 0.00524 radians at the same level of load. This is not entirely explained by local degradation at the top. It could be that some other degradation was taking place at the bottom but did not activate the same obvious level of failure observed at the top.

Load versus bottom rotation response of W2 is plotted in Figure 5.16. It is observed from the plots that the experimental response shows more rotation as compared to the numerical model prior to local failure. The plot shows good agreement of analysis and experimental results up to a load level of 400 kN. However, the slope of the numerical curve differs from the experimental curve after 300 kN. The bond slip at the top of specimen W2 could be the cause of observed discrepancy between numerical and experimental results. It is important to mention that the proposed numerical model does not account for bond slip behavior, hence showed more rotational capacity as compared to the experimental response.

Figure 5.17 shows the load-rotation response of W3. Numerical results show an acceptable fit with the experimental curve. Rotation at bottom of the wall corresponding to the peak load obtained from numerical results is 2.5% higher

than the corresponding experimental value. It is observed from the plot that initial, peak and post-peak response is quite satisfactory and provides good agreement between experimental and numerical results.

The load versus bottom rotation plot for W4 is shown in Figure 5.18. Experimental and numerical responses follow similar slopes up to peak load level; beyond that there is a difference in the slope and the numerical model does not trace a similar post-peak response as the experimental curve. The peak bottom rotation from the numerical analysis is 5 % less than the experimental rotation.

Rotation at the bottom of the wall versus axial load for W5 is shown in Figure 5.19. It is observed from the curve that after reaching a load level of 450kN, the response of the experimental curve softens somewhat which is not reflected in the numerical analysis, and at peak load 35% lesser rotation is obtained in the numerical analysis. It is believed that the rotation meter during the experiment was not working properly, which explains the discrepancy. This argument is further supported by the comparison of load-deflection response, which shows good agreement between numerical and experimental results, as plotted in Figure 5.11.

Figure 5.20 shows the plot of load versus bottom rotation of the wall for W6. The plot shows that the numerical response seems conservative and provides more rotation as compared to the experimental results. The numerical model is in good agreement with test results up to a load level of 300kN. Then the model starts to show lesser stiffness and more rotation which leads to 19% more rotation as compared to the test results at the level of peak load. The probable reason is malfunction of the rotation meter.

Figure 5.21 presents the plot of load versus bottom rotation of wall W7. The curve obtained from the numerical results accurately follows the experimental curve but as it approaches the peak load level, the model shows conservative results and the

bottom rotation corresponding to peak load obtained from numerical model is 15% less than the rotation obtained from experiment.

Load-rotation response of W8 is shown in Figure 5.22. A good agreement between experimental and numerical results can be observed from the plot. The difference in experimental and numerical values of rotation at peak is 7.6%, which is fairly acceptable.

### **5.3.3 Load Moment Characteristics**

To compare the numerical model capability of capturing non-linear effects because of deflection of the wall during the loading history, the history of load versus bending moment at mid height has been plotted.

Figure 5.23 and Figure 5.24 give the load versus mid-span bending moment responses for wall specimen W1 and W2 respectively. The response of specimen W1 shows good agreement between test and numerical results. However, at the point of peak load of test specimen W1 the test results show 11% more mid-span bending as compared to numerical results. In case of wall specimen W2 a good agreement between test and numerical results is observed but because of premature failure during the testing of wall specimen W2 the test results could follow the numerical response up to the level of peak load of test specimen W2.

The numerical and experimental histories of W3, which are plotted in Figure 5.25 agree well up to a load level of 500kN after which there is a difference which grows to 7.3% at failure. The numerical model could not capture the exact behavior of post-peak regime but does not vary by more than 7.8% from the experimental results.

Figure 5.26 shows the load-moment histories of specimen W4. The curve from the numerical analysis follows the experimental curve with the same slope until it

crosses a load level of 750kN, after this the experimental curve shows slightly more axial load (0.3%) than the load obtained from numerical analysis which is reflected in bending moment magnitude (the numerical model gives 3.9% less bending moment as compared to test specimen). The numerical analysis produced a post-peak behavior very close to the experimental response.

It is observed from Figure 5.27 that the experimental and numerical histories for W5 are in good agreement. The difference in mid-span bending moment at peak load is found to be 4.64% and is reasonable. A similar conclusion is drawn for W6 for which the histories are shown in Figure 5.28. Figure 5.29 shows a maximum of 2.5% difference at the same load level of W7 while Figure 5.30 shows a moment difference of 4.3% for W8.

#### **5.3.4 Deflected Shapes**

To further examine the suitability of the numerical model the deflected shapes and the bending moment diagrams obtained from analysis and the tests are compared at the peak load point.

The comparison of bending moments at failure of specimen W1 is shown in Figure 5.31. The bending moment diagram obtained from numerical analysis is in good agreement with test results. The deflected shapes obtained from numerical results and the test results are compared at the peak load level of wall specimen W1 as shown in Figure 5.32. The shapes of the deflection curves of both test results and numerical results follow the similar curvature. It is noticed that the numerical magnitude of mid-span deflection of and test results differs from experimentally obtained mid-span deflection and found to be almost 22% more than the deflection obtained from numerical model. The reason for a stiffer behavior observed in numerical results is that the numerical model does not contain any degradation in stiffness because of bond and anchorage failure and keeps on taking load and at the failure level of the test specimen which mainly

because of bond and anchorage failure the numerical model showed more stiffness and comparatively lesser deflection. The peak load capacity obtained from numerical model i.e. 988.5kN which is about 3% more than the peak load of test specimen W1 and indicates that at failure the test specimen was able to attain most of the axial load capacity and because of bond slip effect failed a little earlier than its actual failure.

For the wall specimen W2 the bending moment diagram and deflected shapes at the peak load level of test specimen W2 are shown in Figure 5.33 and Figure 5.34 respectively. Similar to test specimen W1 the specimen W2 was also not able to attain the full capacity during test. The bending moment diagram in Figure 5.33 shows that the numerical model gives the comparable bending moment with the test results along the wall height except at the bottom part of the wall where numerical results are conservative by 24% as compared to test results. The comparison of deflected shape of the test results and the numerical model shows that both curves follow almost the same curvature. The numerical model shows lesser deflection as compared to test results mainly because that the test specimen was failed because of bond slip at the top and could not carry further axial load, while numerical model was able to take more load without any degradation of the stiffness.

Bending Moment Diagram along the height of the wall is shown in Figure 5.35 for specimen W3. Numerical model demonstrates good agreement with experimental results and exhibiting identical behavior at failure of W4. The point of maximum bending moment appears at the same height for both the analysis at the test, and the magnitude of maximum bending moment is similar.

Deflected shape at failure of W3 is shown in Figure 5.36. The curves extracted from numerical analysis and experimental results follow the same curvature and exhibit the same behavior.

Bending moment diagram for specimen W4 is shown in Figure 5.37. The plot shows that the numerical model produces the same bending moment diagram as obtained from experimental results through out the wall height,. Magnitude of the maximum bending moment obtained from numerical analysis is slightly (3.9%) less than the experimentally obtained moments but the similar shape of the curve subsists for both experimental and numerical bending moment diagrams. Difference bending moment is about 4.2% at the bottom of the wall, while at top of the wall bending moment from experiment is almost same as obtained from numerical analysis.

The deflected shapes corresponding to failure as shown in Figure 5.38, obtained from experiment and numerical analysis are similar and point of maximum deflection moves upward relative to W3 reflecting the effect of simulated support stiffness. However, numerical model shows 0.3 % lesser deflection as compared to experimental results.

The plot of bending moment diagram at failure for specimen W5 is shown in Figure 5.39. The bending moment diagram is similar to the numerical bending moment diagram along the height of the wall except at bottom of wall where numerical model differs and at this location the model provides 13% lesser support moment than experimental results. Difference in the magnitudes of maximum bending moments is about 0.464%. Location of maximum bending moment is identical in both numerical and experimental curves i.e. at  $0.84h$  (Where  $h$ = vertical span of the wall specimen). Magnitude of the bending moments at the top of the wall is same in both experimental and numerical bending moment diagrams. Resisting moment offered by the simulated support stiffness is 13% lesser in case of the numerical model. The deflected shape of W5 at failure is shown in Figure 5.40. Because of effect of simulated support stiffness, clear change in curvature near the bottom part of the curve obtained from numerical analysis can be observed which is similar to experimental curve.

However, maximum deflection in case of numerical analysis is less than the experimental deflection.

Figure 5.41 presents the bending moment diagram for W6 at failure. The numerical analysis is found to be in good agreement with experimental results. Location of maximum bending moment is  $0.82h$  in numerical bending moment diagram, which is similar to experimental bending moment diagram. Magnitude of the top moment from numerical analysis is almost similar to experimental value. The difference between the experimental and numerical values in resistive moment offered by simulated support stiffness is 10%. Figure 5.42 shows the deflection at the failure of W6. There is 13% increase in the maximum value of deflection observed in the experiment and that obtained from analysis results.

The bending moment diagrams obtained from experimental and numerical data for specimen W7 at the failure are shown in Figure 5.43. Location of the maximum bending moment diagram is identical for both experiment and numerical analysis ( $0.86h$ ) but magnitude of the maximum bending moment obtained from numerical model is about 6.3% less than the experimental value of maximum bending moment. Experiment shows 30% more resistance offered by simulated support stiffness as compared to numerical analysis. The magnitude of the top moment is the same for both experiment and numerical analysis. Figure 5.44 demonstrates the deflected shape of W7 at failure. The difference between numerical and experimental values of maximum deflection is found to be 22%. Deflected shape from numerical analysis shows lesser deflection as compared to numerical analysis. However, the numerically obtained shape shows the effect of simulated support stiffness in terms of reduced deflection and the increased load carrying capacity as compared to reference wall of Group-II. The curvature reversal however is not very prominent. This effect will be highlighted in the discussion of flexural rigidity of W7 in the next section.

The numerically obtained bending moment diagram of W8 shows 3% lesser moment capacity compared to the experimental diagram. The bending moment at the top of the wall is the same for both experiment and numerical analysis, and the shape of the curve is also similar. Figure 5.45 shows both diagram for W8.

Figure 5.46 compares the deflected shapes of W8 at failure. The difference in maximum deflection is about 10% and this is located at the mid-height of the wall specimen.

### **5.3.5 Effective Flexural Rigidity ( $EI_{eff}$ )**

To further assess the numerical analysis the effective flexural rigidity of all specimens were plotted by solving representative differential equation as described in Chapter 4 using data obtained from numerical analysis. The curves are drawn for both Group-I and Group-II and compared with the history of flexural rigidity based on experimental results. The effective flexural rigidity of the wall is considered as the flexural rigidity corresponding to the peak load capacity of the wall. The comparison of experimental and numerical results is discussed as follows.

The histories of flexural rigidity based on experimental and numerical results was obtained by using the load, deflection and wall bottom rotation histories and the comparison between experimental and numerical results is shown in Figure 5.47 through Figure 5.54.

In Figure 5.47 and Figure 5.48 it is observed that the flexural rigidity obtained through experimental results of wall specimens W1 and W2 is lower as compared to the flexural rigidity obtained from numerical results. As mentioned in previous sections that these two wall specimens experienced bond slip and could not reach to their full load capacity during testing, while the numerical model does not account for bond slip effect and thus comparatively shows more flexural rigidity

throughout the load history. The effective flexural rigidity from experimental results is 24% less than the numerical model in case of both specimens W1 and W2.

Figure 5.49 compares the history of flexural rigidity of specimen W3 and shows good agreement between test results and numerical results. At peak load the difference between effective flexural rigidity found to be negligible, the numerical value is 1.05% less than the experimental value.

Figure 5.50 provides the history of flexural rigidity of wall specimen W4. The experiment and numerical curves follow the same response and are in good agreement. The effective rigidity from numerical results observed to be 4.5% less than the effective rigidity obtained from test results.

Figure 5.51 traces the load versus flexural rigidity of specimen W5. The numerical model is conservative as compared to experimental results and provides lesser flexural rigidity. The difference becomes 7.5% at peak load.

Figure 5.52 illustrates the comparison of flexural rigidity of specimen W6. As indicated by the plot, the flexural rigidity estimated from numerical model results is 5.6% less than the value obtained from experimental data. The numerical model gives a smooth rate of change of flexural rigidity as compared to curve obtained from test results and comparatively provides the lesser stiffness. Similar response is also observed in case of wall specimen W7 and 14.5% difference between test results and the numerical model is observed.

In case of specimen W8 the numerical model and test results are in good agreement and only 1% difference in the values of effective rigidity is observed, as shown by Figure 5.54.

The numerical and experimental results are in good agreement with each other and validate that the numerical model effectively predicts the behavior of masonry load bearing block walls and can be used to extend the findings of experimental results by analyzing more walls with variety of parameters under the influence of support stiffness.

**Table 5.1 Material parameters of masonry**

<b>Specimen</b>	<b>Modulus of elasticity (E)</b>	<b>Compressive strength (<math>f_m</math>)</b>	<b>Failure tensile stress (<math>\sigma_{to}</math>)</b>	<b>Cracking displacement (<math>u_c</math>)</b>	<b>Poisson's ratio (<math>\nu_c</math>)</b>
	<b>MPa</b>	<b>MPa</b>	<b>MPa</b>	<b>mm</b>	
<b>W1</b>	12500	15.20	1.20	1.80	0.15
<b>W2</b>	12700	15.20	1.20	1.80	0.15
<b>W3</b>	10450	13.20	0.50	0.05	0.15
<b>W4</b>	12400	15.20	0.50	0.05	0.15
<b>W5</b>	13500	15.20	0.50	0.05	0.15
<b>W6</b>	13500	14.10	1.10	1.0	0.15
<b>W7</b>	13300	13.56	0.50	0.05	0.15
<b>W8</b>	13300	13.50	0.50	0.05	0.15

**Table 5.2 Summary of analysis results**

<b>Specimen (1)</b>	<b>E (2)</b>	<b>Pu (3)</b>	<b>Mu (4)</b>	<b><math>\theta</math> (5)</b>	<b>SSSM (6)</b>	<b><math>\Delta</math> (7)</b>	<b>EI (8)</b>
	<b>MPa</b>	<b>kN</b>	<b>kN-m</b>	<b>rad</b>	<b>kN-m</b>	<b>mm</b>	<b>N-mm<sup>2</sup></b>
<b>**W1</b>	12500	963.97	52.14	0.00532	29.14	18.4	1.20E13
<b>**W2</b>	12700	811.98	37.80	0.002337	25.15	10.85	1.40E13
<b>*W3</b>	10450	513.6	29.76	0.001276	0.0	29.66	3.72E12
<b>*W4</b>	12400	753.1	46.33	0.010557	10.5	26.02	6.45E12
<b>*W5</b>	13800	797.25	39.33	0.003228	34.73	21.93	1.31E13
<b>*W6</b>	13500	736.35	38.91	0.00500	27.70	25.45	1.05E13
<b>*W7</b>	13300	600.75	31.3	0.00820	9.72	25.02	7.41E12
<b>*W8</b>	13300	469.4	24.19	0.00924	0.00	24.13	5.03E12

**\*\* All the values are summarized at local failure load level.**

**\* All the values are summarized at failure**

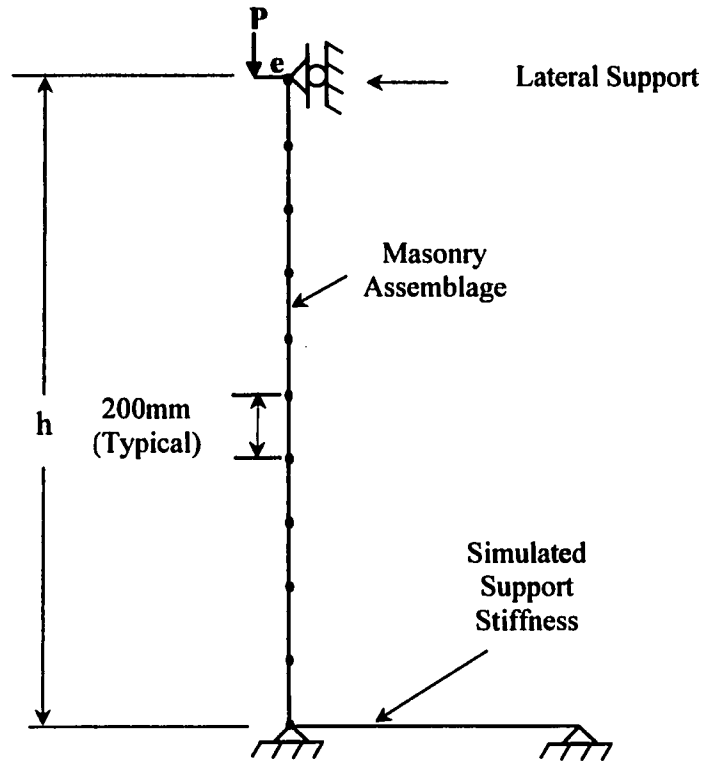


**Figure 5.1 Finite element mesh**

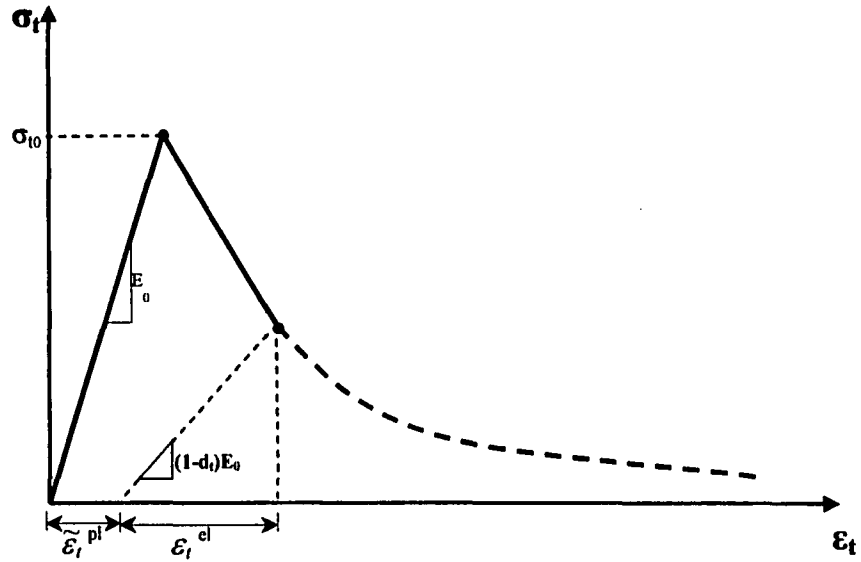


**Figure 5.2(a) Uni-axial response of concrete in tension**  
(after Hibbitt et al. 2002)

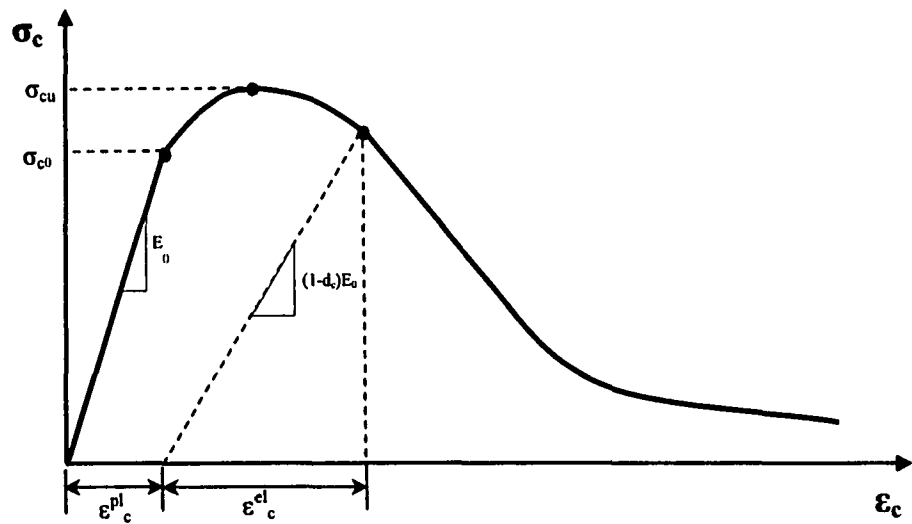


**Figure 5.2(b) Uni-axial response of concrete in compression**  
(after Hibbitt et al. 2002)

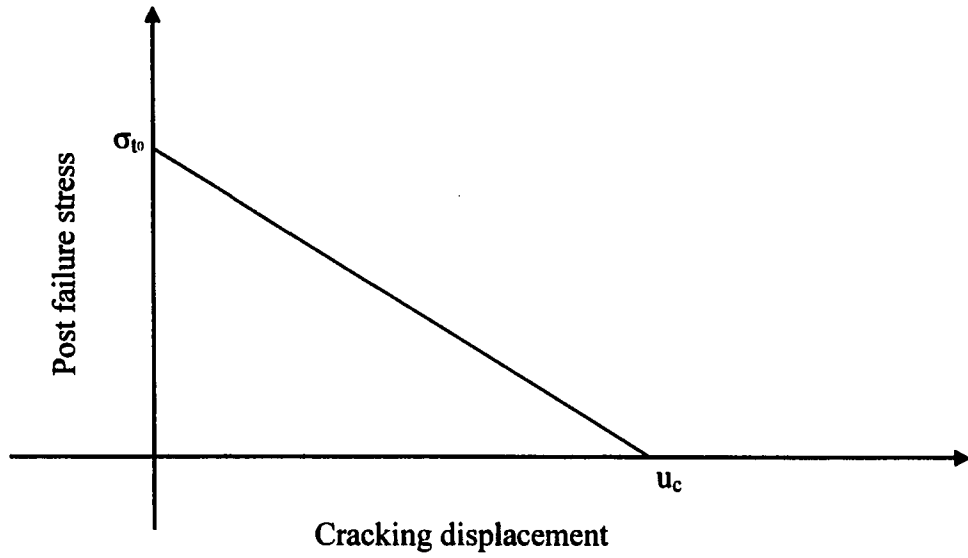


**Figure 5.3(a) Typical stress-displacement curve**

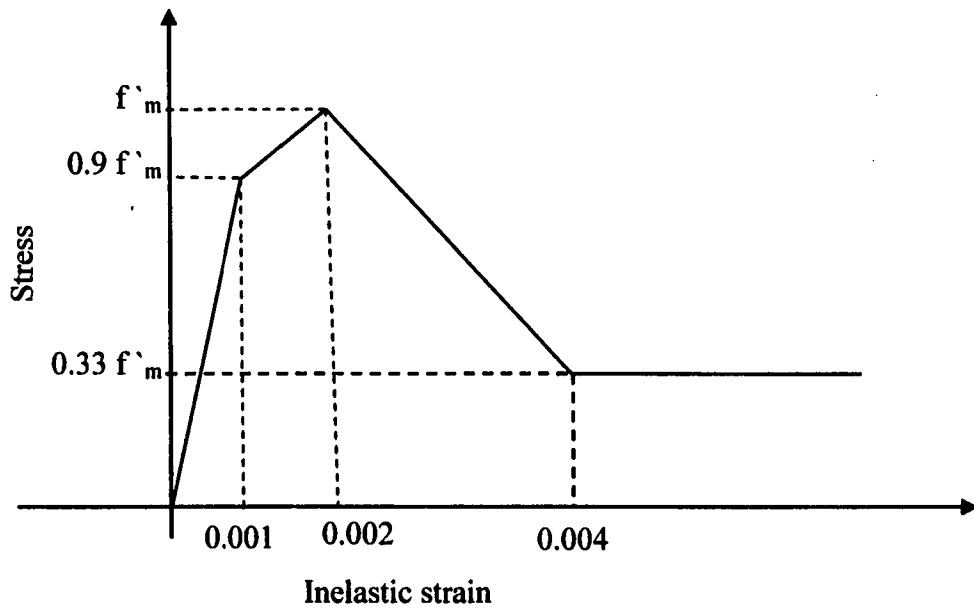


**Figure 5.3(b) Typical stress-strain curve for compression**

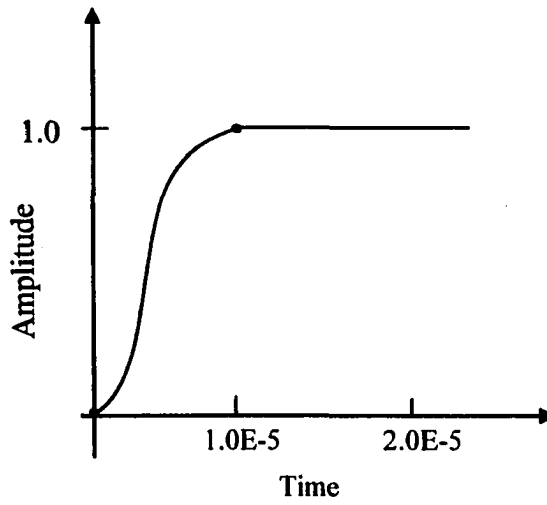


**Figure 5.4 Smooth load step curve**

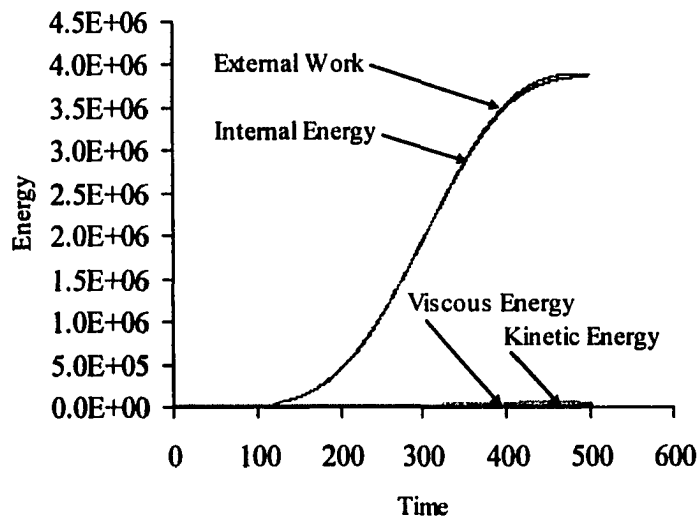


**Figure 5.5 Typical energy history curves**

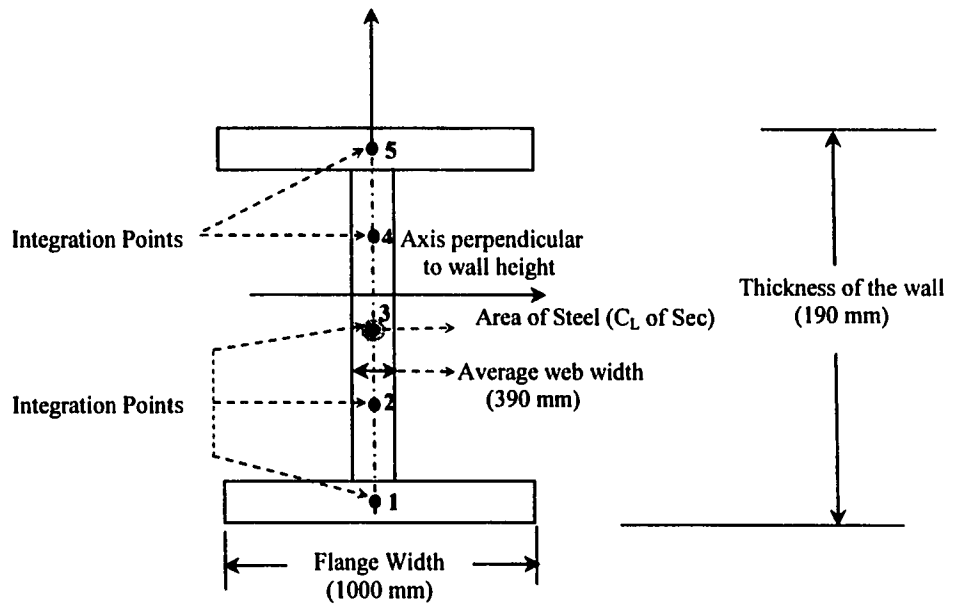


**Figure 5.6 Cross-sectional details of beam element**

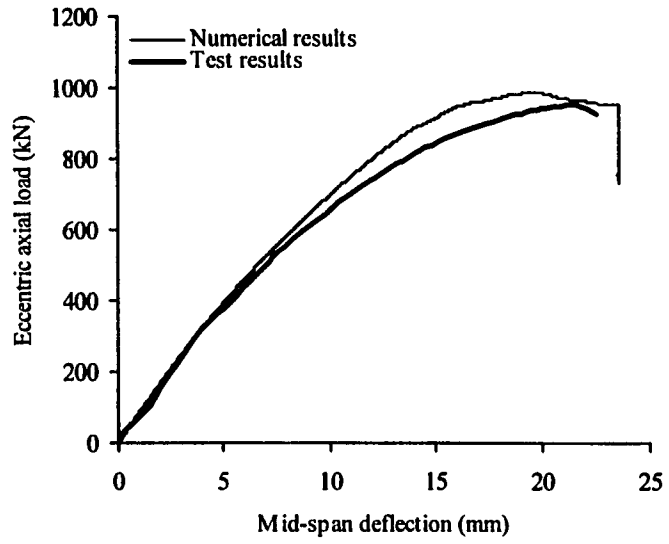


**Figure 5.7 Load deflection response of specimen W1**

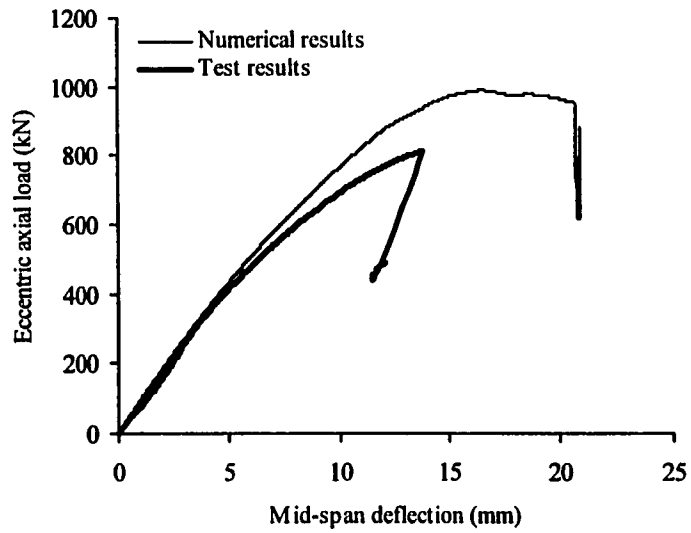


**Figure 5.8 Load deflection response of specimen W2**

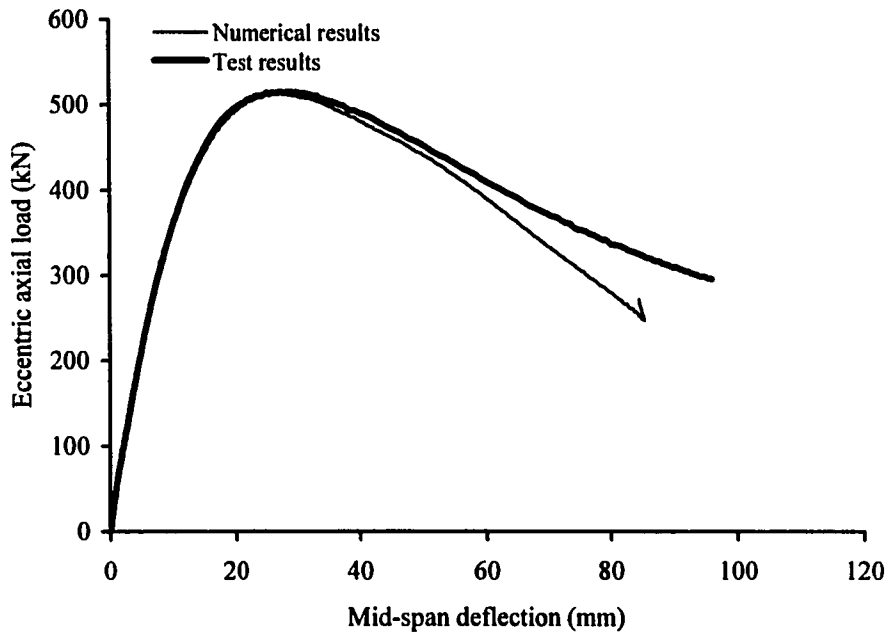


**Figure 5.9 Load deflection response of specimen W3**

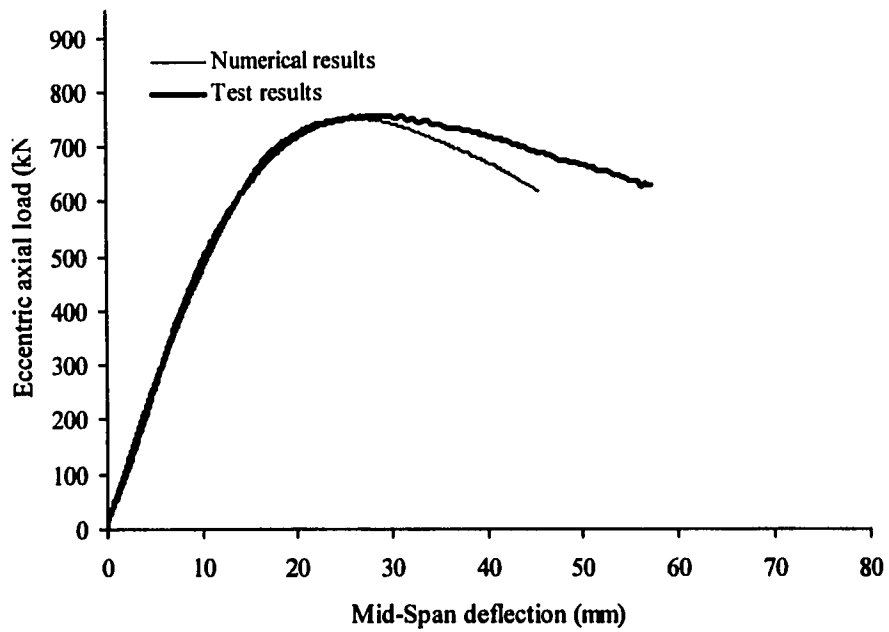


**Figure 5.10 Load deflection response of specimen W4**

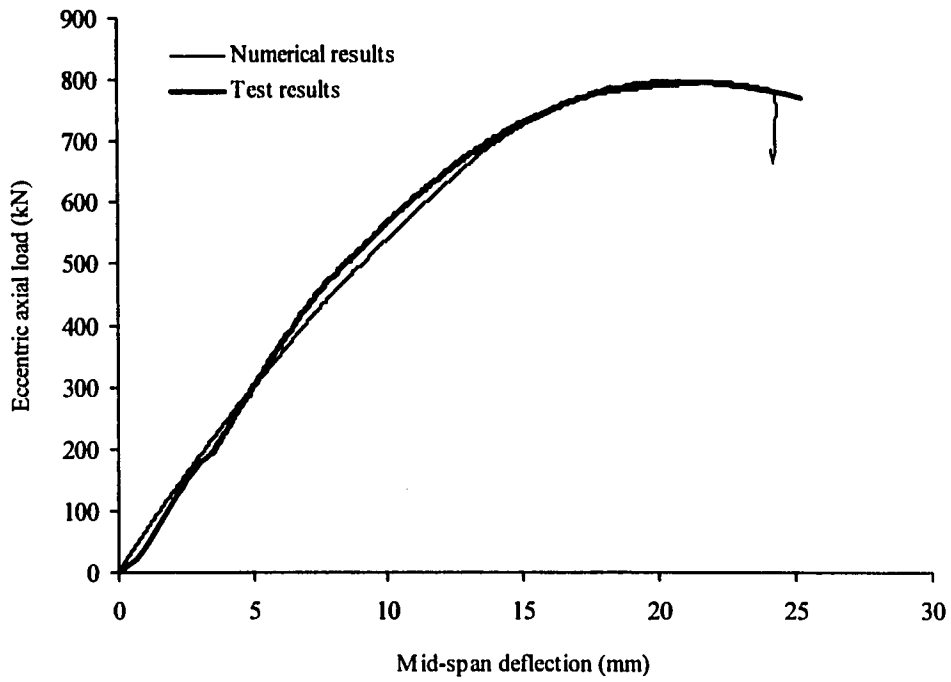


**Figure 5.11 Load deflection response of specimen W5**

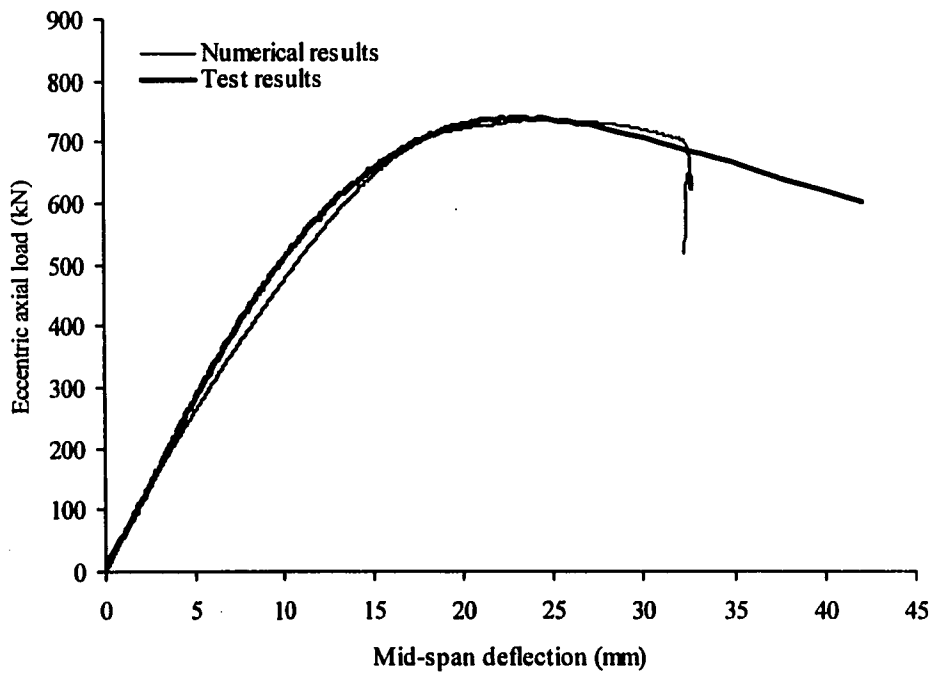


**Figure 5.12 Load deflection response of specimen W6**

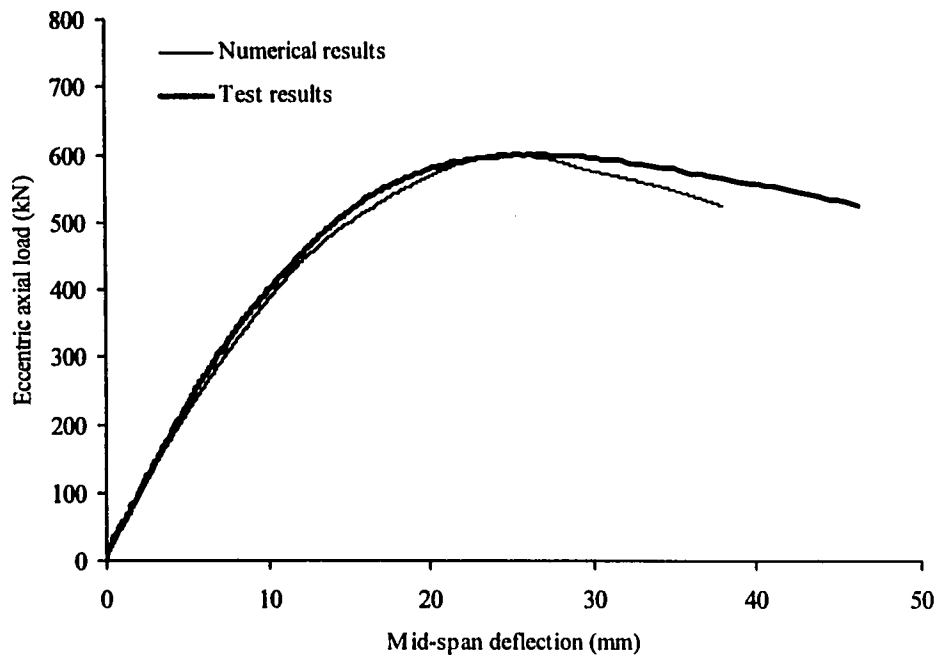


**Figure 5.13 Load deflection response of specimen W7**

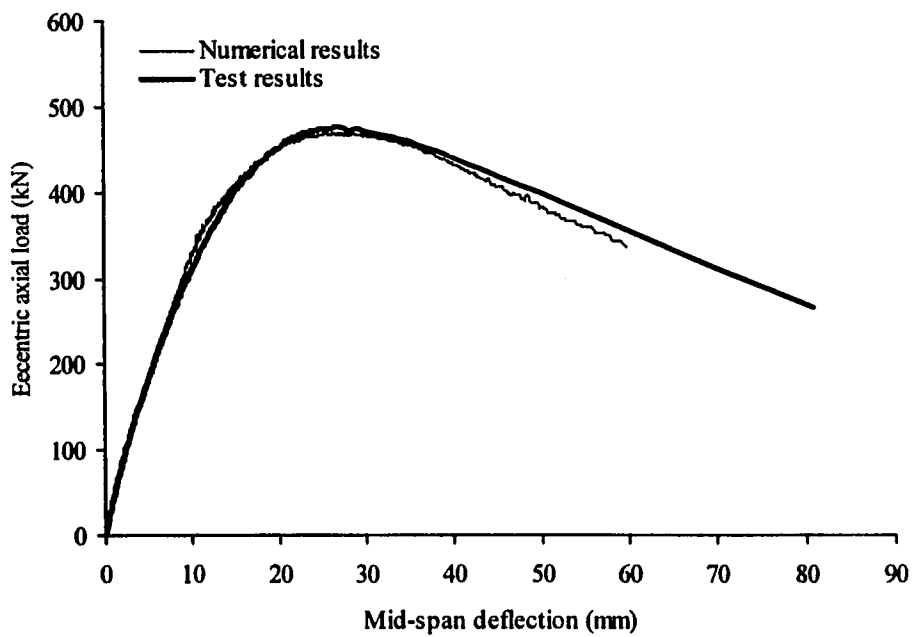


**Figure 5.14 Load deflection response of specimen W8**

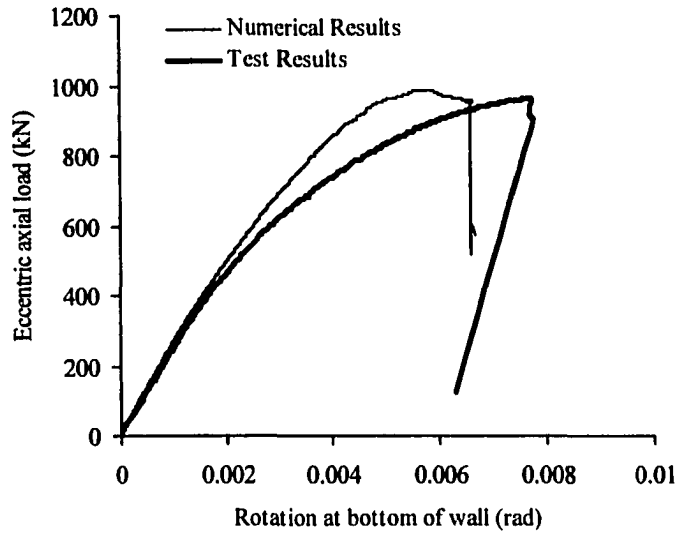


**Figure 5.15 Load versus Bottom rotation of specimen W1**

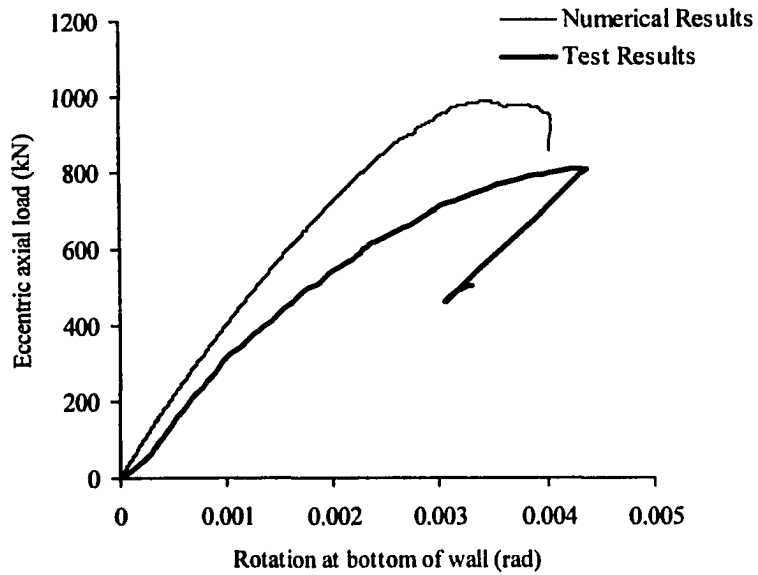


**Figure 5.16 Load versus bottom rotation of specimen W2**

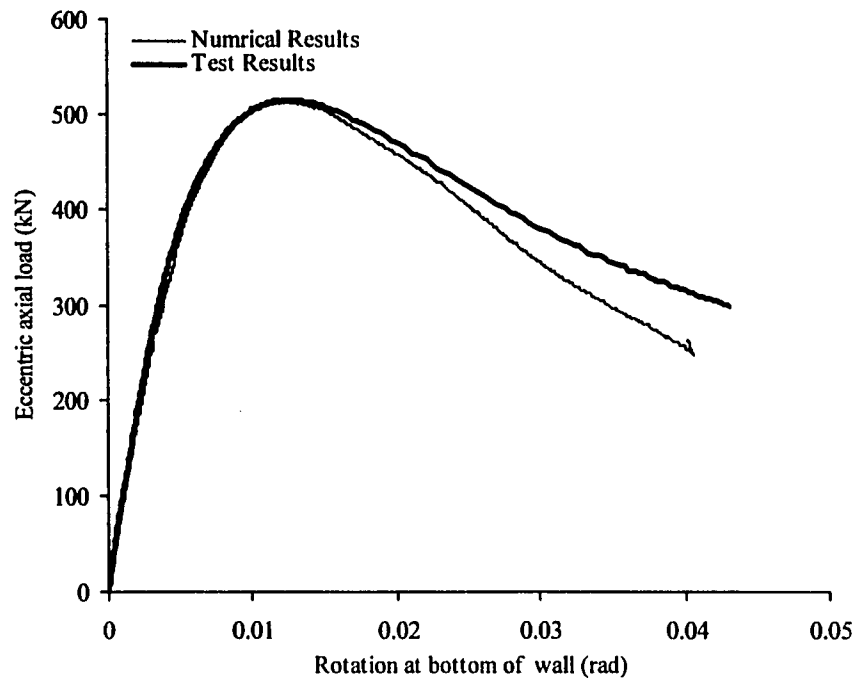


**Figure 5.17 Load versus bottom rotation of specimen W3**

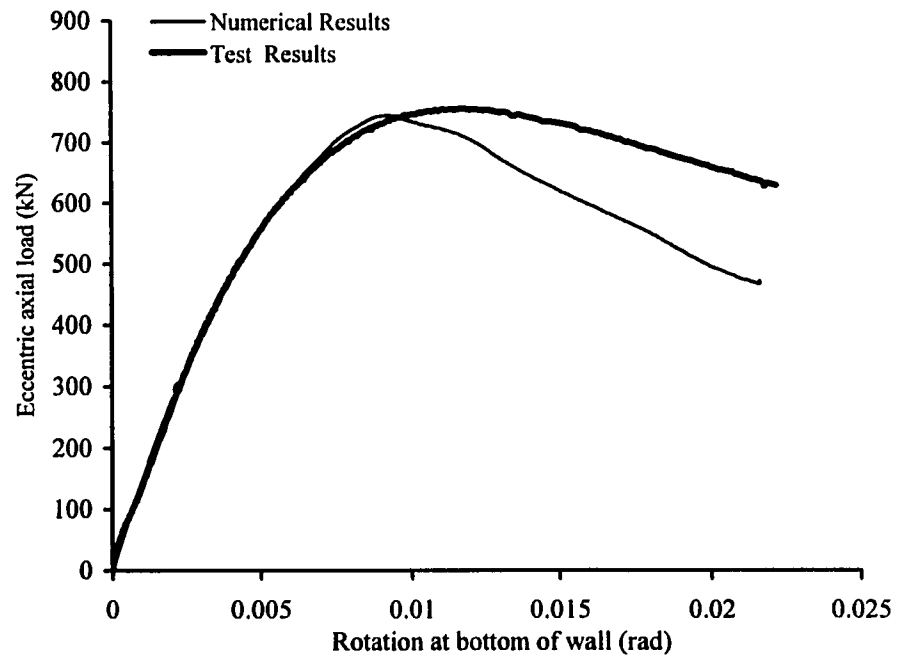


**Figure 5.18 Load versus bottom rotation of specimen W4**

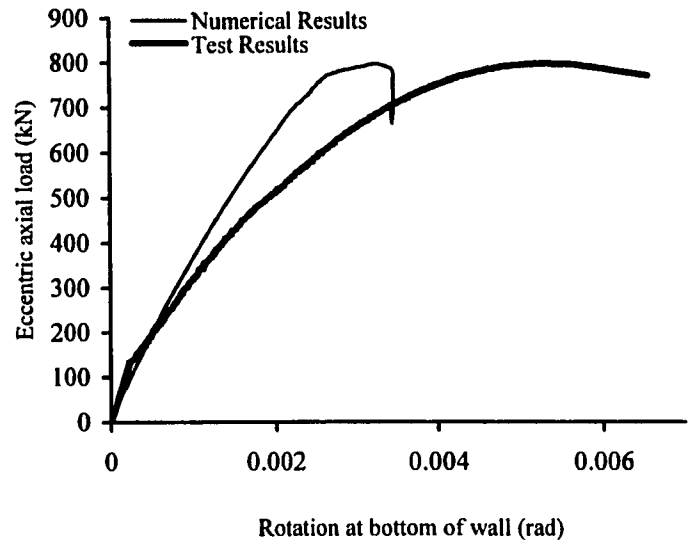


**Figure 5.19 Load versus bottom rotation of specimen W5**

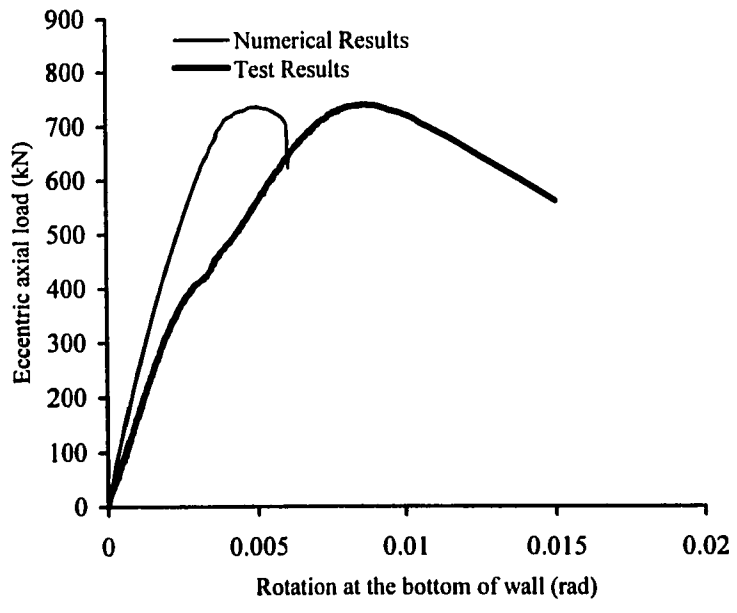


**Figure 5.20 Load versus bottom rotation of Specimen W6**

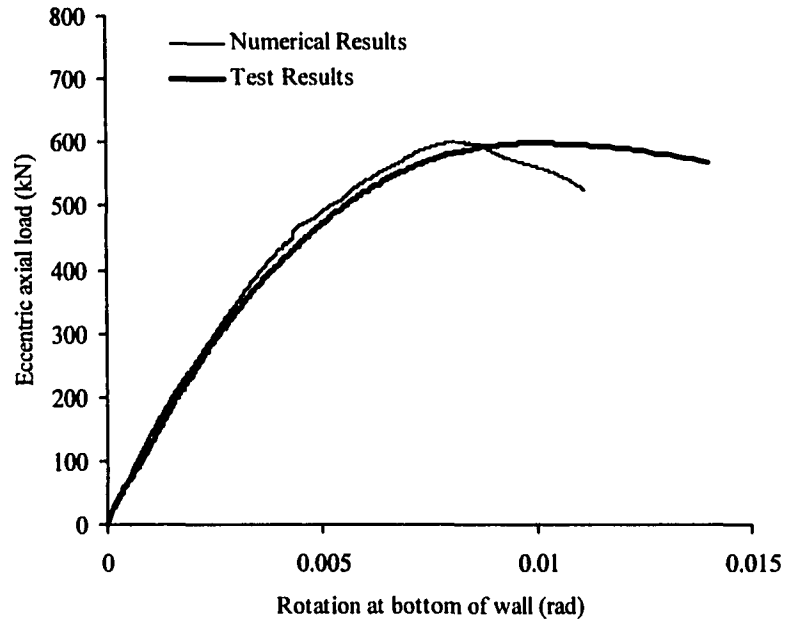


**Figure 5.21 Load versus bottom rotation of specimen W7**

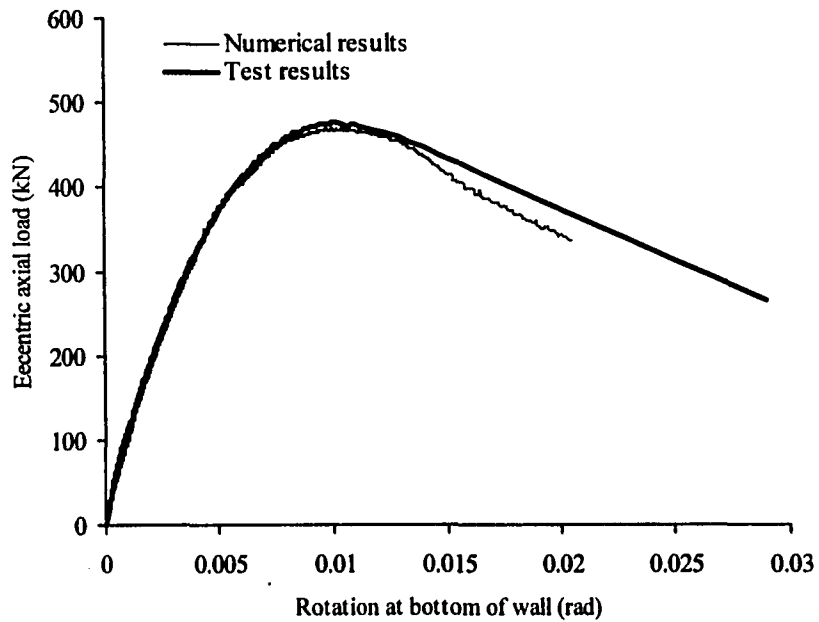


**Figure 5.22 Load versus bottom rotation of specimen W8**

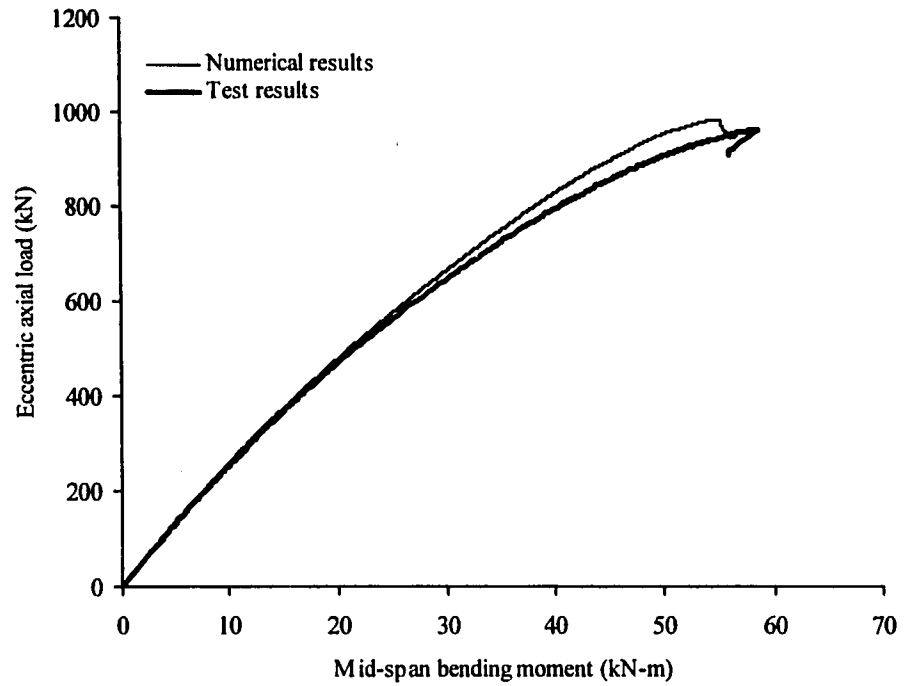


**Figure 5.23 Load versus mid-span bending moment of specimen W1**

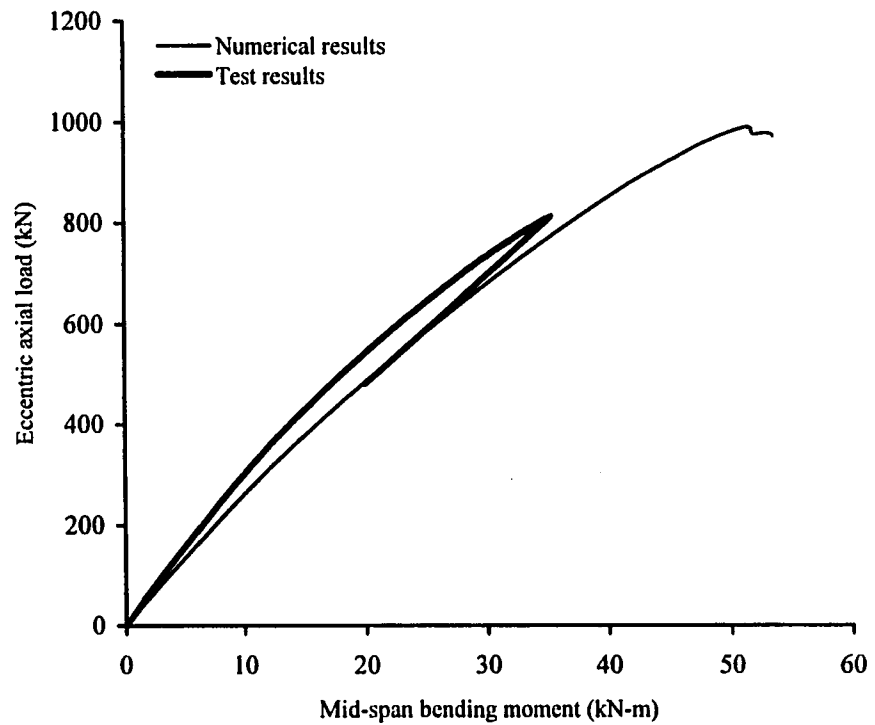


**Figure 5.24 Load versus mid-span bending moment of specimen W2**

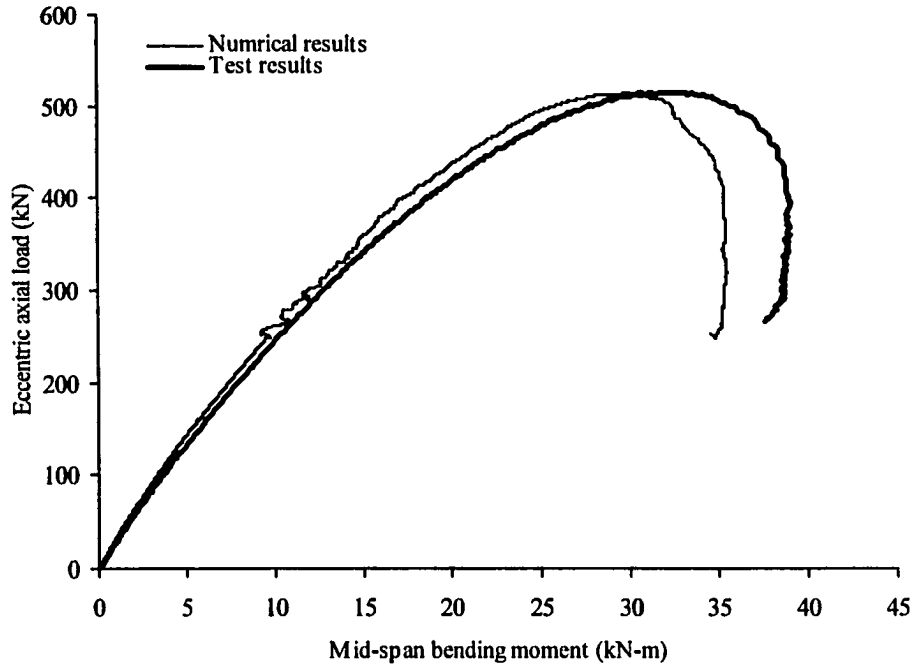


**Figure 5.25 Load versus mid-span bending moment of specimen W3**

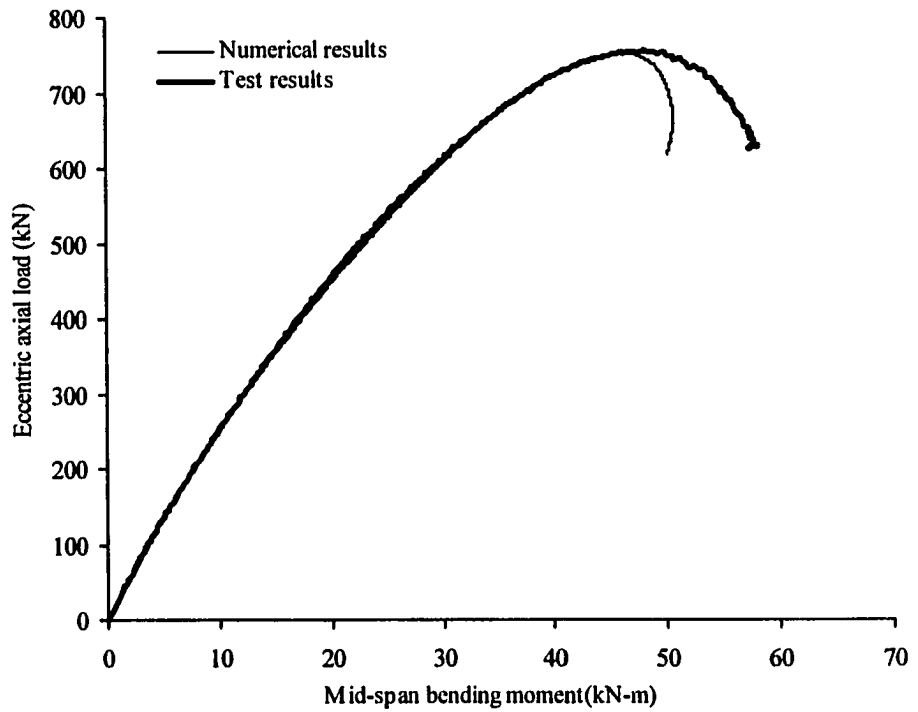


**Figure 5.26 Load versus mid-span bending moment of specimen W4**

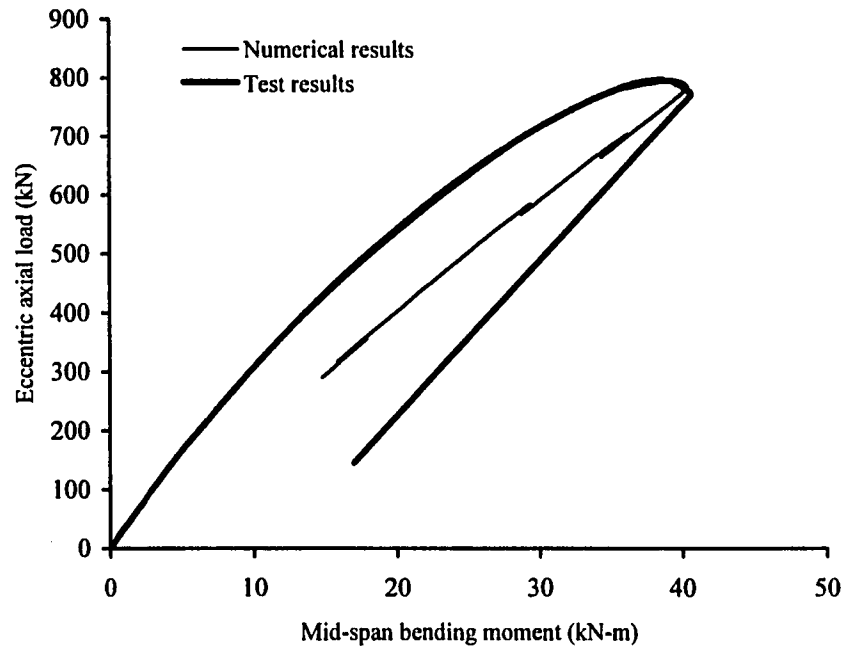


**Figure 5.27 Load versus mid-span bending moment of specimen W5**

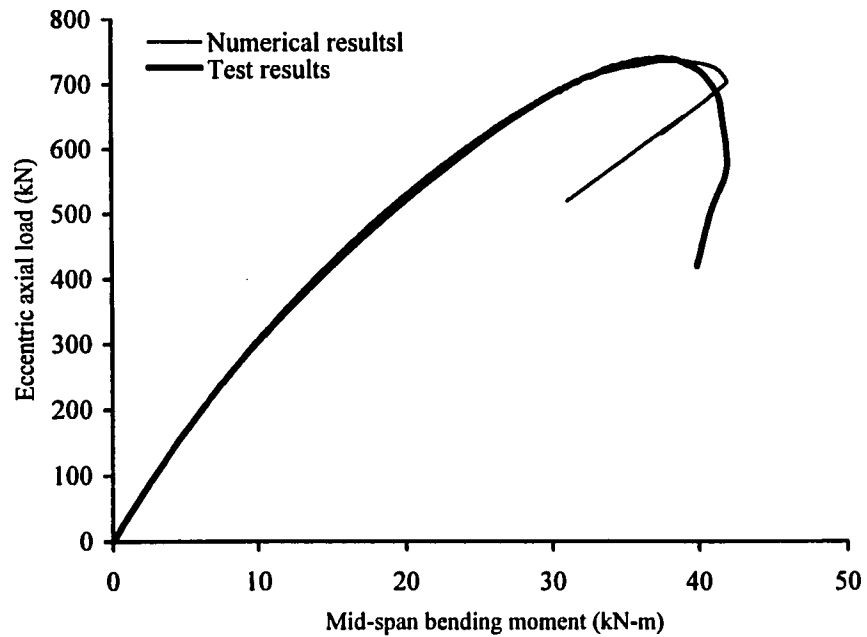


**Figure 5.28 Load versus mid-span bending moment of specimen W6**

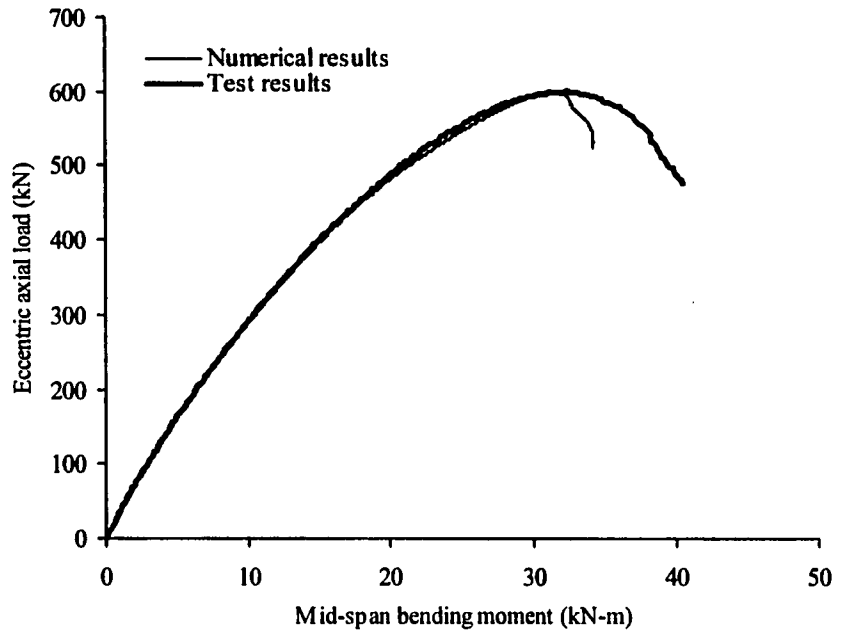


**Figure 5.29 Load versus mid-span bending moment of specimen W7**

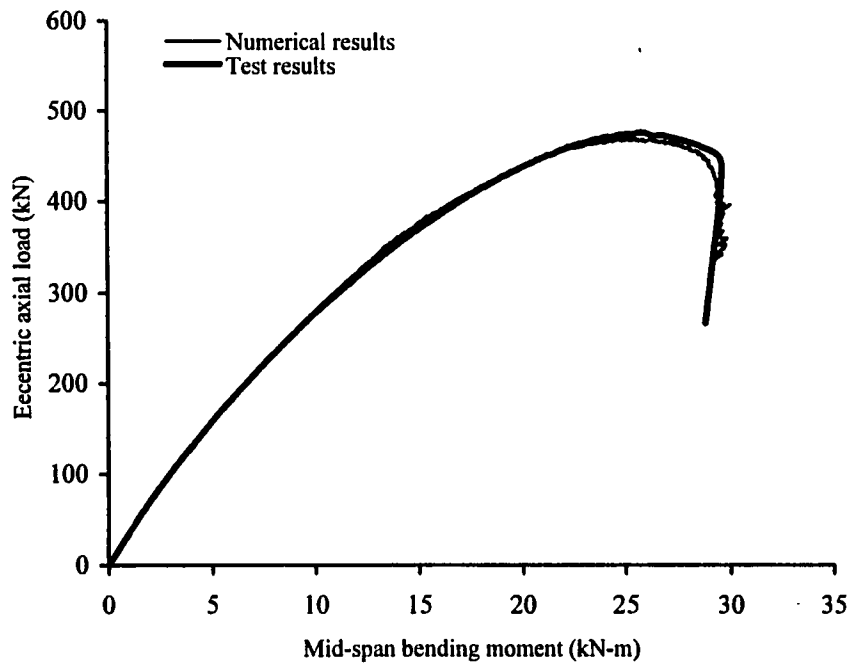


**Figure 5.30 Load versus mid-span bending moment of specimen W8**

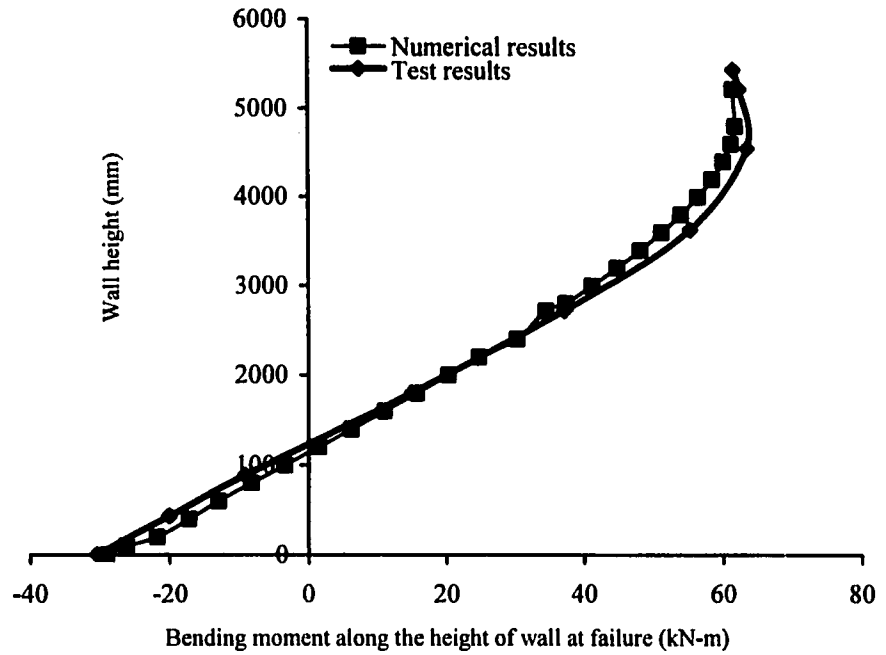


**Figure 5.31 Bending moment along wall height at local failure of specimen W1**

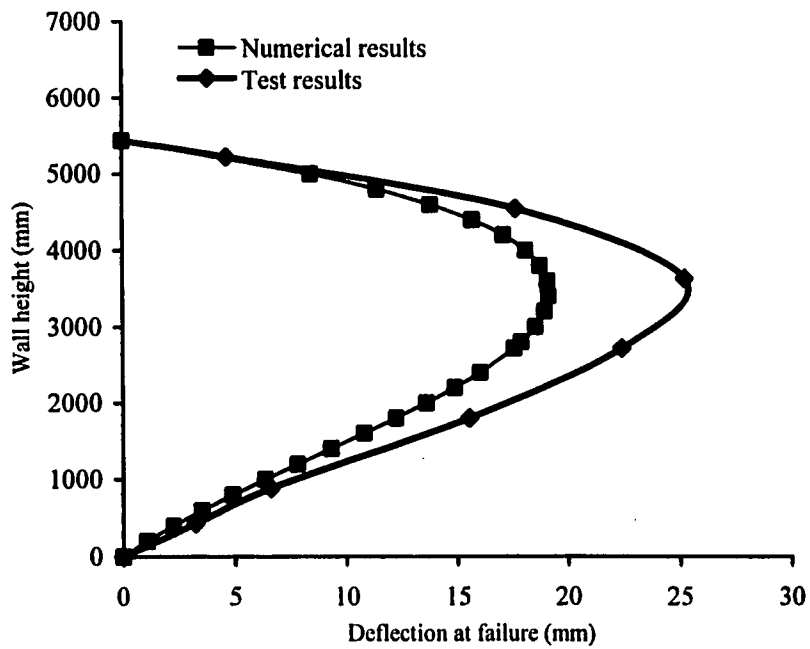


**Figure 5.32 Deflection along wall height at local failure of specimen W1**

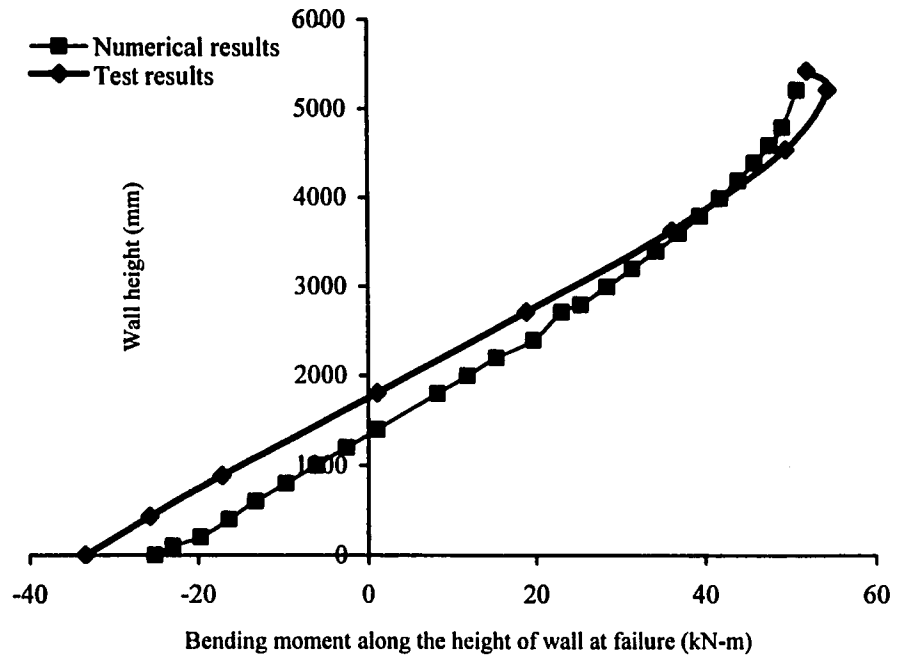


**Figure 5.33 Bending moment along wall height at local failure of specimen W2**

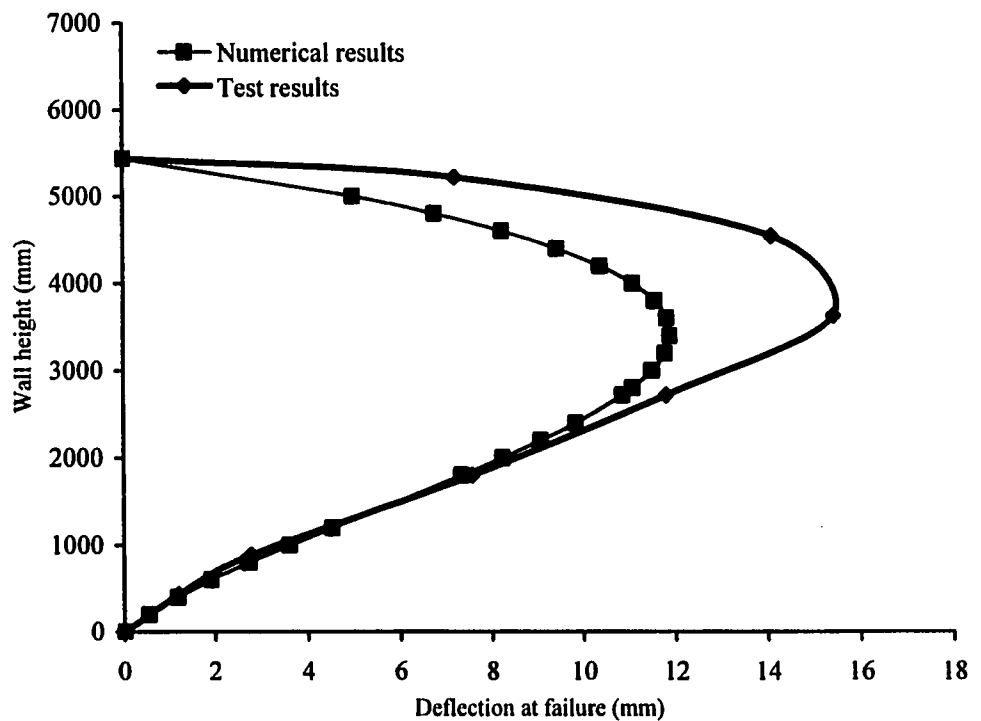


**Figure 5.34 Deflection along wall height at local failure of specimen W2**

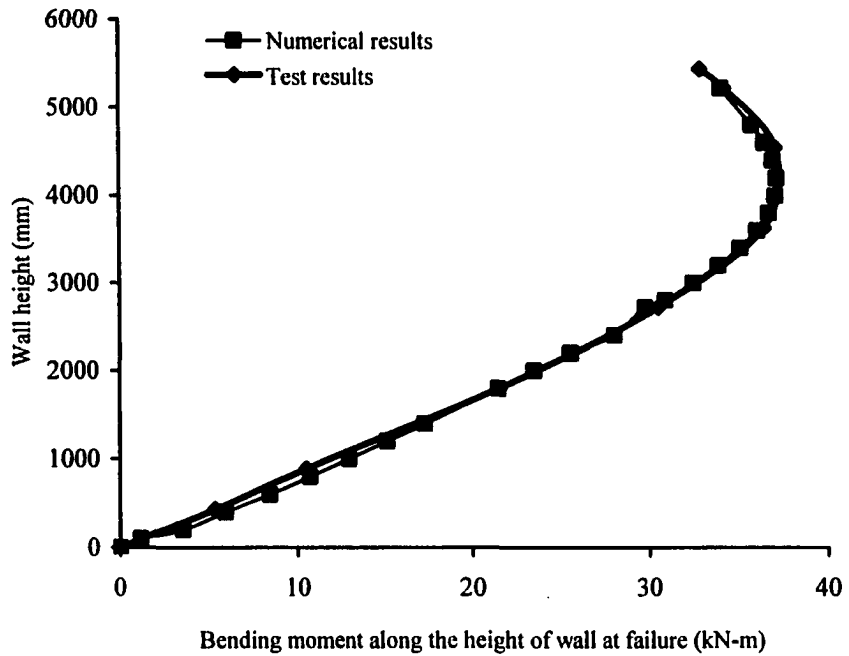


**Figure 5.35 Bending moment along wall height at failure of specimen W3**

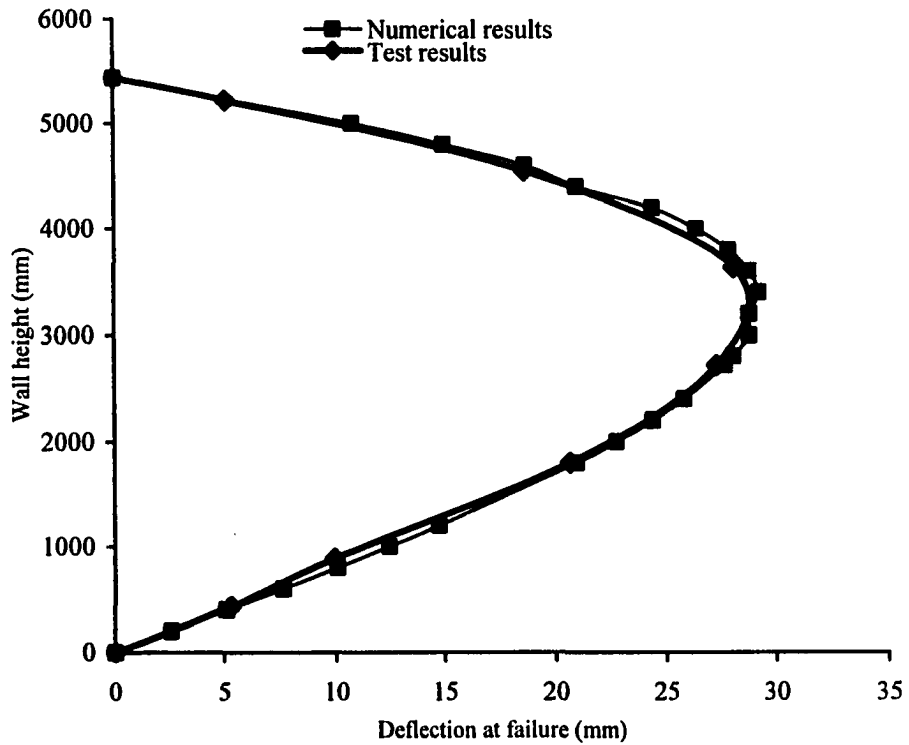


**Figure 5.36 Deflection along wall height at failure of specimen W3**

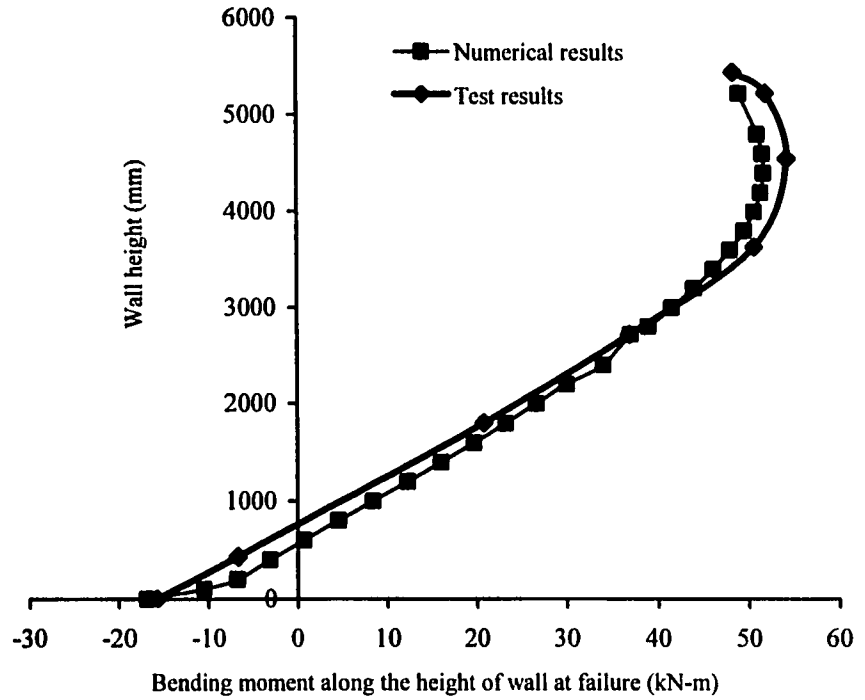


**Figure 5.37 Bending moment along wall height at failure of specimen W4**

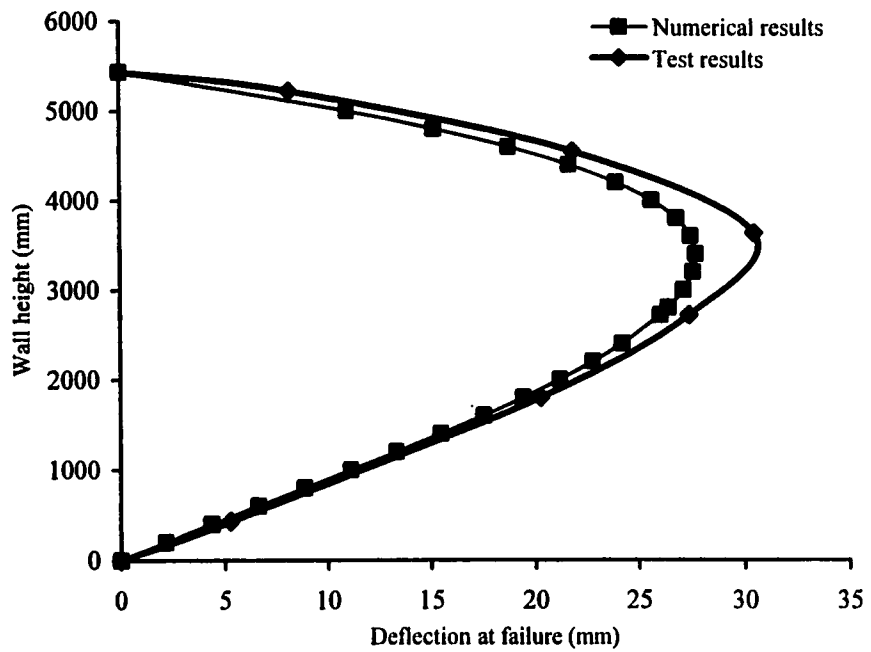


**Figure 5.38 Deflection along wall height at failure of specimen W4**

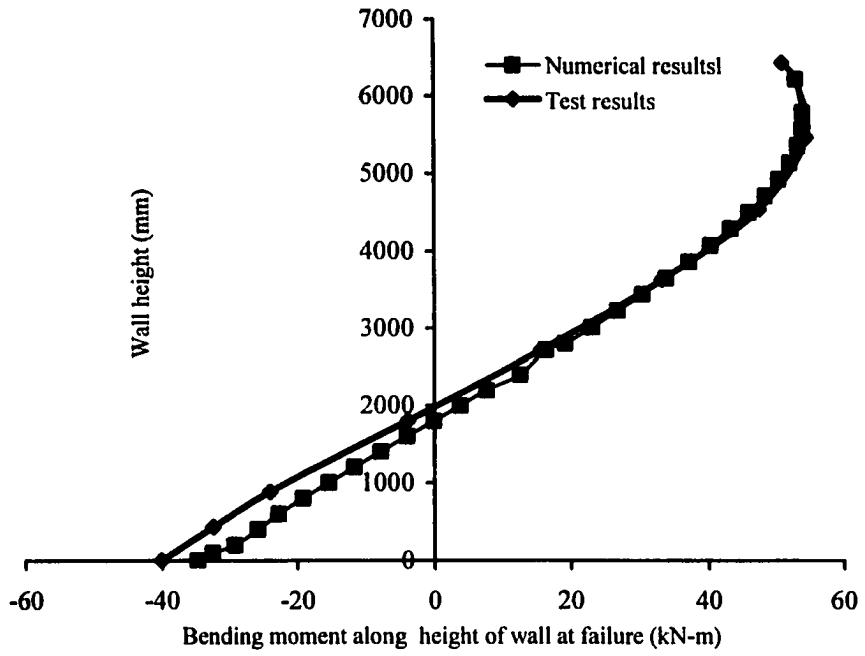


**Figure 5.39 Bending moment along wall height at failure of specimen W5**

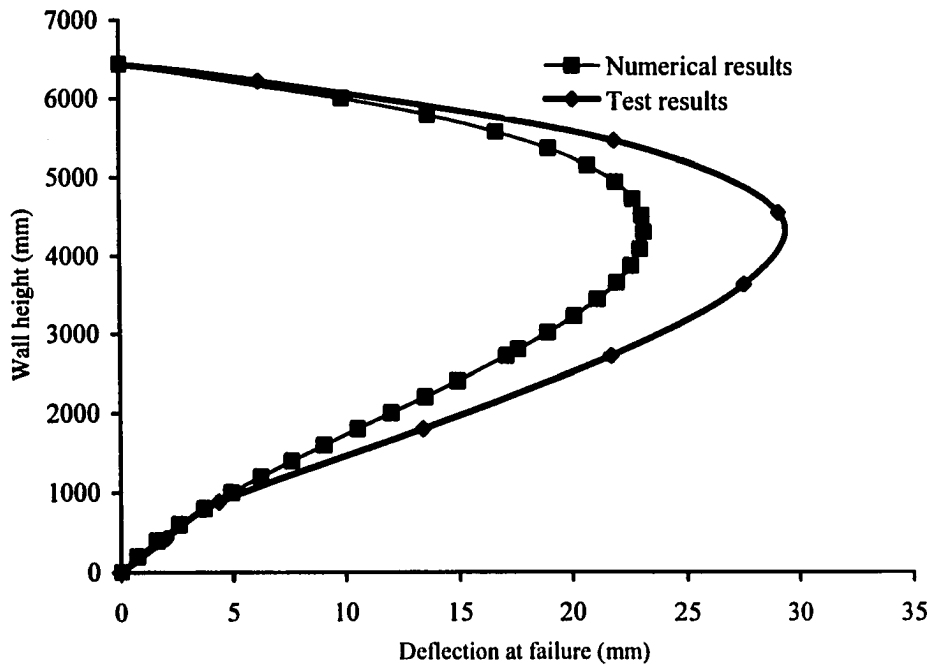


**Figure 5.40 Deflection along wall height at failure of specimen W5**

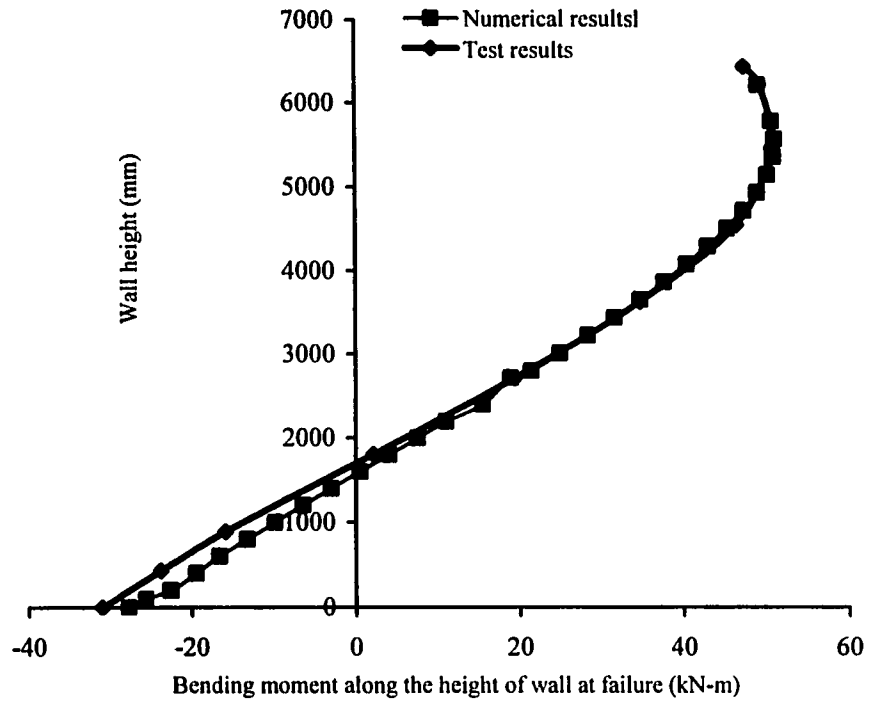


**Figure 5.41 Bending moment along wall height at failure of specimen W6**

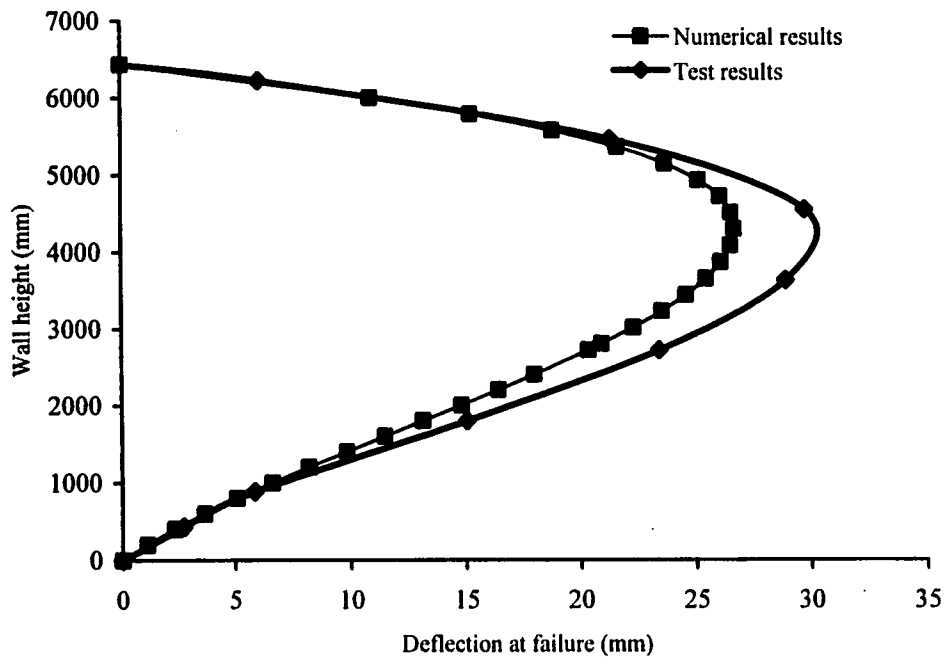


**Figure 5.42 Deflection along wall height at failure of specimen W6**

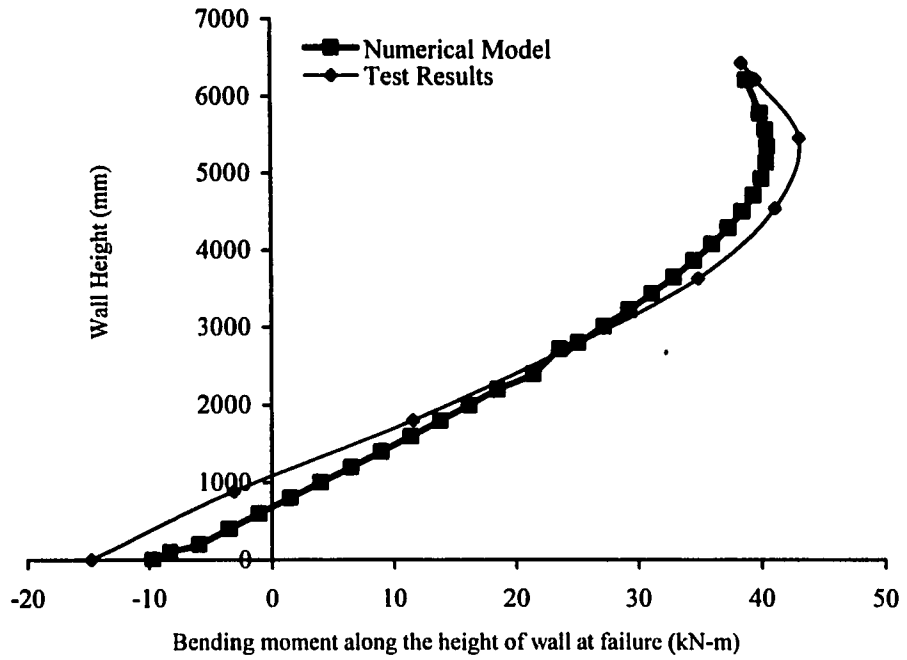


**Figure 5.43 Bending moment along wall height at failure of specimen W7**

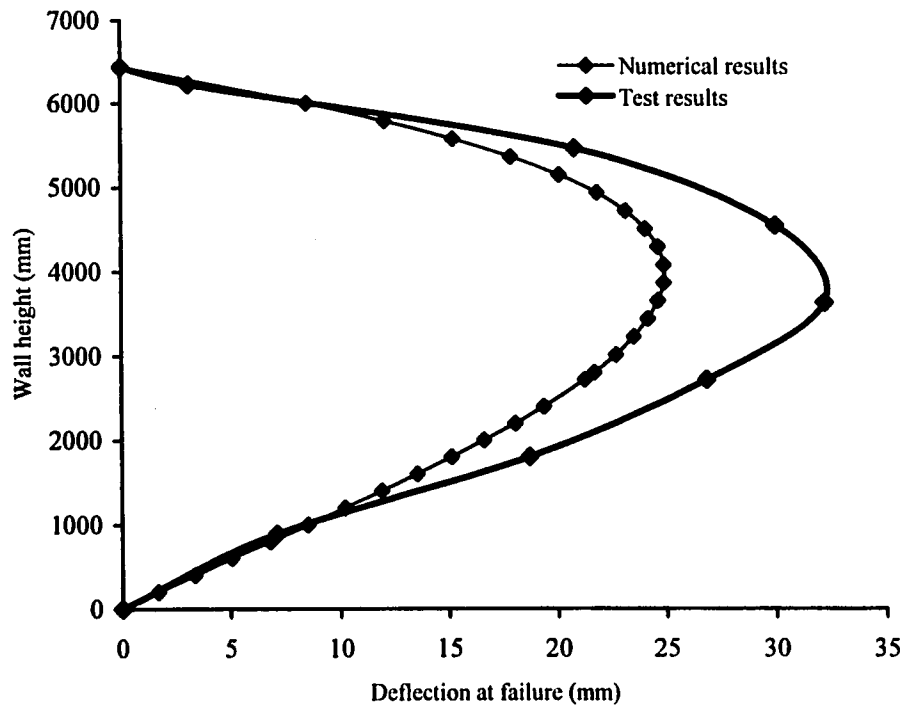


**Figure 5.44 Deflection along wall height at failure of specimen W7**

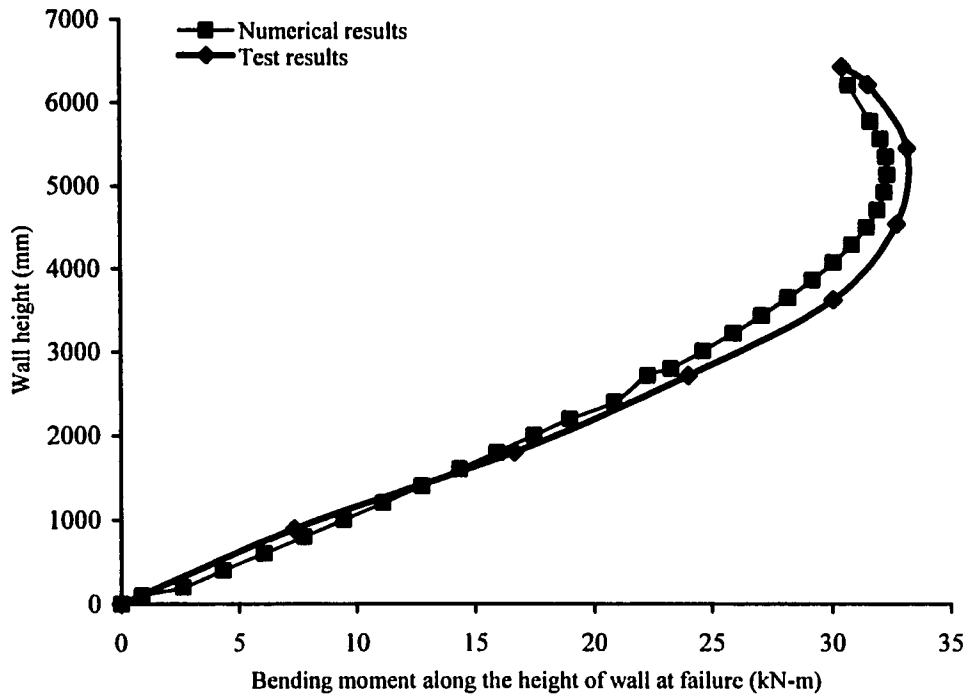


**Figure 5.45 Bending moment along wall height at failure of specimen W8**

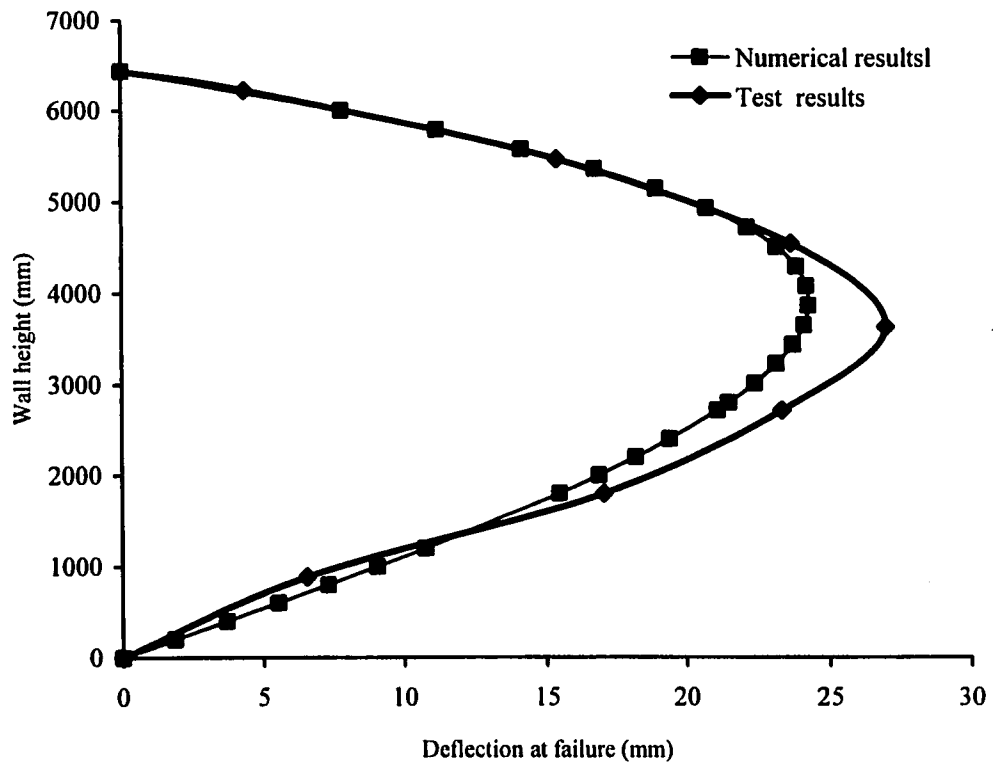


**Figure 5.46 Deflection along wall height at failure of specimen W8**

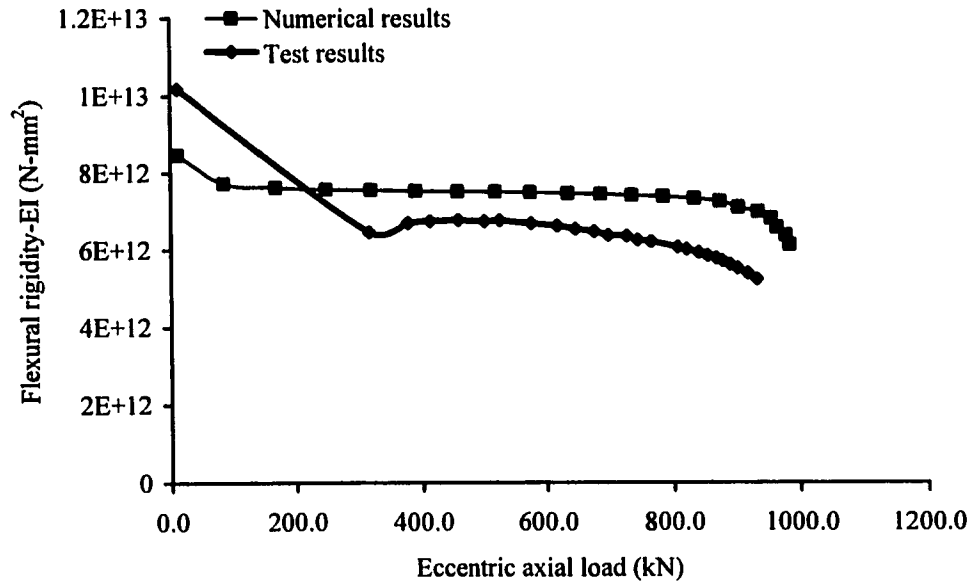


**Figure 5.47 Load versus flexural rigidity of specimen W1**

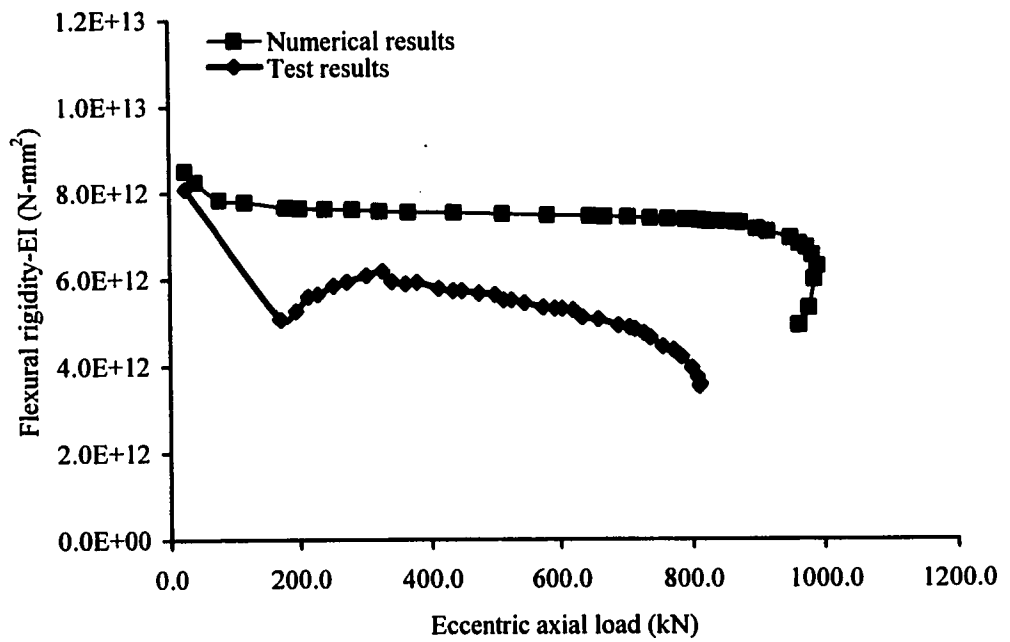


**Figure 5.48 Load versus flexural rigidity of specimen W2**

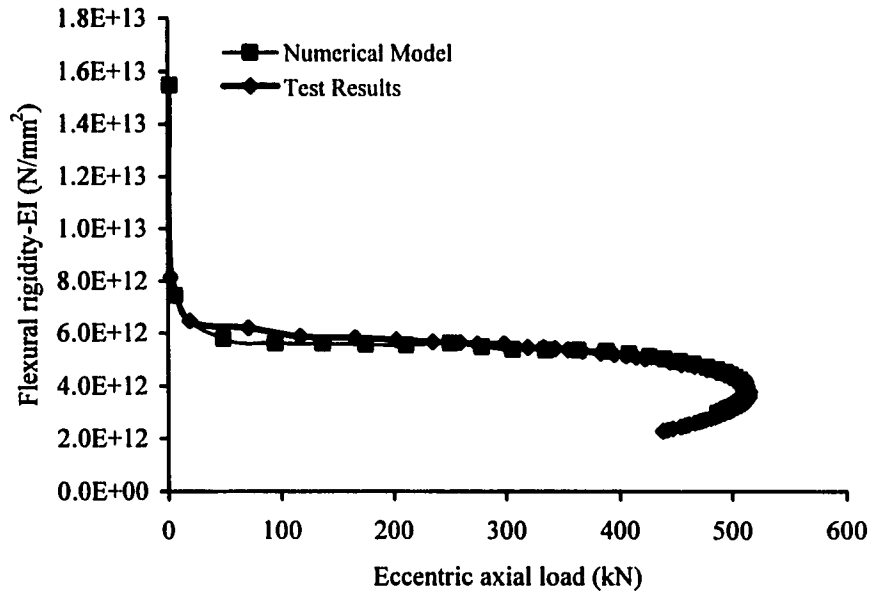


**Figure 5.49 Load versus flexural rigidity of specimen W3**

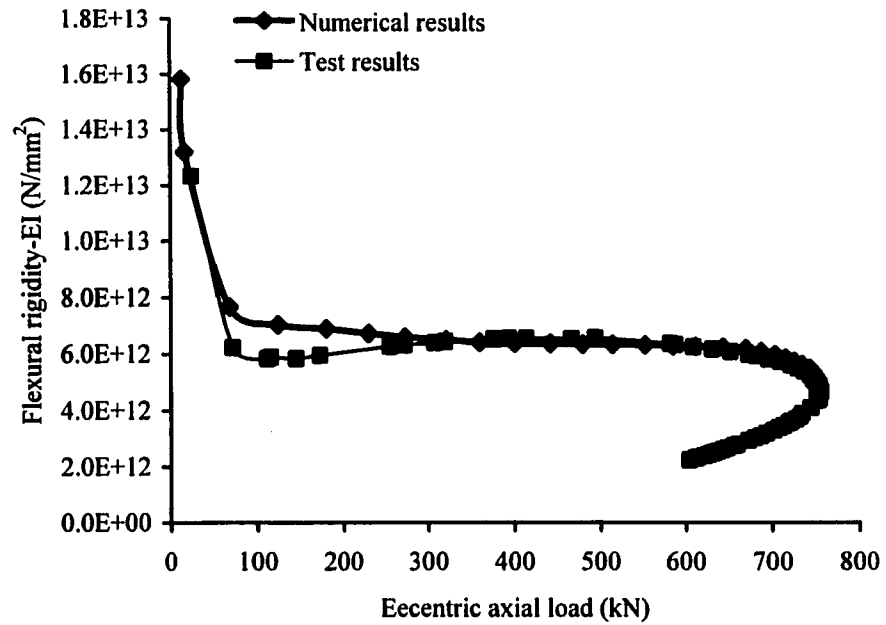


**Figure 5.50 Load versus flexural rigidity of specimen W4**

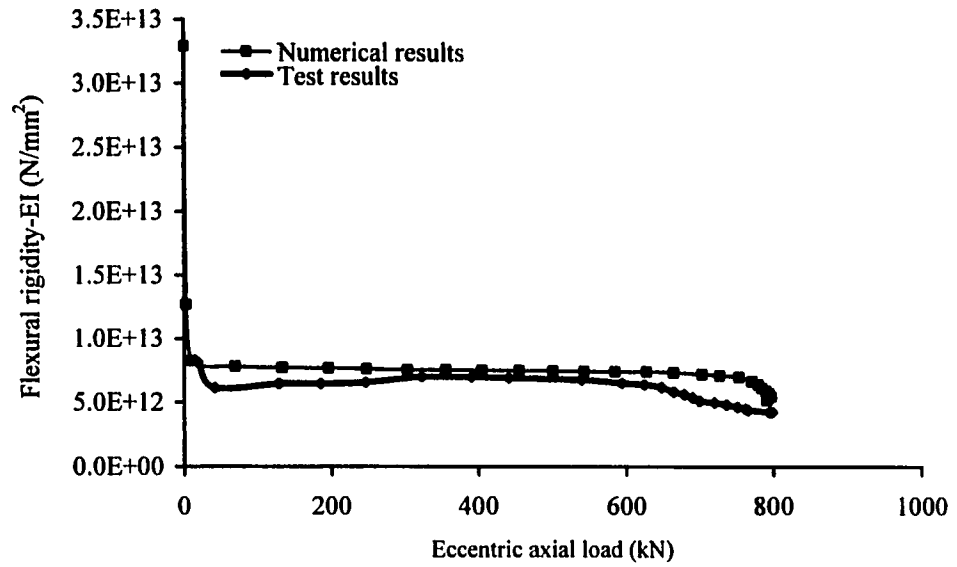


**Figure 5.51 Load versus flexural rigidity of specimen W5**

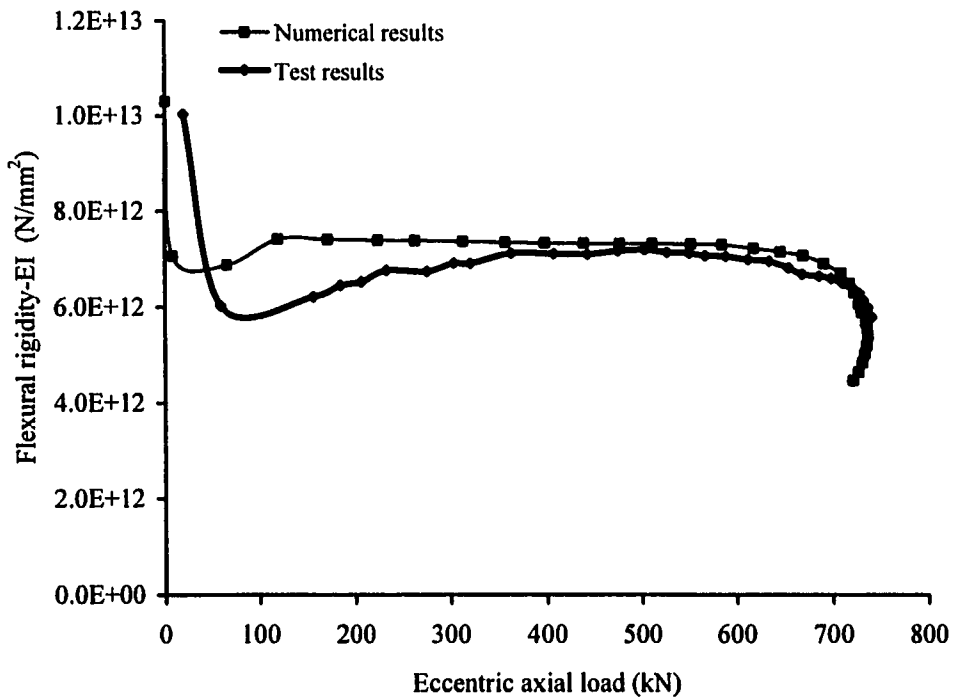


**Figure 5.52 Load versus flexural rigidity of specimen W6**

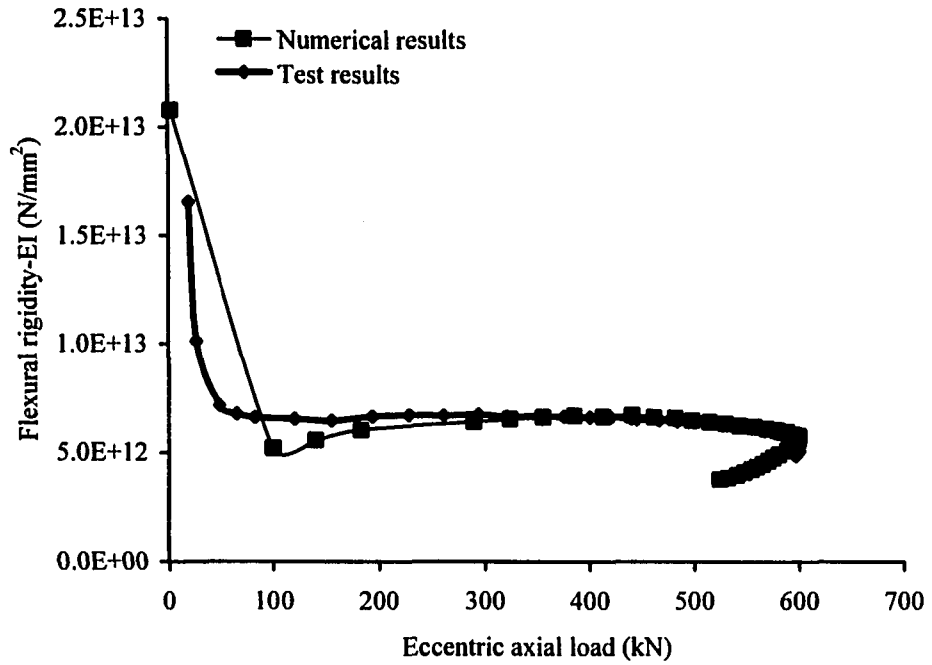


**Figure 5.53 Load versus flexural rigidity of specimen W7**

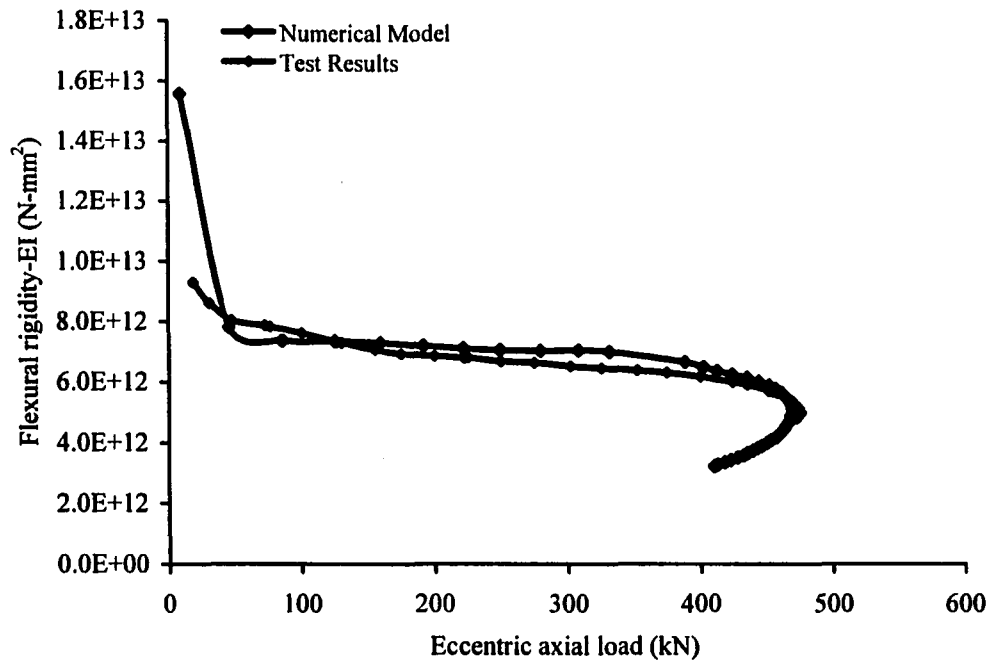


**Figure 5.54 Load versus flexural rigidity of specimen W8**

## **CHAPTER 6**

### **PARAMETRIC STUDY**

#### **6.1 Introduction**

Many geometric, loading and material parameters influence the response of load bearing masonry walls. It is hard to cover the wide range of these parameters by experimental investigation alone. To incorporate all key parameters a numerical model can be used as a tool to perform a comprehensive parametric study. In Chapter 5 a simple numerical model was developed and verified against the test results that were obtained and presented in Chapter 3 and Chapter 4. In this chapter the model is used to carryout an extensive parametric study. The objective is to investigate the effect of support stiffness on stability of masonry load bearing walls under different combinations of geometric, loading and material parameters. It is intended to investigate the interrelationship between the support stiffness and other key parameters as they relate to load carrying capacity, deflection, bending moment, flexural rigidity and failure modes of the masonry block walls so that a comprehensive database can be established.

Considering support stiffness as the primary parameter, the selection of other parameters is based on geometric dimensions, loading intensity and material properties of masonry block walls. This chapter provides details of parameter selection, their combination and the output results obtained from the numerical investigation of different cases generated thorough various combinations of the selected parameters.

#### **6.2 Numerical Model**

The numerical model developed in Chapter 5 was used to perform the parametric study. The study in Chapter 5 showed that the model can capture geometric as

well as material non-linear behavior. The finite element mesh of the model consists of beam-elements having length equal to a masonry course height, which is 200 mm. The boundary conditions of the model incorporate the support stiffness at bottom and a lateral support at the top, as shown in Figure 6.1. To define the characteristics of the material of masonry assemblage the damaged plasticity model is used. This model as described in Chapter 5 incorporates the mechanical behavior of concrete by using non-associated multi-hardening plasticity and isotropic damaged elasticity rules. The uni-axial compressive behavior is considered linear up to the level of an initial yield surface followed by strain hardening, then strain softening beyond the peak stress. In the tensile zone the model allows concrete softening in post-peak stress-strain relationship by using a fracture energy cracking criterion. The failure surfaces in tension and compression are controlled by separately calculating equivalent tensile plastic strain and equivalent compressive plastic strain. The elastic material properties in the numerical model are introduced by defining Young's modulus along with Poisson's ratio. In the inelastic range the compressive strain softening regime is tabulated against corresponding inelastic strain. The tensile material properties are defined by setting the peak tensile stress equal to the bond stress for the mortar-masonry interface, while for the post-peak behavior a stress cracking displacement relation is defined so that the fracture energy density would have a reasonable value.

### **6.3 Selection of Parameters for the Numerical Study**

The parameters were selected under three categories; constant parameters, primary parameters and secondary parameters.

#### **6.3.1 Constant Parameters**

Standard 200 mm concrete block type with 15MPa unit compressive strength and Type-S mortar were selected as the study base throughout. The results were then

normalized so that the conclusions can be generally applicable. Based on 15MPa unit strength the value of  $f_m^d$  was taken from Figure 6.2. The modulus of elasticity,  $E_m$ , was calculated from equation 6.1.

$$E_m = 850 f_m^d \quad [6.1]$$

The typical stress-strain curves in the compression and tension zones are shown in Figure 6.3. The curves are similar to those used in Chapter 5. There may be different kinds of foundations, e.g. pile foundation or grade beam, on which a masonry block wall can stand but the scope of the current study is focused on strip type footings with pin connection to the slab-on-grade. The next section will describe the selection of support stiffness offered by a strip foundation composed of different configurations and resting on various types of soils.

### 6.3.2 Primary Parameter

The current study mainly focuses on the effect of support stiffness on behavior of masonry block walls. Therefore, support stiffness is considered as the primary parameter. Wall-support interface may be subjected to different practical situations, affecting the bottom rotation of the wall. Foundation for masonry load bearing walls may be a strip type foundation wall or a grade beam resting on pile foundation. Selection of the foundation depends on subsoil conditions and the magnitude of the load to be transferred from the wall to the ground. Rotational restraint offered by the foundation depends on factors such as soil type, type of foundation, dimensions of foundation, and its connection to the slab-on-grade. These factors influence the transmission of bending moment at wall-support interface and affect the end rotation of the wall.

To simplify the procedure it is assumed in this study that the connection of slab-on-grade to the wall foundation is a pin connection. Thus only the foundation size and type of soil control the rotational stiffness at the bottom of the wall. If the

foundation is a grade beam on piles, then the rotational stiffness is governed by the torsional stiffness of the beam and the rotational stiffness of the pile heads; both are very low. A simple parametric study was carried out earlier, which yielded a range of stiffness from 500 kN-m/rad to 10,000 kN-m/rad depending on the foundation wall geometry and soil stiffness. For the purpose of the parametric study the support stiffness values  $R=0, 500, 1000, 5000, \text{ and } 10,000$  kN-m/radian were the selected values, which are representative of combinations of soft to stiff soils and different dimensions of strip foundation used in practice.

### **6. 3.3 Secondary Parameters**

Other major variables needed to define the geometric characteristics of a load bearing wall are the height, grouted cores and amount of reinforcement. Some of the geometric variables are transformed into non-dimensional parameters. For example the wall thickness and height are combined in the slenderness ratio ( $h/t$ ). The details of all geometric parameters are described in the following.

#### ***Slenderness ratio ( $h/t$ )***

The slenderness ratio controls the geometric non-linearity in load bearing walls by significantly affecting the wall deflections, which consequently have an influence on the axial load carrying capacity of the walls. It is evident from the current experimental results that the effect of support stiffness was considerably influenced by the slenderness ratio of the load bearing walls. To explore the interdependency of these two parameters moderate to high  $h/t$  ratios were selected. Based on 200 mm nominal wall thickness (190 mm actual thickness)  $h/t=18, 30, 36$  and  $42$  are the selected  $h/t$  ratios. Among the selected slenderness ratios,  $h/t=18$  represent stocky walls,  $30$  falls into the category of moderately slender walls while  $h/t=36$  and  $42$  correspond to highly slender walls, (S304.1 Clause 11.2.4.3.1).

### ***Area of reinforcement and net cross-sectional area of masonry***

The vertical reinforcement of masonry load bearing walls is embedded into the grouted cores. The spacing of the vertical reinforcing bars dictates the amount of grouting. In predicting the cross-sectional strength of load bearing masonry walls cross-sectional variables such as area of reinforcement and spacing of grouted cores play a central role. The grouting not only affects the geometry but also influences the material strength of masonry. Based on the amount of grouting, the net cross-sectional area of masonry was selected and for the corresponding amount of steel, 1-15M bar per grouted core was considered. Thus, in this thesis the masonry material compressive strength is based on partially grouted prism compressive strength plot of Figure 6.2. The modulus of elasticity follows as a function of the prism compressive strength, and so does the amount of reinforcement.

### ***Amount of grouting***

Based on the discussion above it is clear that the amount of grouting falls into the category of both geometric and material parameters. It has been well documented that a grouted masonry wall has lower compressive strength as compared to a hollow wall. On the other hand, an increased amount of grouting increases the net cross-sectional area of the wall and it is expected that it should also increase the axial load carrying capacity of the wall. Keeping in mind the current construction practice this study considers three cases, where every 2<sup>nd</sup>, 3<sup>rd</sup> or 5<sup>th</sup> core is grouted so that 50%, 33% and 20% of cores filled with grout within a one meter length of the wall. Figure 6.2 shows a plot of the compressive strength of a prism built with 15MPa units. All masonry properties are based on the prism compressive strength. While, admittedly, the prism compressive strength could depend on the level of flexure in the test, as well as on the grout strength, no adequate information exists that account for these effects.

### ***Load eccentricity ratio (e/t ratio)***

Load eccentricity plays an important role in establishing the load carrying capacity of masonry load bearing walls by reducing the flexural rigidity. To study the effect of load eccentricity, values of  $e/t=0.1$ , 0.333 and 0.42 have been selected. The smallest  $e/t=0.1$  corresponds to a minimum load eccentricity as recommended by S304.1, while 0.33 and 0.42 represent the cases of higher load eccentricity. The selected range covers the minimum to maximum load eccentricity used in practice.

### **6.4. Combination of Parameters**

The parameters that have been discussed in the previous section are combined in a systematic manner. Considering support stiffness,  $e/t$  ratio and amount of grouting as primary parameters, selected ranges of these parameters are combined with appropriate slenderness ratios within practical considerations. For example, walls with lesser support stiffness are grouped with the highest selected slenderness ratio to justify the fact that very high walls are not designed to carry higher loads and are usually supported by small footings having lesser support stiffness. Stocky walls (e.g.  $h/t=18$ ) are analyzed to study the effect of grouting as this is the most extreme case among the selected  $h/t$  ratios, leading to cross-sectional failure. For particular values of support stiffness, slenderness and eccentricity ratios the analysis is repeated with selected ranges of amount of grouting by assigning the corresponding cross-sectional properties. Table 6.1 shows all parameters. Altogether 135 walls were analyzed.

### **6.5 Output Parameters**

The data bank generated here is required to investigate the effects of all input parameters as discussed in the previous sections. Since the study is focused on overall stability of load bearing masonry walls, it is intended to collect

information necessary to define the stability of the masonry load bearing walls in terms of output parameters, such as axial load, out of plane mid-height deflection, rotation at the bottom of wall and flexural rigidity. These output parameters can further be transformed into dimensionless parameters. For example the deflection at mid-height can be normalized relative to the thickness of the wall, e.g.  $\Delta/t$ . The definition of normalized axial capacity of the wall in the current study corresponds to the ratio of  $P/P_0$ , here, "P" refers to the load carried by the wall and  $P_0$  is the cross-sectional capacity, obtained from Equation 6.2.

$$P_0 = A_e f'_m + A_s f_y \quad [6.2]$$

in which  $A_e$  is the net area of concrete masonry,  $f'_m$  is the prism compressive strength,  $A_s$  is the total area of vertical rebars and  $f_y$  is the yield strength of steel.

Some other output results corresponding to failure, such as deflected shape, bending moment diagram and effective plastic strains are also obtained. It is important to mention that failure of the wall in the current study corresponds to the event at which the wall attains its peak load. All above stated output results are plotted at the instant when the wall reaches its peak load. Using the integration points as shown in Figure 6.4, the plastic strains are plotted at extreme tension and compression faces of the wall cross-section, at the location of highest stressed point along the height of the wall (point of maximum bending moment). Other output parameters such as deflection and bending moments are associated with the mid-height section of the wall.

## 6.6 Failure Modes

There are two specific objectives of the current study. The first deals with examining the failure modes and the capacity as influenced by the support stiffness. The second deals with investigating flexural rigidity. Before going into detailed discussions it is important to define the different failure modes expected

to occur under the influence of the different parameters. There are three expected failure modes, compressive failure, tensile failure and stability failure.

**Compressive failure** is common in stocky walls subjected to small  $e/t$  ratios. It is also expected under low slenderness ratios and high support stiffness.

**Tensile failure** in the form of cracking and bond failure occurs quickly on the bed joints under small curvature values and do not constitute wall failure. Yield of the rebar, however, under high curvatures constitute a serious tensile failure mode.

**Stability failure** is the most important mode of failure for slender walls. It occurs when significant lateral deflection takes place before crushing of the face shell or yield of the rebar. Walls subjected to higher load levels and with higher slenderness ratios are vulnerable. Failure load prediction based on section capacity cannot predict the stability or buckling failure. Support Stiffness at the bottom increases the capacity of the wall by inducing double curvature, which increases the elastic buckling load. However, as the load increases in the presence of high support restraint, the risk of cross-sectional failure becomes significant. This also promotes the development of material nonlinearity, thus reducing the wall stiffness, which in turn affects the wall stability.

## **6.7 Results and Discussions**

### **6.7.1 Effect of Support Stiffness**

As expected the support stiffness influences the load carrying capacity of masonry load bearing walls and also affects the flexural rigidity of the walls. Figure 6.5 exhibits the trend of increase in normalized axial load capacity under influence of support stiffness. There is 12.4%, 14.6% and 33.5% increase in load carrying capacity when support stiffness is increased from 0 kN-m/rad to 500 kN/m/rad, 1000 kN/mrad and 5000 kN/mrad respectively ( $e/t=0.1$ ,  $h/t=30$ ). For the same

walls at  $e/t=0.33$ , the increase in load carrying capacity becomes more significant showing 38.6%, 44% and 64.8% increase under the influence of support stiffness of 500 kN-m/rad, 1000 kN-m/rad and 5000 kN-m/rad support stiffness as compared to the case where no support stiffness (0 kN-m/rad) is applied.

### ***Limit of fixity***

Figure 6.5 demonstrates that there is no considerable increase in load when the support stiffness is increased from 5000 kN-m/rad to 10000 kN-m/rad, i.e. 100% increase in magnitude of support stiffness. For example at  $e/t=0.1$ , 3-cores grouted walls it is noticed that there is only 2.5 % difference in maximum axial load achieved in between support stiffness 5000 kN-m/rad and 10,000 kN-m/rad and wall behavior appears similar under both types of support stiffness, which shows that the former can be considered as the limit of fixity of masonry block wall support.

### ***Load deflection response***

Figure 6.6 shows the effect of various levels of support stiffness on load deflection response of partially grouted (3-cores grouted) wall specimens loaded with  $e/t=0.1$  and with various slenderness ratios. Differences in stiffness and load carrying capacity are low between support stiffness of 5000 kN-m/rad and 10,000 kN-m/rad.

The load deflection responses in Figure 6.6 show that the support stiffness enhances the performance of walls by controlling deflections. Figure 6.7, shows that at failure the normalized mid-span deflection decreases as support stiffness increases. This is because the location of maximum deflection moves up and curvature of the wall transforms from single (with no support stiffness) to double curvature (with increased support stiffness). This effect is common in all slenderness ratios accompanied with  $e/t=0.1$ . This is also exhibited by deflected

geometry of the walls at failure, Figure 6.8 shows the deflection of wall at failure loaded with  $e/t=0.1$  and having  $h/t=30, 36$  and  $42$ .

### ***Bending moments***

To further highlight the bending characteristics of the walls a number of bending moment diagrams at failure are plotted in Figure 6.9. The maximum bending moment moves up with increase in support stiffness. The compressive stresses become higher in the top portion of the wall height. At the point of maximum bending moment along the height of the wall the plastic strains at extreme tension and compression faces of the wall cross-section were examined and it is noted that with increasing support stiffness the compressive plastic strains are increased.

### ***Slenderness ratio***

As the point of inflexion moves up with an increase in support stiffness less of the wall close to mid-height has lower stiffness. Thus, cracks are delayed and the moment of inertia remains high on larger segments of the wall. At ultimate load in case of walls with  $h/t=30$  loaded with  $e/t=0.1$  having no support stiffness, at point of maximum bending moment the wall cross-section is subjected to both tensile cracking and compressive plastic strains. When the support stiffness is increased for the same wall, an increase in the magnitude of the equivalent compressive plastic strain corresponding to maximum bending moment position is observed without any considerable increase in tensile cracking strain. This indicates that for walls with intermediate slenderness ( $h/t=30$ ), increase in support stiffness prompts a compressive failure mode with increased load carrying capacity.

For walls having  $h/t=36$  and with support stiffness in the range from zero to  $500$  kN-m/rad, stability failure occurs, as the level of support stiffness increases to  $1000$  kN-m/rad a transition stage occurs and equivalent plastic strain at the position of maximum bending moment along the height of the wall located at

extreme fiber in the cross-section is observed in both the compressive and tensile zone while beyond 1000 kN-m/rad the failure mode transforms into pure compressive failure and no plastic strains show in the tensile zone.

Walls with  $h/t=36$  show the same behavior as was the case with  $h/t=30$ ; the deflection is decreased as support stiffness is increased. The point of maximum deflection moves up above the mid height point, as shown in deflected shape of the wall at failure in Figure 6.8(b). In case of very tall walls i.e. walls with  $h/t=42$ , with support stiffness in the range from 0 kN-m/rad to 1000 kNm/rad, the failure is caused by excessive deflections and higher tensile stresses. It is observed that within this range of support stiffness the walls stability failure is delayed allowing the walls to undergo excessive deflections and higher tensile stresses with higher load capacity. The increase in support stiffness beyond 1000 kN-m/rad influences the failure mode of these walls and material non-linearity is observed in both tensile and compressive zones indicating the change of failure mode from stability to combined tension-compression failure. Figure 6.10 provides plots of equivalent compressive plastic strain corresponding to maximum bending moment point located at extreme tension and compression faces of the wall cross-section, against support stiffness for walls with  $h/t=30, 36, 42$  and  $e/t=0.1$ . Walls with lower  $h/t$  ratios (i.e.  $h/t=30$  and  $36$ ) are subjected to progressive increase in compression plasticity with increasing support stiffness as compared to walls having  $h/t=42$ , which do not show any plasticity in compression up to a certain level of support stiffness (i.e. 1000 kN-m/rad).

At constant slenderness ratio, walls loaded with  $e/t=0.33$  are exposed to more geometric linearity as compared to walls loaded with  $e/t=0.1$ . The level of geometric non-linearity is enhanced when a higher slenderness ratio is combined with higher load eccentricity. In this case support stiffness is observed to be effective in controlling the non-linearity of the system. Figure 6.11 shows the response of partially grouted walls at various levels of support stiffness for  $h/t=30, 36$  &  $42$  loaded at  $e/t=0.33$ . Comparing Figure 6.11(a), 6.11(b) and 6.11(c)

shows that when the level of support stiffness is increased it not only improves the load carrying capacity but also controls the higher deflections associated with higher slenderness and higher load eccentricity. This improved non-linear response improves the behavior of walls at failure. Figure 6.12 demonstrates the deflection of walls along the height at failure. The bending moment diagram at failure in Figure 6.13 further supports that the point of maximum bending moment moves up to incorporate the change in curvature because of effect of support stiffness.

Figure 6.14 shows the trend of normalized mid-span deflection plotted against various levels of support stiffness for  $h/t=30, 33, 36$  and  $42$ . It is important to mention that walls with  $h/t=33$  were tested in the experimental phase (as discussed in Chapter 3 of the thesis). Figure 6.14 shows that in the cases of  $h/t=30$  to  $h/t=36$  there is a significant influence of support stiffness on deflection at failure as compared to walls with  $h/t=42$ . Walls with  $h/t=42$ , do not show excessive material non-linearity and fail in an inelastic stability failure mode before support stiffness is fully mobilized.

### ***Inelastic strains***

Figure 6.15 compares the equivalent plastic strains corresponding to the point of maximum bending moment at the extreme tension and compression faces of the wall cross-section at various support stiffness values. It is shown that moderately slender walls (e.g.  $h/t=30$ ) are most likely to fail in combined compression-tension failure mode and material non-linearity governs in this case. With increasing support stiffness material non-linearity increases and in turn pushes the wall to experience progressive increase in tensile and compressive strain. As a result walls capability of bearing eccentric axial load increases.

Walls having  $h/t=36$  are subjected to combination of geometric and material non-linear effects under the influence of support stiffness. As shown in Figure 6.15(b),

support stiffness has an effect on failure mode of these walls. With support stiffness ranging from 0 kN-m/rad to 500 kN-m/rad the walls showed zero equivalent plastic strains and stability failure occurred in this range but at the support stiffness ranging from 1000 kN-m/rad and higher there was a consistent increase in equivalent compressive plastic strain combined with increasing tensile equivalent plastic strain, which shows that geometric non-linearity is controlled by the support stiffness and walls were able to undergo material non-linearity, causing the stability mode of failure to transform into compression-tension mode of failure.

In case of wall with  $h/t=42$  loaded with  $e/t=0.33$ , stability mode of failure was observed for all levels of support stiffness. However support stiffness was found to be effective in enhancing the load carrying capacity by controlling geometric non-linearity of the system. Figure 6.15(c) shows no plastic strain in compression, while equivalent tensile plastic strain increases. This indicates that support stiffness caused the wall to undergo more cracking, which is the cause of inelastic stability failure.

### ***Load moment interaction***

It is observed that support stiffness influences the load-moment interaction behavior of masonry block walls, as shown in Figure 6.16. An increase in support stiffness for partially grouted walls having  $h/t=30$  loaded with  $e/t=0.1$  caused the wall to switch from elastic stability failure to combined tension and compression failure by increasing the axial load carrying capacity and controlling the mid-span bending moment. Figure 6.17 shows the trend of change in bending moment with increasing support stiffness for different  $h/t$  ratios. When a lower eccentricity ratio is combined with lower slenderness ratio, walls are most likely to fail in combined tension and compression failure under the influence of increasing support stiffness and in this situation mid-span bending moment is controlled by support stiffness as shown in Figure 6.17(a). Walls with  $h/t=36$  loaded at various  $e/t$  ratios showed

influence of support stiffness on mid-span bending moment specially when level of support stiffness is increased from 500 kN-m/rad to 1000 kN-mrad and more, as illustrated in Figure 6.17(b). For the walls with higher slenderness ratios loaded with higher eccentricity ratios support stiffness does not seem to influence the bending moment at mid-span and almost same magnitude is observed, as shown in Figure 6.17(c).

### ***Grouting***

Unlike compression members an increased amount of grouting does not increase the axial load capacity of slender masonry load bearing walls, loaded under higher eccentricity. Although the effective cross-sectional area is increased, the wall fails because of geometric non-linear effects before the cross-sectional strength is reached. But the current study shows that under the influence of support stiffness the increase in amount of grouting may increase the axial load carrying capacity if the wall is loaded under low  $e/t$  ratio and with higher support stiffness.

Amount of grouting is not an independent parameter and any change in amount of grouting is reflected in the prism compressive strength and as well as in the modulus of elasticity of masonry assemblage. Table 6.1 shows that  $f'_m$  of a solid concrete block masonry assemblage is less than that of a hollow wall. This reduction also affects the modulus of elasticity as represented by equation 6.1. Therefore, in some of the cases in the current study the walls which are subjected to geometric non-linearity are adversely affected by the increase in grouting.

As discussed above the amount of grouting is not an independent parameter. Therefore to show the effect of grouting on behavior of the walls the load deflection response plotted in Figure 6.18 through Figure 6.24, is not normalized by the cross-sectional area of the wall. In the previous cases since the response was plotted for a constant amount of grouting, normalization did not affect the behavior.

For walls with no support stiffness, having intermediate height ( $h/t=30$ ) as well as for very tall walls ( $h/t=36$  and  $42$ ) loaded with  $e/t=0.1$ , increase in amount of grouting did not significantly increase the load carrying capacity of the walls. However, with same conditions when support stiffness was increased from  $0$  kN-m/rad to  $1000$  kN-m/rad and  $5000$  kN-m/rad the effect of increased amount of grouting became significant and load carrying capacity of the same wall increased and the increase is estimated as  $50.5\%$  and  $74.6\%$ . Figure 6.18 shows a substantial increase in load carrying capacity when both support stiffness and grouting amount are increased. This effect is more significant when  $NC=5$  is combined with support stiffness of  $1000$  kN-m/rad and  $5000$  kN-m/rad. The possible reason of the increase in load carrying capacity of these walls is that when grouting amount is substantially increased the increase in cross-sectional area enhances the axial load carrying capacity of the wall.

It is observed that when support stiffness is combined with increased amount of grouting the effect of support stiffness on non-linear characteristics of the walls also becomes significant. In Figure 6.19 the equivalent plastic strains corresponding to maximum bending moment along the height of the wall and at compressive and tensile faces of the wall cross-section are shown. It is observed that with  $NC=5$  the equivalent compressive plastic strain increases with increasing support stiffness and the wall failure transforms from stability to compressive failure mode. In case of walls with  $NC=3$ , the wall showed increase in equivalent compressive plastic strain and decrease in equivalent tensile plastic strain for the range of support stiffness from  $0$  kN-m/rad to  $1000$  kN-m/rad. Beyond  $1000$  kN-m/rad the equivalent tensile strain increased drastically and dominated the failure mode. As a result the wall does not experience significant increase in equivalent compressive plastic strain at support stiffness  $=5000$  kN-m/rad and a combined tension-compression failure occurred. In this case, although support stiffness was active, but because of lesser amount of grouting as compared to  $NC=5$ , the cross-sectional area was reduced and the wall was not able to sustain higher axial load.

In case of walls with  $h/t=36$  and  $e/t=0.1$  the same effect of amount of grouting was observed with increasing support stiffness as was shown by walls with  $h/t=30$  and  $e/t=0.1$ . Figure 6.20 shows the load deflection response of walls having  $h/t=36$  and loaded with  $e/t=0.1$  at various level of support stiffness and variable amount of grouting. An increase in load carrying capacity is observed when amount of grouting is increased with support stiffness. Because of higher slenderness ratio ( $h/t=36$ ), these walls are subjected to higher slenderness effects as compared to walls with  $h/t=30$ . Therefore, at support stiffness =0 kN-m/rad no compression plasticity is observed and stability failure occurred, as shown in Figure 6.21. In the range of support stiffness from 1000 kN-m/rad to 5000 kN-m/rad material non-linearity is developed and a substantial increase in equivalent compressive plastic strain is observed. In case of walls with  $NC=1$ , the equivalent tensile plastic strain was not observed at all levels of support stiffness, while in case of  $NC=3$ , increase in equivalent tensile plastic strain was observed up to level of support stiffness of 1000 kN-m/rad. Beyond 1000 kN-m/rad the strain started to decrease and at 5000 kN-m/rad it became zero.

The possible reason of reduction in equivalent tensile plastic strain is that walls with  $NC=1$  and  $NC=3$  have higher modulus of elasticity as compared to wall with  $NC=5$ , as given in Table 6.1. Therefore, under the influence of support stiffness, the geometric non-linearity of these walls was reduced because of increased modulus of elasticity and as a result tensile cracking was reduced.

The axial load carrying capacity of walls with  $h/t=36$  and  $h/t=30$  was influenced in a similar manner when load eccentricity ratio was increased from  $e/t=0.1$  to  $e/t=0.33$  for various combinations of grouting amount and support stiffness. Figure 6.22 shows that with no support stiffness the increased amount of grouting for wall with  $h/t=30$ , could not increase the load carrying capacity and stability failure was observed at  $NC=3$  and  $NC=5$ . However, the wall with  $NC=1$  showed comparatively higher axial load capacity (10.5% more than  $NC=5$  and 30.4% more than  $NC=3$ ) and existence of equivalent compressive and tensile plastic

strain was observed as shown in Figure 6.23. When support stiffness was increased to 1000 kN-m/rad, the increased amount of grouting with NC=5 became effective and the axial load capacity was enhanced, material non-linearity was also noticed as indicated in Figure 6.22. The same behavior was continued at support stiffness =5000 kN-m/rad.

Similar to wall with  $h/t=30$ , when loaded with  $e/t=0.33$  at no support stiffness the wall with  $h/t=36$  showed more axial load carrying capacity at NC=1 as compared to NC=3 and NC=5, however because of higher slenderness, a stability mode of failure was observed in all three cases. Figure 6.24 shows the load deflection response of wall with  $h/t=36$  under the influence of different combinations of support stiffness and grouting amount. With increase in support stiffness the effect of increased amount of grouting at NC=5 became active and an increase in axial load capacity was observed at support stiffness =1000 kN-m/rad and beyond. Figure 6.25 presents the plots of equivalent plastic strains of the walls with  $h/t=36$ , at failure corresponding to point of maximum bending moment at tensile and compressive faces of the wall cross-section.

Comparing the load deflection response of Figure 6.18, Figure 6.20 and Figure 6.22 and 6.24 it is concluded that increase in amount of grouting positively affects the load carrying capacity when it is combined with support stiffness, specially, for the walls loaded with low eccentricity ratio. When load eccentricity ratio is increased the geometric non-linearity starts to dominate the wall behavior, and increase in amount of grouting becomes comparatively less effective. However under the influence of support stiffness the wall manages to enter into material non-linearity and load carrying capacity is enhanced

### ***Load eccentricity ratio***

Load eccentricity ratio primarily affects the axial load carrying capacity by giving rise to detrimental effects of geometric non-linearity. This effect is found to be

same even under the influence of support stiffness. In the following, the behavior of walls loaded from low to high eccentricity ratios at various levels of support stiffness is discussed.

Figure 6.26 and Figure 6.27 show that with increasing load eccentricity ratio both walls ( $h/t=30$  and  $h/t=36$ ) experienced a significant drop in normalized axial load capacity at all levels of support stiffness. The plot between axial load carrying capacity versus support stiffness at  $e/t=0.1, 0.33$  and  $0.42$  shows that load eccentricity ratio ( $e/t$ ) dominated the behavior of the walls and caused the drastic decrease in load carrying capacity of the wall at higher  $e/t$  ratios at all level of support stiffness. Although support stiffness could not completely eliminate the detrimental effects developed by higher load eccentricity, it helped the wall to bear more load as compared to the wall having no support stiffness, as shown in Figure 6.28.

From the above discussion support stiffness not only affects the load carrying capacity but also influences the non-linear characteristic of the masonry load bearing walls in a systematic manner. The complete set of trends of parameters, highlighting the effect of different secondary parameters under the influence of support stiffness on behavior of the walls is discussed in detail in the next chapter.

### **6.7.2 Effect of Support Stiffness on Flexural Rigidity (EI)**

While effect of support stiffness on axial load capacity was the first target in this thesis, the effect on flexural rigidity (EI) was the second target. Wall flexural rigidity also indirectly influences the axial load capacity of the masonry load bearing wall by introducing combined effects of geometric and material parameters. It is anticipated that primary parameters such as support stiffness, slenderness ratio, load eccentricity, grouting amount and reinforcement ratio should affect the flexural rigidity.

The stress level in wall cross-section determines the amount of cracking and the level of inelasticity in the cross-section and is expected to influence the magnitude of flexural rigidity of the walls. In this study it is intended to estimate flexural rigidity of the walls under various combinations of primary and secondary parameters so that influence of the different parameters can be quantified. The differential equation discussed in Chapter 4 was employed to trace the history of flexural rigidity ( $EI$ ).

To study the effect of support stiffness on flexural rigidity of the walls, the history of flexural rigidity is plotted in Figures 6.29, 6.30 and 6.31 at every load increment for the walls having slenderness ratio  $h/t=30, 36$  and  $42$  at  $NC=3$ , with load eccentricity ratio  $e/t=0.1, 0.33$  and  $0.42$  under different levels of support stiffness. The plots show that support stiffness ranging from  $0$  kN-m/rad to  $1000$  kN-m/rad caused an increase in flexural rigidity with all other parameters kept constant. When support stiffness is increased from  $1000$  kN-m/rad to  $5000$  kN-m/rad, the material non-linearity in the compression zone caused a decrease in flexural rigidity. As discussed previously in this chapter support stiffness plays an important role in improving the non-linear characteristics of the walls by enhancing the capability to undergo more compressive plasticity (Figure 6.11). This may be the reason for the change in flexural rigidity under the influence of support stiffness.

Figures 6.29, 6.30 and 6.31 show that for all the cases the walls, initially, possessed high flexural rigidity, which was initially drastically reduced as wall started to take load and then gradually decreased almost at constant rate throughout the pre-peak load history until the wall approached the full axial load carrying capacity. At this point a rapid decrease in flexural rigidity is observed, which continued to drop with increasing deflection and decreasing load. The rapid decrease in wall rigidity close to peak load and beyond is clearly inelastic.

The flexural rigidity corresponding to failure load is termed as effective flexural rigidity as explained in Chapter 4 of the thesis. In Figure 6.32 the effective flexural rigidity is plotted against support stiffness. Increasing the level of support stiffness for all slenderness ratios up to a support stiffness of 1000 kN-m/rad caused an increase in effective flexural rigidity. However, a decrease in effective flexural rigidity is observed at support stiffness 5000 kN-m/rad because of the associated material non-linearity effect discussed above. For all slenderness ratios, at  $e/t=0.1$  the effect of support stiffness remains unchanged. A considerable decrease in effective flexural rigidity is observed in Figure 6.32, when the load eccentricity ratio is increased beyond  $e/t=0.1$  at constant slenderness ratio and at constant support stiffness. It then concluded that an increase in load eccentricity ratio, generally, has a detrimental effect on flexural rigidity. However, the trend under the influence of support stiffness remains unchanged at all load eccentricity ratios, so that the support stiffness effect could be arguably separated.

At constant slenderness and constant level of support stiffness, walls with  $h/t=30$  and  $h/t=36$  show lower effective rigidity at  $e/t=0.42$  as compared to  $e/t=0.33$ . For the wall with highest slenderness, i.e.  $h/t=42$  at  $e/t=0.42$ , the trend is not shown because the highly unstable behavior at this high eccentricity ratio it was not possible to converge on reasonable values of the effective flexural rigidity from a very erratic load deformation response.

The above discussion showed that the flexural rigidity of the masonry load bearing block wall is significantly affected by level of support stiffness, slenderness ratio and load eccentricity ratio. It is important to mention that support stiffness positively and consistently affected the flexural rigidity and as a result an increase in level of support stiffness caused the progressive increase in axial load carrying capacity of the wall. To express the relationship of all parameters in context of flexural rigidity more trends with detailed discussion are presented in Chapter 7 of the thesis.

## **6.8 Behavior of Masonry Walls with no Support Stiffness**

A separate study was performed to report the behavior of masonry load bearing walls at no support stiffness. The purpose of the study is to describe the individual effect of some of the secondary parameters without any influence of support stiffness. As this section emphasizes the wall behavior with no consideration of support stiffness, it also further validates that the numerical model used in the current study is successfully able to predict masonry load bearing wall behavior similar to the findings of previous research work.

It is a well established fact that for stocky walls amount of grouting plays an important role in increasing the axial load capacity. The current numerical model was used to study the special case of a stocky wall having  $h/t=18$ , to further highlight the effect of increased amount of grouting at no support stiffness. Figure 6.33 shows the load deflection plot at  $h/t=18$ ,  $e/t=0.1, 0.33, 0.42$  and with 0 kN-m/rad support stiffness by combining different amount of grouting. It is observed that amount of grouting significantly influenced the load carrying capacity at low  $e/t$  ratio. The behavior of stocky walls at smaller eccentricity ratio is more close to the behavior of compression members and these walls unlikely to fail in stability mode of failure, therefore when loaded at  $e/t=0.1$ , with  $NC=5$  the increased cross-sectional area resisted the cross-sectional failure and as a result higher axial capacity was observed. When increased amount of grouting is accompanied by increasing load eccentricity ratio a progressive decrease in axial load carrying capacity was observed. At  $e/t=0.1$  the maximum increase in axial load capacity of 35.8% and 74.8% was observed when grouting amount is increased from  $NC=1$  to  $NC=3$  and  $NC=5$  respectively, for the same increase in grouting amount at  $e/t=0.33$  the increase in load capacity dropped to 25.7% and 31.85% respectively, and at the highest load eccentricity ratio,  $e/t=0.42$  only 5% and 22% increase in axial load capacity was obtained.

The possible reasons of decrease in load capacity at high  $e/t$  ratios are the inclusion of slenderness effects and the non-uniform stress distribution over the wall cross-section. When load eccentricity ratio is increased, the load path moves away from the center of cross-section and the stress distribution does not remain uniform resulting in failure of the wall at smaller load level without utilizing its full cross-sectional strength and the increased cross-sectional area because of effect of increased amount of grouting remains inactive in increasing the axial load capacity of the wall.

As discussed earlier, the increase in slenderness ratio enhances the non-linear geometric effects and because of secondary effects tall masonry walls are more susceptible to elastic buckling failure. Higher slenderness ratio causes the geometric failure and in post-buckling zone material failure occurs. To further highlight the slenderness effects the behavior of the wall was studied at no support stiffness from stocky to very tall walls at  $NC=3$ . Figure 6.40 illustrates the normalized load deflection response at  $h/t=18, 30, 36$  and  $42$  under different  $e/t$  ratios and at zero support stiffness.

It is evident from the plots that slenderness ratio effects the load carrying capacity of the walls by increasing out-of-plane deflection at mid span. This effect appears more significant for the walls subjected to higher load eccentricity. Figure 6.33 (a) shows that wall with  $h/t=18$  gives higher axial load carrying capacity as compared to wall with  $h/t=42$ , mainly because of the reason that wall with  $h/t=18$  is subjected to compressive failure and goes up to 70% of cross-sectional axial capacity of the wall as compared to wall with  $h/t=42$ , which is subjected to excessive out-of-plan deflection intercepting the load carrying capacity and making the wall able to attain only 24% of the cross-sectional strength.

Walls subjected to higher load eccentricity and increased slenderness ratio (Figure 6.34(b) and Figure 6.34(c)) fail at low load level and lower out-of-plan deflection confirming the fact that combination of higher load eccentricity and higher

slenderness ratio change the failure mode to a stability type failure. For example normalized deflection in case of  $e/t=0.1$  for the wall with  $h/t=42$  is 0.196 while for the same wall with  $e/t=0.42$  normalized deflection drops to 0.060.

Figure 6.34 shows that there is a significant increase in load carrying capacity with decrease in slenderness ratio. The plot for  $e/t=0.1$  and  $h/t=30$  shows 48.5 % more load carrying capacity as compared to the plot with  $h/t=42$ . The wall with  $h/t=36$  show an increase in load of 28.7% as compared to wall with  $h/t=42$ . In Figure 6.35 the effect of slenderness on axial load capacity is plotted, the trend shows that at higher eccentricity ratios the drop in axial load capacity is vital with increasing slenderness ratio.

**Table 6.1 (a) Combination of different parameters at support stiffness = 0kN-m/rad**

NC	R kN-m/rad	h/t	L (mm)	e/t	f <sub>m</sub> (MPa)	I (mm <sup>4</sup> )	A <sub>c</sub> (mm <sup>2</sup> )	E (MPa)	A <sub>s</sub> (mm <sup>2</sup> )
1	0	42	7980	0.1	9.6	4.68E+08	9.83E+04	8160	200
3	0	42	7980	0.1	8.4	5.20E+08	1.44E+05	7140	600
5	0	42	7980	0.1	7.5	5.72E+08	1.90E+05	6375	1000
1	0	42	7980	0.33	9.6	4.68E+08	9.83E+04	8160	200
3	0	42	7980	0.33	8.4	5.20E+08	1.44E+05	7140	600
5	0	42	7980	0.33	7.5	5.72E+08	1.90E+05	6375	1000
1	0	42	7980	0.42	9.6	4.68E+08	9.83E+04	8160	200
3	0	42	7980	0.42	8.4	5.20E+08	1.44E+05	7140	600
5	0	42	7980	0.42	7.5	5.72E+08	1.90E+05	6375	1000
1	0	36	6840	0.1	9.6	4.68E+08	9.83E+04	8160	200
3	0	36	6840	0.1	8.4	5.20E+08	1.44E+05	7140	600
5	0	36	6840	0.1	7.5	5.72E+08	1.90E+05	6375	1000
1	0	36	6840	0.33	9.6	4.68E+08	9.83E+04	8160	200
3	0	36	6840	0.33	8.4	5.20E+08	1.44E+05	7140	600
5	0	36	6840	0.33	7.5	5.72E+08	1.90E+05	6375	1000
1	0	36	6840	0.42	9.6	4.68E+08	9.83E+04	8160	200
3	0	36	6840	0.42	8.4	5.20E+08	1.44E+05	7140	600
5	0	36	6840	0.42	7.5	5.72E+08	1.90E+05	6375	1000
1	0	30	5700	0.1	9.6	4.68E+08	9.83E+04	8160	200
3	0	30	5700	0.1	8.4	5.20E+08	1.44E+05	7140	600
5	0	30	5700	0.1	7.5	5.72E+08	1.90E+05	6375	1000
1	0	30	5700	0.33	9.6	4.68E+08	9.83E+04	8160	200
3	0	30	5700	0.33	8.4	5.20E+08	1.44E+05	7140	600
5	0	30	5700	0.33	7.5	5.72E+08	1.90E+05	6375	1000
1	0	30	5700	0.42	9.6	4.68E+08	9.83E+04	8160	200
3	0	30	5700	0.42	8.4	5.20E+08	1.44E+05	7140	600
5	0	30	5700	0.42	7.5	5.72E+08	1.90E+05	6375	1000
1	0	18	3420	0.1	9.6	4.68E+08	9.83E+04	8160	200
3	0	18	3420	0.1	8.4	5.20E+08	1.44E+05	7140	600
5	0	18	3420	0.1	7.5	5.72E+08	1.90E+05	6375	1000
1	0	18	3420	0.33	9.6	4.68E+08	9.83E+04	8160	200
3	0	18	3420	0.33	8.4	5.20E+08	1.44E+05	7140	600
5	0	18	3420	0.33	7.5	5.72E+08	1.90E+05	6375	1000
1	0	18	3420	0.42	9.6	4.68E+08	9.83E+04	8160	200
3	0	18	3420	0.42	8.4	5.20E+08	1.44E+05	7140	600
5	0	18	3420	0.42	7.5	5.72E+08	1.90E+05	6375	1000

**Table 6.1 (b) Combination of Different Parameters at Support Stiffness =500 and 1000 kN-m/rad**

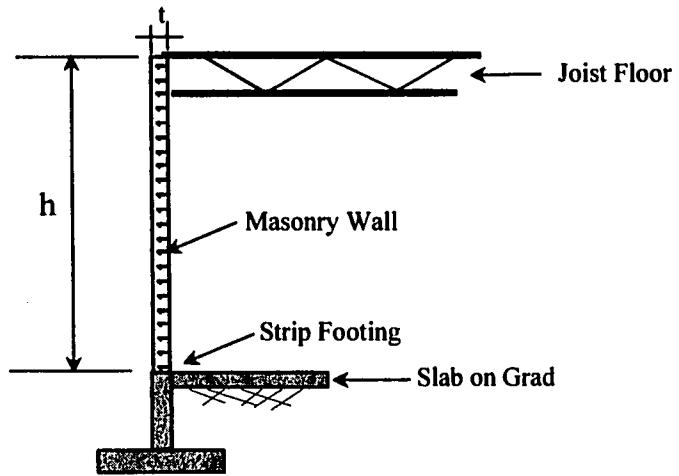
NC	R kN-m/rad	h/t (mm)	L	e/t	f <sub>m</sub> MPa	I (mm <sup>4</sup> )	A <sub>e</sub> (mm <sup>2</sup> )	E MPa	A <sub>s</sub> mm <sup>2</sup>
3	500	42	7980	0.1	8.4	5.20E+08	1.44E+05	7140	600
3	500	42	7980	0.33	8.4	5.20E+08	1.44E+05	7140	600
3	500	42	7980	0.42	8.4	5.20E+08	1.44E+05	7140	600
3	500	36	6840	0.1	8.4	5.20E+08	1.44E+05	7140	600
3	500	36	6840	0.33	8.4	5.20E+08	1.44E+05	7140	600
3	500	36	6840	0.42	8.4	5.20E+08	1.44E+05	7140	600
3	500	30	5700	0.1	8.4	5.20E+08	1.44E+05	7140	600
3	500	30	5700	0.33	8.4	5.20E+08	1.44E+05	7140	600
3	500	30	5700	0.42	8.4	5.20E+08	1.44E+05	7140	600
1	1000	42	7980	0.1	9.6	4.68E+08	9.83E+04	8160	200
3	1000	42	7980	0.1	8.4	5.20E+08	1.44E+05	7140	600
5	1000	42	7980	0.1	7.5	5.72E+08	1.90E+05	6375	1000
1	1000	42	7980	0.33	9.6	4.68E+08	9.83E+04	8160	200
3	1000	42	7980	0.33	8.4	5.20E+08	1.44E+05	7140	600
5	1000	42	7980	0.33	7.5	5.72E+08	1.90E+05	6375	1000
3	1000	42	7980	0.42	8.4	5.20E+08	1.44E+05	7140	600
1	1000	30	5700	0.1	9.6	4.68E+08	9.83E+04	8160	200
3	1000	30	5700	0.1	8.4	5.20E+08	1.44E+05	7140	600
5	1000	30	5700	0.1	7.5	5.72E+08	1.90E+05	6375	1000
1	1000	30	5700	0.33	9.6	4.68E+08	9.83E+04	8160	200
3	1000	30	5700	0.33	8.4	5.20E+08	1.44E+05	7140	600
5	1000	30	5700	0.33	7.5	5.72E+08	1.90E+05	6375	1000
3	1000	30	5700	0.42	8.4	5.20E+08	1.44E+05	7140	600
1	1000	36	6840	0.1	9.6	4.68E+08	9.83E+04	8160	200
3	1000	36	6840	0.1	8.4	5.20E+08	1.44E+05	7140	600
5	1000	36	6840	0.1	7.5	5.72E+08	1.90E+05	6375	1000
1	1000	36	6840	0.33	9.6	4.68E+08	9.83E+04	8160	200
3	1000	36	6840	0.33	8.4	5.20E+08	1.44E+05	7140	600
5	1000	36	6840	0.33	7.5	5.72E+08	1.90E+05	6375	1000
3	1000	36	6840	0.42	8.4	5.20E+08	1.44E+05	7140	600

**Table 6.1 (c) Combination of different parameters at support stiffness =5000kN-m/rad**

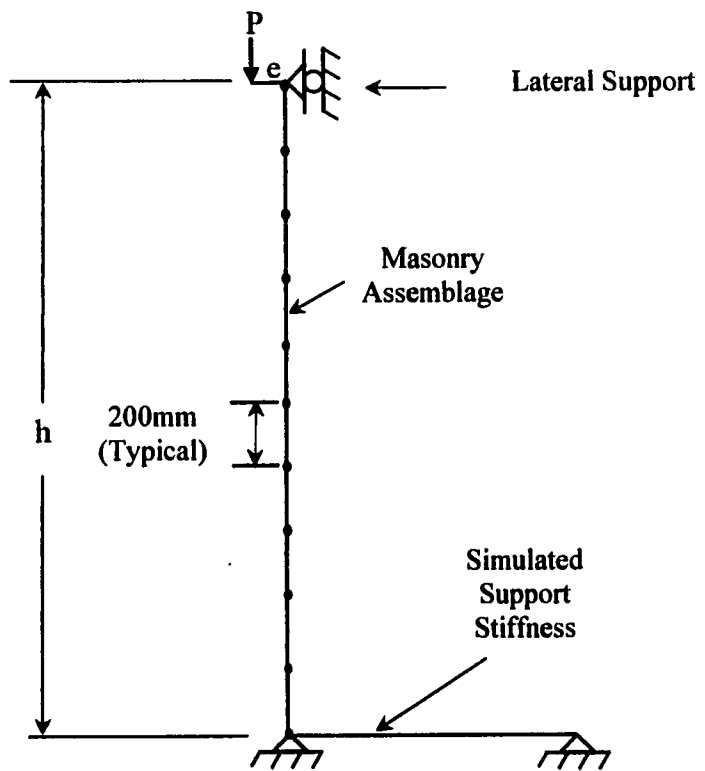
NC	R	h/t	L	e/t	f <sub>m</sub>	I	A <sub>c</sub>	E	A <sub>s</sub>
	kN-m/rad				MPa	mm <sup>4</sup>	mm <sup>2</sup>	(MPa)	mm <sup>2</sup>
1	5000	42	7980	0.1	9.6	4.68E+08	9.83E+04	8160	200
3	5000	42	7980	0.1	8.4	5.20E+08	1.44E+05	7140	600
5	5000	42	7980	0.1	7.5	5.72E+08	1.90E+05	6375	1000
1	5000	42	7980	0.33	9.6	4.68E+08	9.83E+04	8160	200
3	5000	42	7980	0.33	8.4	5.20E+08	1.44E+05	7140	600
5	5000	42	7980	0.33	7.5	5.72E+08	1.90E+05	6375	1000
1	5000	42	7980	0.42	9.6	4.68E+08	9.83E+04	8160	200
3	5000	42	7980	0.42	8.4	5.20E+08	1.44E+05	7140	600
5	5000	42	7980	0.42	7.5	5.72E+08	1.90E+05	6375	1000
1	5000	36	6840	0.1	9.6	4.68E+08	9.83E+04	8160	200
3	5000	36	6840	0.1	8.4	5.20E+08	1.44E+05	7140	600
5	5000	36	6840	0.1	7.5	5.72E+08	1.90E+05	6375	1000
1	5000	36	6840	0.33	9.6	4.68E+08	9.83E+04	8160	200
3	5000	36	6840	0.33	8.4	5.20E+08	1.44E+05	7140	600
5	5000	36	6840	0.33	7.5	5.72E+08	1.90E+05	6375	1000
1	5000	36	6840	0.42	9.6	4.68E+08	9.83E+04	8160	200
3	5000	36	6840	0.42	8.4	5.20E+08	1.44E+05	7140	600
5	5000	36	6840	0.42	7.5	5.72E+08	1.90E+05	6375	1000
1	5000	30	5700	0.1	9.6	4.68E+08	9.83E+04	8160	200
3	5000	30	5700	0.1	8.4	5.20E+08	1.44E+05	7140	600
5	5000	30	5700	0.1	7.5	5.72E+08	1.90E+05	6375	1000
1	5000	30	5700	0.33	9.6	4.68E+08	9.83E+04	8160	200
3	5000	30	5700	0.33	8.4	5.20E+08	1.44E+05	7140	600
5	5000	30	5700	0.33	7.5	5.72E+08	1.90E+05	6375	1000
1	5000	30	5700	0.42	9.6	4.68E+08	9.83E+04	8160	200
3	5000	30	5700	0.42	8.4	5.20E+08	1.44E+05	7140	600
5	5000	30	5700	0.42	7.5	5.72E+08	1.90E+05	6375	1000
1	5000	18	3420	0.1	9.6	4.68E+08	9.83E+04	8160	200
3	5000	18	3420	0.1	8.4	5.20E+08	1.44E+05	7140	600
5	5000	18	3420	0.1	7.5	5.72E+08	1.90E+05	6375	1000
1	5000	18	3420	0.33	9.6	4.68E+08	9.83E+04	8160	200
3	5000	18	3420	0.33	8.4	5.20E+08	1.44E+05	7140	600
5	5000	18	3420	0.33	7.5	5.72E+08	1.90E+05	6375	1000
1	5000	18	3420	0.42	9.6	4.68E+08	9.83E+04	8160	200
3	5000	18	3420	0.42	8.4	5.20E+08	1.44E+05	7140	600
5	5000	18	3420	0.42	7.5	5.72E+08	1.90E+05	6375	1000

**Table 6.1 (d) Combination of different parameters at support stiffness =10,000kN-m/rad**

NC	R kN-m/rad	h/t	L	e/t	f <sub>m</sub> MPa	I mm <sup>4</sup>	A <sub>c</sub> mm <sup>2</sup>	E (MPa)	A <sub>s</sub> mm <sup>2</sup>
1	10000	42	7980	0.1	9.6	4.68E+08	9.83E+04	8160	200
3	10000	42	7980	0.1	8.4	5.20E+08	1.44E+05	7140	600
5	10000	42	7980	0.1	7.5	5.72E+08	1.90E+05	6375	1000
1	10000	42	7980	0.33	9.6	4.68E+08	9.83E+04	8160	200
3	10000	42	7980	0.33	8.4	5.20E+08	1.44E+05	7140	600
5	10000	42	7980	0.33	7.5	5.72E+08	1.90E+05	6375	1000
1	10000	42	7980	0.42	9.6	4.68E+08	9.83E+04	8160	200
3	10000	42	7980	0.42	8.4	5.20E+08	1.44E+05	7140	600
5	10000	42	7980	0.42	7.5	5.72E+08	1.90E+05	6375	1000
1	10000	36	6840	0.1	9.6	4.68E+08	9.83E+04	8160	200
3	10000	36	6840	0.1	8.4	5.20E+08	1.44E+05	7140	600
5	10000	36	6840	0.1	7.5	5.72E+08	1.90E+05	6375	1000
1	10000	36	6840	0.33	9.6	4.68E+08	9.83E+04	8160	200
3	10000	36	6840	0.33	8.4	5.20E+08	1.44E+05	7140	600
5	10000	36	6840	0.33	7.5	5.72E+08	1.90E+05	6375	1000
1	10000	36	6840	0.42	9.6	4.68E+08	9.83E+04	8160	200
3	10000	36	6840	0.42	8.4	5.20E+08	1.44E+05	7140	600
5	10000	36	6840	0.42	7.5	5.72E+08	1.90E+05	6375	1000
1	10000	30	5700	0.1	9.6	4.68E+08	9.83E+04	8160	200
3	10000	30	5700	0.1	8.4	5.20E+08	1.44E+05	7140	600
5	10000	30	5700	0.1	7.5	5.72E+08	1.90E+05	6375	1000
1	10000	30	5700	0.33	9.6	4.68E+08	9.83E+04	8160	200
3	10000	30	5700	0.33	8.4	5.20E+08	1.44E+05	7140	600
5	10000	30	5700	0.33	7.5	5.72E+08	1.90E+05	6375	1000
1	10000	30	5700	0.42	9.6	4.68E+08	9.83E+04	8160	200
3	10000	30	5700	0.42	8.4	5.20E+08	1.44E+05	7140	600
5	10000	30	5700	0.42	7.5	5.72E+08	1.90E+05	6375	1000
1	10000	18	3420	0.1	9.6	4.68E+08	9.83E+04	8160	200
3	10000	18	3420	0.1	8.4	5.20E+08	1.44E+05	7140	600
5	10000	18	3420	0.1	7.5	5.72E+08	1.90E+05	6375	1000
1	10000	18	3420	0.33	9.6	4.68E+08	9.83E+04	8160	200
3	10000	18	3420	0.33	8.4	5.20E+08	1.44E+05	7140	600
5	10000	18	3420	0.33	7.5	5.72E+08	1.90E+05	6375	1000
1	10000	18	3420	0.42	9.6	4.68E+08	9.83E+04	8160	200
3	10000	18	3420	0.42	8.4	5.20E+08	1.44E+05	7140	600
5	10000	18	3420	0.42	7.5	5.72E+08	1.90E+05	6375	1000



a) Masonry wall with actual boundary conditions



b) Finite element mesh

**Figure 6.1 Finite element modeling of masonry wall**

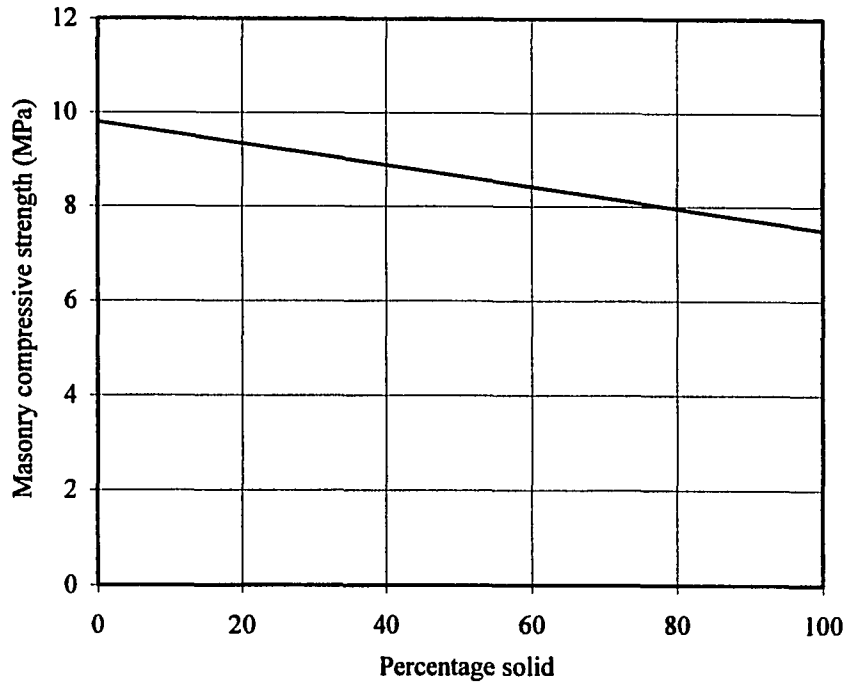
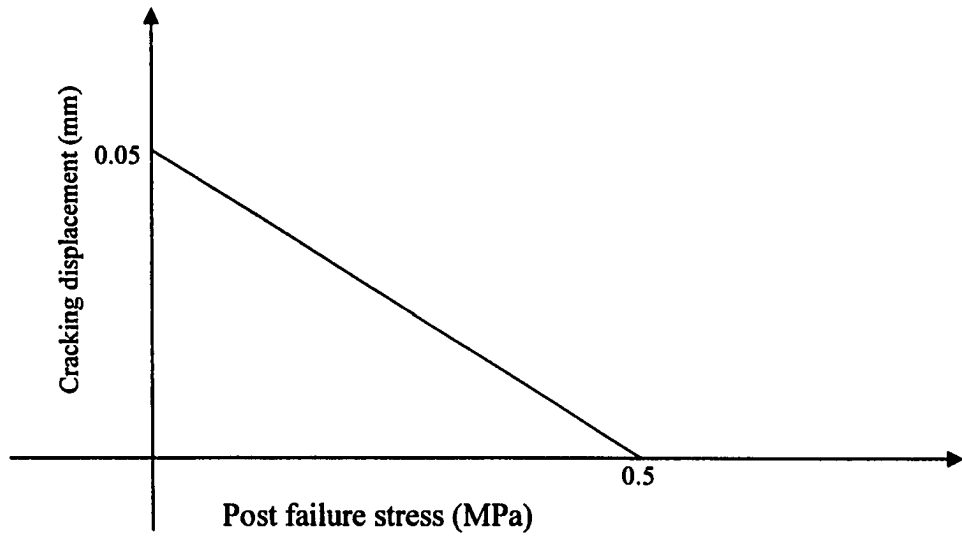
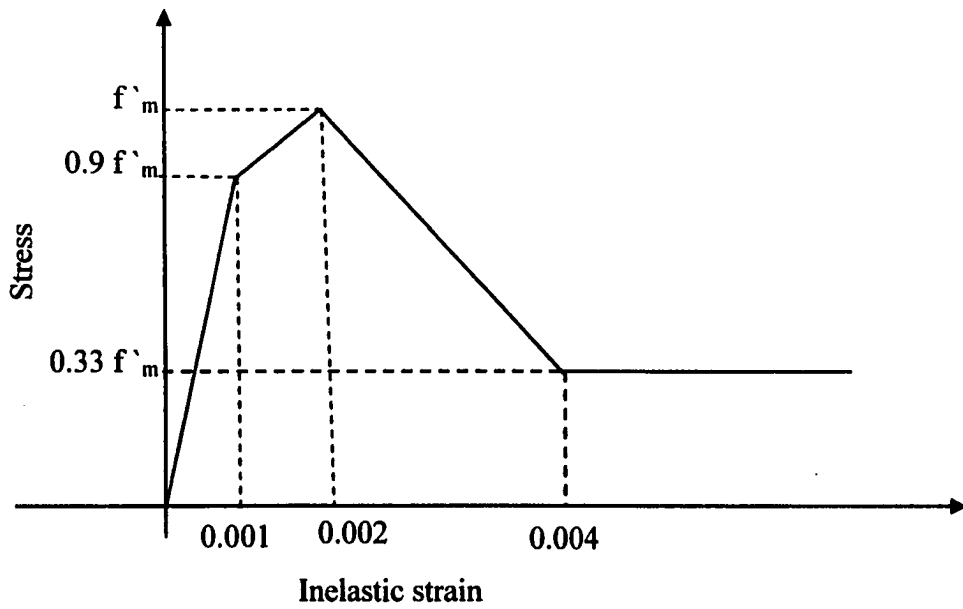


**Figure 6.2 Compressive strength of masonry for 15 MPa unit strength**



**(a) Typical stress-displacement curve**



**b) Typical stress-strain curve for compression**

**Figure 6.3 Typical material curves**

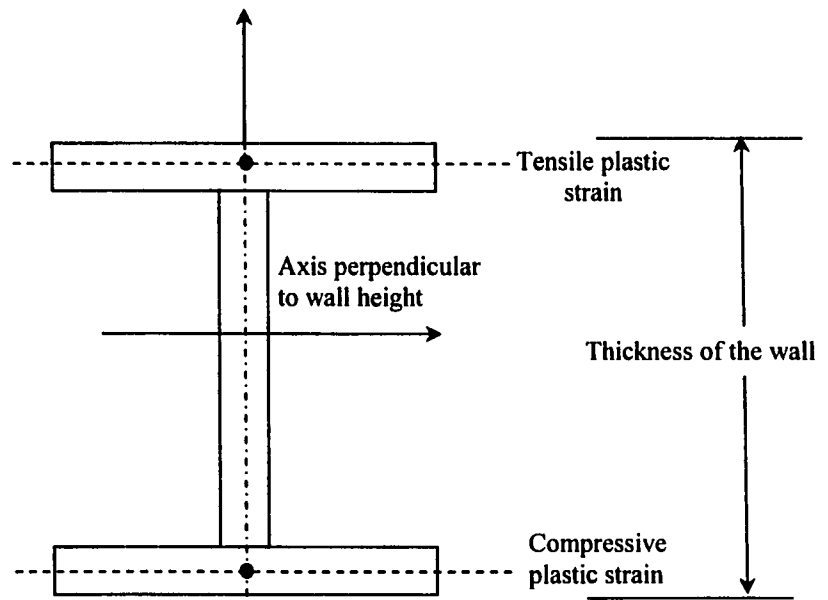
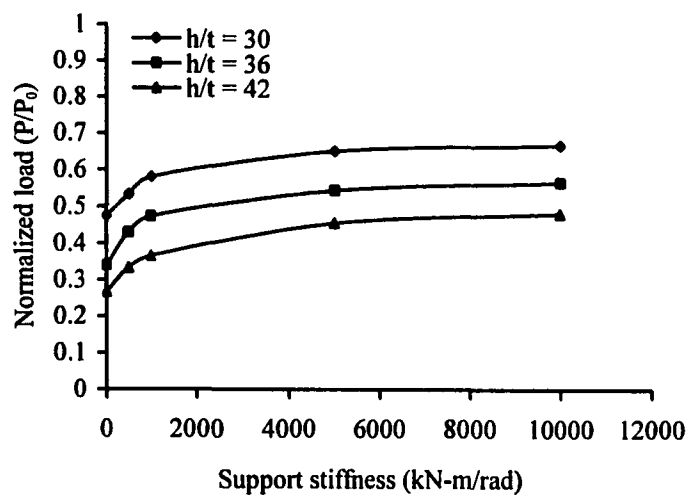
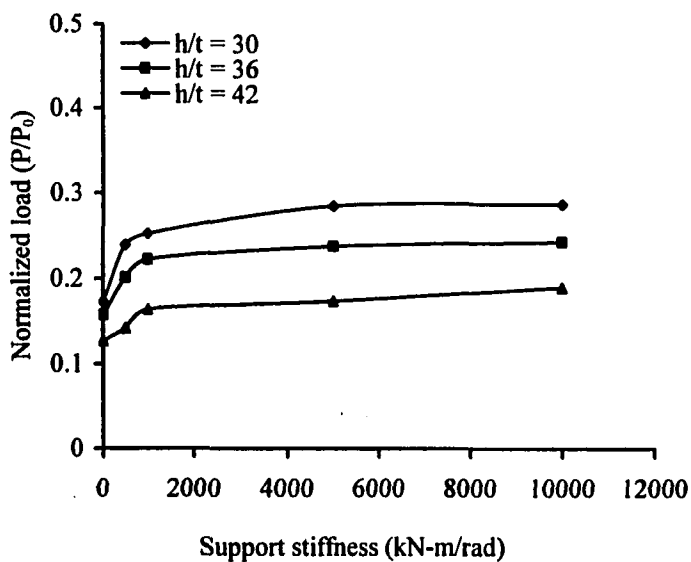


**Figure 6.4 Location of equivalent plastic strains in the wall cross-section**

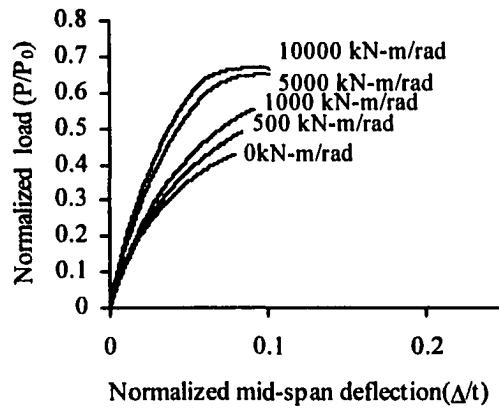


a)  $e/t = 0.1$

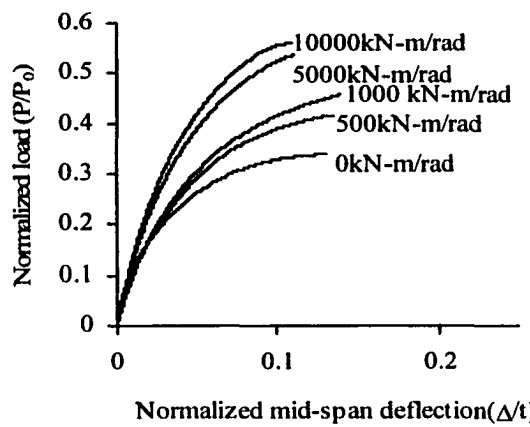


b)  $e/t = 0.33$

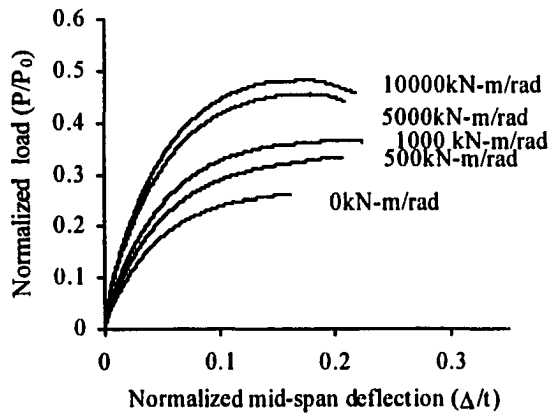
**Figure 6.5 Normalized axial load capacity versus support stiffness for variable slenderness ratio  $NC = 3$**



a)  $h/t = 30$



b)  $h/t = 36$



c)  $h/t = 42$

**Figure 6.6 Normalized load deflection response showing effect of support stiffness at various slenderness ratios ( $e/t = 0.1$ ,  $NC = 3$ )**

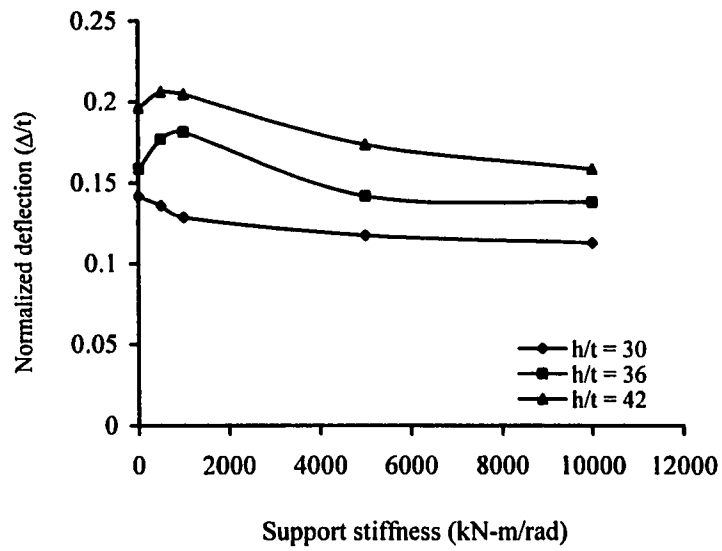
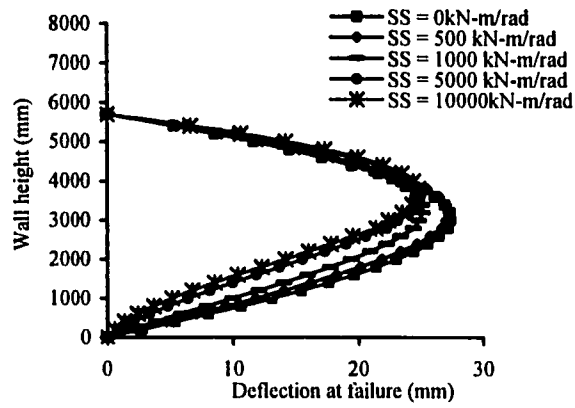
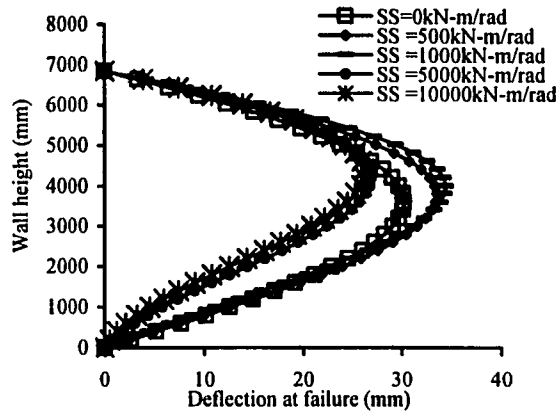


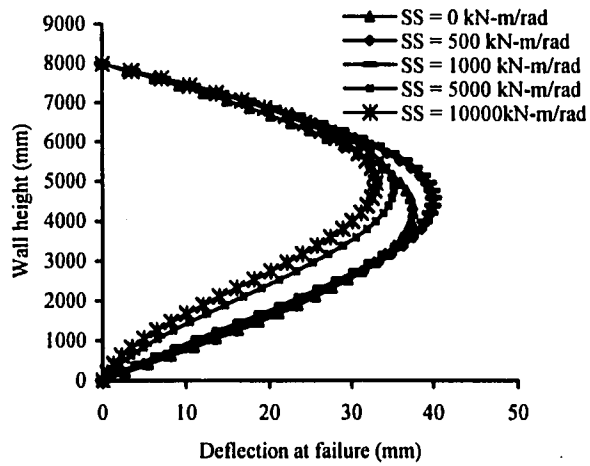
**Figure 6.7 Normalized mid-span deflection versus support stiffness at various slenderness ratios ( $e/t = 0.1$ ,  $NC = 3$ )**



a)  $h/t = 30$

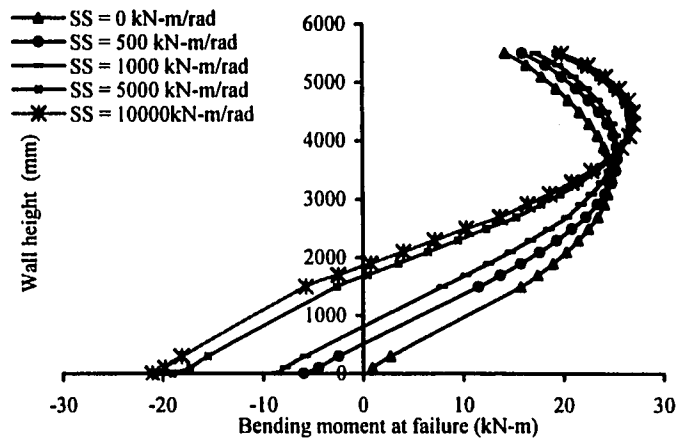


b)  $h/t = 36$

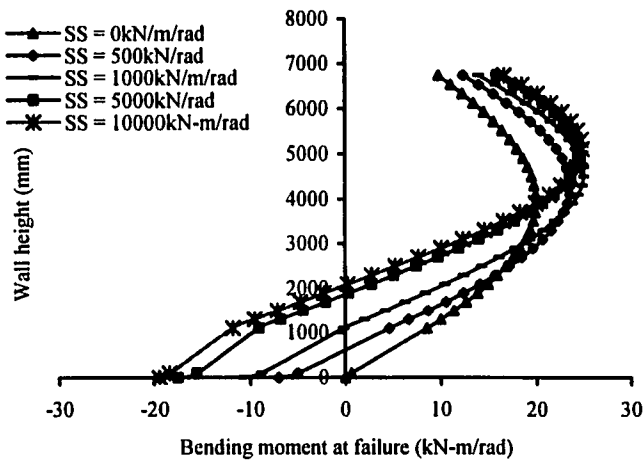


c)  $h/t = 42$

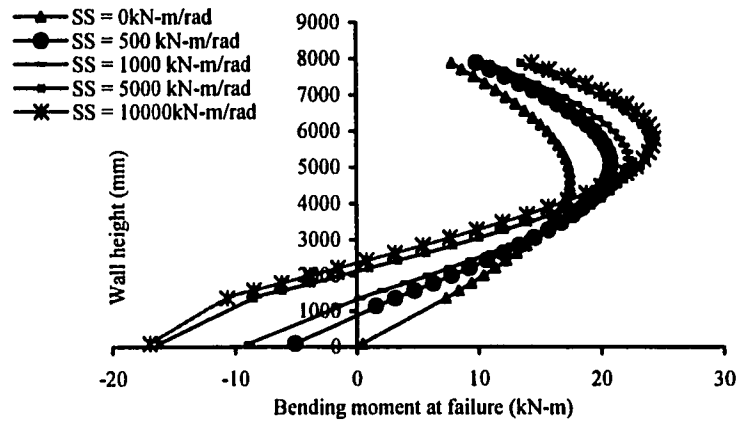
**Figure 6.8 Wall deflection at failure under influence of support stiffness at various slenderness ratios ( $e/t = 0.1$ ,  $NC = 3$ )**



a)  $h/t = 30$

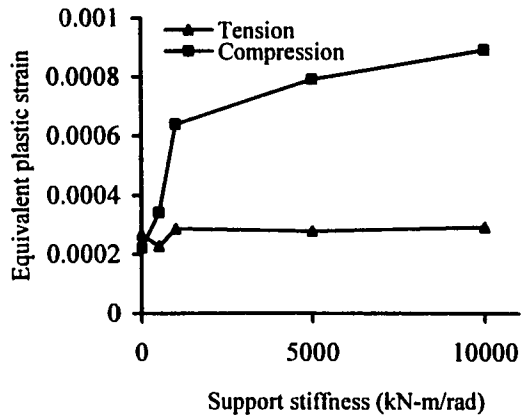


b)  $h/t = 36$

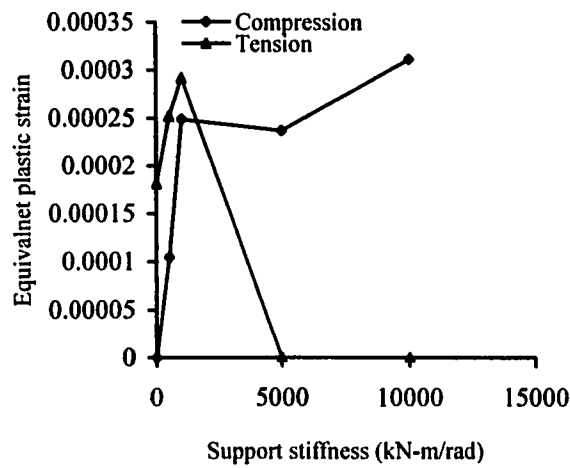


c)  $h/t = 42$

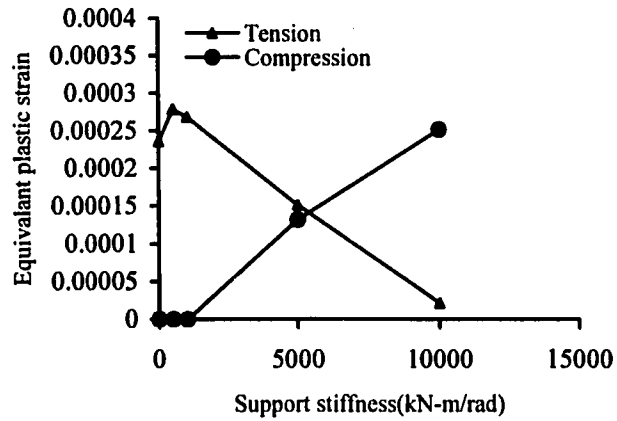
**Figure 6.9 Bending moment along the wall height at failure under influence of support stiffness at various slenderness ratios ( $e/t = 0.1$ ,  $NC = 3$ )**



a)  $h/t = 30$

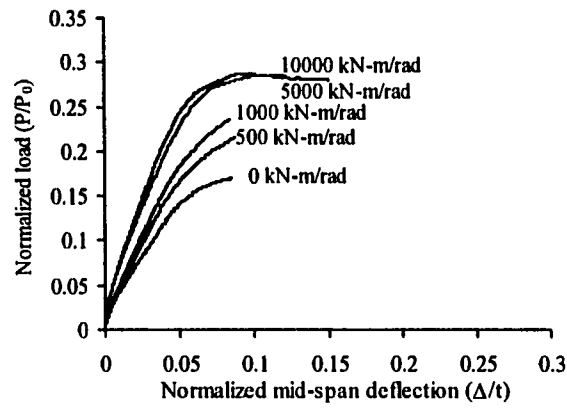


b)  $h/t = 36$

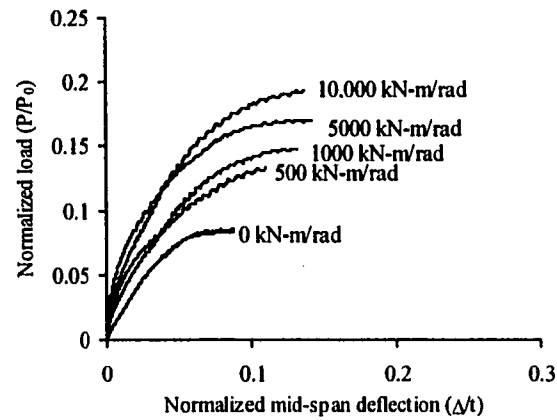


c)  $h/t = 42$

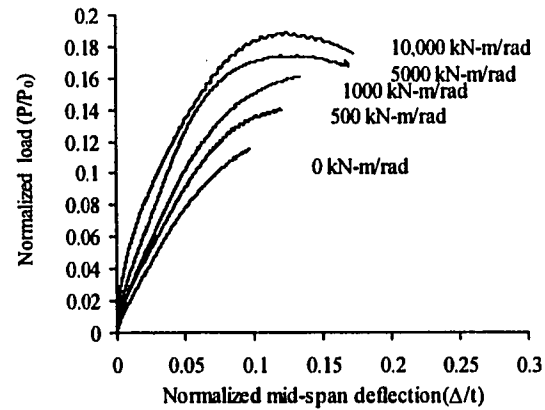
**Figure 6.10 Equivalent plastic strains versus support stiffness ( $e/t = 0.1$ ,  $NC = 3$ )**



a)  $h/t = 30$

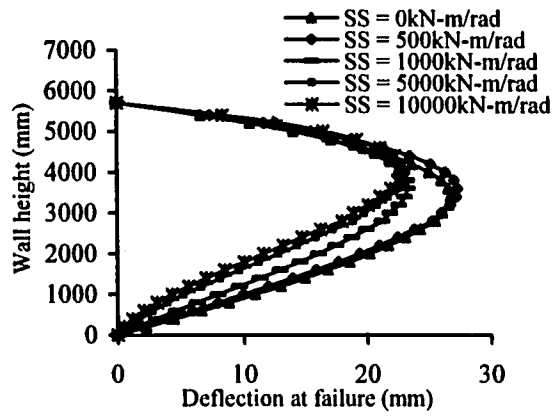


b)  $h/t = 36$

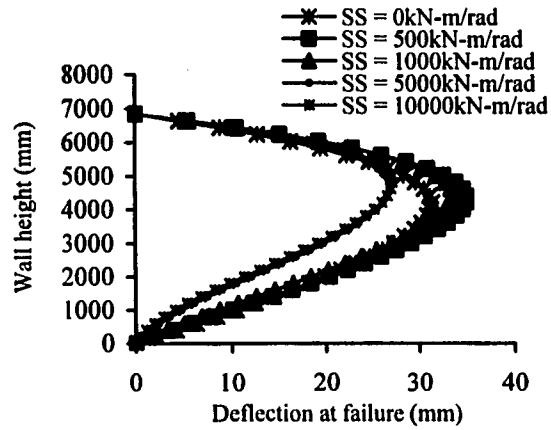


c)  $h/t = 42$

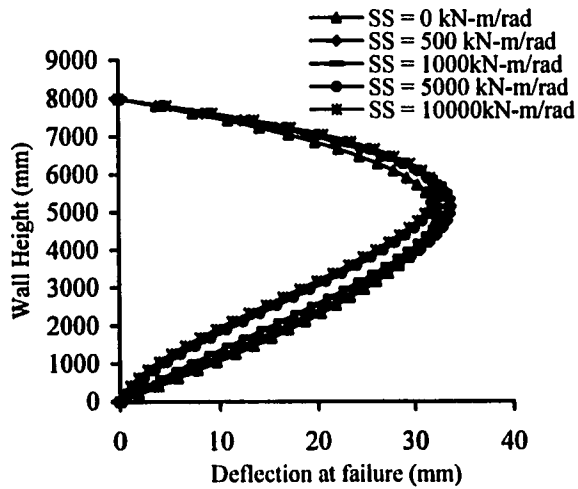
**Figure 6.11 Normalized load deflection response showing effect of support stiffness at various slenderness ratios ( $e/t = 0.33$ ,  $NC = 3$ )**



a)  $h/t = 30$

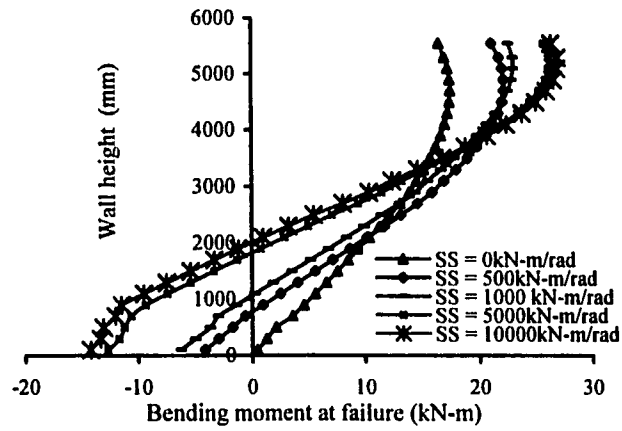


b)  $h/t = 36$

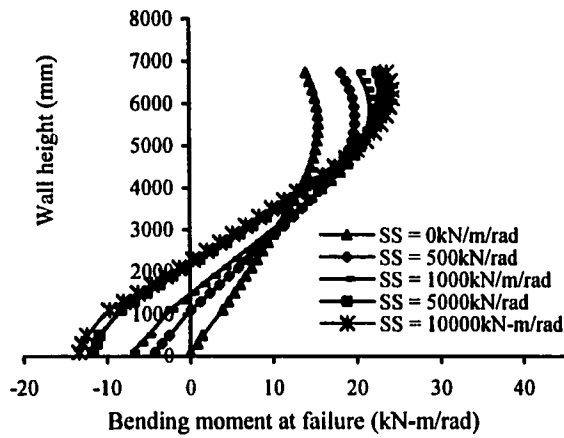


c)  $h/t = 42$

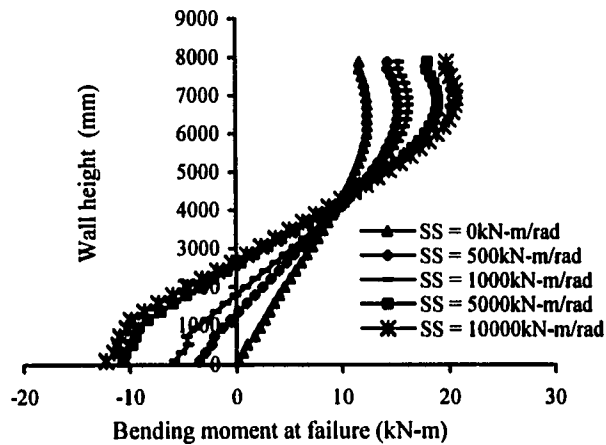
**Figure 6.12 Wall deflection at failure under influence of support stiffness at various slenderness ratios ( $e/t = 0.33$ ,  $NC = 3$ )**



a)  $h/t = 30$



a)  $h/t = 36$



b)  $h/t = c$

**Figure 6.13 Bending moment along the wall height at failure under influence of support stiffness at various slenderness ratios ( $e/t = 0.33$ ,  $NC= 3$ )**

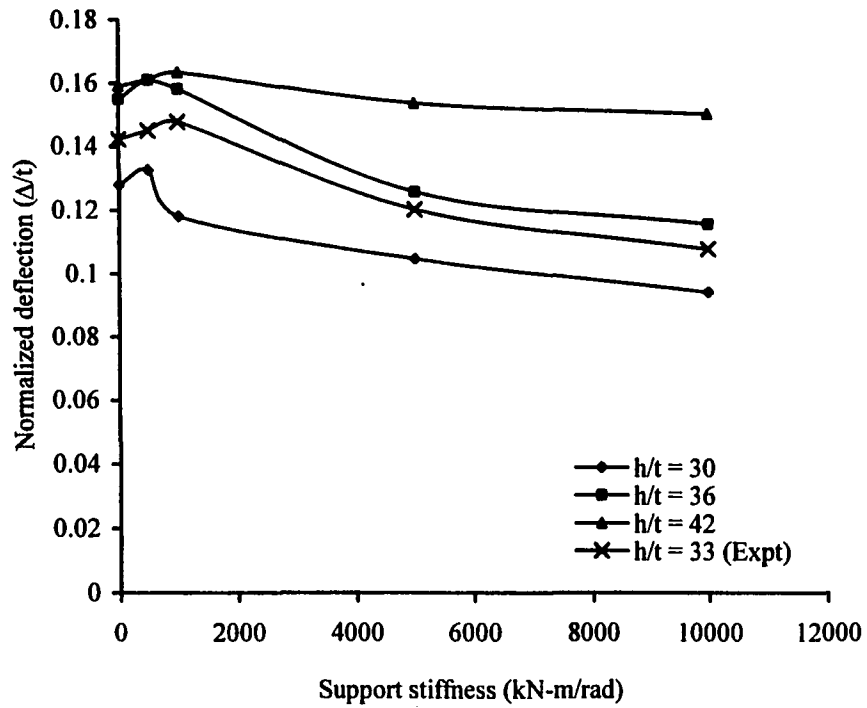
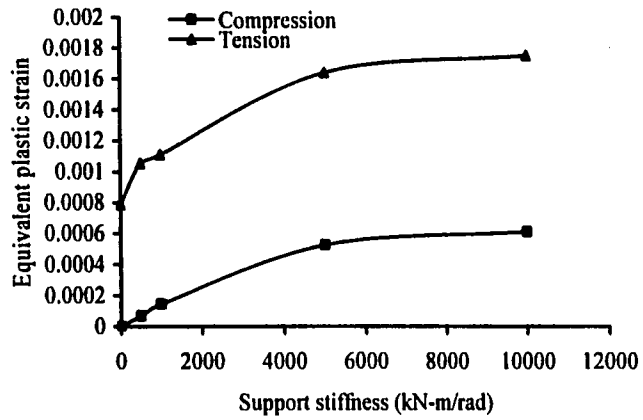
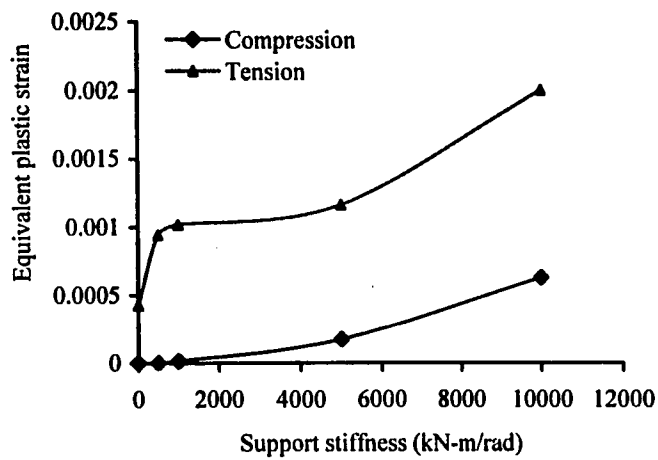


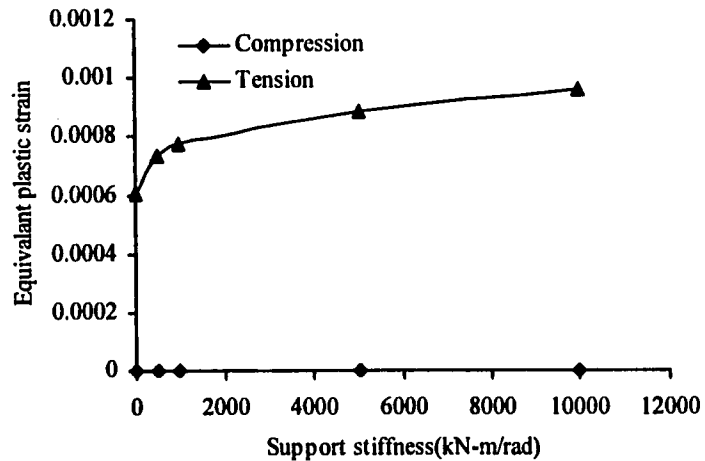
**Figure 6.14 Normalized mid-span deflection versus support stiffness at various slenderness ratios ( $e/t = 0.33$ ,  $NC = 3$ )**



a)  $h/t = 30$



b)  $h/t = 36$



c)  $h/t = 42$

**Figure 6.15 Equivalent plastic strains versus support stiffness ( $e/t = 0.33$ ,  $NC = 3$ )**

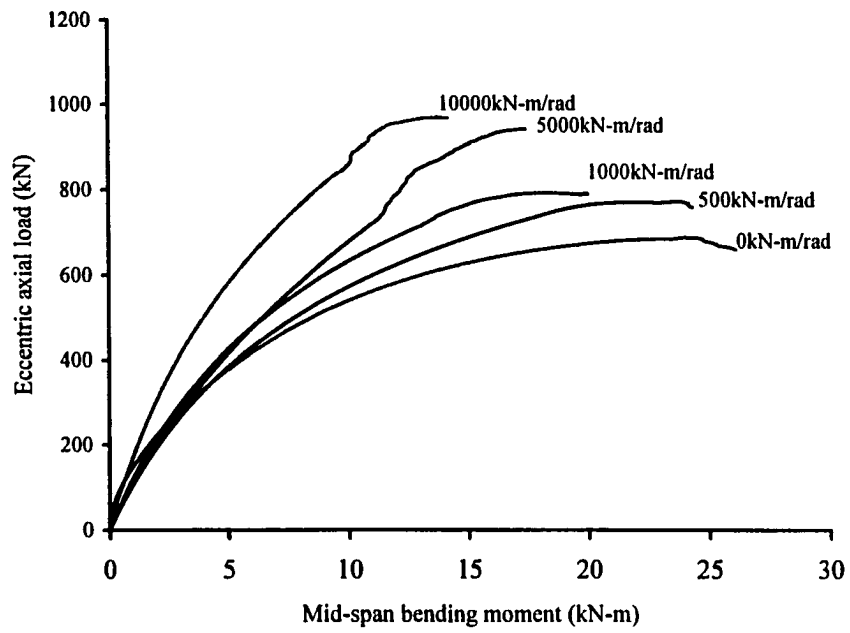
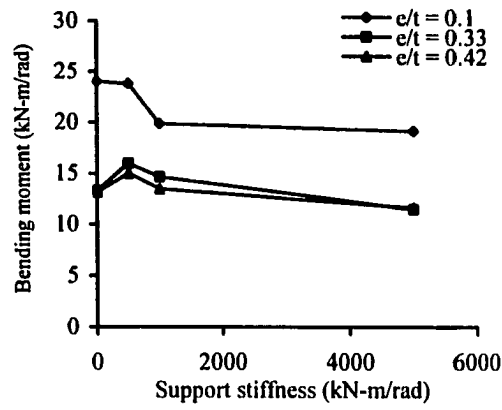
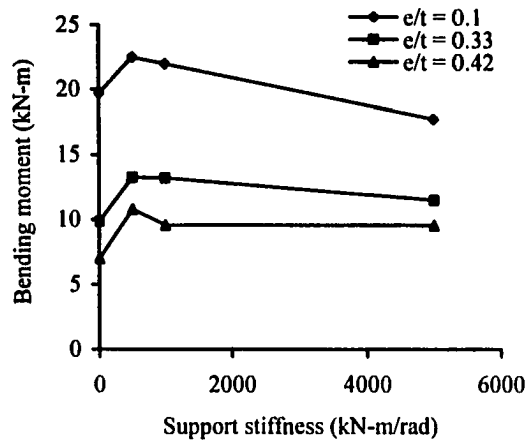


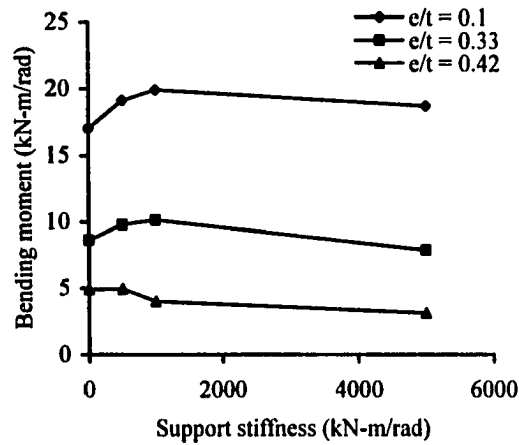
**Figure 6.16 Load versus mid-span bending moment ( $h/t = 30$ ,  $e/t = 0.1$ ,  $NC = 3$ )**



a)  $h/t = 30$

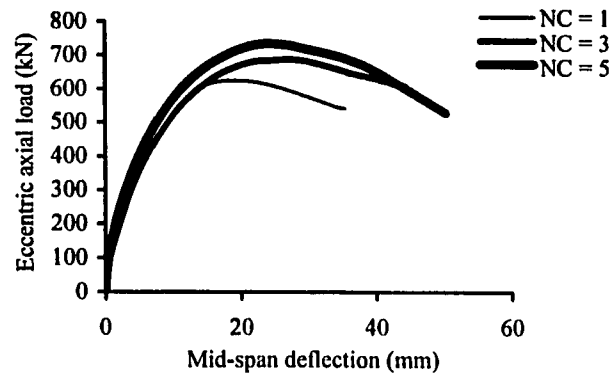


b)  $h/t = 36$

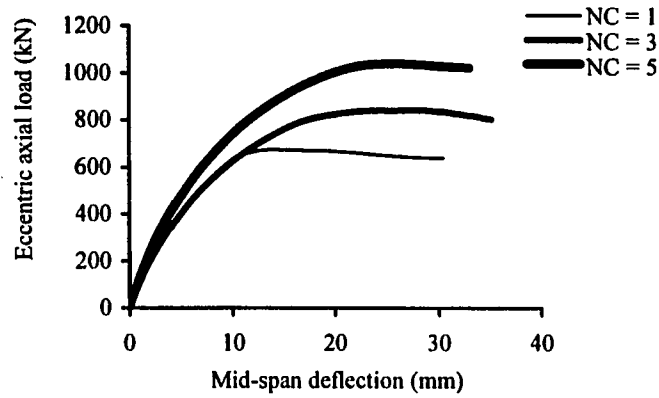


c)  $h/t = 42$

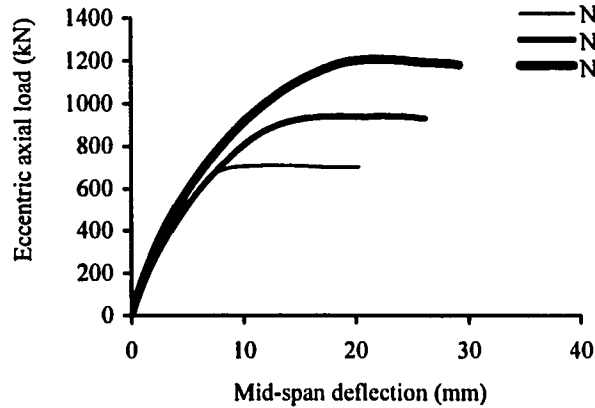
**Figure 6.17 Mid-span bending moment versus support stiffness for constant slenderness ratios ( $NC = 3$ )**



a) Support stiffness = 0kN-m/rad

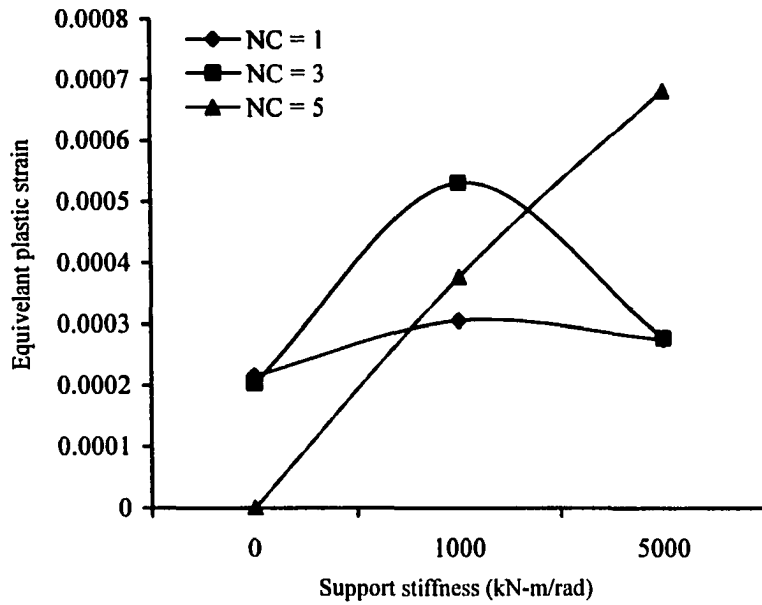


b) Support stiffness = 1000kN-m/rad

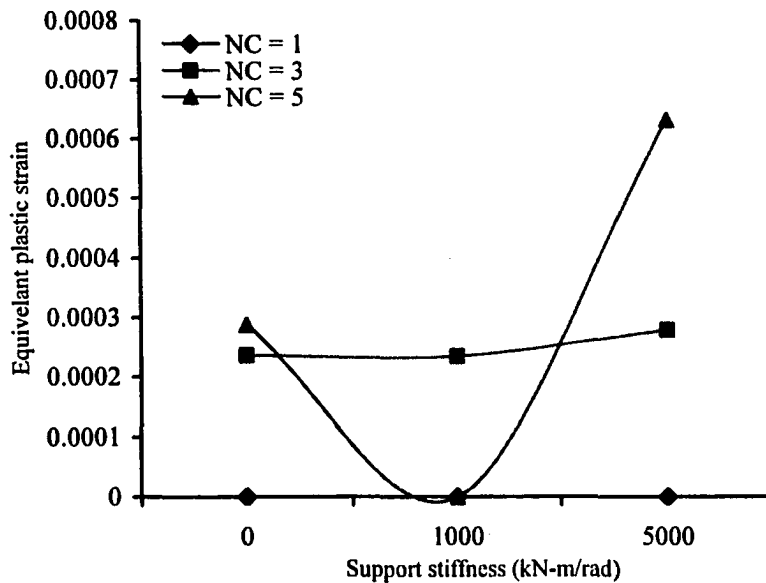


c) Support stiffness = 5000kN-m/rad

**Figure 6.18 Load deflection response for variable amount of grouting at constant support stiffness ( $h/t = 30, e/t = 0.1$ )**

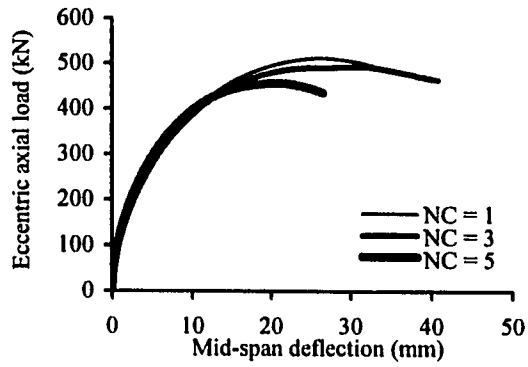


a) Equivalent compressive plastic strain

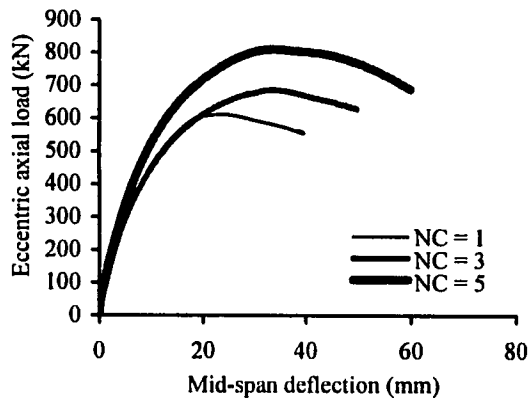


b) Equivalent tensile plastic strain

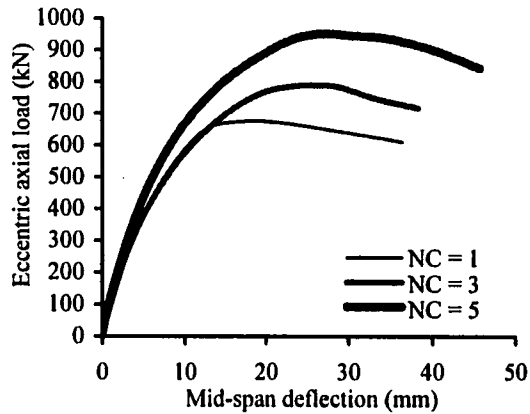
**Figure 6.19 Plots of equivalent plastic strain showing effect of grouting under the influence of support stiffness ( $h/t = 30$ ,  $e/t = 0.1$ )**



a) Support stiffness = 0kN-m/rad

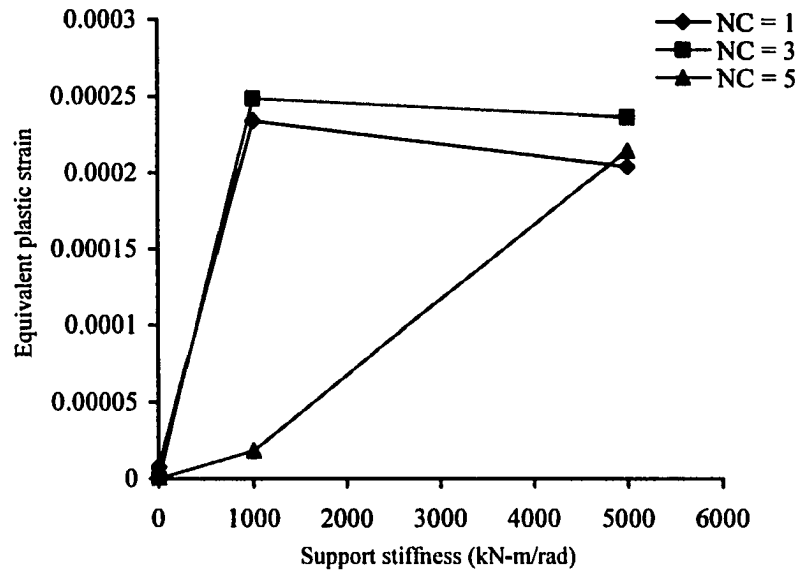


b) Support stiffness = 1000kN-m/rad

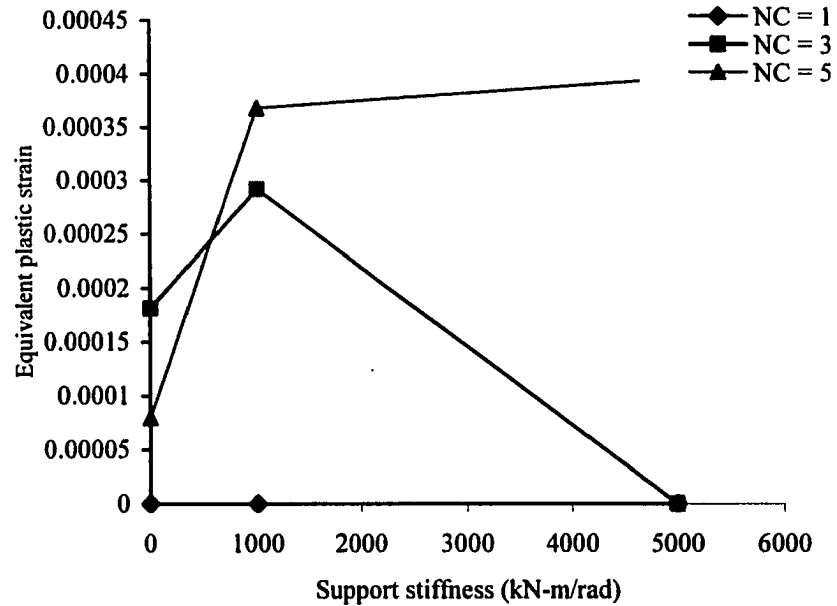


c) Support stiffness = 5000kN-m/rad

**Figure 6.20 Load deflection response showing effect of grouting at various support stiffness ( $h/r = 36$ ,  $e/t = 0.1$ )**

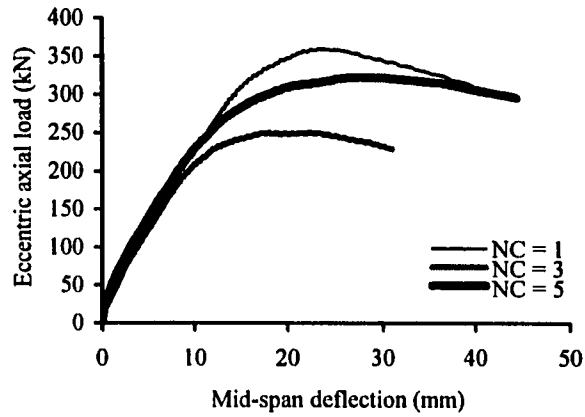


a) Equivalent compressive plastic strain

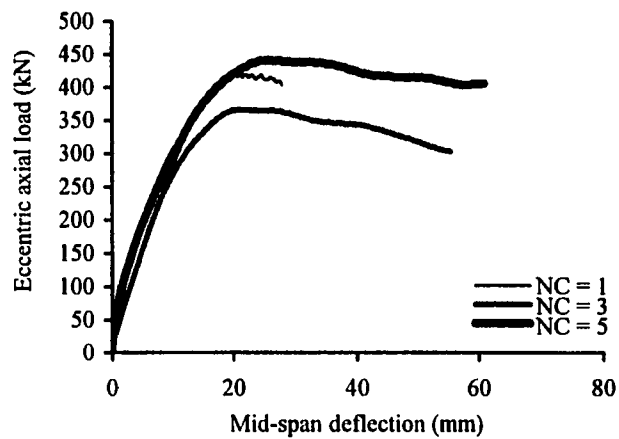


b) Equivalent tensile plastic strains

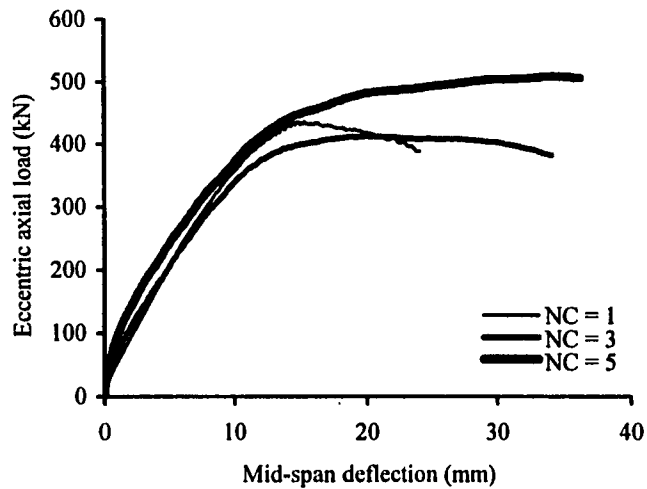
**Figure 6.21 Equivalent plastic strain showing effect of grouting under the influence of support stiffness**



a) Support stiffness = 0kN-m/rad

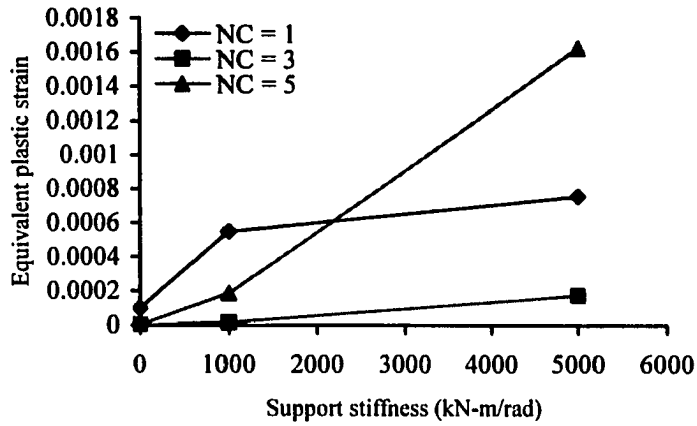


b) Support stiffness = 1000kN-m/rad

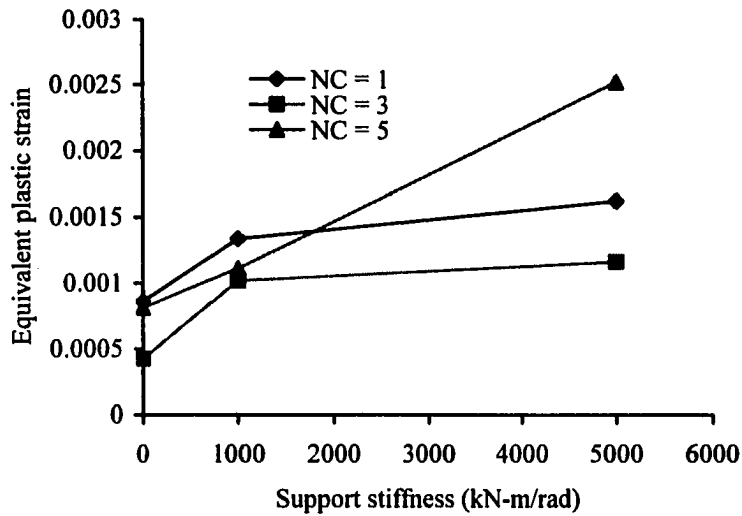


c) Support stiffness = 1000kN-m/rad

**Figure 6.22 Load deflection response showing effect of grouting ( $h/t = 30, e/t = 0.33$ )**

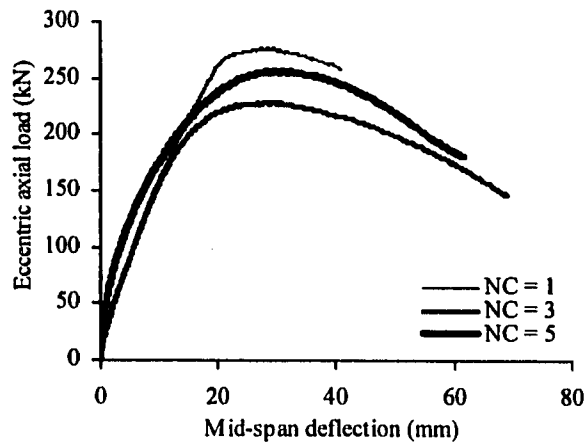


a) Equivalent compressive plastic strain

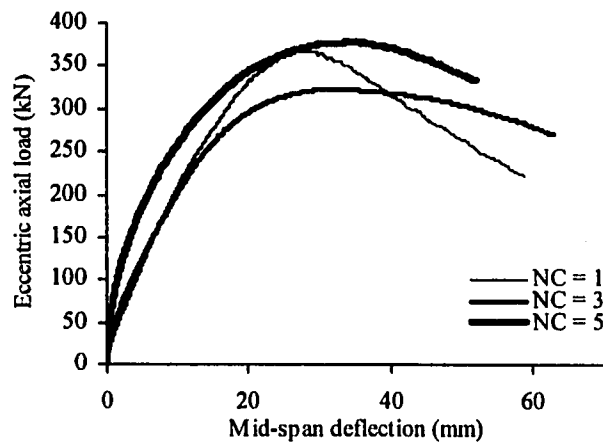


b) Equivalent tensile plastic strain

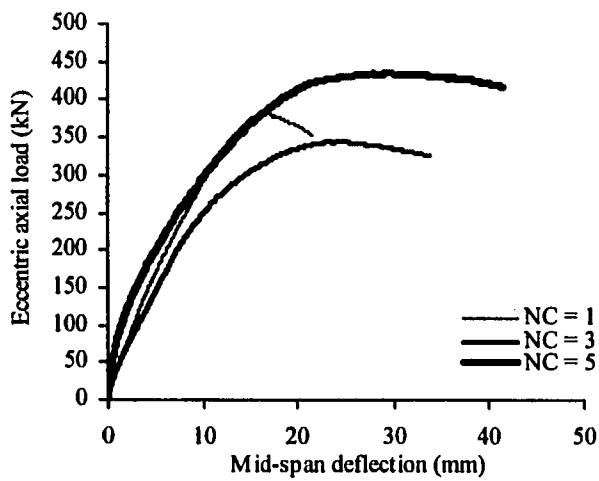
**Figure 6.23 Equivalent plastic strain showing effect of grouting under influence of support stiffness ( $h/t = 30$ ,  $e/t = 0.33$ )**



a) Support stiffness 0kN-m/rad

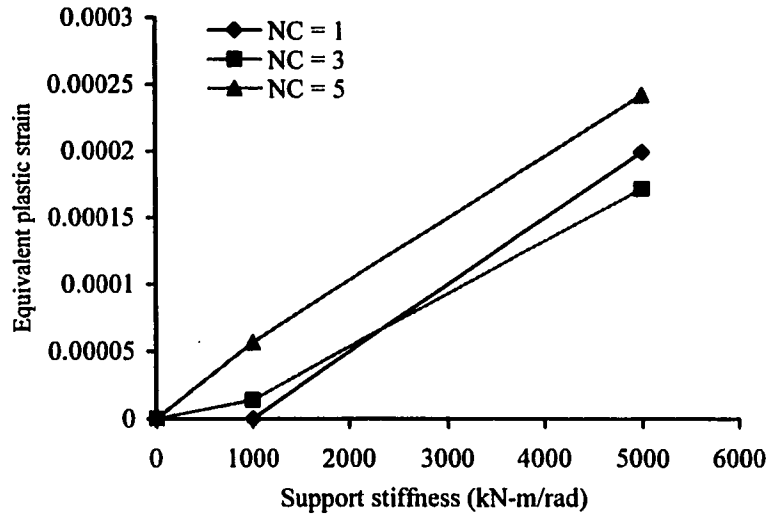


b) Support stiffness = 1000kN-m/rad

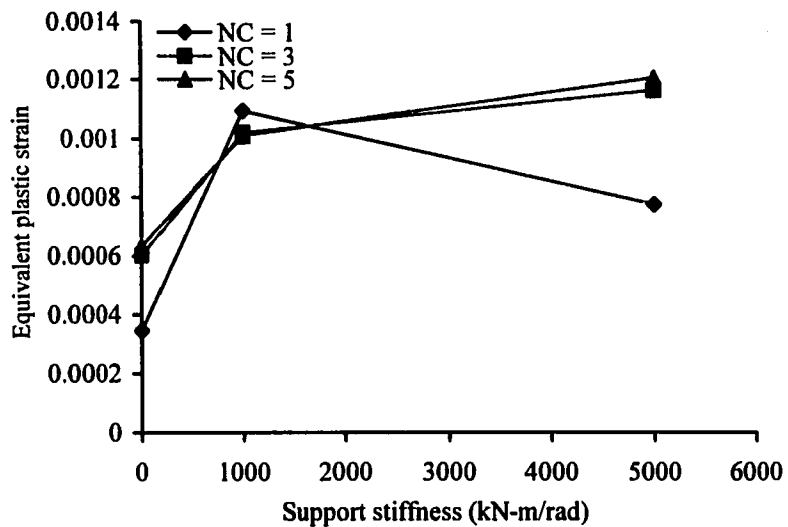


c) Support stiffness = 5000kN-m/rad

**Figure 6.24 Load deflection response showing effect of grouting under influence of support stiffness ( $h/t = 36, e/t = 0.33$ )**

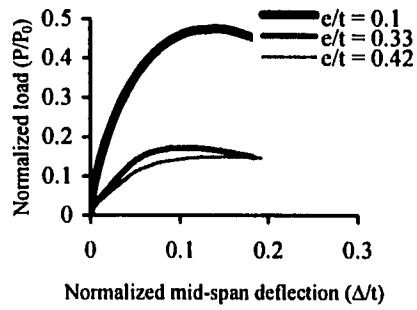


a) Equivalent compressive plastic strain

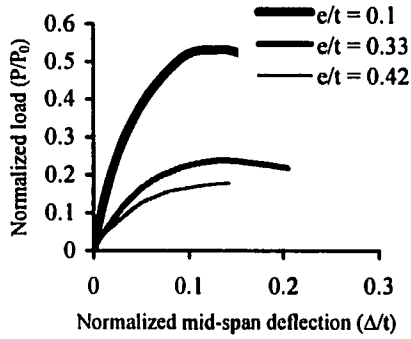


b) Equivalent tensile plastic strain

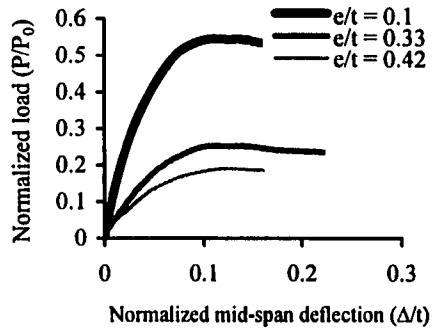
**Figure 6.25** Equivalent plastic strain showing effect of grouting under influence of support stiffness ( $h/t = 36$ ,  $e/t = 0.33$ )



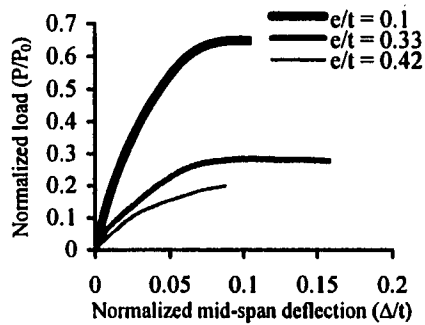
a) Support stiffness = 0kN-m/rad



b) Support stiffness = 500kN-m/rad

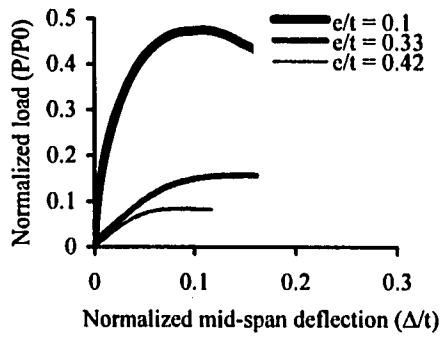


c) Support stiffness = 1000kN-m/rad

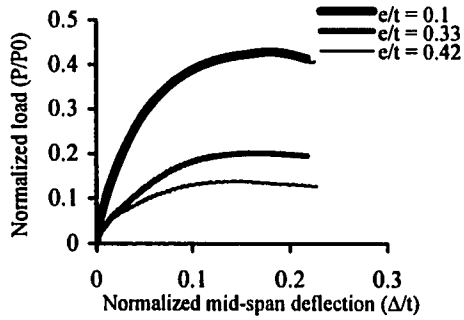


d) support stiffness = 5000kN-m/rad

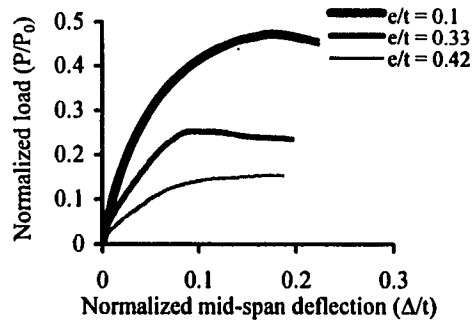
**Figure 6.26 Effect of load eccentricity at various levels of support stiffness ( $h/t = 30, NC = 3$ )**



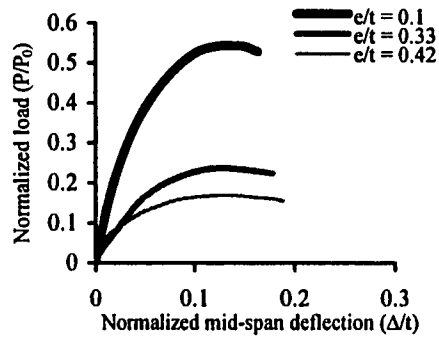
a) Support stiffness = 0kN-m/rad



b) Support stiffness = 500kN-m/rad

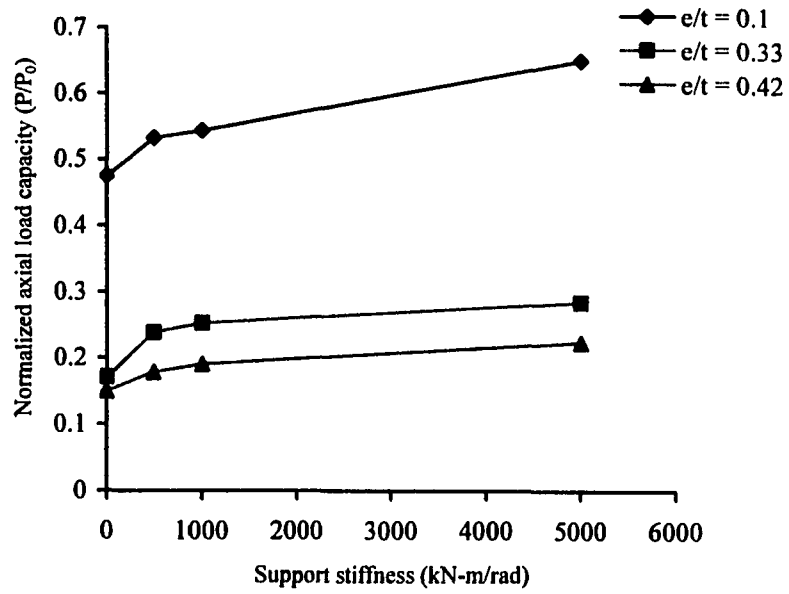


c) Support stiffness = 1000kN-m/rad

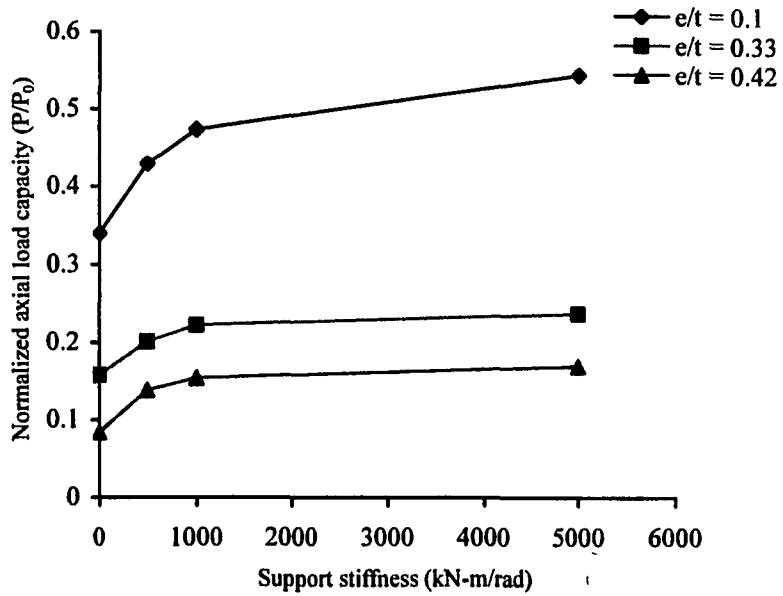


d) Support stiffness = 5000kN-m/rad

**Figure 6.27 Effect of load eccentricity at various levels of support stiffness ( $h/t = 36$ ,  $NC = 3$ )**

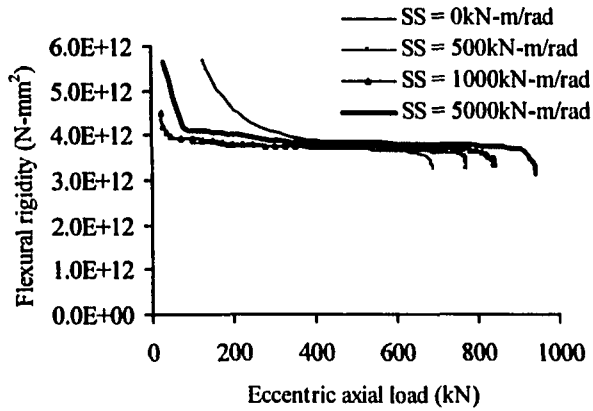


a)  $h/t = 30$

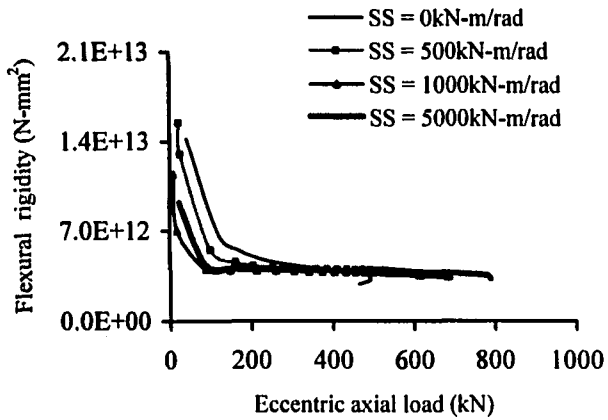


b)  $h/t = 36$

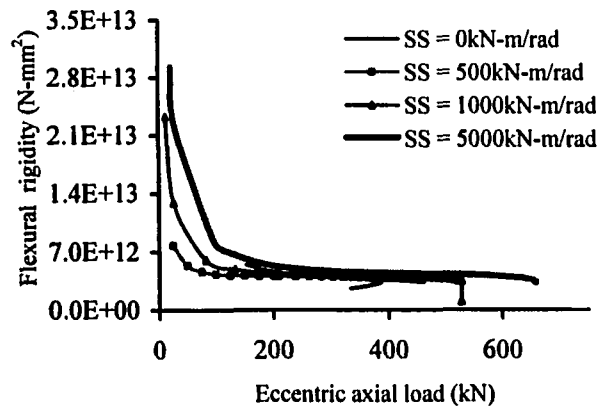
**Figure 6.28 Normalized axial load capacity versus support stiffness at various  $e/t$  ratios ( $NC = 3$ )**



a)  $h/t = 30$

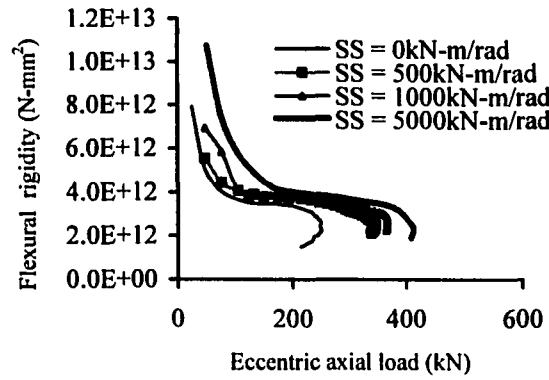


b)  $h/t = 36$

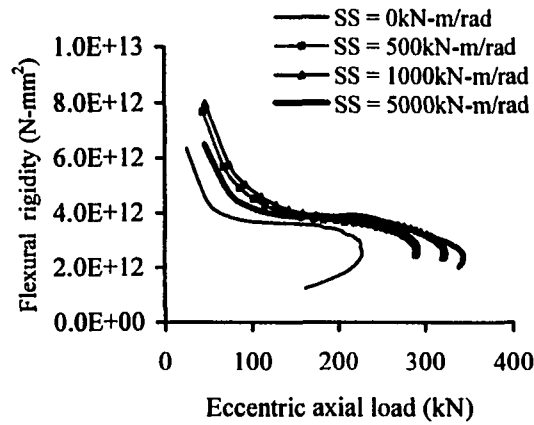


c)  $h/t = 42$

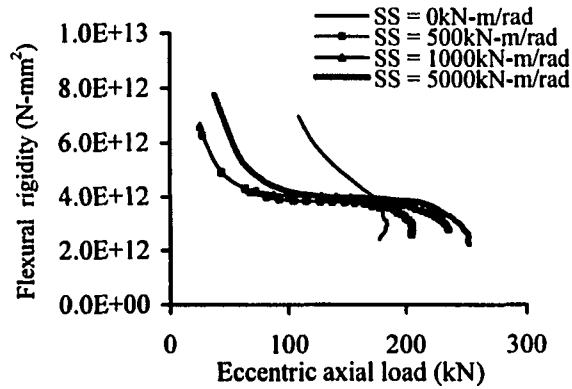
**Figure 6.29 Flexural rigidity versus eccentric axial load (NC=3,  $e/t=0.1$ )**



a)  $h/t = 30$

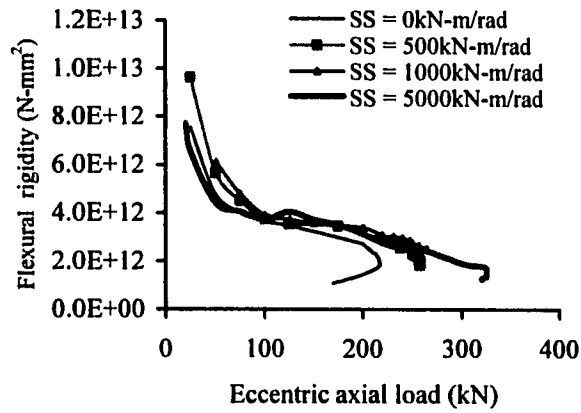


b)  $h/t = 36$

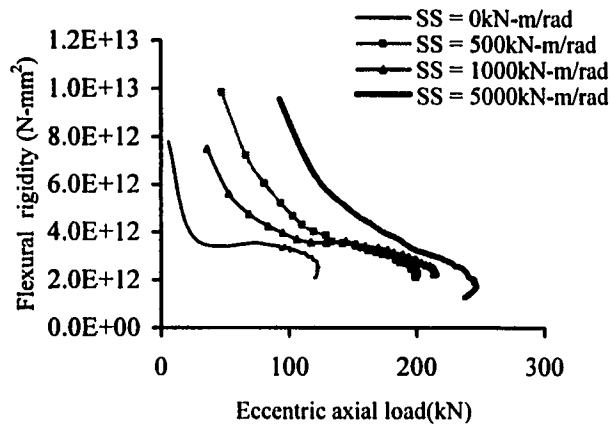


c)  $h/t = 42$

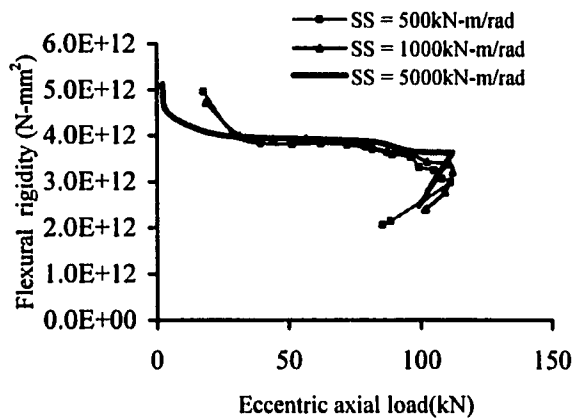
**Figure 6.30 Flexural rigidity versus eccentric axial load (NC=3,  $e/t=0.33$ )**



a)  $h/t = 30$

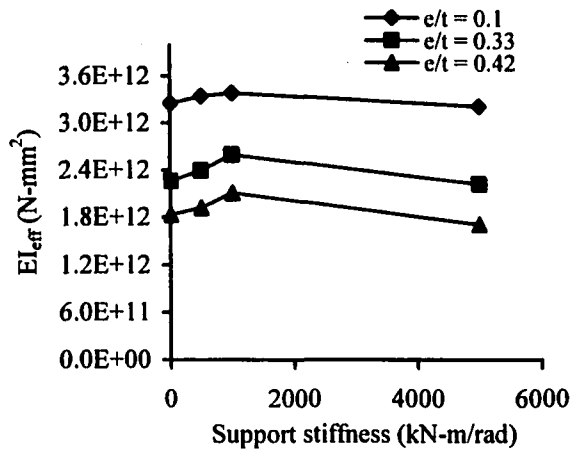


b)  $h/t = 36$

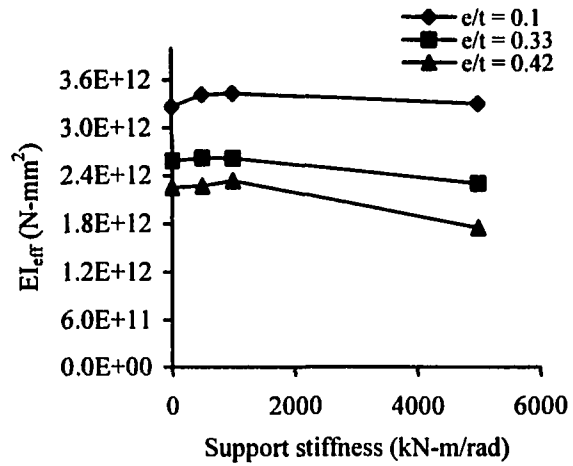


c)  $h/t = 42$

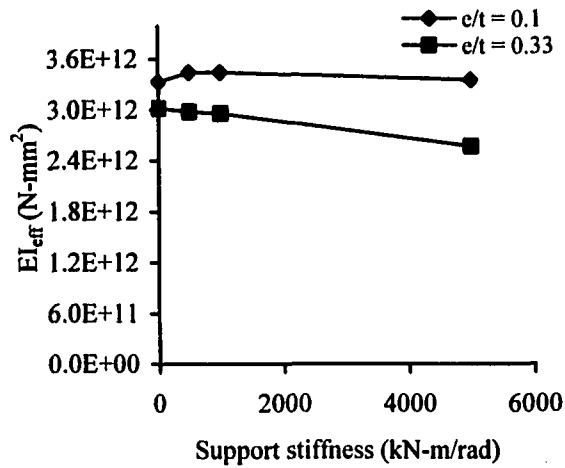
**Figure 6.31 Flexural rigidity versus eccentric axial load (NC=3,  $e/t=0.42$ )**



a)  $h/t = 30$

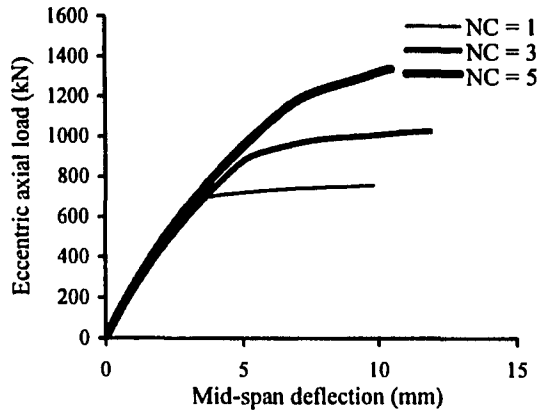


b)  $h/t = 36$

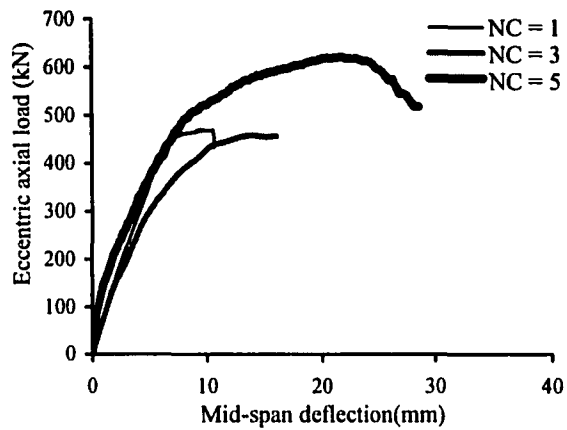


c)  $h/t = 42$

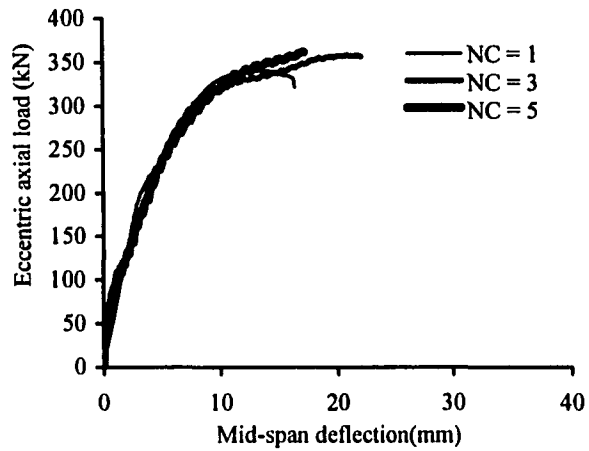
**Figure 6.32 Effective flexural rigidity versus support stiffness (NC=3)**



a)  $e/t = 0.1$

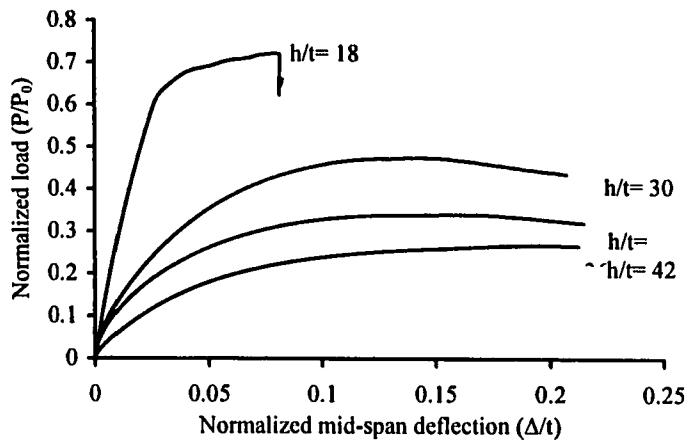


b)  $e/t = 0.33$

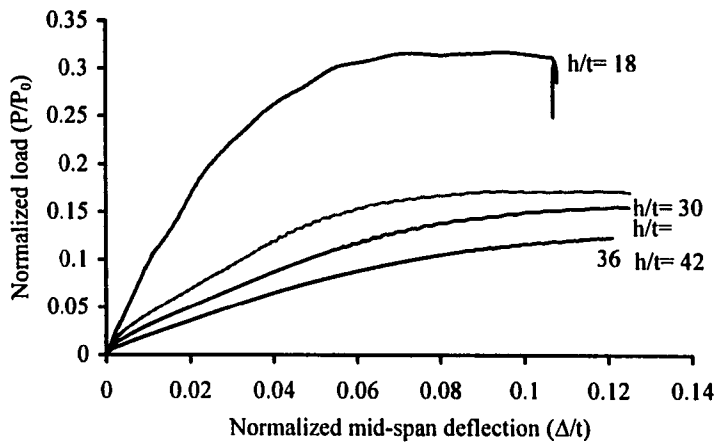


c)  $e/t = 0.42$

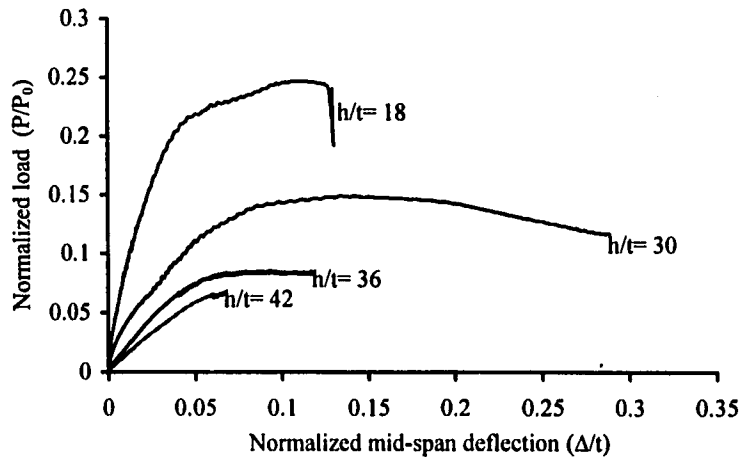
**Figure 6.33 Load deflection response of stocky walls without support stiffness at variable amount of grouting ( $h/t = 18$ )**



a)  $e/t = 0.1$



b)  $e/t = 0.33$



c)  $e/t = 0.42$

**Figure 6.34 Normalized load deflection response without support stiffness for various slenderness ratios**

## CHAPTER 7

### REGRESSION MODEL FOR AXIAL LOAD CAPACITY AND FLEXURAL RIGIDITY

#### 7.1 Introduction

Axial load carrying capacity of slender masonry load bearing walls is a function of several independent variables related to the material and geometry of the walls. Primarily, the axial load capacity of the walls depends on load eccentricity ratio, slenderness ratio, material properties and the boundary conditions including support stiffness. Literature review in chapter two of the thesis showed that there has been valuable research conducted to explore the effect of different geometric and material parameters on axial load carrying capacity of tall masonry load bearing walls. However, no research work was performed to study the effect of support stiffness on performance of slender masonry walls. The discussion in the previous chapters showed that support stiffness has a significant effect on the strength and stiffness of such walls. It is vital, therefore, to include the effect of support stiffness in predicting the axial load carrying capacity. In this chapter it is intended to find an expression to predict axial load carrying capacity by correlating the geometric and material parameters with support stiffness.

This chapter presents a non-linear regression analysis based on the results of the parametric study described in chapter six of the thesis. The chapter includes two sections of regression analysis. The first section presents regression analysis for normalized axial load capacity and provides the mathematical expression for the prediction of the capacity. The second presents regression analysis for the rigidity ratio\* and reports the mathematical expression to calculate effective flexural rigidity. A comparison of proposed equations with experimental work and previous research work of similar conditions will be performed.

---

\* The rigidity ratio here is the ratio of the effective wall stiffness to gross or nominal wall stiffness

It is also aimed in this chapter to compare the FEM results with current Canadian Code–S304.1 provisions. The regression analysis and the code comparison presented in this chapter are intended to provide the necessary information regarding the influence of support stiffness on behavior of masonry load bearing block walls. The equations presented in this chapter are anticipated to formulate the basis of future extension of the work in terms of their incorporation into conventional masonry wall design procedures.

## **7.2 Axial Load Capacity**

### **7.2.1 Parameters affecting the Axial Load Capacity**

The parametric study in chapter six showed that support stiffness, slenderness ratio, load eccentricity ratio, compressive strength of masonry, modulus of elasticity, grouting amount and area of steel are the parameters, that influence the wall response. It is tedious to incorporate all these parameters within in a single mathematical model by treating them individually. To avoid complexity it is effective to use normalized form of the parameters, specially, when there is a chance of variability or when a single parameter is linked to magnitude of other parameters. Masonry material and cross-sectional properties are the best examples of this type of parameters. Hence in this study it is intended to use the normalized form of some of the material and cross-sectional parameters so that they can be effectively introduced in a mathematical expression.

In the current study the normalized axial load capacity of masonry load bearing walls is used to present the effect of different parameters on wall response. The normalized axial load is computed as  $P/P_0$ , where,  $P$  is the axial load capacity of the walls and  $P_0$  is the cross-sectional strength computed by Equation 7.1.

$$P_0 = A_e f'_m + A_s f_y \quad [7.1]$$

in which  $A_c$  is the net area of concrete masonry,  $f_m$  is the compressive strength of prism,  $A_s$  is the total area of vertical rebars and  $f_y$  is the yield strength of steel.

Equation 7.1 combines the effect of cross-sectional as well as material properties of the wall and eliminates the use of compressive strength, net area and area of steel as separate entities. Other key parameters are support stiffness, slenderness ratio and load eccentricity ratio. Since all parameters including axial load ratio, load eccentricity ratio and slenderness ratio are non-dimensional, hence for the purpose of regression analysis the support stiffness is also non-dimensionalized relative to the gross wall section rigidity,  $E_m I_g$ , so that,

$$r = \frac{Rt}{E_m I_g} \quad [7.2]$$

in which, “r” is the support stiffness ratio, R is the support stiffness, “t” is the nominal thickness of the wall,  $E_m$  is the modulus of elasticity of masonry and  $I_g$  is the gross moment of inertia of the wall.

Table 7.1 shows the normalized axial load ratio,  $P/P_0$  and the corresponding slenderness ratio ( $h/t$ ), load eccentricity ratio ( $e/t$ ) and support stiffness ratio ( $r$ ) of different walls numerically tested in the parametric study. After highlighting the parameters having direct influence on axial load capacity of the wall it is important to present the effect of each parameter separately on the axial load ratio of the walls. The axial load ratio of the walls is plotted against each parameter to see how the wall capacity is influenced by a particular parameter.

Figure 7.1 presents the relationship between load eccentricity ratio and axial load ratio of the wall specimens listed in Table 7.1. It is observed that  $e/t$  has an obvious detrimental effect on axial load capacity. However, this effect is reduced when support stiffness ratio is increased at a constant level of slenderness. Similarly, when the slenderness ratio is increased at constant eccentricity ratio  $P/P_0$  is decreased. Conversely when support stiffness ratio is increased, the

detrimental effect caused by wall slenderness is diminished, as shown in Figure 7.2. The relationship between normalized axial load capacity with slenderness ratio, load eccentricity ratio and support stiffness ratio is further illustrated in Figure 7.3 and Figure 7.4.

### **7.2.2 Development of Equation for the estimation of the normalized Axial Load Capacity**

The literature review showed that most of the previous research work emphasized the moment magnifier method to estimate axial load capacity of masonry load bearing walls. The current study mainly focuses on support stiffness effects on the axial load capacity rather than concentrating on already well-researched methods of estimating axial load capacity of the walls.

After identifying the key parameters affecting the axial load capacity of the walls it is required to mathematically relate them in the form of an equation so that the normalized axial load capacity can be predicted by using a simple mathematical expression. To achieve this goal the data listed in Table 7.1 was statistically examined to perform regression analysis.

Firstly the whole data was taken to perform regression analysis, and an attempt was made to develop an equation for the broad range of independent variables ( $r$ ,  $h/t$  and  $e/t$ ) but the statistical assessment showed that in order to obtain an accurate estimate of the dependent variable (axial load ratio) it is necessary to present more than one equation by restricting the limits of independent variables.

Based on trends shown in Figure 7.1 through Figure 7.4, it was observed that the trend of support stiffness ratio " $r$ " is quite uniform up to the highest value of  $r = 0.26$  (corresponding to  $R = 5000\text{kN-m/rad}$ ) for  $h/t = 30$  to  $h/t = 42$  and  $e/t = 0.1$  to  $e/t = 0.33$ . However, when  $e/t$  is increased from 0.33 to 0.42 the trend becomes different because of the excessive geometric non-linearity and the vulnerability of

walls to stability failure. Therefore, based on load eccentricity ratio it was decided to perform regression analysis into two categories by using a common range of support stiffness ratio and the slenderness ratio in both categories as  $0 \leq r \leq 0.26$  and  $30 \leq h/t \leq 42$  respectively. Using similar data ranges for support stiffness ratio and the slenderness ratio, the first category covered the range of load eccentricity ratio of  $0.1 \leq e/t \leq 0.33$ , while in the second category the load eccentricity ratio was ranging from,  $0.33 < e/t \leq 0.42$ . As shown by the plots for the walls having slenderness ratio higher than  $h/t = 36$ , the support stiffness does not play any significant role to increase axial load carrying capacity. Therefore, the walls with  $h/t = 42$  and  $e/t = 0.42$  are mostly susceptible to stability type of failure. Because of the unstable behavior of the walls with  $h/t = 42$  and  $e/t = 0.42$  the current regression analysis could not obtain an equation for the data range of  $h/t > 36$  and  $e/t > 0.33$ . Hence, beyond eccentricity ratio of 0.33 the analysis is restricted for slenderness ratio of  $h/t < 42$ .

Using the above described data ranges, the regression analysis was performed for two categories of the range of independent variables so that the normalized axial load capacity can be predicted for a broad range of combination of the variables. As shown in Figure 7.1 to Figure 7.4 the interrelationships are not linear. Therefore, non-linear regression analysis was used to obtain interrelationship of all the variables. The process of regression analysis is an iterative procedure, and in case of non-linear regression, requires computer software to make it faster and more precise. There are various computer programs, which can perform non-linear regression analysis, in the current study; "Sigma-Plot 8.0" (SPSS, 2003) was used. The software is able to provide varieties of functions to express the behavior of dependent variables and also provides the flexibility to code equation of the user's choice. The above mentioned software provides some important measures of determining the accuracy and capability of the regression model. The primary measure of the accuracy is the coefficient of multiple determinations,  $R^2$ , which shows the efficiency of the regression model to predict value of dependent variable. The value of  $R^2$  closer to 1 shows how accurate is the

regression model in describing the data, while the value of  $R^2$  closer to 0 shows the unsuitability of the regression equation to describe the data.

The following preliminary form was adopted for the required equations:

$$\frac{P}{P_0} = f [f_1(r), f_2(e/t), f_3(h/t)] \quad [7.3]$$

in which  $f_1$ ,  $f_2$  and  $f_3$  are the individual functions to reflect behavior of independent variables  $r$ ,  $e/t$  and  $h/t$  respectively, in the regression equation of normalized axial load capacity.

The coefficient of multiple determinations ( $R^2$ ) was set as a primary criterion of measuring the level of accuracy of regression analysis. Different types of functions were tried. Using equation 7.3 as the preliminary form several attempts were made to find a fit between available data and the predicted value. The crucial step of the regression analysis was the selection of suitable function, which can best incorporate the relationship between dependent and independent variables. Initially, the linear function for  $h/t$ , two-parameters single exponential decay function for  $e/t$  and quadratic function for “ $r$ ” were chosen. Iterations were performed to find a good fit and to bring the value of  $R^2$  closer to 1. Even after many trials the maximum value of  $R^2$  obtained was around 0.6, which was not satisfactory and indicated the need to change the type of functions. Therefore, to improve the quality of regression equation as well as to make it more user friendly, it was decided to disregard exponential decay type of function for the variable  $e/t$  and a single parameter inverse type of linear function was tried.

Several trials were attempted to obtain the best fit by monitoring the  $R^2$  values. Finally, the following two equations were obtained to cover previously mentioned categories of the independent variables.

For  $0.1 \leq e/t \leq 0.33$ :

$$\frac{P}{P_0} = \frac{1}{\left(\frac{h}{t}\right)} \left[ \left( 0.46 + \frac{0.21}{\left(\frac{e}{t}\right)} \right) (5 - 100r^2 + 36r) \right] \quad [7.4]$$

in which,  $0 \leq r \leq 0.26$  (or  $R = 0\text{kN-m/rad}$  to  $5000\text{kN-m/rad}$ ) and  $30 \leq h/t \leq 42$ .

For  $0.33 < e/t \leq 0.42$ :

$$\frac{P}{P_0} = \frac{1}{\left(\frac{h}{t}\right)} \left[ \left( 0.23 + \frac{1}{\left(\frac{e}{t}\right)} \right) (5 - 180r^2 + 59r) \right] \quad [7.5]$$

in which,  $0 \leq r \leq 0.26$  (or  $R = 0\text{kN-m/rad}$  to  $5000\text{kN-m/rad}$ ) and  $30 \leq h/t \leq 36$ .

Equations 7.4 and 7.5 were preliminary and resulted in a coefficient of determination  $R^2 = 0.97$  and  $R^2 = 0.88$  respectively. The value of  $R^2$  should not be the only criterion of validity of the regression model. It was also required to check the behavior of the model for the data points out-side the range used in regression analysis, as well as to check the scatter of the data about the regression model. The next section describes the assessment of the regression model.

### 7.2.3 Assessment of Regression Model for Axial Load Capacity

The correlation between dependent and independent variables was checked by plotting the normalized axial load capacity obtained from regression model and from FEM model against all independent variables. Figures 7.5 through 7.8 show the comparison of FEM results and the predicted values from regression models against support stiffness ratios at various combinations of slenderness ratio and load eccentricity ratios. It is observed from the plots that in most of the cases the

regression model closely follows the FEM results. In case of walls with  $h/t = 42$  the regression model appears to be over conservative and shows a slightly higher normalized axial load capacity with increasing support stiffness ratio, but the error does not exceed 10%.

Figures 7.9 through 7.12 show the comparison between FEM and regression models against variable load eccentricity ratio at constant slenderness and support stiffness ratios. It is evident from the plots that regression model is able to predict a normalized axial load capacity close to the normalized capacity obtained from FEM model at various load eccentricity ratios. The capability of the regression model to relate slenderness ratio with rest of the variables was checked by plotting FEM and regression models against slenderness ratio at constant load eccentricity and support stiffness ratio in Figures 7.13 through 7.16. The regression model reasonably predicted the normalized axial load capacity and showed moderate agreement between FEM results and the predicted capacity.

It is concluded that the regression model is able to estimate the response in the range of the data for which regression was performed. For further verification and check for the validity of the regression model it is essential to predict the normalized axial load capacity of some physically tested walls using the proposed equations and then compare the predictions with the actual capacity of the tested walls. To examine the capability of the regression model of predicting response, it is best to plot scatter of the data around the regression line. The scatter of the data was obtained by plotting the predicted capacity ratio " $(P/P_0)_{\text{predicted}}$ " versus actual capacity ratio " $(P/P_0)_{\text{actual}}$ ". Figure 7.17 shows the scatter of the data including FEM results and some experimental results. For verification purpose the data point obtained from full scale masonry load bearing block wall testing performed by Goyal (1992), Kuzik (2001) and from current study were also plotted in Figure 7.17. Table 7.2 shows the details of the full-scale wall specimens of these three studies.

As shown in Figure 7.17 the regression model is able to provide a reasonable estimate of the normalized axial load capacity of masonry load bearing block walls. The scatter of the data lies within 10% error band and the data points are closely clustered around the regression line. It is interesting to mention that two data points obtained from Kuzik (2001) corresponding to the wall specimens constructed with externally glued FRP sheets are located out-side the 10% error band but still clustered around the regression line despite that fact that the regression model does not include the effect of FRP. The data point from Goyal (1992) corresponds to data range of  $h/t < 30$  and showed reasonable agreement with the regression model and demonstrated the capability of the regression model to predict capacity of wall out-side the data range used to generate the model. Similarly, the data points from the walls of Group-I of the current study also belong to the data range of  $h/t < 30$  which falls outside the data range of regression model but still closely located around the regression line.

The above discussion illustrated that the predictions from the regression model compare well with available full scale testing results. In order to use the proposed regression model in design of masonry load bearing walls it is required to apply a performance factor to account for variability related to actual construction and the parameters having direct influence on response of the walls. This type of investigation is beyond the scope of the current study and is recommended for future extension of the work. Although the proposed regression equations do not have direct application within the design procedure of masonry load bearing walls recommended by S304.1 they provide a good measure of axial capacity of masonry load bearing walls supported under different boundary conditions with higher ratios of load eccentricity and slenderness.

## **7.3 Flexural Rigidity**

### **7.3.1 Parameters affecting the Flexural Rigidity**

The flexural rigidity is a function of all the variables influencing the load capacity of the walls. As described in the previous section the support stiffness ratio, load eccentricity ratio and slenderness ratio are key parameters, which affect the masonry wall behavior.

It is evident from chapter 6 that the effective flexural rigidity depends on wall response and its failure mode. These factors are basically influenced by the amount of cracking and the stress level attained during the load history of the wall. It is observed that walls with smaller slenderness ratios have a tendency to carry higher axial loads and this tendency increases when the load eccentricity decreases and the support stiffness ratio increases. Therefore, walls with higher axial loads are vulnerable to crushing failure, which is a manifestation of material non-linearity which, in turn, decreases the effective flexural rigidity. At a constant level of support stiffness, walls with intermediate slenderness ratio loaded with lower load eccentricity (for example wall with  $h/t = 30$  and  $e/t = 0.1$ ) show lesser effective flexural rigidity as compared to walls with higher slenderness ratio loaded with higher eccentricity (for example wall with  $h/t = 42$  and  $e/t = 0.33$ ). The walls with intermediate slenderness ratio carry higher axial loads and their cross-sections are subjected to both compressive and tensile stresses. Therefore, the combined effect of high level of cross-sectional stresses and slenderness reduces the modulus of rigidity and effective moment of inertia, which results in comparatively reduced effective flexural rigidity. Conversely, the walls with higher slenderness ratio loaded with higher load eccentricity show higher flexural rigidity at failure primarily because these walls explicitly fail due to stability failure and carry lower axial load, without giving rise to cross-sectional stresses, and the modulus of rigidity is not reduced.

An increase in the support stiffness ratio is also observed to lead to higher cross-sectional stresses, specially, when higher support stiffness ratio is combined with intermediate slenderness and lower load eccentricity due to enhanced effect of material non-linearity. For example a wall with a support stiffness ratio of  $r = 0.26$  ( $R = 5000\text{kN}\cdot\text{m}/\text{rad}$ ) and slenderness ratio of  $h/t = 30$  loaded with  $e/t = 0.1$  possess lower flexural rigidity at failure as compared to a wall with similar conditions except with  $r = 0.05$  (or  $R = 1000\text{kN}\cdot\text{m}/\text{rad}$ ). As discussed in Chapter 6 of the thesis that the listed parameters control the wall behavior throughout the load history till the failure of the wall, therefore the flexural rigidity at failure is greatly influenced by these parameters.

Figure 7.18 through Figure 7.21 show the relationship of support stiffness ratio, slenderness ratio and load eccentricity ratio. It is observed that lower slenderness ratios possess lower rigidity ratios because they carry higher axial loads and are subjected to higher stress level and more severe material non-linearity. Similarly in case of higher eccentricity ratios the walls are subjected to out of plane deflections and exhibit higher amounts of cracking. Therefore, the resulting reduction in moment of inertia of the wall cross-section causes reduction in rigidity ratio. When a lower slenderness ratio combines with higher support stiffness ratio cracking is controlled but material non-linearity under compression increases which causes the reduction in rigidity ratio. However this increase in material non-linearity in compression zone occurs when the support stiffness ratio exceeds  $r = 0.05$ . Below this limit the axial load capacity is increased but the level of cross-sectional stresses is not large enough to create any material non-linearity. Therefore, no significant reduction in flexural rigidity is evident. It is observed that any increase in support stiffness ratio from  $r = 0$  to  $r = 0.05$  at constant slenderness and constant load eccentricity, causes an increase in effective flexural rigidity mainly because the support stiffness ratio within this range controls the out of plane deflection, thus limiting the level of severe material nonlinearity in the compression zone.

Keeping in mind the above observations the regression model was developed and discussed in the following section.

### 7.3.2 Development of Equation for the Estimation of Effective Flexural Rigidity

Table 7.1 shows the data for the rigidity ratio,  $\frac{EI_{eff}}{E_m I_g}$ , and corresponding independent variables ( $r$ ,  $e/t$ ,  $h/t$ ) for which the regression analysis was performed.  $EI_{eff}$  is the value of flexural rigidity corresponding to the peak load attained by the wall and  $E_m I_g$  describes the initial (un-cracked) flexural rigidity of the wall.

To obtain an equation for the estimation of the ratio of effective rigidity of the wall, considering all the key parameters the following preliminary format is selected to describe the rigidity ratio.

$$\frac{EI_{eff}}{E_m I_g} = f [f_1(r), f_2(e/t), f_3(h/t)] \quad [7.6]$$

in which  $f_1$ ,  $f_2$  and  $f_3$  are the individual functions to reflect behavior of independent variables “ $r$ ”,  $e/t$  and  $h/t$  respectively. In equation 7.6 the selection of the functions to incorporate the behavior of the above mentioned parameters is based on their interaction with rigidity ratio.

The discussion in section 7.3.1 emphasizes that in equation 7.6 the selection of individual functions to represent the parameters “ $r$ ”,  $e/t$  and  $h/t$  should be carried out by observing how the different combinations of these three parameters affect the rigidity ratio. As shown in Figure 7.18 through Figure 7.21, the rigidity ratio is affected differently in different ranges of the key parameters.

Based on the trends shown in previous sections it is observed that for all load eccentricity ratios and at all levels of support stiffness increasing the slenderness ratio causes an increase in the effective flexural rigidity ratio. Similarly increasing the eccentricity ratio always causes decay in the flexural rigidity at constant slenderness and constant support stiffness ratio, except in case of  $h/t = 42$  in which when the eccentricity ratio increased to 0.42, the rigidity ratio increased. This was caused by an early stability failure during the load history with the wall undergoing larger deflections and cracking and as a result failed at a very low level of load without any reduction in rigidity ratio because of material or geometric non-linearity. As explained in chapter 6 increasing the support stiffness allows the wall cross-section to undergo higher levels of plastic strains. This phenomenon affects the rigidity ratio. It is observed that when “r” is increased from 0.05 ( $R = 1000\text{kN-m/rad}$ ) to 0.26 ( $R = 5000\text{kN-m/rad}$ ) reduction in rigidity ratio is observed. The phenomenon is more severe in case of lower eccentricity ratio and lower slenderness ratio because of the combined effect of material and geometric non-linearity.

The regression model is divided into three ranges reflecting the changing effect of combining parameters. The first part covers the data range of  $0 \leq r \leq 0.26$ ,  $0.1 \leq e/t \leq 0.33$  and  $30 \leq h/t \leq 42$ . The second part covers the range  $0 \leq r \leq 0.26$ ,  $0.33 \leq e/t < 0.42$  and  $30 \leq h/t \leq 42$ , while in the third part regression was performed over the range of data,  $0 \leq r \leq 0.051$ ,  $0.33 \leq e/t < 0.42$  and  $30 \leq h/t \leq 36$ .

Sigmaplot 8.0 (SPSS, 2003) was employed to perform the regression analysis. The preliminary criterion of selecting the best equation was based on monitoring the coefficient of determination “ $R^2$ ” as was used in development of the regression model for axial load capacity. During the process of regression analysis all the necessary checks were performed and the regression model was developed as:

$$\frac{EI_{eff}}{E_m I_g} = [\{5 + 0.32(h/t) - 0.0039(h/t)^2\} \{0.0158e^{-0.0158(e/t)}\} \{5 + 2.9r - 12r^2\}] \quad [7.7]$$

Equation 7.7 is valid for the data range:  $e/t < 0.33$ ,  $h/t \leq 42$  and  $r \leq 0.26$   
(or  $R = 5000 \text{ kN-m/rad}$ ).

$$\frac{EI_{eff}}{EI_0} = [\{0.01 + 0.12(h/t) - 0.00094(h/t)^2\} \{0.0787e^{-0.0787(e/t)}\} \{3 + 1.836r - 12r^2\}] \quad [7.8]$$

Equation 7.8 is valid for the data range:  
 $0 \leq r \leq 0.26$ ,  $0.33 \leq e/t < 0.42$  and  $30 \leq h/t \leq 42$

$$\frac{EI_{eff}}{EI_0} = [\{1 - 0.05(h/t) + 0.000892(h/t)^2\} \{1.7024e^{-0.0133(e/t)}\} \{1 + 2.2r - 12r^2\}] \quad [7.9]$$

Equation 7.9 is valid for the data range:  
 $0 \leq r \leq 0.051$ ,  $0.33 \leq e/t < 0.42$  and  $30 \leq h/t \leq 36$

The equations 7.7, 7.8 and 7.9 reflect a coefficient of determination “ $R^2$ ” of 0.7 0.88 and 0.78. For further verification of the model, an assessment was performed by checking the scatter of the data. The details are discussed in the next section.

### 7.3.3 Assessment of Regression Model for Rigidity Ratio

The capability of the regression model to describe good correlation between dependent and independent variables was examined by plotting FEM and regression model results together. Figure 7.22 through Figure 7.35 show the comparison of FEM and regression model results. The plots show that the regression model is able to predict the rigidity ratio reasonably and has the capability to capture the influence of all key parameters on the rigidity ratio.

In some of the cases the regression model differs from FEM results. For example as shown in Figure 7.22 the regression model gives a higher value of rigidity ratio at  $e/t = 0.1$ ,  $h/t = 30$  and  $r = 0.05$  but the error does not exceed 1.5%. Similarly, at  $e/t = 0.42$ ,  $h/t = 36$  and  $r = 0.26$  (Figure 7.25) the regression model showed conservative estimate of rigidity ratio but the difference did not exceed 10%. The plots given in Figure 7.22 through Figure 7.35 show that in some of the cases the regression model and the FEM results are in complete agreement (e.g. Figure 7.26).

To check whether the regression model has the ability to cover a wide range of the parameters affecting the masonry wall behavior the scatter of data points was plotted about the regression line as shown in Figure 7.36. The scatter contains the rigidity ratio obtained from test results performed in the experimental program of the current study, and the rigidity ratio obtained from FEM results. As illustrated by Figure 7.36, all the data points are closely clustered around the regression line and are located within a 7% error range.

Figure 7.36 shows that the regression model best estimates the rigidity ratio in the range of the data upon which it was based, but if the model is close to the physical behavior of the real structure it should be able to reasonably predict the response out-side the data range of regression analysis. To confirm the capability of the model of capturing the real behavior, the rigidity ratio of test results of Group-I specimens of the current study were also included. The test specimen of Group-I of the experimental program had slenderness ratio of 28.6, as described in chapter three of the thesis. Since the regression analysis was performed for the minimum slenderness ratio of  $h/t = 30$ , the wall specimens of Group-I were outside the data range of regression analysis. As shown in Figure 7.36, the data points of Group-I specimens were situated within a 7% error range about the regression line.

#### 7.4 Comparison of Regression Model with Current Canadian Masonry Design Code-S304.1-94

The literature review shows that the current Canadian Code conservatively estimates the load capacity of masonry load bearing walls. The moment magnifier method is recommended by the code (clause 11.2.5) for the estimation of axial load capacity of the walls, but the method restricts the slenderness ratio to be less than or equal to 30. Walls with  $h/t > 30$  are categorized as very slender walls and the code recommends that these walls be designed as structural members having symmetrical single curvature with pin end conditions with a maximum allowable axial load of:

$$P_f \leq 0.1\Phi_m f'_m A_e \quad [7.10]$$

in which  $P_f$  is the factored axial load,  $\Phi_m = 0.55$  is the resistance factor of the ultimate limit states,  $f'_m$  is the masonry prism compressive strength and  $A_e$  is the effective cross-sectional area of the load bearing masonry wall.

The effective flexural rigidity as recommended by the code is also estimated with some restrictions and provides conservative estimates of the flexural rigidity of masonry load bearing walls [Liu et al. (1998), Liu and Dawe (2003)].

For reinforced masonry walls clause 11.2.5.4 recommends the following equation for the estimation of effective flexural rigidity ( $EI_{eff}$ ):

$$EI_{eff} = E_m \left[ 0.25I_0 - (0.25I_0 - I_{cr}) \left[ \frac{(e - e_k)}{2e_k} \right] \right] \quad [7.11]$$

and

$$E_m I_c \geq EI_{eff} \leq 0.25E_m I_0 \quad [7.12]$$

in which,  $E_m = 850f_m$  is the modulus of elasticity of the masonry assemblage,  $I_0$  is the moment of inertia of the effective area of the cross-section,  $e$  is the load eccentricity calculated by taking the ratio of the primary moment and axial load, while  $e_k = \frac{S}{A_c}$ , where  $S$  is the section modulus. Equation 7.12 provides recommendation of the code for the upper and lower bound values of the  $EI_{ff}$ .

To compare the code recommendations for the design of eccentrically loaded masonry load bearing walls the axial load capacity and the effective flexural rigidity of all the specimens given in Table 7.1 were estimated. Table 7.2 provides a comparison of the values estimated according to the code recommendations and the values obtained from regression model.

In Table 7.2 the normalized axial load capacity for walls with  $h/t = 30$  and with  $r > 0$ , was calculated with minimum effective length factor  $K = 0.8$  as allowed by the code to simulate hinged top and elastic bottom support conditions. For walls with  $h/t > 30$  the code does not allow the use of effective length factor in computing the axial load capacity or in other words always considers a pin-support condition at the bottom of the wall.

As illustrated by Table 7.2, FEM model shows considerably increased axial load capacity for all masonry walls. Even walls with pinned end condition showed more capacity as compared to the capacity obtained from S304.1. The use of an effective length factor as recommended by the code for the walls having  $h/t \leq 30$  does not reflect the actual support conditions and the wall behavior. As shown in Table 7.2 for wall specimens having  $h/t = 30$  (wp1 to wp4 and wp13 to 16 and wp25 to wp28) using  $K = 0.8$  in estimating the load capacities according to the code recommendations does not follow the actual effect of support stiffness and it showed different values of load capacity than the FEM results. As observed in Table 7.2, that at higher load eccentricity ratios the code procedure for slender walls gives smaller capacity than the value obtained from equation 7.10.

The code is particularly more conservative in case of walls with high  $h/t$  ratios loaded with low eccentricity. For example wall specimen wp5 with  $h/t = 36$ ,  $e/t = 0.1$  and  $r = 0$ , showed a much higher capacity as compared to the code recommended value. It is also important to observe that according to the code recommendations walls with  $h/t = 36$  or  $h/t = 42$  have the same load capacity by applying code rule given in equation 7.9. (For walls with  $h/t > 30$  the allowable axial load capacity  $\leq 0.1f'_m A_c$ .) This brings up an important issue that even with pinned end conditions the walls with  $h/t > 30$  have much more capacity as opposed to the recommendations of the current code.

For walls with  $h/t > 30$  tested with  $e/t=0.33$  the code gives comparatively less conservative values than the same walls loaded with  $e/t=0.1$ . Nonetheless FEM results showed almost 46 % more capacity as compared to the code at pinned end conditions. In case of walls with  $h/t = 42$  the difference between the code and the FEM predictions were found to be around 34%. However at very high load eccentricity ratio i.e.  $e/t = 0.42$  the FEM and the code predicted almost the same capacities for both walls with  $h/t = 36$  (specimen wp29) and the wall with  $h/t = 42$  (specimen wp33) at pinned end conditions.

All walls with non zero support stiffness ratio, showed considerably higher capacities as compared to the current code recommended wall capacities. At lower load eccentricity and slenderness ratios the effect of support conditions allowed the walls to attain much higher loads as compared to code recommended capacities. For example in Table 7.2, the specimen wp2, wp3 and wp4, which were tested with  $r > 0$ , showed capacities more than twice those recommended by the code.

In case of walls with  $h/t > 30$ ,  $e/t > 0.1$  and  $r > 0$  the code predicts highly conservative load capacities for two reasons. First the code estimates very low values of the effective flexural rigidity. Secondly, it does not account for support

conditions and assumes pinned end conditions. The same walls when tested under the influence of support conditions showed a substantially higher load capacity (e.g. wall specimens wp6, wp7 and wp8 with  $h/t = 36$ ,  $e/t = 0.1$  and  $r > 0$  and the wall specimens with  $h/t = 42$ ,  $e/t = 0.1$  and  $r > 0$ , as shown in Table 7.2).

It is important to mention that the current Canadian code does not differentiate between masonry walls with respect to the eccentricity ratio and only categorizes the walls by limiting the slenderness ratio. However, it is observed through FEM results that even the walls with  $h/t > 30$  (very tall walls as per the code) when loaded with lower  $e/t$  ratios showed considerably higher load capacities. The FEM results indicated that the code is conservative in estimating wall capacities for the cases when  $h/t > 30$  and  $e/t \leq 0.33$  the difference increases with increasing support stiffness ratio.

For walls loaded with  $e/t > 0.333$ ,  $r = 0$  and  $h/t > 30$  the code appeared to be accurate. However the code becomes conservative when support stiffness is considered (i.e.  $r > 0$ ) for walls having  $h/t \leq 36$  loaded with  $e/t > 0.33$ , as shown in Table 7.2 for the wall specimens wp30, wp31 and wp32.

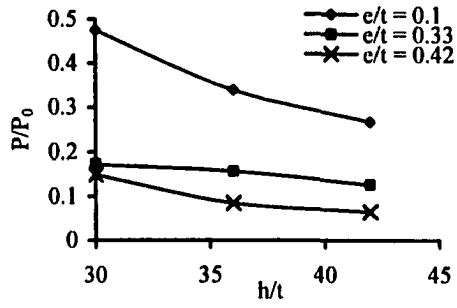
As shown by Table 7.2, the regression model proposed in this chapter reasonably estimates the load capacity for all cases except for walls with  $h/t = 42$ , loaded with  $e/t = 0.42$  and with all support stiffness ratios (i.e. wall specimens wp33 to wp36 in Table 7.2). Therefore, the application of regression models of both axial load capacity and rigidity ratio are restricted, as shown in equation 7.5 and equation 7.8, to walls with  $h/t \leq 36$  for  $e/t > 0.33$  due to increased level of instability caused by the combined effect of high load eccentricity and high slenderness it is recommended not to consider the effect of support conditions in this range of load eccentricity with high slenderness ratio.

From the above discussion it is clear that the current Canadian code (S304.1-94) underestimates the load capacity and flexural rigidity of masonry load bearing

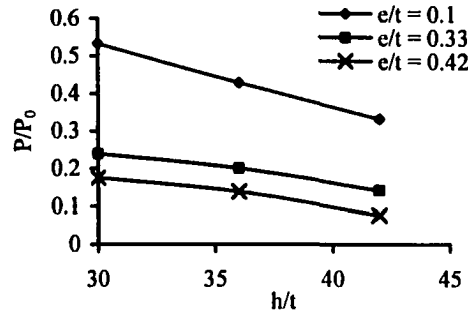
walls. The code is highly conservative in treating walls with slenderness ratio greater than 30 and subjected to load eccentricity less than or equal to 0.33. Consideration of support condition in estimating the wall capacity is also a very important issue. The FEM results clearly showed the support stiffness effect on the wall capacity and verified that in case of walls with  $h/t > 30$  ignoring the support stiffness influence by assuming a pinned end condition as recommended by the code, results in under-estimation of wall capacity. The use of effective length factor in the current code provisions in estimating the wall capacity, when  $h/t \leq 30$  is crude and does not correlate with the actual support stiffness and its influence on wall behavior.

The effective flexural rigidity of the walls estimated according to code recommendations is quite conservative. The estimation of effective flexural rigidity obtained from FEM results showed much higher values than the code. Even if conservatively 50% of the FEM value of effective flexural rigidity is considered, the code still seems to underestimate the rigidity.

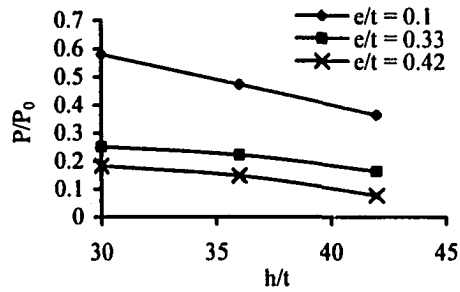
In the context of regression analysis presented in this chapter it is recommended to further extend the current research towards the incorporation of suggested equation of axial load capacity and the effective flexural rigidity into conventional moment magnifier method by translating them into more realistic estimation of effective length factor.



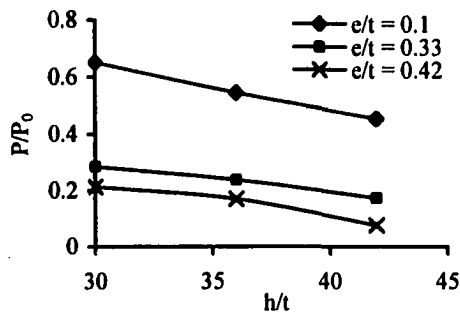
a)  $r = 0$



b)  $r = 0.025$

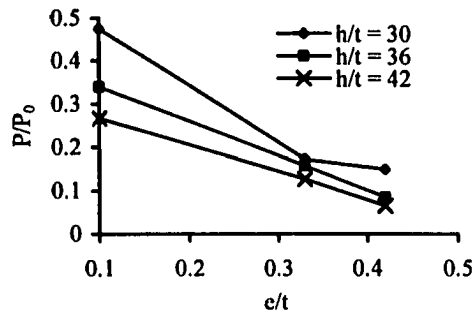


c)  $r = 0.05$

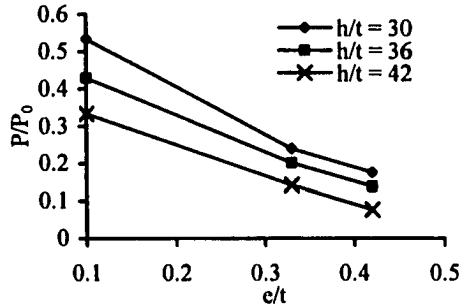


b)  $r = 0.05$

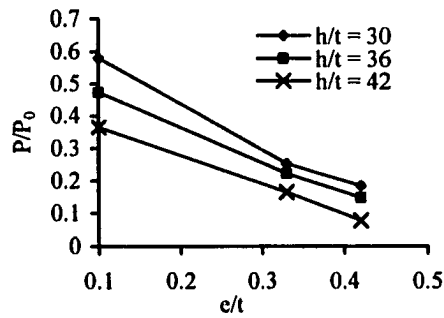
**Figure 7.1 Normalized axial load capacity versus slenderness ratio at NC = 3 for constant support stiffness ratio**



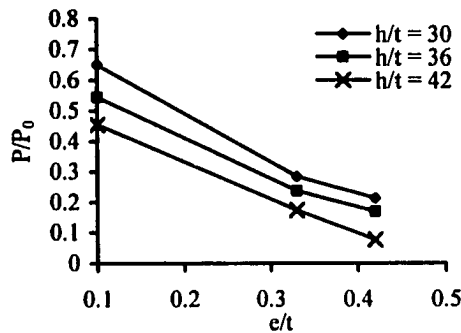
a)  $r = 0$



b)  $r = 0.026$

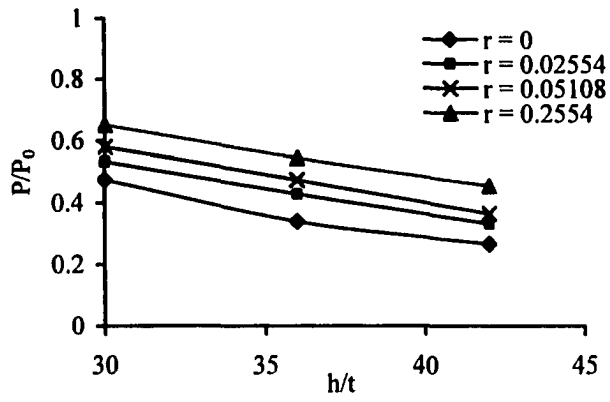


c)  $r = 0.05$

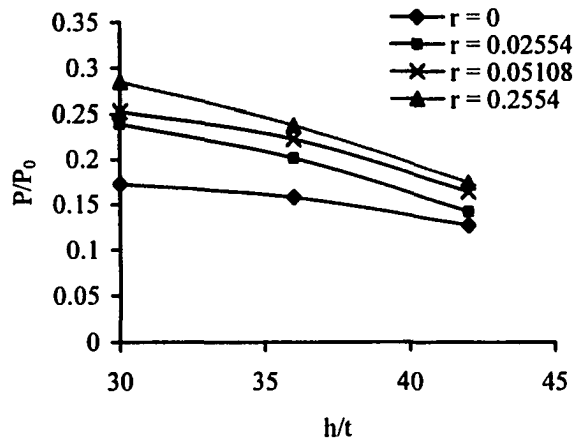


d)  $r = 0.26$

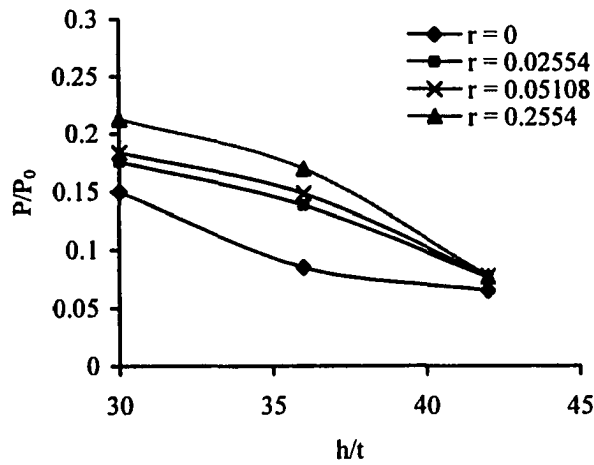
**Figure 7.2 Normalized axial load capacity versus load eccentricity ratio at NC = 3 for constant support stiffness ratio**



a)  $e/t = 0.1$

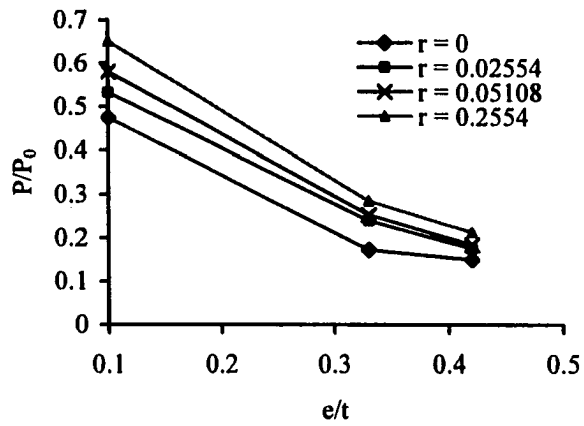


b)  $e/t = 0.33$

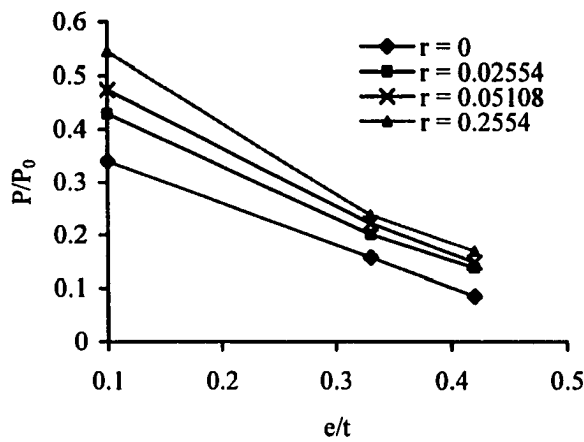


c)  $e/t = 0.42$

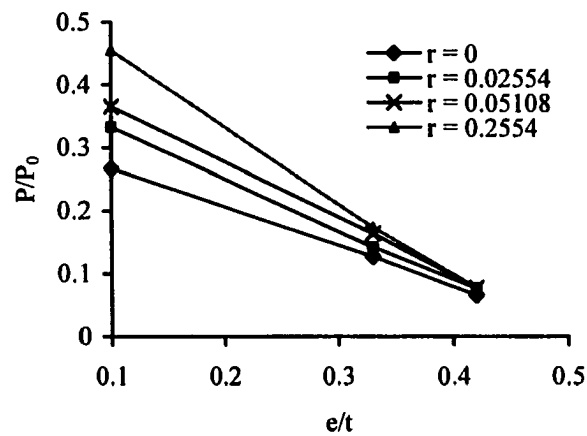
**Figure 7.3 Normalized axial load capacity versus slenderness ratio at NC = 3 for constant support stiffness ratio**



a)  $h/t = 30$

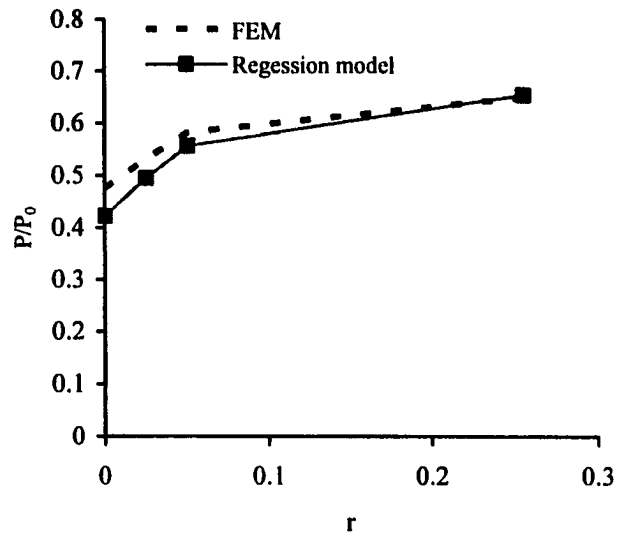


b)  $h/t = 36$

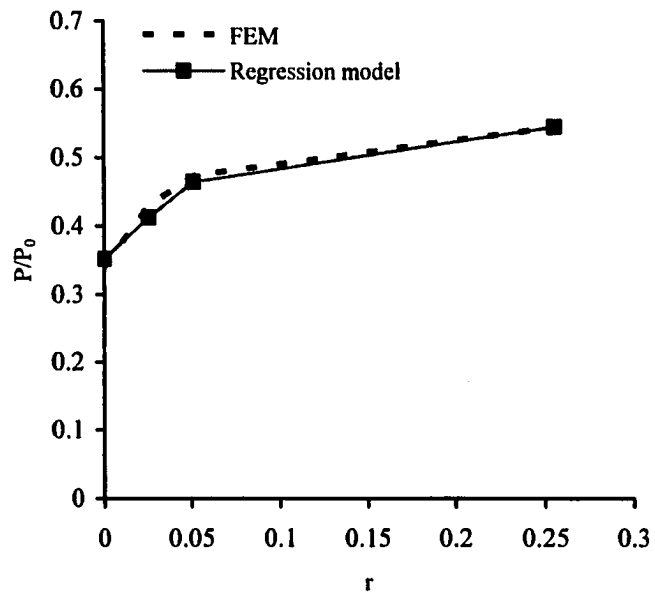


c)  $h/t = 42$

**Figure 7.4 Normalized axial load capacity versus load eccentricity ratio at  $NC = 3$  for constant support stiffness ratio**

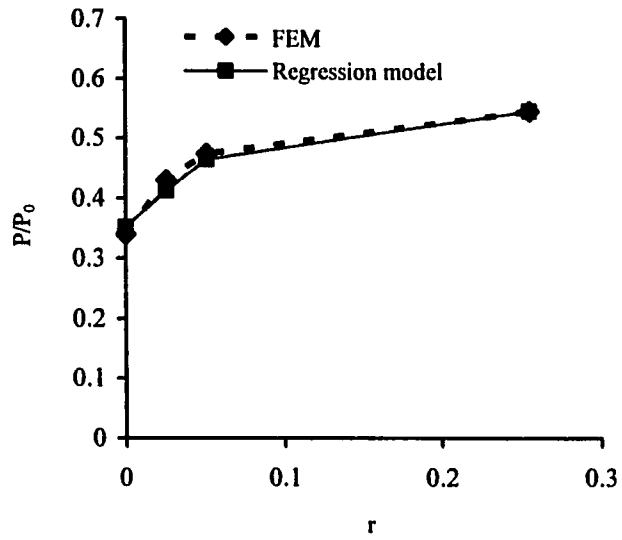


a)  $e/t = 0.1$

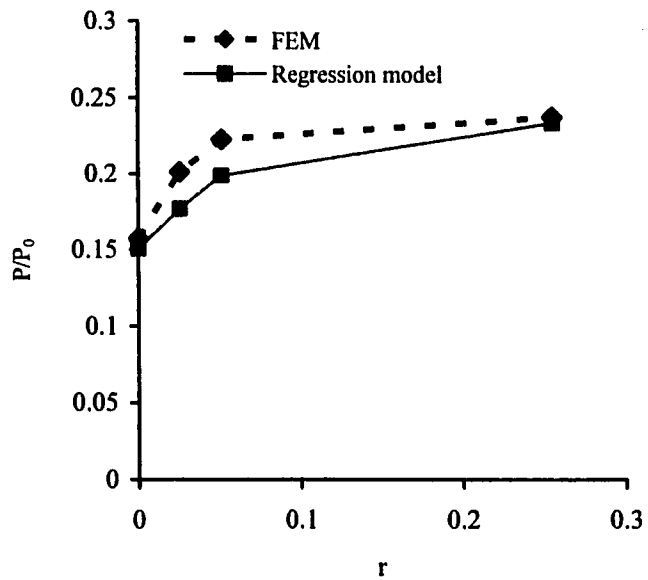


b)  $e/t = 0.33$

**Figure 7.5 Variation of normalized axial load predictions against support stiffness ratio at  $h/t = 30$**

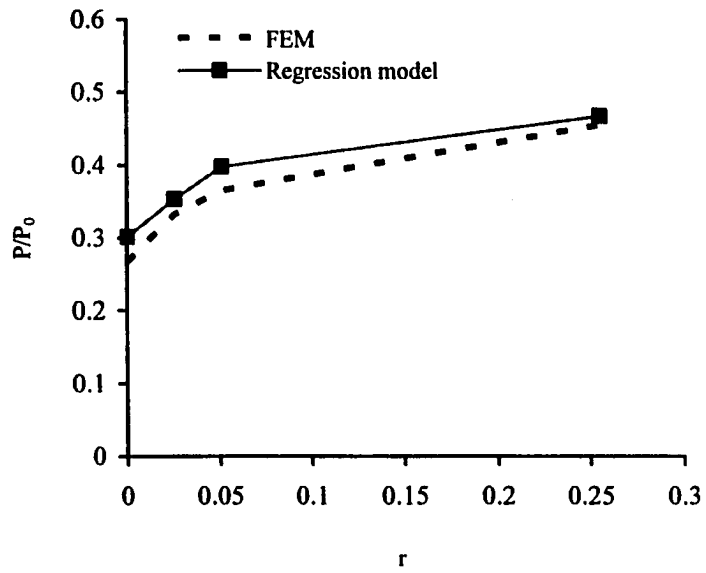


a)  $e/t = 0.1$

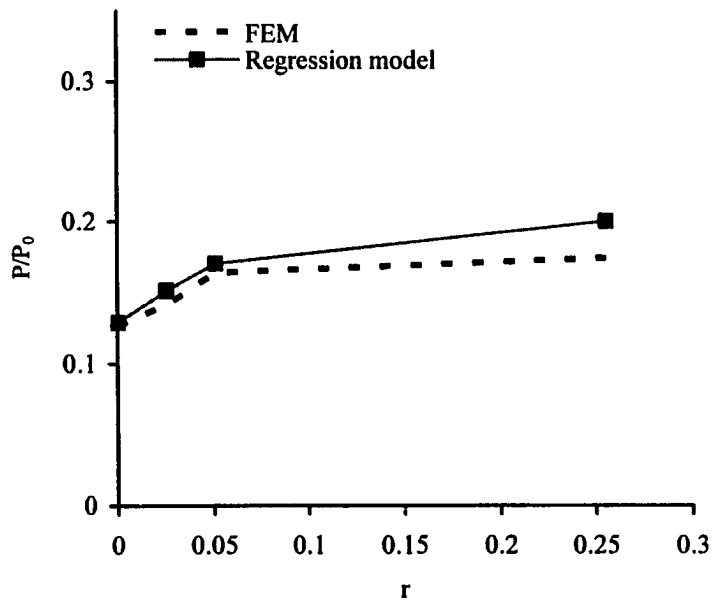


b)  $e/t = 0.33$

**Figure 7.6 Variation of normalized axial load predictions against support stiffness ratio at  $h/t = 36$**

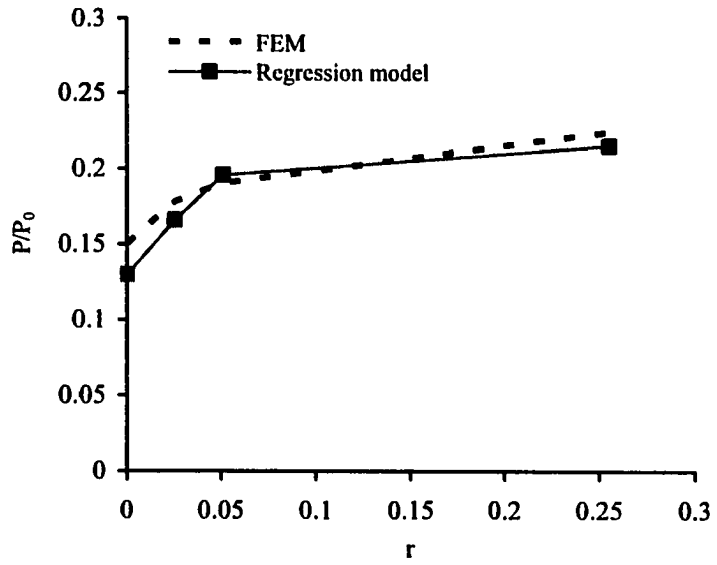


a)  $e/t = 0.1$

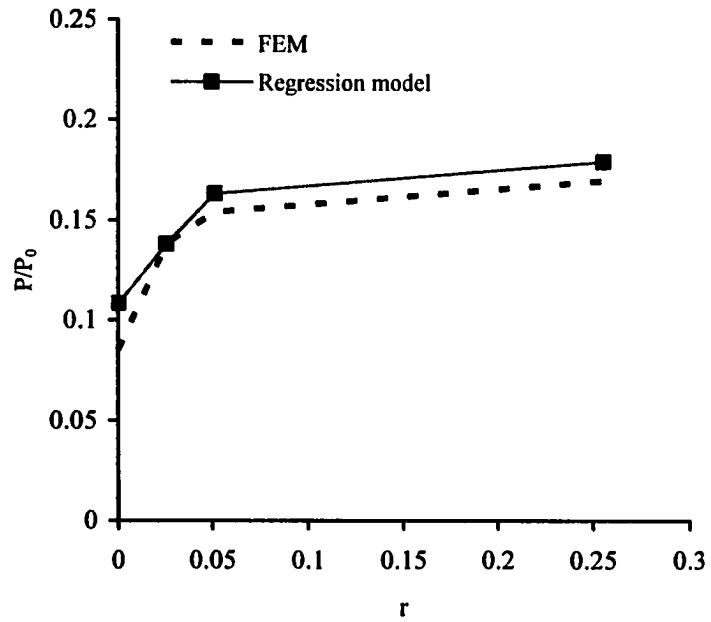


b)  $e/t = 0.33$

**Figure 7.7 Variation of normalized axial load predictions against support stiffness ratio at  $h/t = 42$**

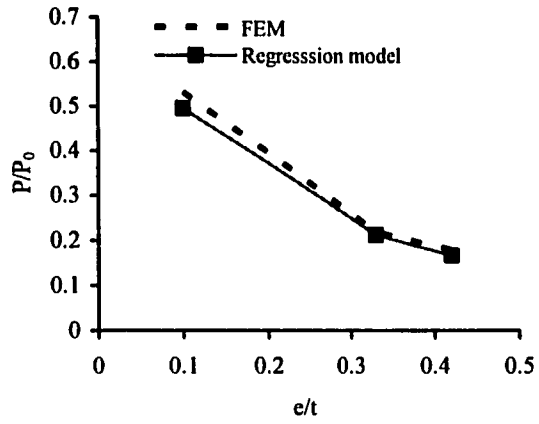


a)  $h/t = 30$

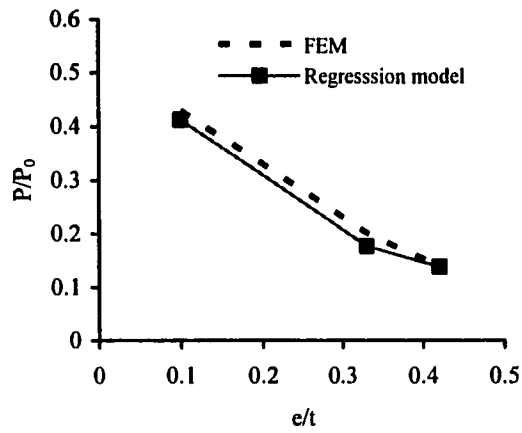


b)  $h/t = .36$

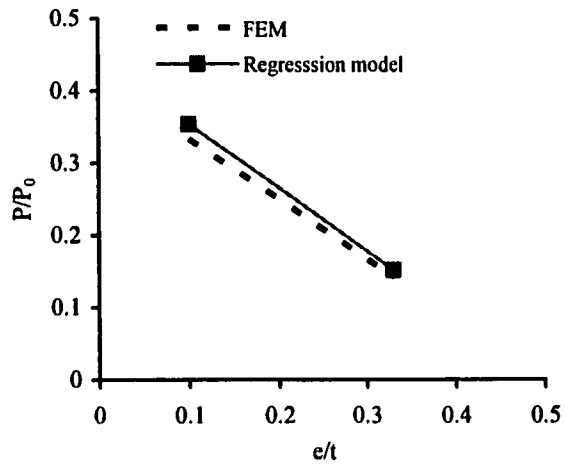
**Figure 7.8 Variation of normalized axial load predictions against support stiffness ratio at  $e/t = 0.42$**



a)  $h/t = 30$

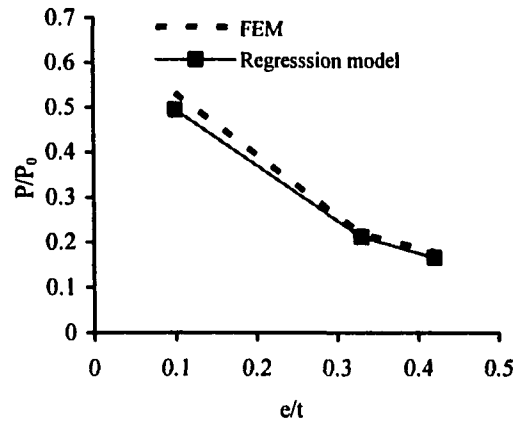


b)  $h/t = 36$

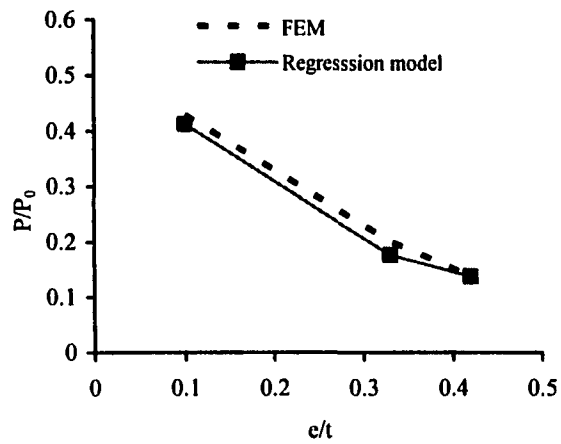


c)  $h/t = 42$

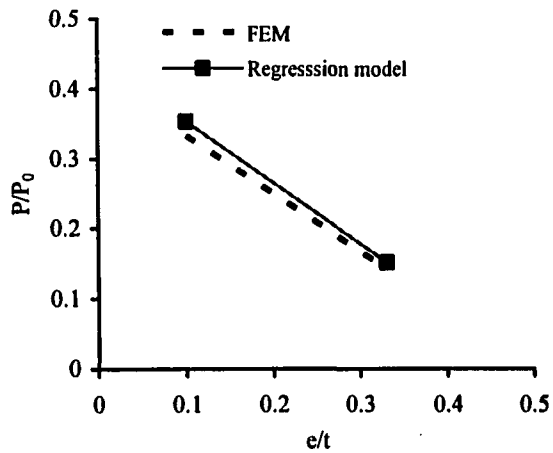
**Figure 7.9** Variation of normalized axial load predictions against load eccentricity ratio at  $r = 0$



a)  $h/t = 30$

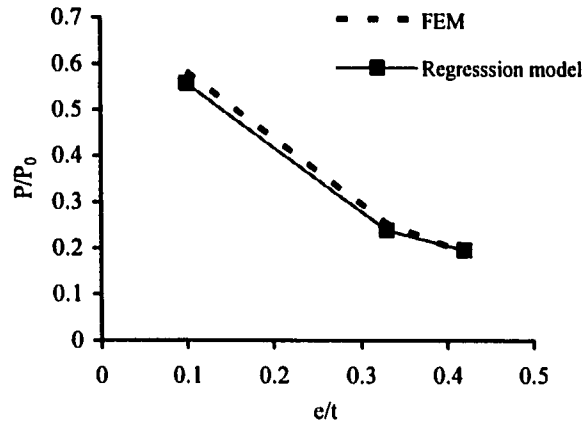


b)  $h/t = 36$

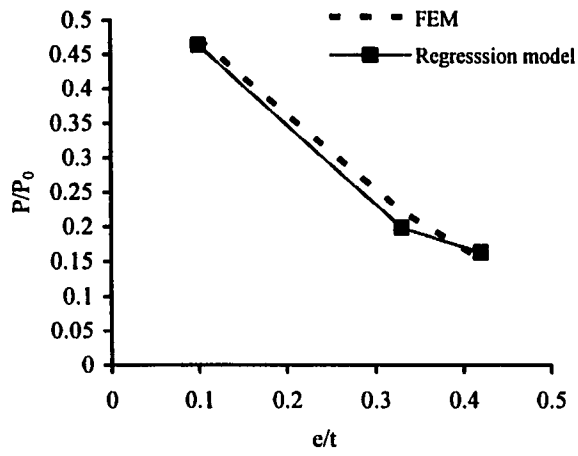


c)  $h/t = 42$

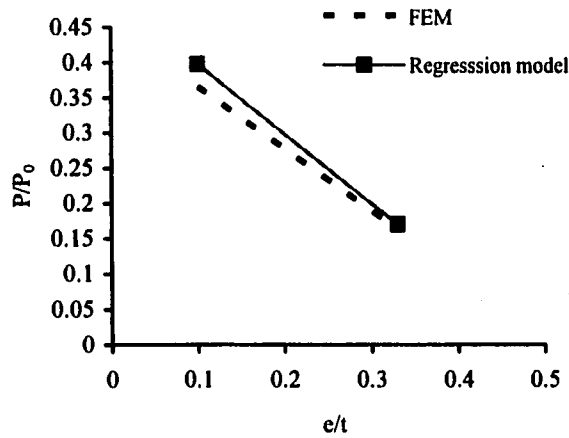
**Figure 7.10 Variation of normalized axial load predictions against load eccentricity ratio at  $r = 0.03$**



a)  $h/t = 30$

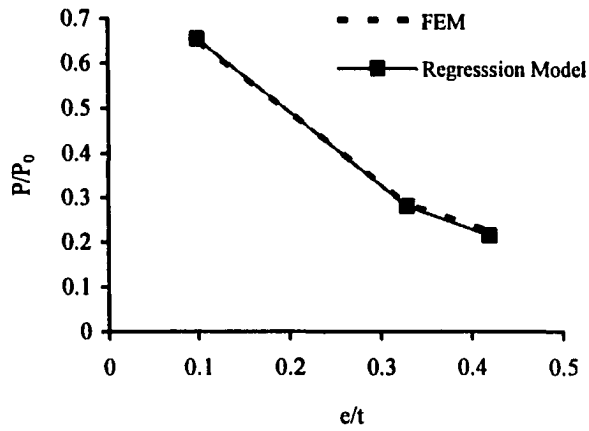


b)  $h/t = 36$

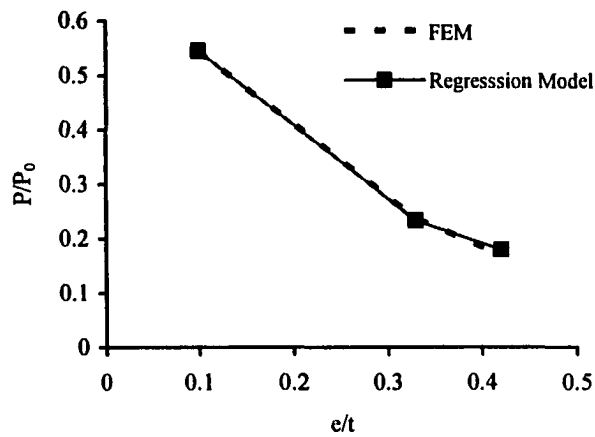


c)  $h/t = 42$

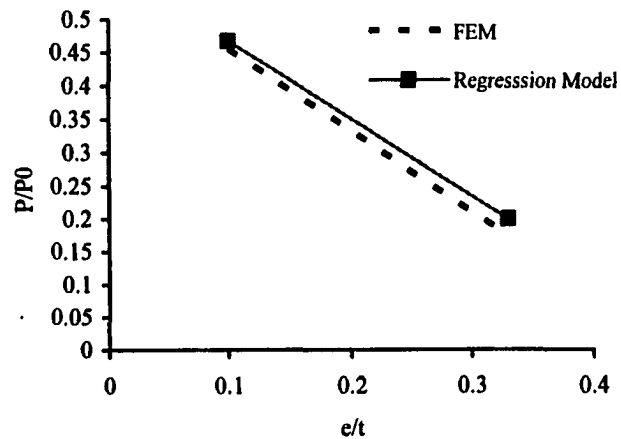
**Figure 7.11 Variation of normalized axial load predictions against load eccentricity ratio at  $r = 0.05$**



a)  $h/t = 30$

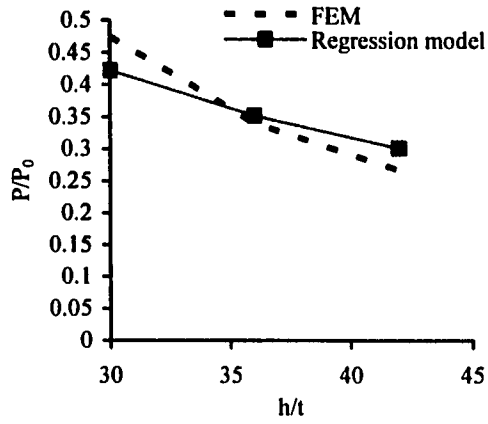


b)  $h/t = 36$

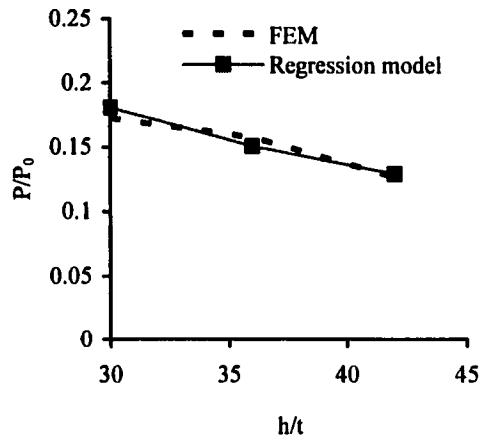


c)  $h/t = 42$

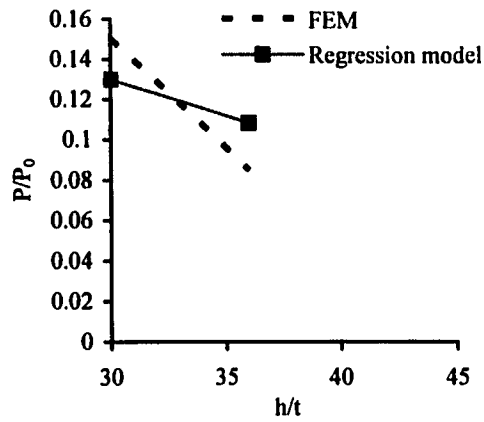
**Figure 7.12 Variation of normalized axial load predictions against load eccentricity ratio at  $r = 0.26$**



a)  $e/t = 0.1$

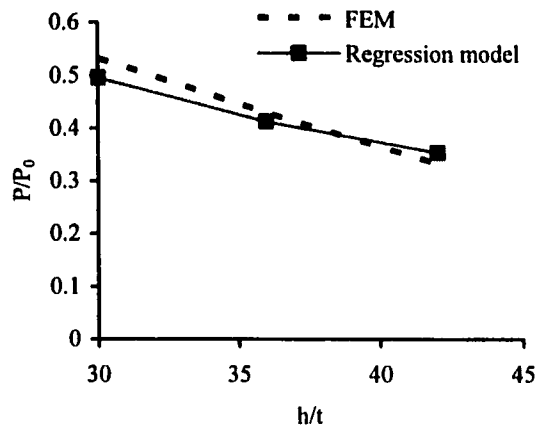


b)  $e/t = 0.33$

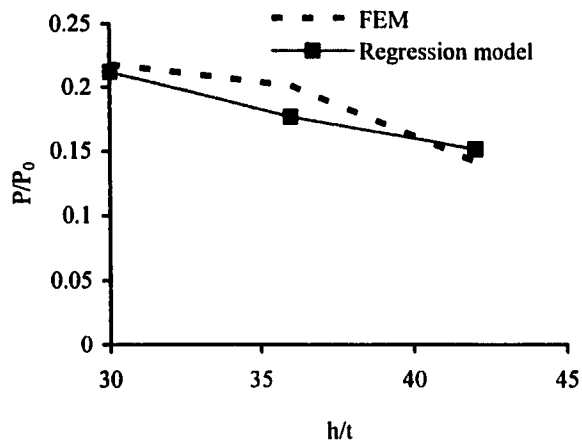


c)  $e/t = 0.42$

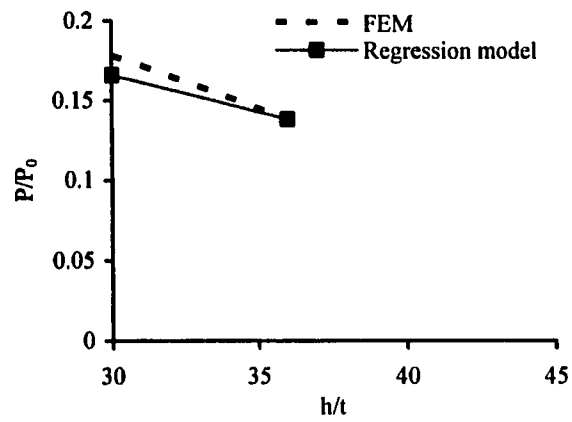
**Figure 7.13 Variation of normalized axial load predictions against slenderness ratio at  $r = 0$**



a)  $e/t = 0.1$

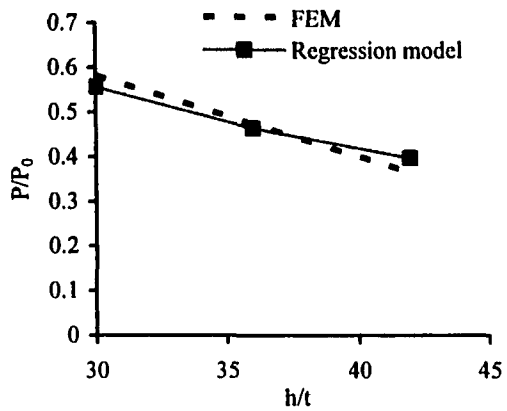


b)  $e/t = 0.33$

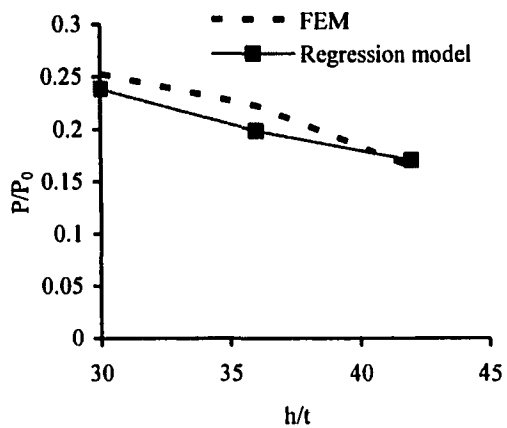


c)  $e/t = 0.42$

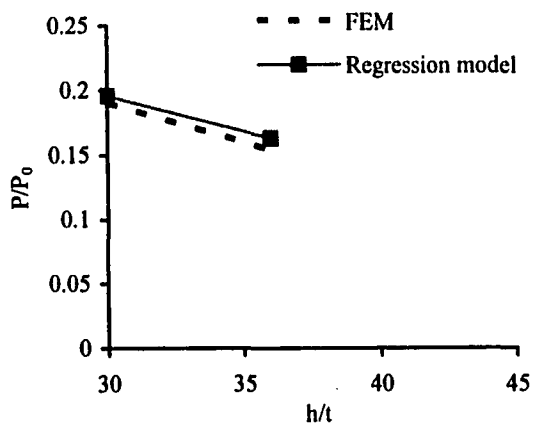
**Figure 7.14 Variation of normalized axial load predictions against slenderness ratio at  $r = 0.03$**



a)  $e/t = 0.1$

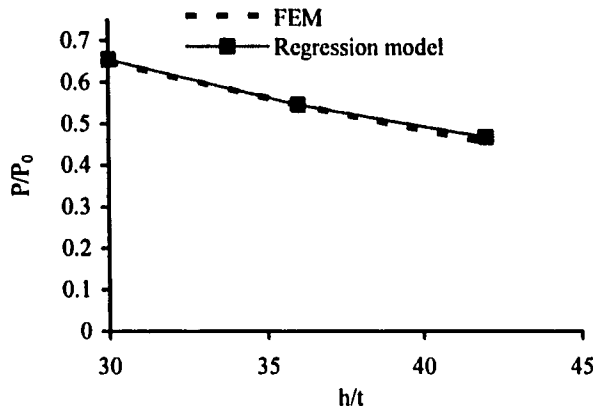


b)  $e/t = 0.33$

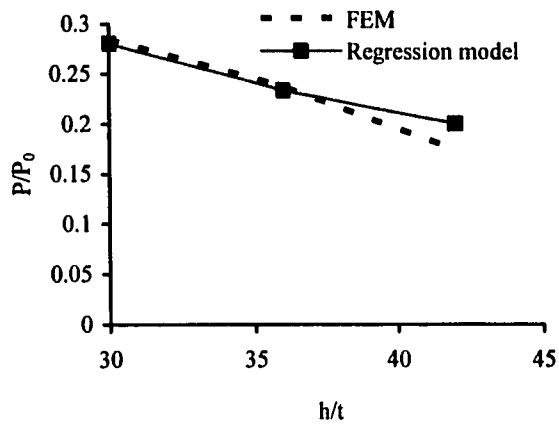


c)  $e/t = 0.42$

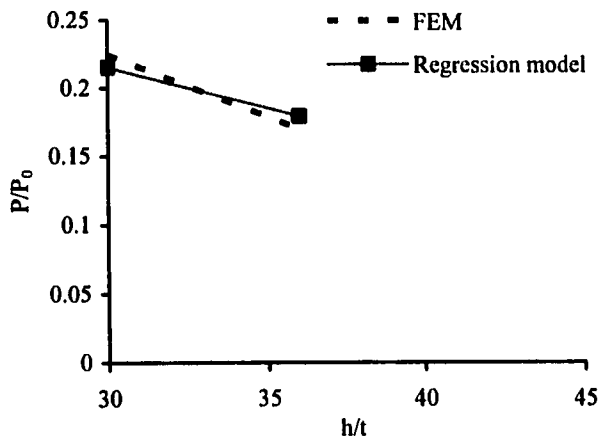
**Figure 7.15** Variation of normalized axial load predictions against slenderness ratio at  $r = 0.05$



a)  $e/t = 0.1$



b)  $e/t = 0.33$



c)  $e/t = 0.42$

**Figure 7.16 Variation of normalized axial load predictions against slenderness ratio at  $r = 0.26$**

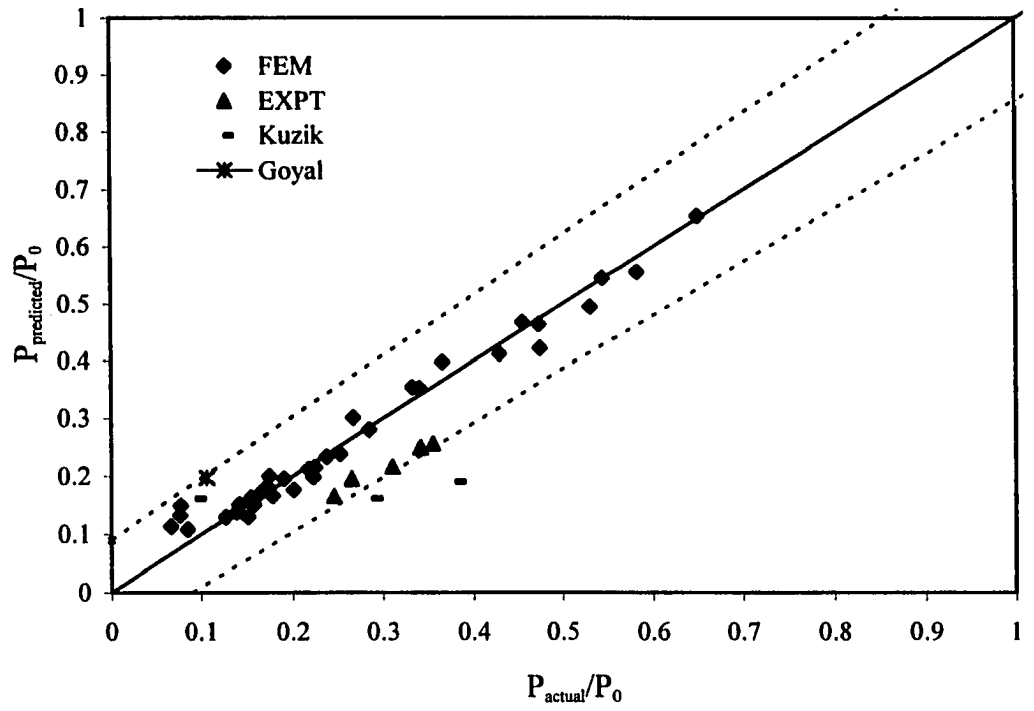
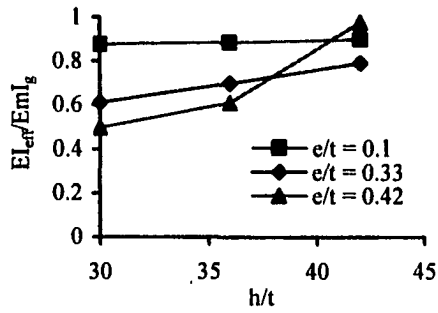
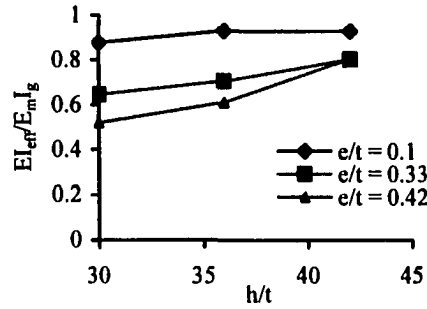


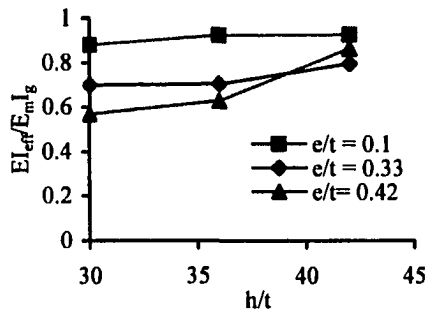
**Figure 7.17 Scatter of the normalized axial load data**



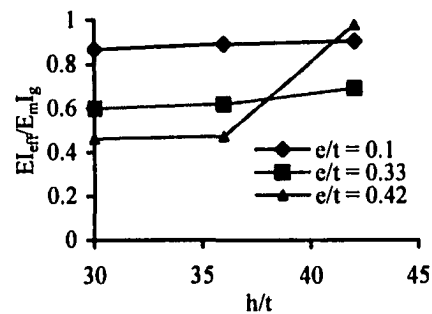
a)  $r = 0$



b)  $b = 0.03$

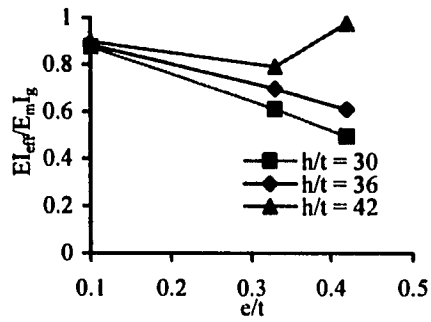


c)  $r = 0.05$

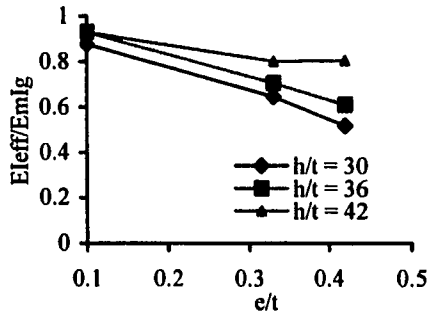


d)  $r = 0.26$

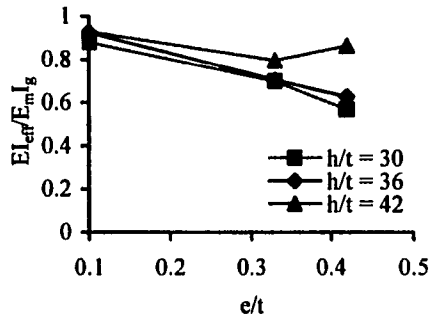
**Figure 7.18 Correlation between flexural rigidity ratio and slenderness ratio at constant support stiffness ratio**



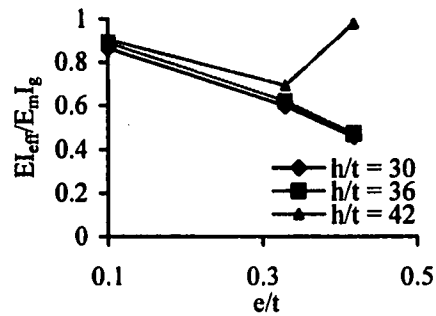
a)  $r = 0$



b)  $r = 0.03$

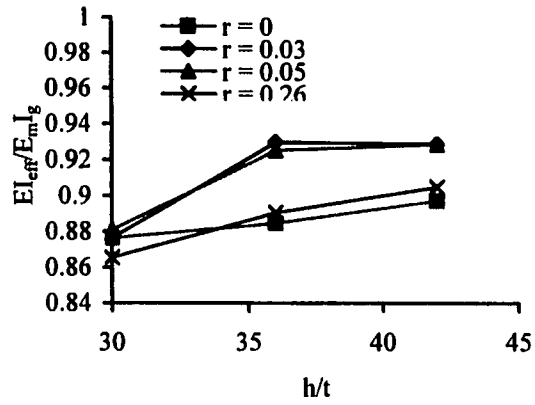


c)  $r = 0.05$

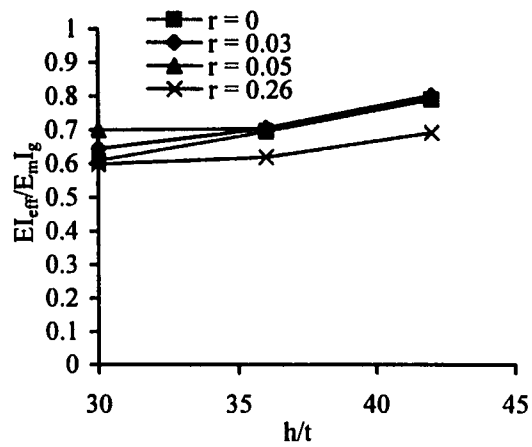


d)  $r = 0.26$

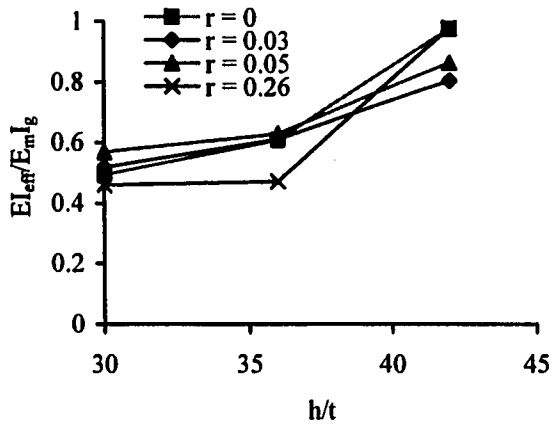
**Figure 7.19 Correlation between flexural rigidity ratio and load eccentricity ratio at constant support stiffness ratio**



a)  $e/t = 0.1$

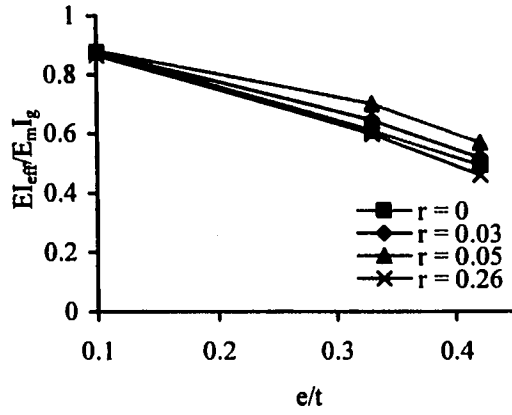


b)  $e/t = 0.33$

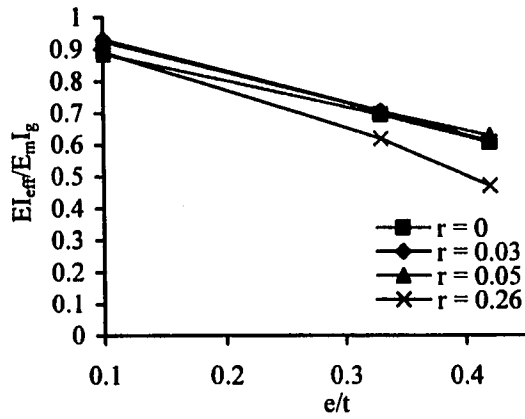


c)  $e/t = 0.42$

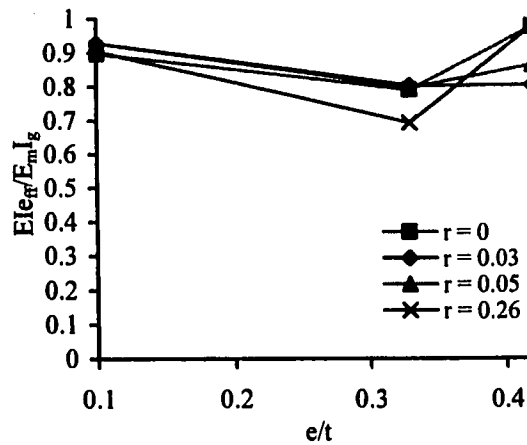
**Figure 7.20 Correlation between flexural rigidity ratio and slenderness ratio at constant load eccentricity ratio**



a)  $h/t = 30$

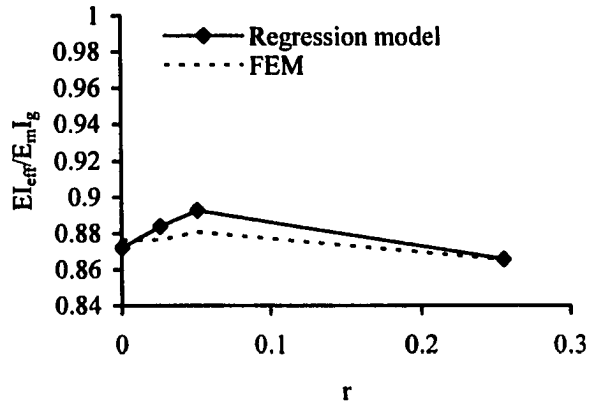


b)  $h/t = 36$

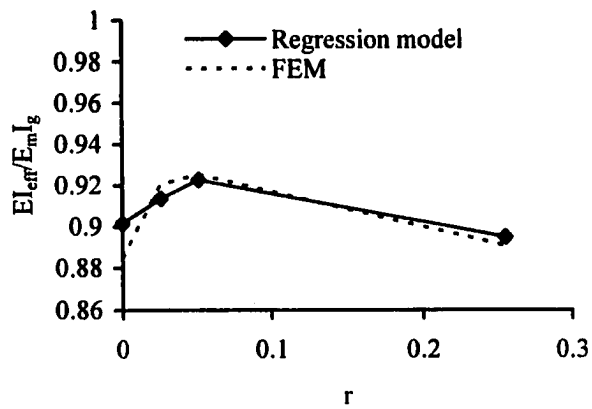


c)  $e/t = 42$

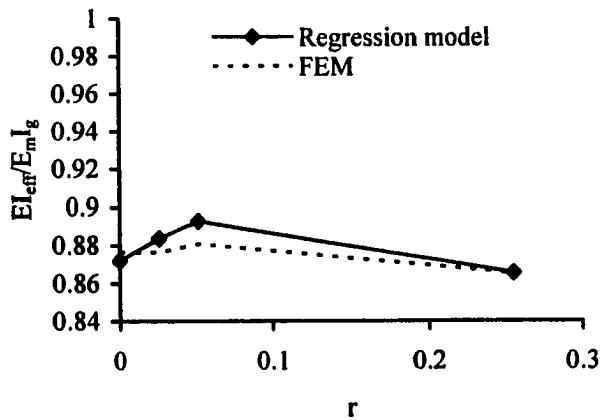
**Figure 7.21 Correlation between flexural rigidity ratio and load eccentricity ratio at constant slenderness ratio**



a)  $h/t = 30$

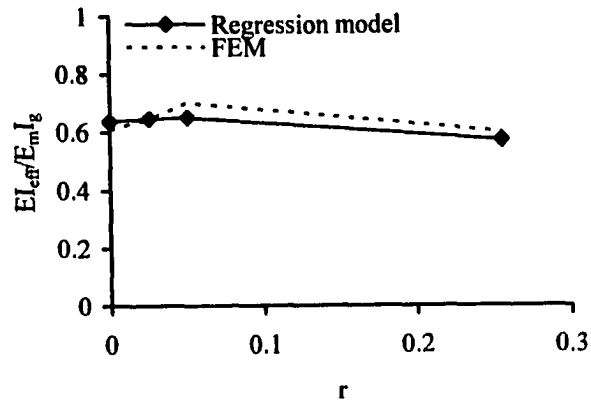


b)  $h/t = 36$

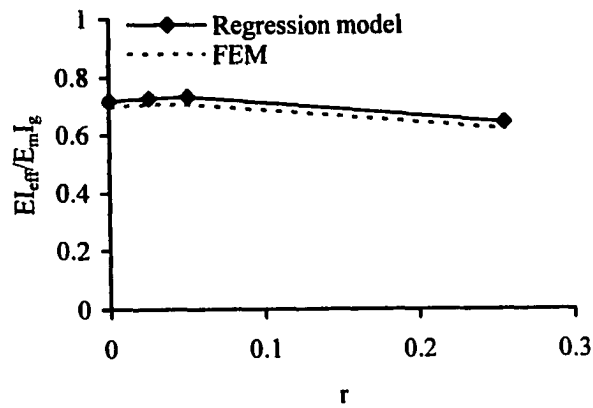


c)  $h/t = 36$

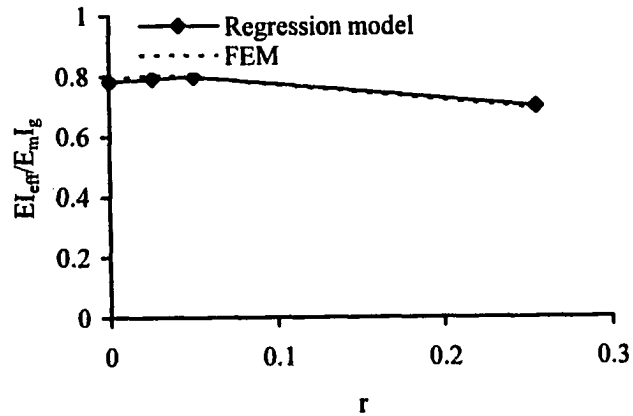
**Figure 7.22** Variation of flexural rigidity ratio predictions against support stiffness ratio at  $e/t = 0.1$



a)  $h/t = 30$

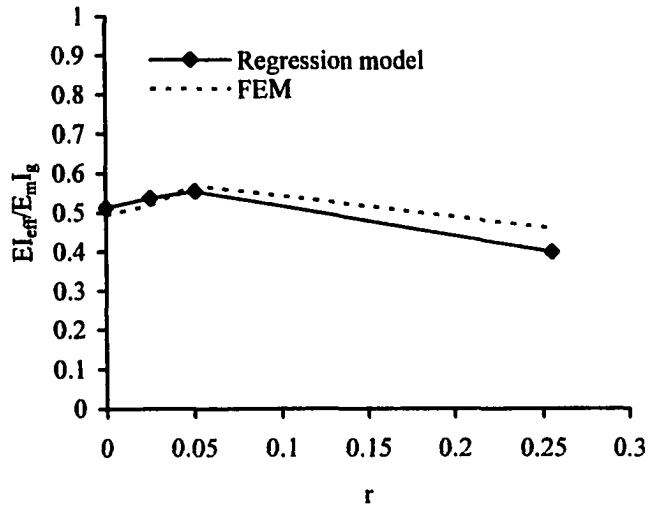


b)  $h/t = 36$



c)  $h/t = 42$

**Figure 7.23 Variation of flexural rigidity ratio predictions against support stiffness ratio at  $e/t = 0.33$**



a)  $h/t = 30$

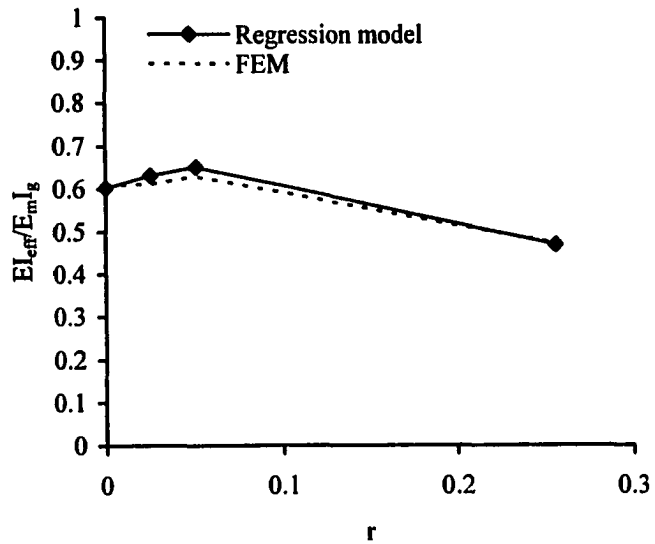
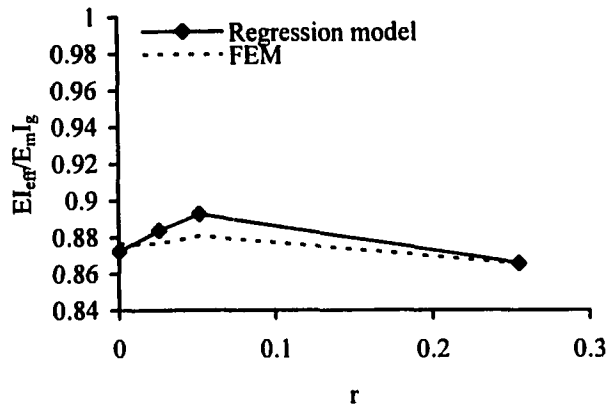
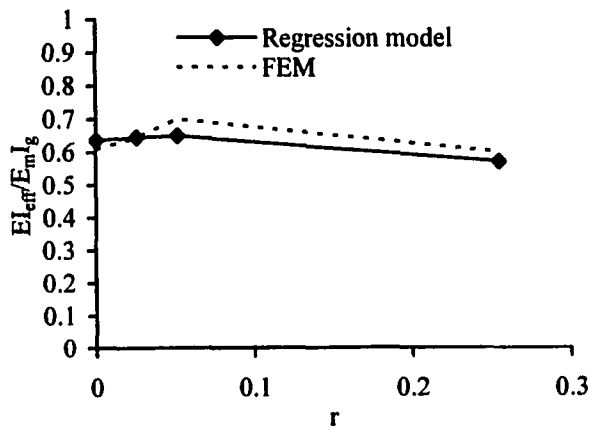


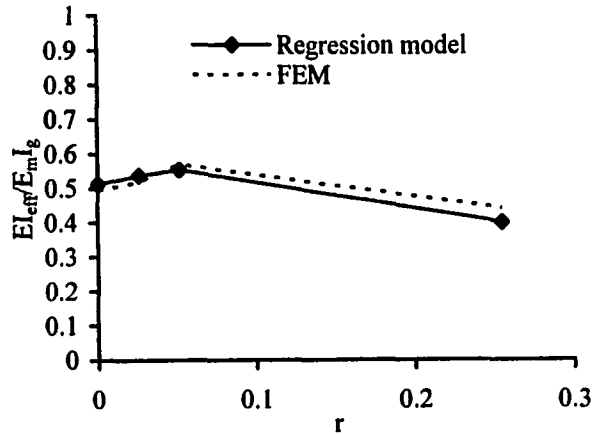
**Figure 7.24 Variation of flexural rigidity ratio predictions against support stiffness ratio at  $e/t = 0.42$**



a)  $e/t = 0.1$

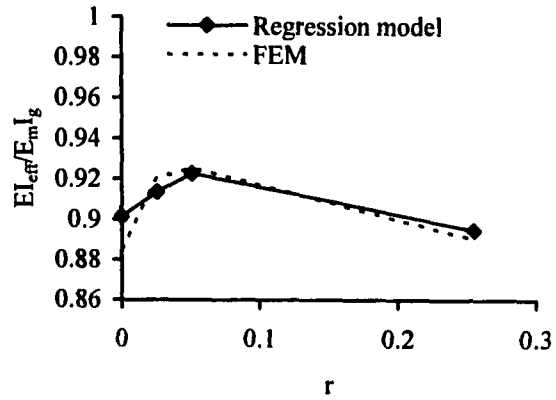


b)  $e/t = 0.33$

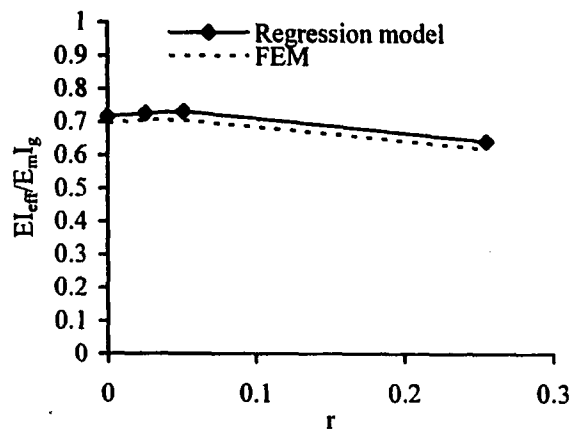


c)  $h/t = 0.42$

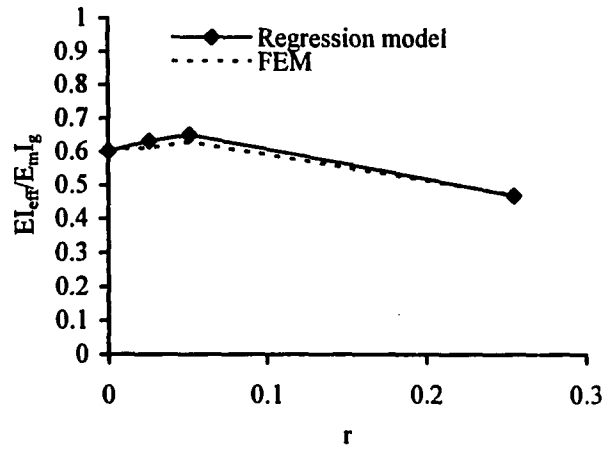
**Figure 7.25 Variation of flexural rigidity ratio predictions against support stiffness ratio at  $h/t = 30$**



a)  $e/t = 0.1$

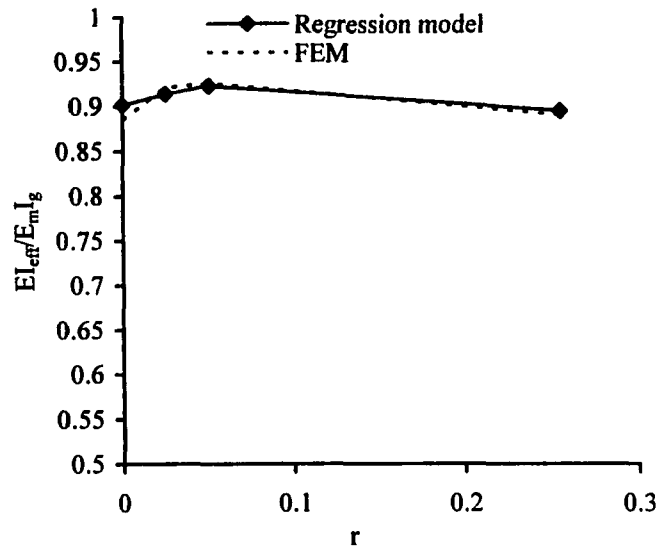


b)  $e/t = 0.33$

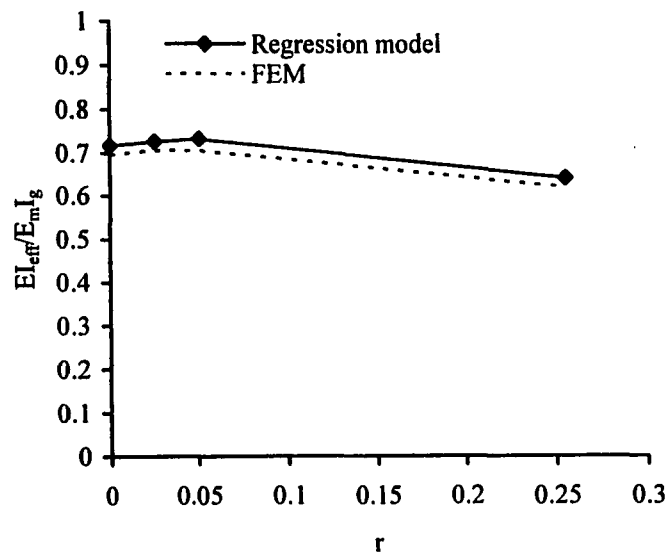


c)  $e/t = 0.42$

**Figure 7.26 Variation of flexural rigidity ratio predictions against support stiffness ratio at  $h/t = 36$**

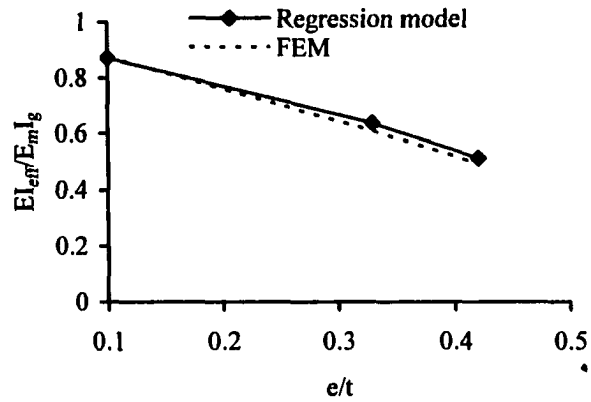


a)  $e/t = 0.1$

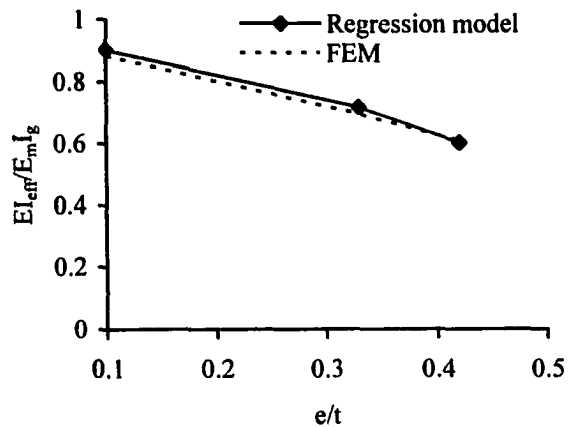


b)  $e/t = 0.33$

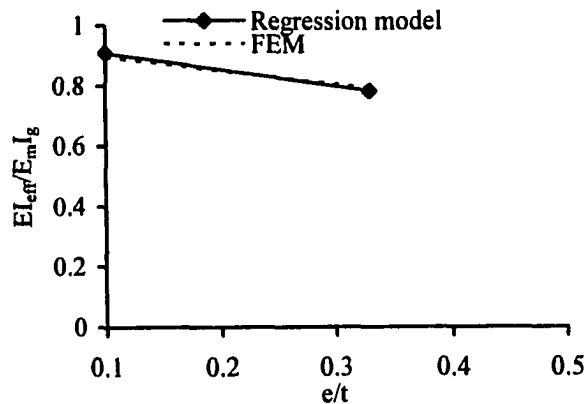
**Figure 7.27** Variation of flexural rigidity ratio predictions against support stiffness ratio at  $h/t = 42$



a)  $h/t = 30$

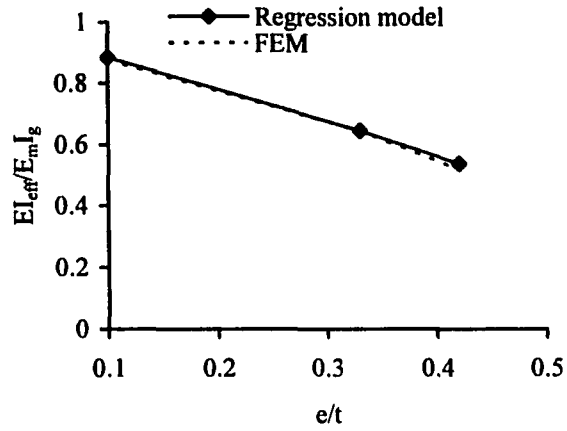


b)  $h/t = 36$

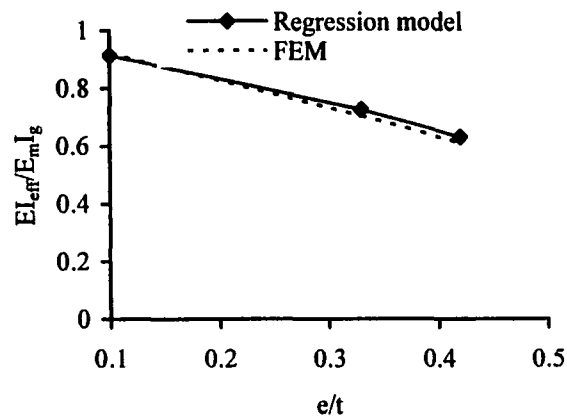


c)  $h/t = 42$

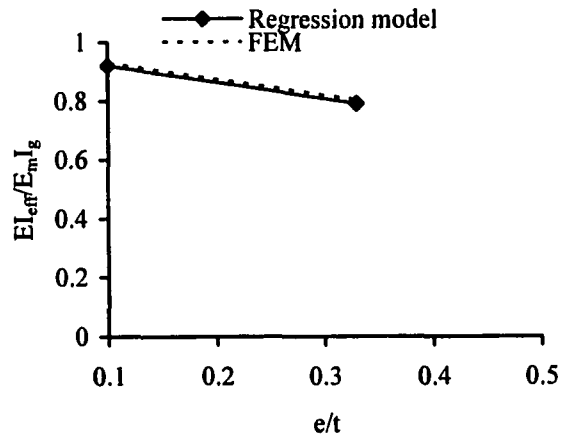
**Figure 7.28 Variation of flexural rigidity ratio predictions against load eccentricity ratio at support stiffness ratio = 0**



a)  $h/t = 30$

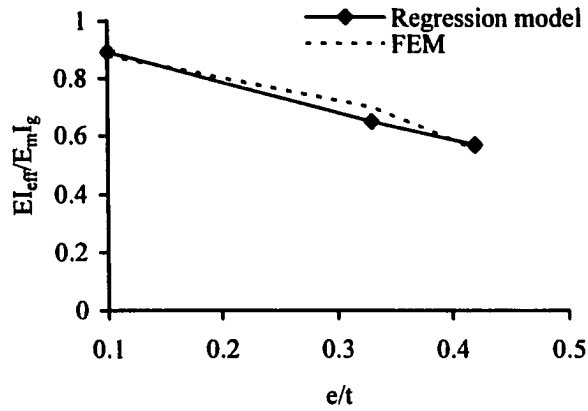


b)  $h/t = 36$

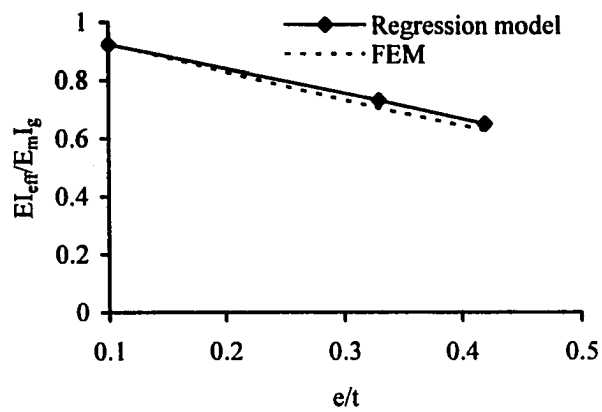


c)  $h/t = 42$

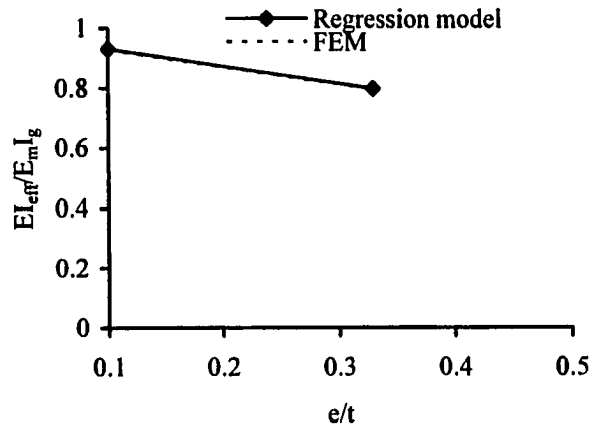
**Figure 7.29 Variation of flexural rigidity ratio predictions against load eccentricity ratio at support stiffness ratio = 0.03**



a)  $h/t = 30$

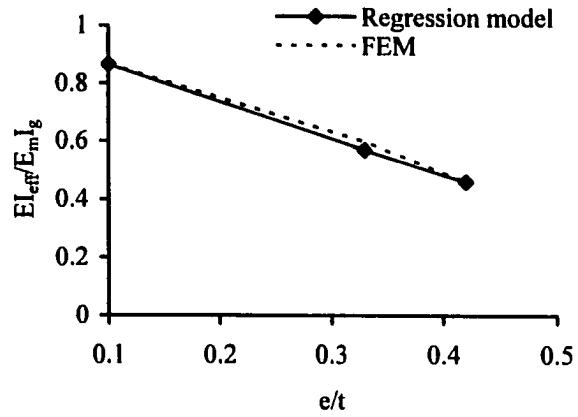


b)  $h/t = 36$

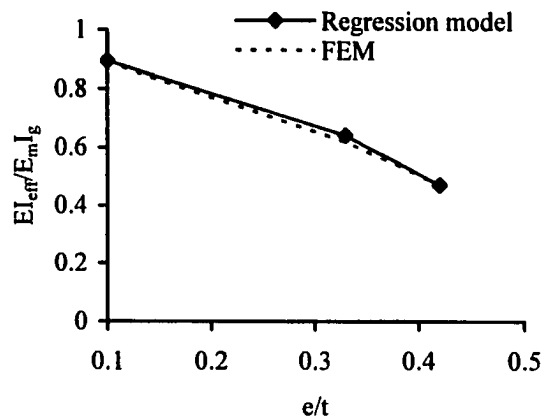


c)  $h/t = 42$

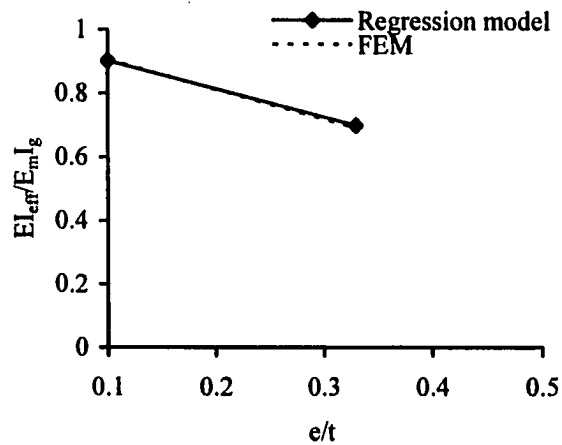
**Figure 7.30 Variation of flexural rigidity ratio predictions against load eccentricity ratio at support stiffness ratio = 0.05**



a)  $h/t = 30$

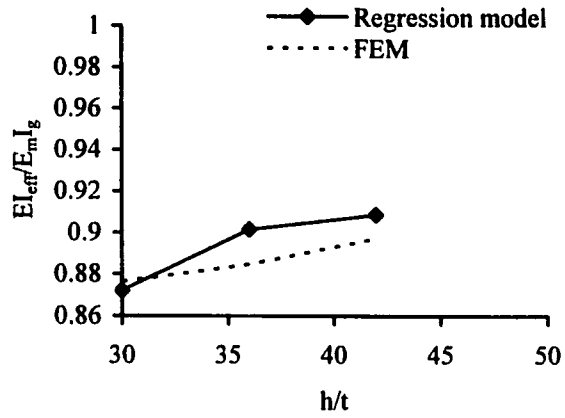


b)  $h/t = 36$

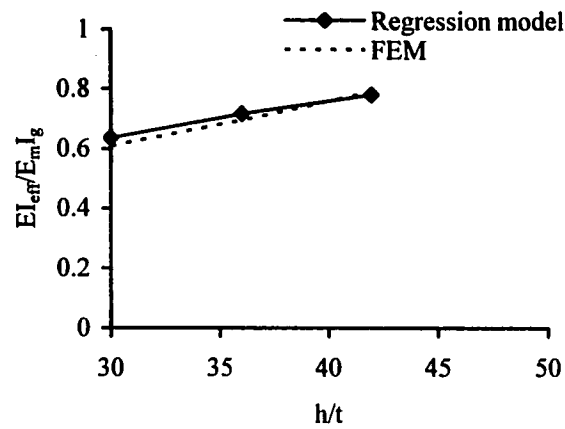


c)  $h/t = 42$

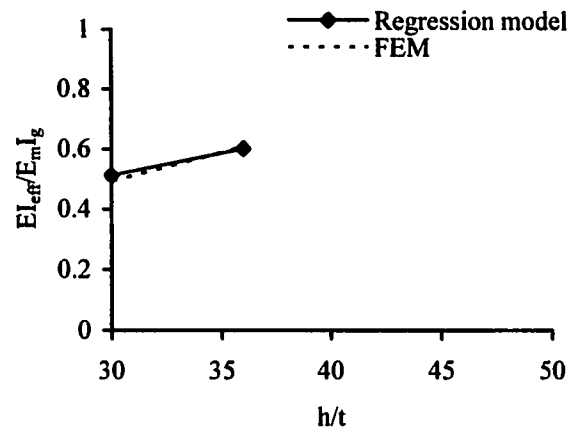
**Figure 7.31 Variation of flexural rigidity ratio predictions against load eccentricity ratio at support stiffness ratio = 0.26**



a)  $e/t = 0.1$

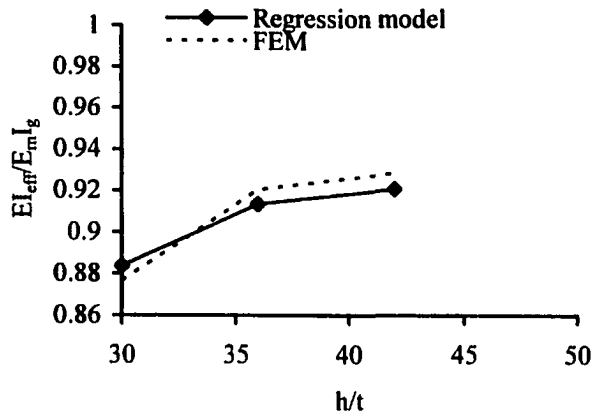


b)  $e/t = 0.33$

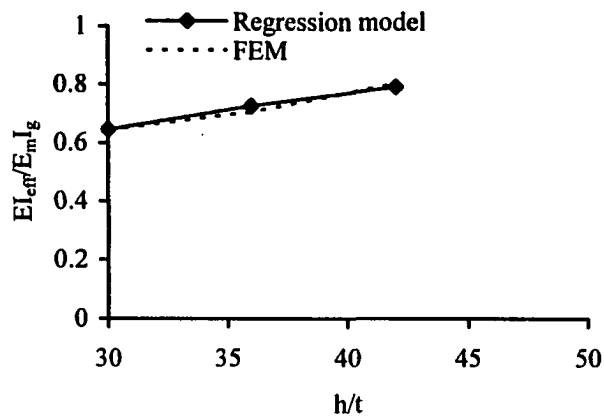


c)  $e/t = 0.42$

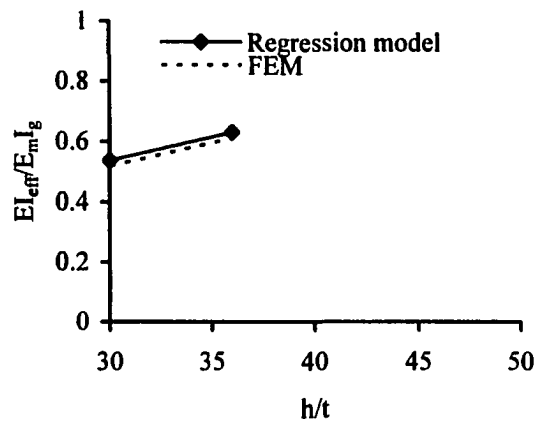
**Figure 7.32 Variation of flexural rigidity ratio predictions against slenderness ratio at support stiffness ratio = 0**



a)  $e/t = 0.1$

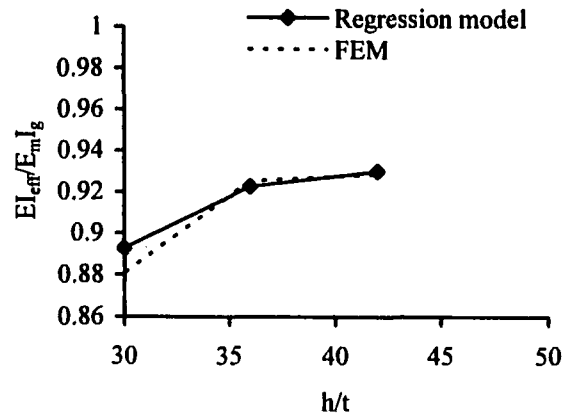


b)  $e/t = 0.33$

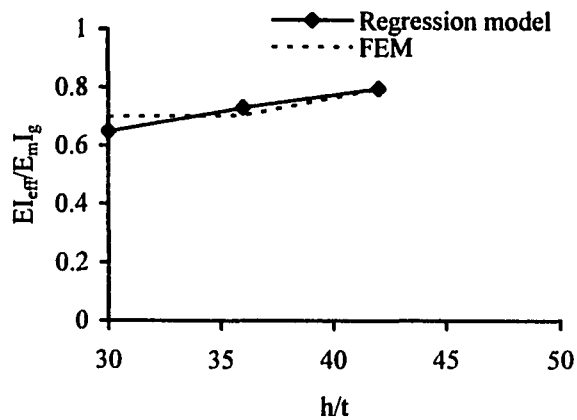


c)  $e/t = 0.42$

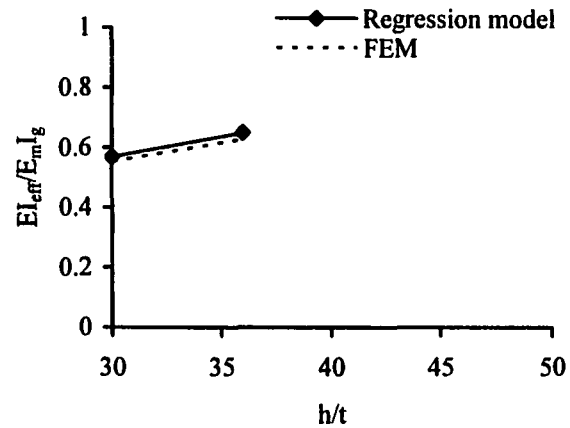
**Figure 7.33 Variation of flexural rigidity ratio predictions against slenderness ratio at support stiffness ratio = 0.03**



a)  $e/t = 0.1$

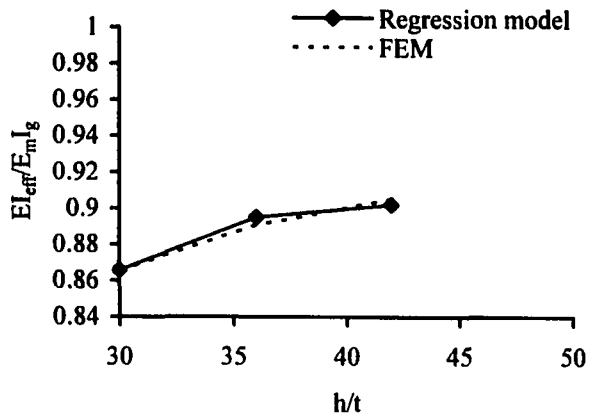


b)  $e/t = 0.33$

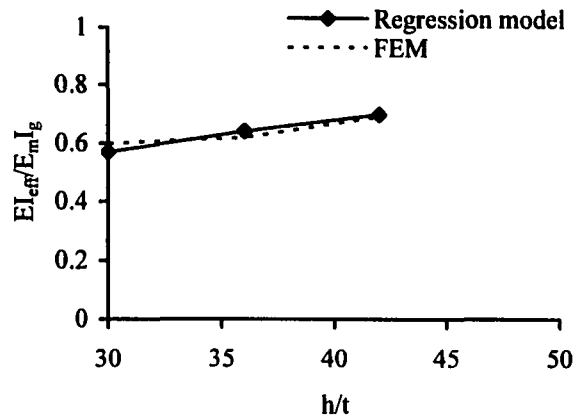


c)  $e/t = 0.42$

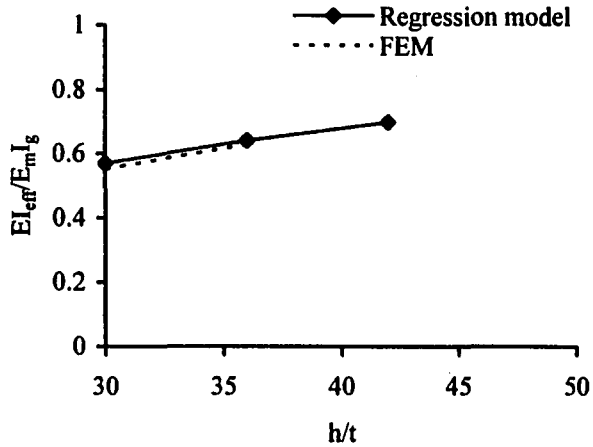
**Figure 7.34 Variation of flexural rigidity ratio predictions against slenderness ratio at support stiffness ratio = 0.05**



a)  $e/t = 0.1$



b)  $e/t = 0.33$



c)  $e/t = 0.42$

**Figure 7.35 Variation of flexural rigidity ratio predictions against slenderness ratio at support stiffness ratio = 0.26**

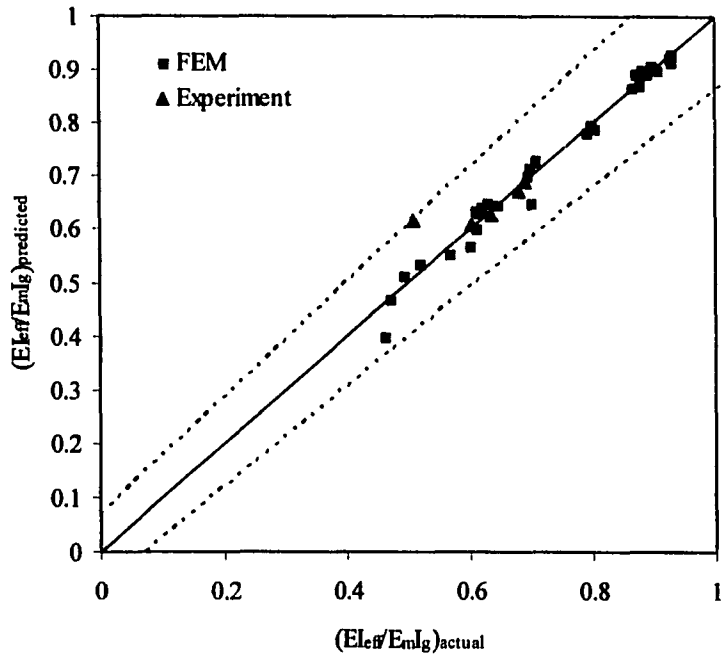


**Figure 7.36 Scatter of flexural rigidity ratio data**

## CHAPTER 8

### SUMMARY, CONCLUSIONS AND RECOMMENDATIONS

#### 8.1 Summary

The objective of this thesis was to study the behavior of tall masonry walls under the influence of implied fixity offered by the masonry wall support. It was evident from an extensive literature search that no research study was available about the masonry wall support interaction. To develop an understanding of the behavior of masonry walls under reactive support conditions the testing of full-scale wall specimens and the development of finite element model for further expansion of the work were the main objectives of the project. The study was specifically focused on slender masonry walls subjected to eccentric axial load supported on strip type foundation.

Extensive numerical studies were performed to estimate the range of rotational stiffness offered by strip footings as a function of field based parameters of modulus of sub-grade reaction of soil and the footing dimensions. Numerically estimated rotational stiffness of support of masonry block walls was then simulated in the laboratory ranging from low to high support stiffness. A total of eight full-scale masonry block wall specimens were divided into two groups of walls with slenderness ratio ( $h/t$ ) of 28.6 and 33.9. Each group was tested under eccentric axial load with  $e = t/3$  and with four common support conditions having rotational capacity of 0kN-m/rad, 1000kN-m/rad, 5000kN-m/rad and 10,000kN-m/rad. Two wall specimens of first group, having  $h/t = 28.6$  and tested with support stiffness 5000kN-m/rad and 10,000kN-m/rad failed locally due to bond and anchorage failure at the top portion of the walls without reaching their full capacity. The bond slip problem was fixed by welding the vertical rebars to steel plate provided at the top of the wall specimens. This technique was able to overcome the problem of bond slip and provided enough moment capacity to

resist the primary moment generated due to eccentrically applied axial load at the top of wall specimens. The rest of the wall specimens attained the full capacity and no further bond slip failure was observed. Despite the fact that first two wall specimens were prematurely failed, the effect of support stiffness was significant on their behavior. The test results were successful and showed a consistent effect of the rotational stiffness of the support on the behavior of masonry block walls at failure. Material testing was also the part of experimental program. Standard prism test was performed on 5 grouted and 5 un-grouted specimens and compressive strength and modulus of elasticity of masonry assemblage were obtained from the prism test results. Material testing phase also included the standard tests of rebar, grout, and mortar.

The load-deflection response and rotation at the bottom of the wall specimens were used to estimate the effective flexural stiffness variation along test history for each specimen. This was done using an analytical solution of the governing differential equation of beam-column subjected to axial load and flexural moment with rotational spring at the bottom.

After completion of the experimental program, a simple and efficient non-linear finite element model was developed, incorporating material and geometric non-linear aspects of the test specimens. The analysis is based on macroscopic analysis approach, which is best suited to capture global behavior of masonry load bearing walls. The finite element model was validated using the experimental results of each tested specimen. The adequacy of the model was demonstrated against the test results by comparing the responses of axial load versus out-of-plane deflections, axial load versus out-of-plane rotations, bending moments and also axial load versus flexural stiffness response.

The numerical and experimental results were in good agreement with each other showing that the numerical model effectively predicts the behavior of masonry load bearing block walls and can be used to extend the findings of experimental

results by analyzing more walls with variety of parameters under the influence of support stiffness. Using the finite element model an extensive parametric study was performed. The support stiffness was considered as the primary parameter and was combined with other key parameters related to geometry and the material properties of the wall. The effect of support stiffness on load carrying capacity, deflection, bending moment, flexural rigidity and failure modes of the masonry block walls was investigated and a comprehensive database was established.

A non-linear regression analysis was conducted on the results obtained from parametric study. The mathematical expressions to estimate normalized axial load capacity and the flexural rigidity under the influence of support conditions were developed. The validity of the proposed mathematical expression was assessed using the available experimental results and found satisfactory.

## **8.2 Conclusions**

The experimental, analytical and numerical investigations of the project lead towards the following conclusions.

The resistance offered by the masonry wall support can be quantified as a function of soil characteristics, type of foundation and the size of foundation.

The full scale testing of eccentrically loaded block wall specimens confirmed the consistent increase in load carrying capacity of the walls under the influence of support stiffness and neglecting the support stiffness leads to underestimation of the wall capacity.

The response of the wall was observed to be affected by level of rotational stiffness offered by the support. The point of maximum deflection shifted upwards along the wall height with increasing magnitude of rotational resistance of reactive support.

The support stiffness improves the behavior of the wall throughout the load history by controlling the detrimental effects caused by wall slenderness and load eccentricity ratio which leads towards the change in failure mode from stability failure to pure compressive failure depending on level of slenderness.

The non-linear characteristics of the wall are influenced by the level of support stiffness. The increasing level of support stiffness influences the cross-sectional behavior and makes the wall to undergo enhanced plastic strains and as a result the wall failure load is increased. For highly slender walls the support stiffness makes the wall cross-section to undergo more tensile-plastic strains, while for the walls with intermediate slenderness ratio the increase in support stiffness decreases the tensile plastic strains by giving rise to compressive plastic strains and as a result in both cases an improved behavior is observed as compared to the situation when no support stiffness is considered.

Support stiffness affects the flexural rigidity of the wall. At constant slenderness and constant load eccentricity the effective flexural rigidity increases when support stiffness is increased from 0 kN-m/rad to 1000 kN-m/rad. Beyond this the increase in support stiffness induces more cross-sectional strains as a result decreases the effective flexural rigidity of the wall at failure.

The current Canadian code which neglects the effect of support stiffness specially, in case of walls with slenderness ratio  $\geq 30$  is quite conservative. The comparison of the axial load capacity of the walls tested and analyzed in the current study with the values as per the Canadian code S304.1-94 recommendation shows that the code underestimates the wall capacities. Similarly a comparison of effective flexural rigidity also indicates that the current Canadian code conservatively provides the effective flexural rigidity of the wall.

The proposed equations reasonably incorporate the support stiffness in estimation of the axial load capacity and the effective flexural stiffness of the walls. There is

however a need of further investigation to make use of these equations in estimation of realistic effective length factor.

### **8.3 Recommendations for Future Research**

In the current study only strip footings were considered. It is recommended to expand the database of support stiffness for other foundation types which are conventionally used in the construction of masonry load bearing walls.

The current study dealt only with eccentrically load walls, it is important to extend the investigations to other loading conditions considering the effect of variety of support conditions.

The definitions of slender and very slender walls provided by the current Canadian Code is very conservative and requires reconsideration.

The proposed equations in the current study for the estimation of axial load capacity and the effective flexural rigidity require further investigation in order to use them for the estimation of effective length factor based on actual support conditions so that use of actual support conditions can be implemented in the conventionally used moment magnification method.

## REFERENCES

- Abboud B.E., Lu X. and Becica I.J. (1995) "Deflection of Reinforced Masonry Walls under Out-of-Plane Loads", 7<sup>TH</sup> Canadian Masonry Symposium, June 1995, McMaster University, Hamilton Ontario, pp. 895-910.
- Ali,S., Page A.W. and Kleeman P.W.(1986)" Non-Linear Finite Element Model for Concrete Masonry with Particular Reference to Concentrated Loads", 4<sup>th</sup> Canadian Masonry Symposium-1986, New Brunswick, pp. 137-148.
- Amrhein, S.E, Lawrance S.G. and Ralph S.Mclean, S.E. (1982) "Testing of Tall Slender Reinforced Concrete and Reinforced Masonry Walls Subjected to Vertical and Lateral Loads" , Proceedings of Second North American Conference, University of Maryland, College Park Maryland, August 1982, pp. 6-1 – 6-8.
- Aridru, G.G. and Dawe J.L. (1995) "Flexural Rigidity of Concrete Masonry Walls" , 7<sup>th</sup> Canadian Masonry Symposium June, 1995, McMaster University, Hamilton Ontario, p.p 1152-1163.
- Chen, W.F. and Atsuta, T. (1973),"Strength of Eccentrically Loaded Walls" , International Journal of Solids and Structures, Vol.9, 1973, pp. 1283-1300.
- Cecchi, A. and Marco R.D. (2002), "Homogenized Strategy toward Constitutive Identification of Masonry", Journal of Engineering Mechanics, Vol. 128, No.6, June 2002, pp. 688-697.
- Cloville, J (1979) "Stress Reduction Design Factors for Masonry Walls" , Journal of The Structural Division, ASCE, Vol. 105, No. ST10, October, pp. 2035-2051.
- Cloville, J. (1992) "Stability of Hollow Masonry Walls" The masonry Society Journal, August 1992, pp. 61-74

Cranston, W.B and Roberts, J.J. (1976) "The Structural Behavior of Concrete Masonry Reinforced and Un-reinforced" The Structural Engineer, No. 11, Volume 54, November 1976.

Creazza G., Matteazzi R., Saetta A. and Vitaliani R.(2002) " Analysis of Masonry Vaults: A macro Approach based on Three-Dimensional Damage Model" , Journal of Structural Engineering Vol. 128, N0.5 May 2002, pp. 646- 654.

CSA Standard CAN3-S304.1-94 (1994) "Masonry Design for Buildings (Limit State Design)" Rexdale, Ontario, 73 pages

Drysdale, and R.G Hamid, A.A., (1984) "Tensile Failure Criteria for Plain Concrete Masonry", Journal of Structural Engineering, Vol. 110, No.2 February, 1984, pp. 228-244.

El-Metwally,Saleh E.E, Ashour, A.F. and Chen W.F. (1991) " Behavior and Strength of Concrete Masonry Walls" , ACI Structural Journal, Vol.88,No.1, January-February 1991, pp.42-48.

Giambanco, G., Rizzo Santi and Spallino R.(2001)"Numerical analysis of masonry structures via interface models", Computer Methods in Applied Engineering Mechanics and Engineering, Vol. 190 2001, pp. 6493-6511

Giordano A., Mele,E. and Luca, A. D. (2002) "Modelling of historical masonry structures: comparison of different approaches through a case study", Engineering Structures Vol. 24, No.8, August 2002, pp. 1057-1069.

Goyal A., (1992), "Shear Connected Cavity Walls under Vertical Loads", MSc. Thesis, University of Alberta, September 1992.

Hamid, A.A., and Drysdale, R.G. ( 1979), “Suggested Failure Criteria for grouted Concrete Masonry Under Axial Compression”, ACI Journal Oct., pp. 1047-1067.

Hatzinikolas, M.A., Longworth, J. and Warwaruk, J. (1978), “ Buckling of Plain Masonry Walls with Initial Double Curvature” North American Masonry Conference, University of Colorado, Boulder, Colorado USA, pp. 87-2 -87-14.

Hatzinikolas, M.A., Longworth, J. and Warwaruk, J. (1980), “Failure Modes for Eccentrically Loaded Concrete Block Masonry Walls”, ACI Journal No.17-28, July –August 1980.

Hibbit, Karlsson and Sorensen(2002), ABAQUS, Version 6.3, (software package) Hibbit Karlsson and Sorenson Inc., Pawtucket, RI.

Hibbit, Karlsson and Sorensen,(2002), ABAQUS/Explicit User’s Manual Explicit Getting Started Manual, Version 6.3, Vol.-I and Vol.-II, Hibbit Karlsson and Sorenson Inc., Pawtucket, RI.

Jäger,W. and Pflücke,T. (2001) “ Buckling Safety of Masonry Walls Under Consideration of Nonlinear Stress-Strain-Relationships”, 9<sup>th</sup> Canadian Masonry Symposium, Department of Civil Engineering, University of New Brunswick, June 2001.

Liu,Y., Aridru, G.G. and Dawe J.L. (1998) “Effective Flexural Rigidity of Concrete Masonry Walls” , 8<sup>th</sup> Canadian Masonry Symposium June, 1998, Jasper, Alberta, p.p 18-24.

Liu, Y. and Dawe J.L. (2001) “Experimental determination of masonry beam-column behavior”, Canadian Journal of Civil Engineering, Vol. 28, pp. 794-803, October,2001.

Liu, Y. and Dawe J.L. (2003) "Analytical Modeling of Masonry Load-Bearing Walls", Canadian Journal of Civil Engineering, Vol.30,2003, pp.795-806.

Lopez, J. Oller, S., Onate, E. and Lubliner J.(1999) " A homogeneous Constitutive Model for Masonry" , International Journal for Numerical Methods in Engineering, Vol. 46, pp. 1651-1671, 1999.

Lotfi, H.R., P.B. Shing (1994) "Interface Model Applied to Fracture of Masonry Structures", Journal of Structural Engineering, ASCE, Vol.120, No.1, pp.63-80.

Ma,G.,Hao H.,Lu Y. (2001) " Homogenization of Masonry Using Numerical Simulations", Journal of Engineering Mechanics, Vol. 127,No.5 May 2001, pp. 421-431.

Maksoud, A. and Drysdale R.G.,(1993,a) "Numerical Modeling of Masonry Walls" 6th North American Masonry Symposium, Saskatoon, Saskatchewan, June 15-17, pp. 801-811.

Maksoud, A. and Drysdale R.G., (1993,b) "Rational Moment Magnification Factor for Slender Un-reinforced Masonry Walls" The 6<sup>th</sup> North American Masonry Conference Philadelphia, Pennsylvania, The Masonry Society, June 6-9, pp. 443-454.

Page, A.W. (1978), "Finite Element Model for Masonry" Journal of Structural Division, ASCE, Vol. 104, No. ST, August 1978, pp. 1267-1285.

Sayed-Ahmed, E.Y. and Shriver, N.G. (1993) "A Model of Face-Shell Bedded Hollow Masonry Using 2-D Finite Element" Sixth North American Masonry Conference June 6-9, pp. 419-430.

Sayed-Ahmed, E.Y. and Shrive, N.G. (1996) "Nonlinear Finite Element Model of Hollow Masonry" *Journal of Structural Engineering*, Vol.122, No.6 June 1996, pp. 683-1587.

Schultz, A.E., Ojard N.J. and Stolarski, H.K. (2001) "Critical Loads for Transversely Loaded Masonry Walls" , 9<sup>th</sup> Canadian Masonry Symposium , Department of Civil Engineering, University of New Brunswick, June 2001.

SPSS, Inc., 2003 SigmaPlot 8.0 (Software Package), SPSS Inc. Chicago Illinois.

Suwalski, P.D., Drysdale, R.G. (1986), "Influence of Slenderness on the Capacity of Block Walls" *Proceedings of the Fourth Canadian Masonry Symposium*, pp 122-135.

Wang, R., Elwi, A.E., Hatzinikolas, M.A. (1997b) and Wawaruk, J., "Tests of Tall Masonry Cavity Walls Subjected to Eccentric Loading," *ASCE Journal of Structural Engineering*, 123(7), July 1997, pp. 912-919

Yao, C. (1989), "An Alternate Basis for Concrete Masonry Under Eccentric Compression" *Proceedings Fifth Canadian Masonry Symposium*, June 1989, Vancouver B.C., pp 145-154.

Yao. C. and N.D. Natahn (1989) "Axial Capacity of Grouted Concrete Masonry" *Fifth Canadian Masonry Symposium*, June, University of British Columbia, Vancouver, B.C., Canada

Yi J. Shrive, N.G. (2001), "3-D Finite Element Models of Plain and Bond-Beamed Hollow Masonry Walls subjected to Concentric and Eccentric Concentrated Loads" *Ninth Canadian Masonry Symposium Canadian Journal of Civil Engineering*, February 2003, vol. 30, no. 1, pp. 203-211.

Yokel, F.Y. and Dikkers, R.D. (1971,b), "Strength of Load Bearing Masonry Walls", *Journal of the Structural Division, Proceedings of the ASCE*, Vol.97, May 1971, pp. 1593-1609.

Yokel, F.Y. (1971), "Stability and Load Capacity of Members with no Tensile Strength", *Journal of the Structural Division, Proceedings of the ASCE*, Vol.97, No. ST7, July 1971, Proc. Paper 8253, pp. 1913-1926.